Experimental Investigation into the Behavior of Geocell-Reinforced Bases under Freeze-Thaw Cycles

by

Mian Huang

B.Sc., Chinese University of Mining and Technology-Beijing, 2012

M.Sc., Chinese University of Mining and Technology-Beijing, 2015

A Dissertation Submitted in Partial Fulfillment of the

Requirements for the Degree of

DOCTOR OF PHILOSOPHY

in the Department of Civil Engineering

University of Victoria

We acknowledge and respect the lək̓ʷəŋən peoples on whose traditional territory the university stands and the Songhees, Esquimalt and W̱SÁNEĆ peoples whose historical relationships with the land continue to this day.

Experimental Investigation into the Behavior of Geocell-Reinforced Bases under Freeze-Thaw Cycles

by

Mian Huang

B.Sc., Chinese University of Mining and Technology-Beijing, 2012

M.Sc., Chinese University of Mining and Technology-Beijing, 2015

Supervisory Committee

Dr. Cheng Lin, Supervisor

Department of Civil Engineering

Dr. Min Sun, Departmental Member

Department of Civil Engineering

Dr. Sanat Pokharel, Outside Member

Stratum Logics

Abstract

Freeze-thaw (F-T) cycles significantly contribute to the deterioration of roadways in seasonal frost regions. Among various countermeasures to mitigate F-T damages, the application of geocells for base stabilization has demonstrated its effectiveness in enhancing the F-T performance of road bases due to their three-dimensional stiffening and reinforcing effects. Despite the practical success of the use of geocells in base stabilization, a scarcity of research has focused on qualitative or quantitative evaluation on the benefits of geocells in improving the F-T performance of bases.

To address this research gap and assess the F-T performance of geocell-stabilized bases, this study conducted a series of laboratory element and model tests as well as full-scale field tests. This study first introduced the development of a customized model test apparatus capable of performing unidirectional F-T tests and plate loading tests on the geosynthetics-stabilized bases in Chapter 1. Utilizing this apparatus, influencing factors of fines content (Chapter 2), water supply and compaction degree (Chapter 3) were investigated directly. Furthermore, the F-T effect on the mechanical behavior of geocell-stabilized soils was explored through elements tests, serving as a complement to the comprehensive assessment (Chapter 4).

A significant portion of this study involved comprehensive full-scale field tests that comparatively investigated the efficacy of applying geocells and geogrid composites in a flexible pavement in Alberta, Canada. This comparison was made across three test sections stabilized with two types of Novel Polymeric Alloy (NPA) geocells and a geocomposite. A full instrumentation program with the design and installation of different sensors such as earth pressure cells, thermocouples, and moisture sensors was introduced in Chapter 5. Short-term testing and long-term monitoring were implemented. Short-term tests included plate loading tests and trafficking tests before and after the first seasonal F-T cycles, while the long-term monitoring focused a 12-

month monitoring of soil temperatures, moisture contents and loads transferred to the subbases after open to general traffic (Chapter 6).

The results of the experimental tests including element and model tests was field investigations significantly contributed to the understanding of the effectiveness of geocell stabilization in mitigating F-T induced damages, providing insights into the underlying stabilization mechanisms.

Table of Contents

Table of Tables

Table of Figures

Acknowledgements

Completing the doctoral program at the University of Victoria has been an incredibly transformative experience, a journey that I could not have embarked on without the support, guidance, and encouragement of many individuals and institutions.

Firstly, I am profoundly grateful to my supervisor, Dr. Cheng Lin, for not only offering me this PhD position but also for opening doors to academic and industrial opportunities. His support in teaching assistance, academic conferences, and internships has been pivotal in refining my professional skills and gaining invaluable field experience. Dr. Cheng Lin's expertise, guidance, and encouragement have been instrumental in the completion of my research. I am deeply thankful for his supervision, which challenging me to expand my boundaries and approach my research with greater critical and thoughtful consideration.

My heartfelt thanks extend to my outside committee member, Dr. Sanat Pokharel of Stratum Logics, whose professional insights and supports in both laboratory model tests and full-scale field tests have been invaluable. His contributions have not only enriched manuscripts by tightly integrating industrial perspectives but also supported me to undertake full instrumentation of flexible pavements and perform full-scale field tests. His guidance and management were crucial in the completion of my dissertation. I am also grateful to my department committee member, Dr. Min Sun, for his insightful comments and encouragement. His challenging questions inspired me to broaden my research from various perspectives, and his feedback was instrumental in shaping my research proposal.

I would like to express my appreciation to the faculty and staff in the Department of Civil Engineering at the University of Victoria. Special thanks to Dr. Armando Tura for his work on the thermodynamic simulation and mechanical design of the model test apparatus. My gratitude also

goes to Dr. Phalguni Mukhopadhyaya and Ms. Bohan Shao for their support in obtaining the thermal properties of soils for the thermodynamic simulation. I am thankful for the department technicians - Geoff Burton, Mitch Anderson, Solomon Rosenberg, Bastien Lanusse, and Arielle Garrett - for their assistance in setting up the model test apparatus and preparing for the tests.

My profound gratitude is extended to Mr. Marc Breault, Mr. Arghya Chatterjee, Ms. Taylor Dagenais, Mr. Murtaza Ali, Mr. Arnold Gozales, and other staff from Stratum Logics for their assistance during the full-scale field tests. Their support has been greatly appreciated. I am also thankful to Ian Milne from Campbell Scientific for his assistance in setting up and repairing the data acquisition system.

I am grateful to my colleagues Yunjie Lin, Randall Wu, Jefferson Wu, Jiming Liu, Minghao Liu, and Teddy Zhou for their help with the laboratory model tests and field tests.

Special appreciation goes to my parents, and my wife, Xu Yang, for their unwavering support and continuous encouragement throughout my years of study and the research and writing process of this dissertation. This accomplishment would not have been possible without them. Thank you, Mom, Dad, and Xu Yang, for always believing in me.

Lastly, I must acknowledge the communities and institutions that financially supported my study, Natural Sciences and Engineering Research Council (NSERC), MITACS, and the Geosynthetic Institute (GSI).

Dedication

The author dedicates this work to his families, supervisors, and friends.

Chapter 1 Model Tests of Freeze-Thaw Behavior of Geocell-Reinforced Soils

1.1 Abstract

Freeze-thaw cycles are a major cause for destabilizing pavements in cold regions. Among countermeasures for freeze-thaw damages, use of geocells to reinforce pavement bases is an effective solution in practice. However, as opposed to widespread applications, research concerning freeze-thaw behavior of geocell-reinforced bases is limited, probably due to a lack of proper devices for conducting experimental tests. This paper presents a new model-test device capable of performing both freeze-thaw tests and plate loading tests on geocell-reinforced soils. A thermodynamic numerical model was developed to assist with the design of freeze-thaw component of the device, while the design of plate loading component was developed by referring to features of existing devices. Eleven tests were run on geocell-reinforced and unreinforced sands to confirm the effectiveness of the proposed device. The test results showed the device successfully provided vertical heat transfer in sands during freeze and thaw. After five freeze-thaw cycles, geocells reduced peak frost heave and thaw settlement of sands by 18% and 34%, respectively, and increased the stiffness and bearing capacity by 40% and 253%, respectively. It was found a temperature drop occurred at the interface between cooling plate and sands, which was due to the existence of thermal contact resistance.

1.2 Introduction

Freeze-thaw (F-T) cycles, a natural phenomenon resulting in frost heave and thaw weakening of soils, are a major cause for pavement damage in seasonal frost regions. The freeze-thaw related damage is more severe in unpaved roads as the surface layer that consists of unbound granular base materials is more prone to water infiltration and distress by heavy traffic loads. A comprehensive review by Qi et al. (2006) indicates that F-T cycles play an important role in

altering engineering properties of soils: for example, compacted soils may become looser due to the F-T induced microstructural changes to the soils (Viklander, 1998); soils experience apparent reduction in resilient modulus (Lee et al., 1995; Simonsen et al., 2002) and undrained shear strength (Leroueil et al., 1991) when subjected to only one or two F-T cycles in a closed system. Experimental investigation indicates that even F-T insusceptible gravels could undergo a remarkable decrease in California Bearing Ratio (CBR) (by approximately 40%) after five F-T cycles in a closed system (Kawabata et al., 2016). The F-T damage is mainly attributed to the frost heave and thaw weakening of soils induced by the change of water phase and water redistribution. During the freezing process, a frozen fringe is formed, behind which water in the pore of soils turns into ice, causing the volume increase in the frozen zone (Andersland and Ladanyi, 2004; Zeinali et al., 2016). The phase change of water creates suction that forces the water to migrate towards the frozen fringe (Bing et al., 2015; Zhang et al., 2018). During the thawing process, ice in the frozen zone gradually melts and the melted water accumulates in the thawed soils above the remaining frozen zone, therefore weakening the soils. This is why the pavement damage often occurs in the spring thaw (Simonsen and Isacsson, 1999) and substantial reduction in the modulus of base and subgrade is found by the end of thawing seasons (Jong et al., 1998).

In practice, many measures are taken for mitigating the F-T damage of roads, which include replacing frost susceptible fines with gravels, spraying calcium chloride on road surfaces, stabilizing subgrade with chemical additives such as cement, draining subgrade with aggregate columns, reinforcing bases with geosynthetics, draining base courses with wicking geotextiles, and creating drainage layer and capillary barrier with geocomposite (Christopher et al., 2000; Edil et al., 2002; Guo et al., 2019; Helstrom et al., 2006; Henry et al., 2000; Lai et al., 2012; Li et al., 2017a, 2017b, 2019). Among these countermeasures, geosynthetics has been widely used to

reinforce subbase and base courses to improve the performance of roadways since 1970s (Giroud and Han, 2004a; Han and Jiang, 2013). As a special type of geosynthetics, geocells are three-dimensional forms of honeycomb-like interconnected geosynthetic cells that provide effective confinement of the encapsulated soils. Increasing evidence from practical applications has demonstrated that geocells are effective in enhancing the durability of pavements in seasonal frost regions (Henry et al., 2005; Pokharel et al., 2015, 2017). Based on a full-scale test, Henry et al. (2005) showed the benefit of geocells in preventing the distress of unpaved roads subjected to one F-T cycle in Vermont, US. Pokharel et al. (2015) also reports the successful use of geocells to improve serviceability of heavy-volume roads in British Columbia and Alberta, Canada. Based on a long-term (2-3 years) monitoring of a test section of paved road in Alberta, Canada, Pokharel et al. (2017) found that the section with geocell-reinforced bases performed better than that with cement treated bases. Although it is important to perform field tests, they suffer from disadvantages of high construction cost, prolonged testing time, and the difficulty in controlling the test conditions and conducting parametric studies. Laboratory model tests are therefore an important complement to the field tests as they are cost-effective and particularly useful in evaluating the various key factors affecting the performance of geocell-reinforced soils. However, experimental investigation of the F-T behavior of geocell-reinforced soils is rather scarce.

At present, the laboratory model tests, also known as plate loading tests, are commonly conducted in room temperature to investigate the behavior of geosynthetics-reinforced soils and calibrate the corresponding design methods (Giroud and Han, 2004b; Mehrjardi et al., 2019; Pokharel, 2010; Shadmand et al., 2018; Wang et al., 2018). However, it is important to note that these devices are run only in room temperature, which, however, are unable to implement F-T cycles to the soils.

The objective of this study is to develop a new model test device, which enables F-T tests and plate loading tests to be run on geocell-reinforced soils. Using the proposed device, F-T tests were conducted to investigate the distribution of temperatures in soils and verify the feasibility of the device in performing F-T cycles. After F-T tests, plate loading tests were conducted to investigate the effects of F-T cycles on the mechanical behavior of both geocell-reinforced and unreinforced soils.

1.3 Development of the Test Device

The proposed device includes an F-T component, a rail connecting component, and a plate loading component. The F-T component was developed utilizing the results of thermodynamic numerical analyses, the rail connecting component was designed to connect the F-T component and the plate loading component, and the plate loading component was developed by referring to the basic information of the existing plate loading devices in the literature, as summarized in Table 1.1. Table 1.1 shows that a typical setup of a laboratory-scale plate loading test consists of a box filled with geosynthetics-reinforced soils and a loading frame. The box is primarily square with the side width between 0.5 m and 3 m, and the loading plate is circular with the diameter ranging between 150 mm and 300 mm. The load imposed by the plate is static or cyclic. The information of Table 1.1 enables us to identify the proper size of the F-T box and the size of loading plate for our device, and therefore the plate-loading results obtained from our tests can be comparable to those from others.

Table 1.1. Summary of plate loading test devices for geosynthetics-reinforced soils

References	Box		Loading plate		Loading type	Geosynthetics	Infill materials	Foundation materials
	Length × width (mm)	Material	Shape	Size (mm)				
Rea and Mitchell (1978)	914 × 914	- [a]	Circular	51 - 152 [b]	Static and cyclic	Geocell	Fine sand	Spring base
Guido et al. (1986)	1220 × 1220	Plexiglas	Square	305 × 305 [c]	Static	Geogrid and geotextile	Sand	Sand
Al-Qadi et al. (1994)	3100 × 1800	Reinforced concrete	Circular	300	Cyclic	Geogrid and geotextile	Granite aggregate	Silty sand
DeMerchant et al. (2002)	3200 × 2200	-	Circular	305	Static	Geogrid	Lightweight aggregate	Lightweight aggregate
Tingle and Jersey (2005)	1830 × 1830	Steel	Circular	305	Cyclic	Geogrid and geotextile	Limestone	High-plasticity clay
Chang et al. (2007)	457 × 457	Steel	Circular	51	Cyclic	Geocell	Sand	Sand
Chang et al. (2007)	1500 × 900	Steel	Circular	200	Static	Geocell	Sand	Sand
Emersleben and Meyer (2008)	2000 × 2000	-	Circular	300	Static	Geocell	Sand	Mixture of glycerin and bentonite
Pokharel et al. (2010)	600 × 600	Wood	Circular	150	Static	Geocell	Sand and quarry waste	Rigid base [d]
Zhang et al. (2010)	1300 × 650	Reinforced concrete	Circular	236	Static	Geocell	Crushed stone	Clay
Thakur et al. (2012)	2200 × 2000	Steel	Circular	300	Cyclic	Geocell	Recycled asphalt pavement	Mixture of sand and kaolin
Tanyu et al. (2013)	3000 × 3000	Reinforced concrete	Circular	250	Cyclic	Geocell	Gravel	Expanded polystyrene

Rajagopal et al. (2014)	1200 × 1200	Steel	Circular	150	Static and cyclic	Geogrid, geotextile, and geocell	Gravel	Sand
Hedge et al. (2014)	900 × 900	Cast iron	Square	150 × 150	Static	Geocell and geogrid	Sand	Sand
Saride et al. (2015)	1000 × 1000	Steel	Circular	150	Cyclic	Geocell	Sand	Sand
Abu-Farsakh et al. (2016)	2000 × 2000	Steel	Circular	305	Cyclic	Geogrid and geotextile	Limestone	High-plasticity clay
Dutta and Mandal (2016)	850 × 750	Steel	Square	170 × 170	Static	Geocell	Fly ash	Soft clay
Nair and Latha (2016)	750 × 750	Steel	Circular	150	Cyclic	Geogrid, geotextile, and geocell	Aggregate	Low-plasticity clay
Tafreshi et al. (2016)	1000 × 1000	Plexiglas and steel	Circular	112.8	Static	Geocell and geotextile	Sand	Sand
Aghda et al. (2019)	1200 × 700	Fiberglass	Circular	150	Cyclic	Geocell	Sand	Dredge sand
George et al. (2019)	1830 × 1830	Steel	Circular	152.4	Cyclic	Geocell	Recycled asphalt pavement	Low-plasticity clay
Mamatha and Dinesh (2019)	2000 × 2000	Steel	Square	300 × 300	Cyclic	Geocell	Gravel	Expansive soil

[a] Not given in references.
[b] Diameter of circular loading plate.
[c] Length × width of square loading plate.
[d] Box bottom acting as foundation

Fig. 1.1 shows the schematic layout of the testing equipment that is composed of an F-T component, a rail connecting component, and a plate loading component. The F-T component is built to mimic the natural F-T process in the pavement layers. This component consists of a cooling plate connected to a chiller and a square F-T box with 750 mm in width and four walls that can be adjusted for the height through adding or removing detachable plates (with 230 mm height for a plate) in the walls. The adjustable wall height (up to 760 mm maximum) enables investigating various thickness of soils. As noted later, the present test only required one plate for each wall as only 170-mm thick soils were investigated. To achieve the vertical temperature change in soils, the horizontal heat exchange between soils and the surrounding air should be minimized during the freeze and thaw process. This is normally achieved by covering the box with insulation. However, for the size of the proposed F-T box, to maintain the vertical heat transfer in soils would require impractically thick insulation and a large temperature chamber to maintain relatively low ambient temperature. This would increase the cost and require additional laboratory space. To overcome these limitations, in our preliminary design, we considered the use of a thermal shield, consisting of an aluminum enclosure, to substantially reduce the insulation thickness. It was hypothesized that the aluminum walls, if connected to the cooling plate, could function as a heat sink, minimizing thermal leaks from the environment into the soil sample during the F-T process. This way, the F-T tests can be performed at room temperature with relatively thin insulation foam. During the thawing process, the cooling plate is heated to transfer warm temperature to soils, and the cooling plate is disconnected from the aluminum walls to prevent the soils from being heated from the sides and the bottom. The above design concept for the F-T component could help to achieve the unidirectional F-T process in the soils. To confirm this, a thermodynamic numerical analysis was performed. The numerical analysis results were also used

to determine the proper thickness of insulation and of the aluminum plates and fine tune other design details, such as controlling the thermal bridging between the cooling plate and the thermal shield. The thermal shield wall thickness and its thermal connection to the cooling plate play a critical role to minimize environmental thermal leaks, while not introducing cooling from the sides and the bottom of the aluminum box.

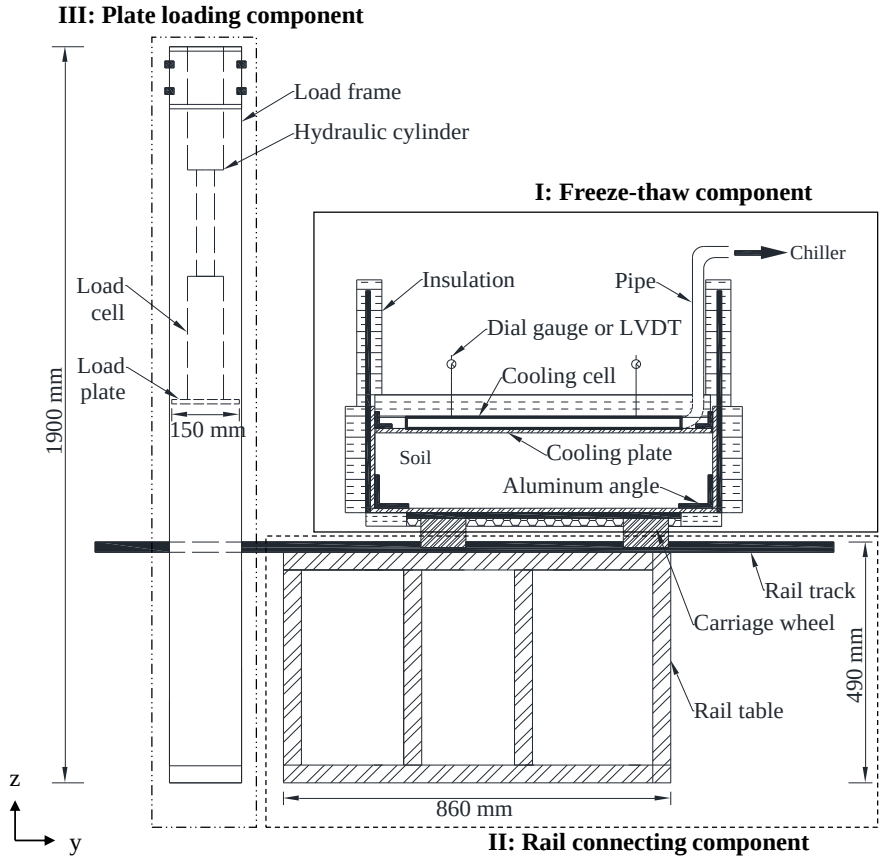

Fig. 1.1. Schematic of the proposed test device

1.3.1 Thermodynamic simulation

Thermodynamic simulation was carried out for the preliminary design of F-T box using a commercial software package, *SolidWorks* where only freezing process was considered. Fig. 1.2 shows the numerical model for the F-T box filled with sands.

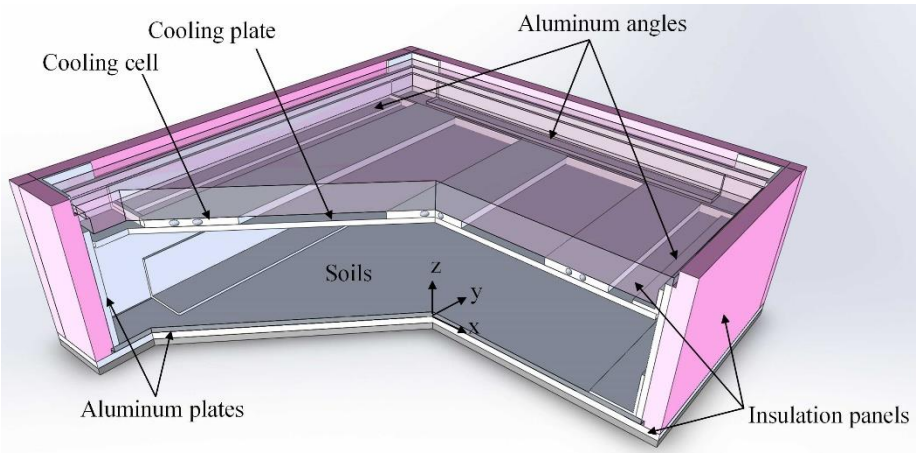

Fig. 1.2. Numerical model for thermodynamic analysis

Table 1.2 presents input parameters for the numerical model, including the basic properties of soils, aluminum walls, and insulation. Soils used were poorly graded sands with moist density of 2.15 g/cm^3. The soil-water matrix in this model was lumped as a homogenous and isotropic medium whose thermal conductivity was measured by using NETZSCH® Heat Flow Meter *436 Lambda* based on the method by Clarke et al. (2017). The thickness of aluminum walls was determined based on their thermal property to shield against thermal leaks from environment. The insulation considered was rigid insulation panels whose thermal conductivity was same as the parameter of commercial insulation foam and whose thickness was predetermined to be 50.8 mm (2 inches) based on the typical values ranging between 25.4 m (1 inch) and 101.6 mm (4 inches). If the numerical simulation indicates the predetermined thickness is inadequate, thicker aluminum walls and insulation panels will be used. In the numerical model, the aluminum-sand interface was assumed to provide negligible thermal contact resistance. The cooling plate was connected to the box walls. Therefore, the model was symmetric along y-axis as shown in Fig. 1.2, and only half-size numerical model was built. The boundary conditions of the numerical model included the heat transfer of coolant circulated between chiller and cooling plate, and the convection between the device and ambient environment.

Table 1.2. Parameters used in the thermodynamic numerical model

Properties	Value
Thermal conductivity of sand (W/m °C)	3.72
Thermal conductivity of aluminum wall (W/m °C)	140
Thermal conductivity of insulation foam (W/m °C)	0.04
Thickness of sand (mm)	170
Thickness of aluminum wall (mm)	10
Thickness of insulation foam (mm)	50.8
Ambient temperature (ºC)	20
Natural convection between device and ambience (W/m^2 °C)	10

The numerical analysis was only focused on thermal behavior of soils at the steady freezing as the numerical software could not simulate the latent heat during water phase change. Moreover, we assumed that the inclusion of geocells in the soils had no effect on the heat transfer, and therefore, the heat transfer in geocell-reinforced soils was not analyzed. Fig. 1.3 depicts the cross-sectional contour of temperature in soils when the averaged soil temperature was around -14°C (steady freezing state). It shows that the cold temperature in general progressed uniformly downward during the freezing process. It is also evident that the rapid temperature drop occurred at the exterior surface of the aluminum walls, confirming the heat sink effect of the aluminum walls.

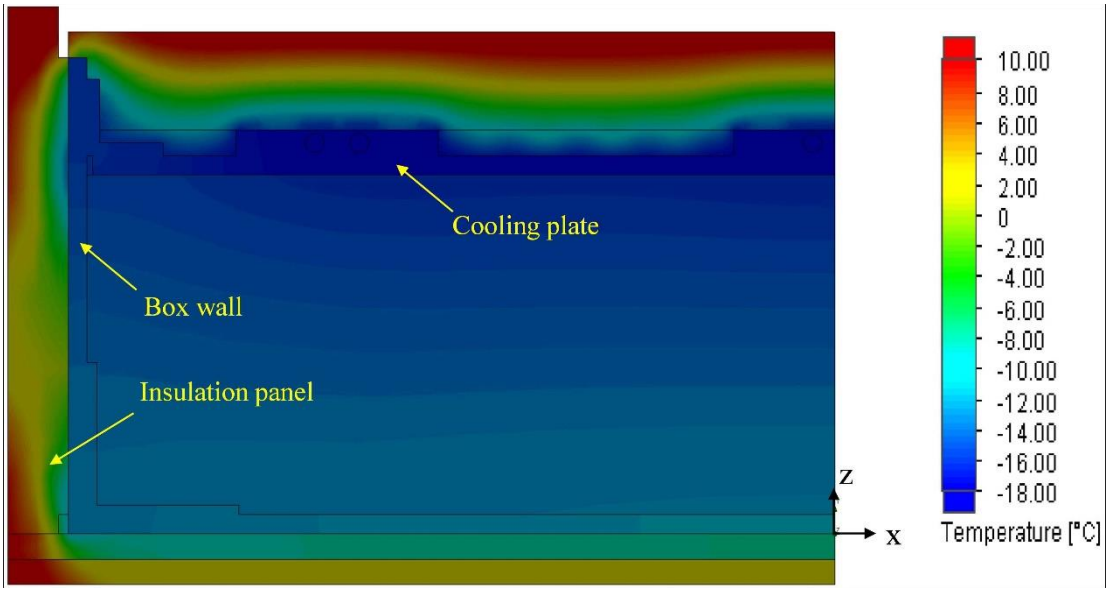

Fig. 1.3. Calculated cross-sectional distribution of temperature at steady freezing state

Overall, the numerical modeling results demonstrate that the proposed device with aluminum walls is able to achieve vertical freezing in soils. The predetermined thickness of insulation (50.8 mm) and aluminum wall (10 mm) was found to be adequate and will be used for the design and fabrication of the F-T component.

1.3.2 Freeze-thaw component

The refined design of F-T component including an F-T box, a cooling plate, and a chiller is indicated in Figs. 1.4 and 1.5. Fig. 1.4(a) presents the design details of the F-T box resting on the rail track, while Figs. 1.4(b) and 1.4(c) show the photographs of F-T box in operation and the empty box, respectively. The box's dimensions remain the same as those in the preliminary design. The thickness of aluminum walls and insulation is consistent to that used in the numerical modeling. The walls are made of the aluminum rectangular plates bolted to the four vertical aluminum angles [Fig. 1.4 (c)] so the wall height is adjustable by adding or removing the aluminum plates. The bottom plate of the box is also made of aluminum with the same thickness as the aluminum walls. A layer of insulating neoprene sponges [in black in Fig. 1.4(c)] is attached to the

exterior side of the aluminum plates to fill the gap between insulation and the plates. This gap results from the discontinuous surface between the plates and the aluminum angles. If the gap is not filled, it could result in the water condensation and ice formation on the walls during the freezing process. The insulation is made of rigid polystyrene insulation panels, which are used to seal around the box except the box bottom as it sits on the rail track [Fig. 1.4(a)]. The details of insulation for the box bottom will be described in the section of rail connecting component. A brass inlet port with a valve is mounted at the box bottom [Fig. 1.4(a)] to control the water supply so that both closed and open systems can be tested in the F-T component.

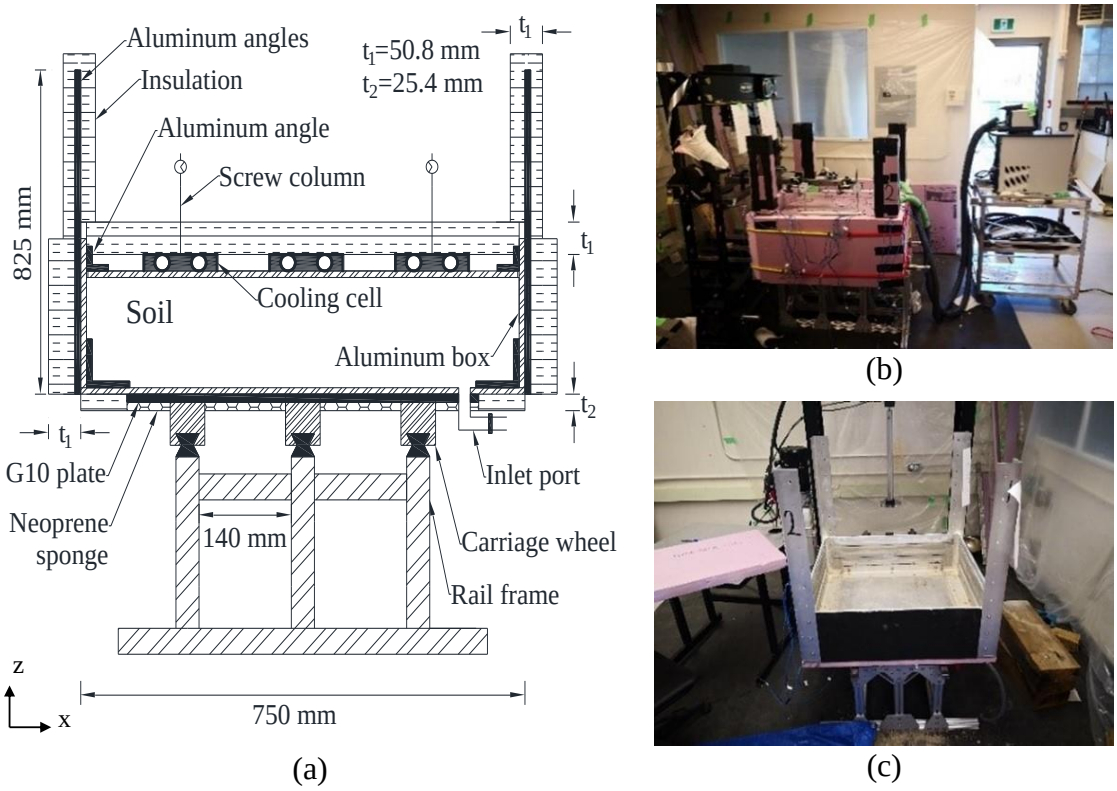

Fig. 1.4. Freeze-thaw component: (a) design of freeze-thaw box, (b) photograph of freeze-thaw component in operation, and (c) photograph of empty box

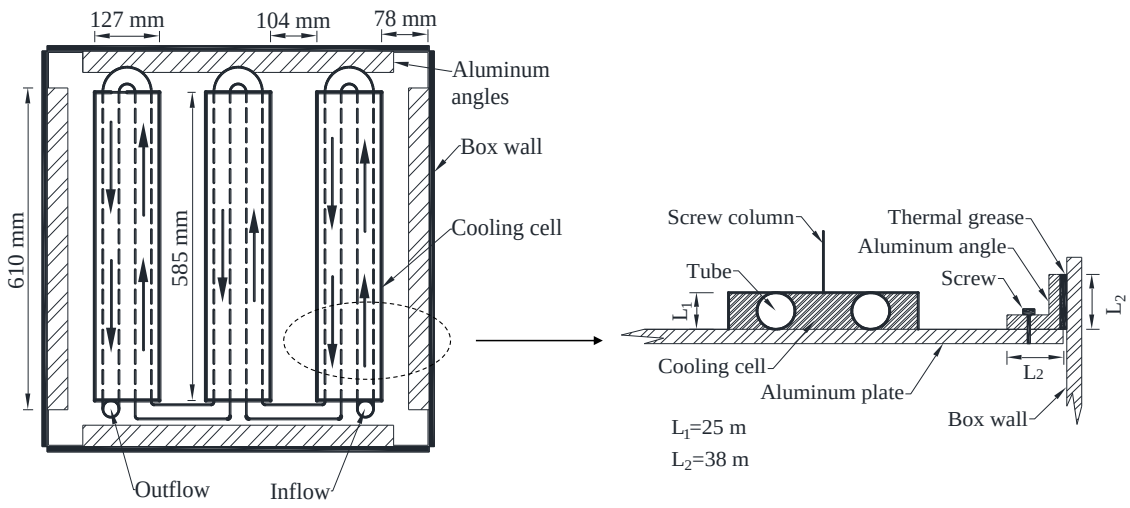

(a)

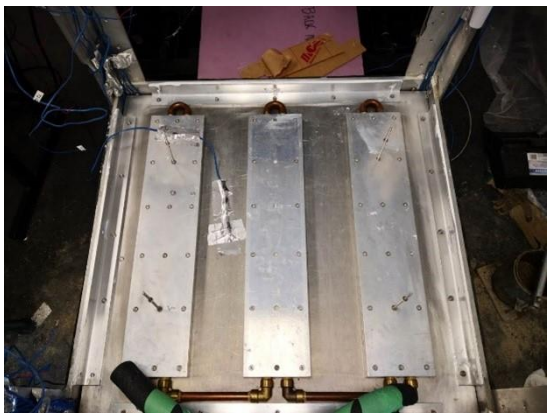

(b)

Fig. 1.5. Cooling plate: (a) design details and (b) photograph

Figs. 1.5(a) and 1.5(b) show the design and photograph of the cooling plate, respectively. Three cooling cells are mounted on a square aluminum plate with the width of 745 mm and thickness of 10 mm. The cooling cells are linked by a serpentine copper tube with its two ends connected to a chiller. By circulating the coolants in the copper tube, the cooling plate is either cooled or heated. The chiller is the VWR® refrigerated circulating bath with working temperatures ranging from -40°C to 200°C and temperature stability of ±0.01°C. The coolant is a mixture of 70% LORDCO® antifreeze and 30% water and has freezing and boiling temperatures of -64°C and 135°C, respectively.

The width of cooling plate is 5 mm shorter than the inside width of F-T box. Therefore, there is a 2.5-mm gap between the lid of cooling plate and the box walls. The small gap is needed for placement of the cooling plate and the free vertical movement of the plate during the F-T process. However, the gap blocks the heat transfer between the cooling plate and the walls during the freezing process, which disables the walls as a heat sink. To address this issue, four horizontal aluminum angles are installed to connect the cooling plate and four walls [Figs. 1.5(a) and 1.5(b)]. The wires of embedded sensors could come out from the gaps at the corners [see Fig. 1.5(a)]. One side of the aluminum angle is screwed to the cooling plate while the other side is attached to the walls with thermally conductive grease. The use of thermally conductive grease can not only maintain high interface thermal conduction but also minimize the interface friction that may resist the vertical movement of the cooling plate caused by soil freeze and thaw. It is noted that the aluminum angles are only used in the freezing process. They are removed in the thawing process to prevent soils from absorbing excessive heat through the box walls.

1.3.3 Rail connecting component

The rail connecting component is used to connect the F-T component and the plate loading component. The schematic of the rail connecting component is shown in Fig. 1.1, the connection between F-T box and rail track in Fig. 1.6(a), and its photograph in Fig. 1.6(b). The advantage of using rail is that soil/geocell preparation, installation of cooling plate and insulation, and F-T tests can be all completed outside the loading frame. When plate loading tests are to be performed, the F-T box is moved back to the loading frame through the rail tracks.

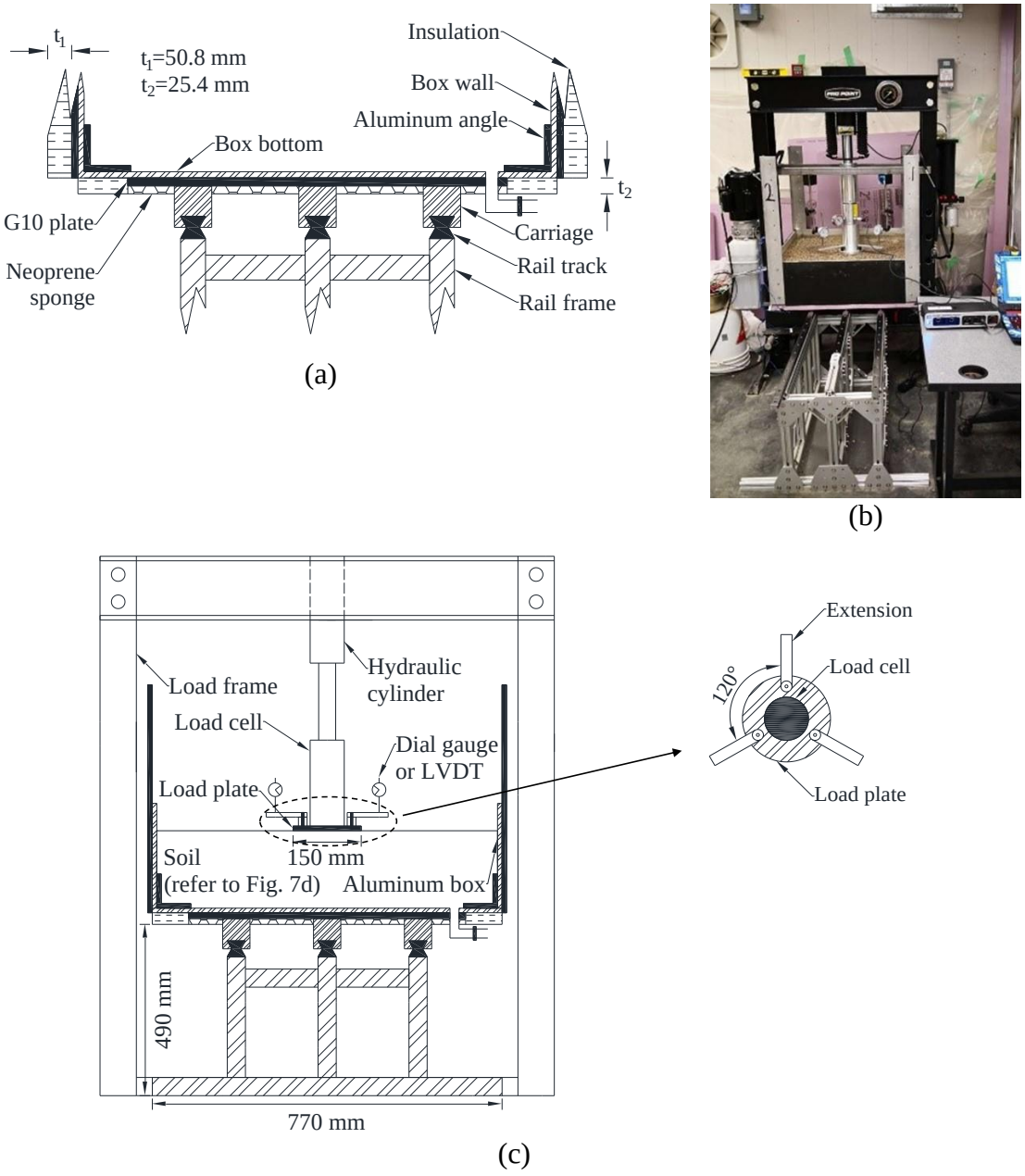

Fig. 1.6. Rail and plate-loading components: (a) details of box bottom and rail, (b) photograph of rail and plate loading components, and (c) plate loading component

The rail connecting component consists of three parts: rail frame, rail track, and carriage. The rail frame measuring 860 mm (length) × 770 mm (width) × 490 mm (height) is assembled with 80/20® T-slotted aluminum bars. On top of the rail frame are mounted three rail tracks that are 1.65 m long for two exterior tracks and 1 m long for the interior track [Fig. 1.6(b)]. Five carriage wheels are installed to bear the F-T box and allow the box to move along the rail tracks. A hand

brake is added to lock the box in position when soil preparation, F-T tests, or plate loading tests are performed. The rail component can carry the maximum static and dynamic loads of 262 kN and 232 kN, respectively.

As mentioned previously, special consideration is given to the bottom of the F-T box as it rests on the rail tracks, and the details are shown in Fig. 1.6(a). To reduce the heat exchange between the box and the rail tracks, a fiberglass laminate (G10) plate with the dimensions of 610 mm by 610 mm and thickness of 12.7 mm is inserted between the box bottom and carriage wheels. The remaining area of G10 plate is glued with thermally resistant neoprene sponges. The edge of the box bottom that the G10 plate does not cover is glued by the insulation panel.

1.3.4 Plate loading component

This component is developed based on the extensive review of the existing model test devices as summarized in Table 1.1. Figs. 1.6(b) and 1.6(c) show its photograph and design drawing, respectively. The plate loading component also consists of three parts: loading frame, static loading system, and dynamic loading system.

Two loading mechanisms employing PRO.POINT® 50-ton pneumatic/hydraulic shop press are used to apply static and dynamic loads, respectively. The static loading system contains a pneumatic/hydraulic pump, hydraulic cylinder, load cell, and a circular loading plate. Static loads are applied manually by operating a handle in the pneumatic/hydraulic pump, and the hydraulic cylinder transfers the pressure to the load cell and the loading plate. The loading plate has diameter of 150 mm and thickness of 10 mm. The applied static loads can be monitored by a load cell. The maximum plate load that the static loading system can apply is approximately 109 kN. The dynamic loading system includes a hydraulic power unit, control valves, pressure transducers connected to a data logger, a hydraulic cylinder, and a circular loading plate with the same size as

the static loading plate. The maximum plate load that dynamic system can add is approximately 19 kN.

1.4 Freeze-Thaw and Plate-Loading Tests

Eleven model tests were performed on both geocell-reinforced and unreinforced sands. Each test involved zero, one, or five F-T cycles, followed by a static plate loading test. The details of the experimental program are given in Table 1.3. All the F-T tests were conducted in a closed system. This section presents the properties of test materials and test procedures.

Table 1.3. Details of model test program

Test No.	Test material	Number of F-T cycle	Temperature monitoring	Heave monitoring	Volumetric moisture content	Plate loading test
1-4	Geocell-reinforced sands	0	No	No	No	Yes
5		1	No	Yes	No	Yes
6		5	No	Yes	Yes	Yes
7-9	Unreinforced sands	0	No	No	No	Yes
10		1	Yes	Yes	No	Yes
11		5	No	Yes	No	Yes

1.4.1 Test materials

Geocells used in this test were nano-polymeric alloy (NPA) Type-C geocells donated by PRS Geo-Technologies®. Their basic properties are given in Table 1.4, in which the seam strength is related to the parameter for geocell while the other parameters are specified for the sheet. The geocells consist of perforated walls with the height of 150 mm and the thickness of 1.1 mm, and the opening of one cell is 245 mm in the strong axis (i.e., parallel to the welded seam) and 210 mm in the weak axis.

Table 1.4. Properties of the NPA Type-C geocell

Properties	Value	Test standard
Seam weld splitting strength (kN/m)	19	ISO-13426-1
Tensile strength (kN/m)	19	ISO 10319
Dynamic modulus (MPa) at 30°C	775	ASTM E2254
Brittle temperature (°C)	-70	
Coefficient of soil-cell friction efficiency	0.95	ASTM D5321
Coefficient of thermal expansion (ppm/°C)	135	ASTM E831
Long-term plastic deformation at 65°C	3%	ASTM D6992
Resistance to UV and Oxidation degradation (minute)	1600	ASTM D5885

Soils used in the model tests were poorly graded sands with the mean particle size (d_{50}) of 0.72 mm, coefficient of uniformity of 4.43, and coefficient of curvature of 0.87. The specific gravity of the sands was 2.7. The sands had maximum dry density of 1.9 g/cm^3 and optimum water content of 12.9% determined by the standard Proctor compaction tests (ASTM D698). The unsoaked California Bearing Ratio (CBR) of sands was determined to be 37% when the sands were compacted to the dry density of 1.9 g/cm^3 and moisture content of 11%.

1.4.2 Test procedures and instrumentation

In these tests, a thin layer of 170 mm thick base courses consisting of poorly graded sands was investigated in a closed system while the subgrade layer was considered to be rigid. Therefore, the base courses were resting directly on the rigid box bottom. The rigid bottom can represent a real case scenario in permafrost areas, where only the surficial layer of soils experiences F-T cycles while the deeper layer of soils remains frozen (Bolch and Christiansen, 2015). In other cases, roads during midwinter or during early spring can experience thawing in their surface layer but the underlying layer remains frozen (NCHRP, 1974). The rigid box bottom was to simulate this frozen layer and traffic load was simulated by the plate loading tests. In addition, the thin base

layer would save the testing time as the purpose of these tests were to evaluate the effectiveness of the proposed device.

Both reinforced and unreinforced sands were compacted to the dry density of 1.9 g/cm^3 and moisture content of 12.9%. During the compaction, the valve at the bottom was closed. The compaction was completed in four lifts, with 50 mm per lift for the lower three layers and 20 mm for the top layer. After the completion of the compaction of each layer except the top layer, T-type thermocouples were laid out on the finished surface. Fig. 1.7 shows the layout of thermocouples for both reinforced and unreinforced soils under one F-T cycle.

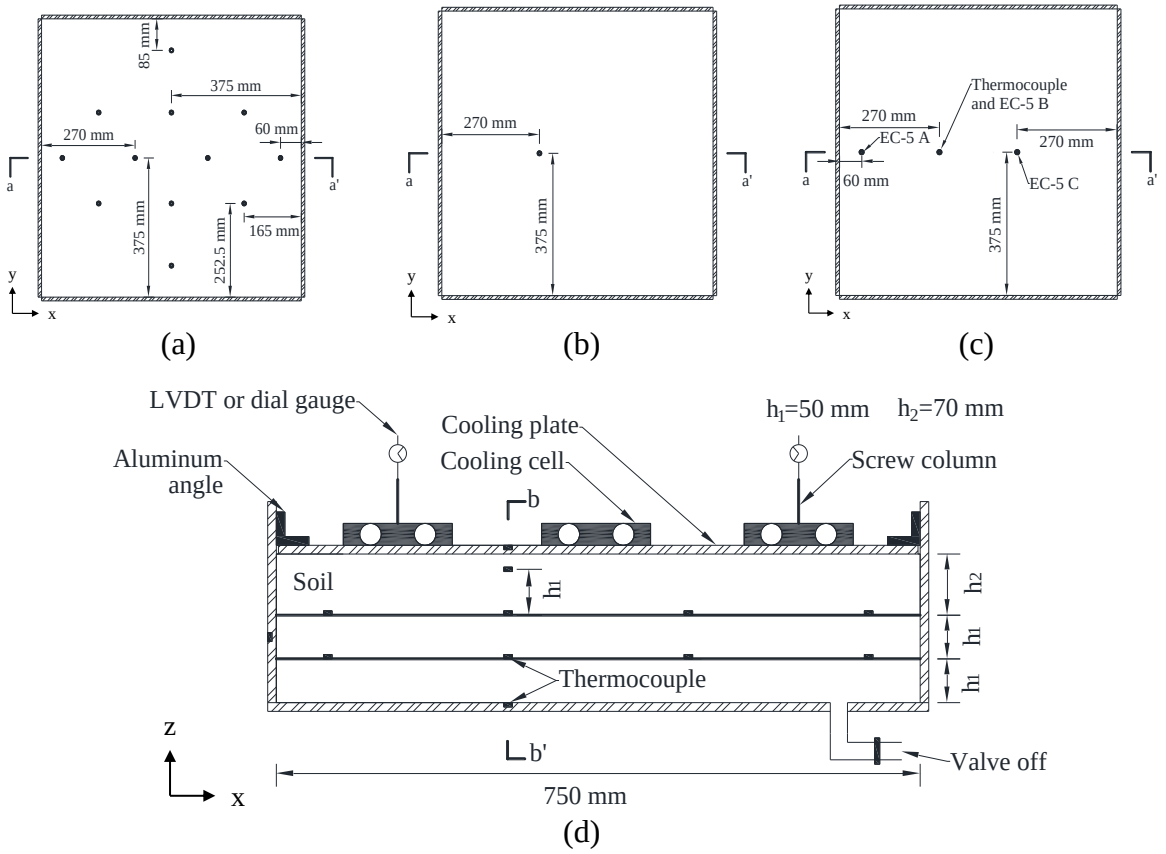

Fig. 1.7. Instrumentation of sensors in sands: (a) plan view of thermocouples at heights of 50 and 100 mm above the box bottom, (b) plan view of thermocouples at 150 mm height, in the bottom plate, and in the cooling plate, (c) plan view of moisture sensors at 150 mm height, and (d) vertical cross section cut at a-a´

However, for the soils under five F-T cycles, there was only one thermocouple embedded in each layer of lower three layers and the plan view position is shown in Fig. 1.7(b). For reinforced soils under five F-T cycles, five soil moisture sensors (METER Environment® EC-5) were embedded in soils to measure volumetric moisture contents. Three of them were located in the proximity to T-type thermocouples at each layer, while at the 150-mm layer two more moisture sensors [EC-5A and EC-5C in Fig. 1.7(c)] were added, as illustrated. Besides the instrumentation in soils, cooling plate, bottom aluminum plate, and aluminum wall were also embedded with a thermocouple as indicated in Fig. 1.7(d). Three Linear Variable Differential Transformers (LVDTs) or dial gauges were placed on the heads of screw columns that were mounted on the cooling plate to measure the frost heave and thaw settlement during the F-T cycles [see Fig. 1.7(d)]. National Instruments® data logger was used to take readings of T-type thermocouples and LVDTs every 30 minutes. The accuracy of T-type thermocouple, LVDT, and EC-5 moisture sensors is 1°C, 0.01 mm and 3%, respectively. Figs. 1.8(a) and 1.8(b) show the photographic layout of multiple-geocell-reinforced sands and the corresponding sketch of vertical cross-section, respectively.

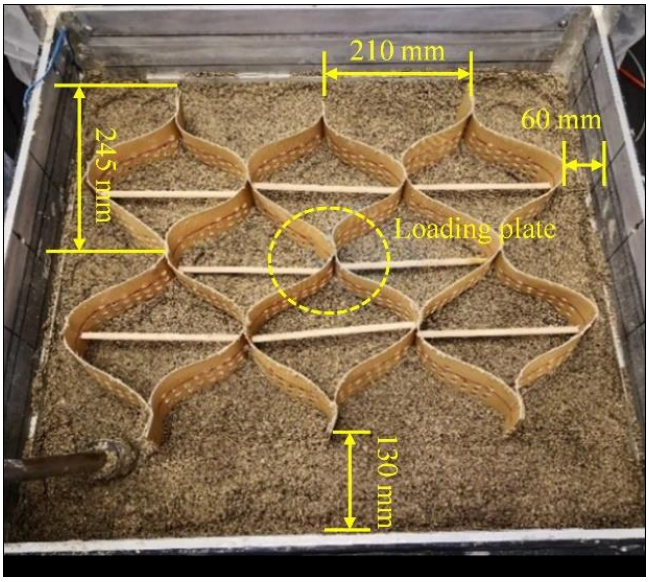

(a)

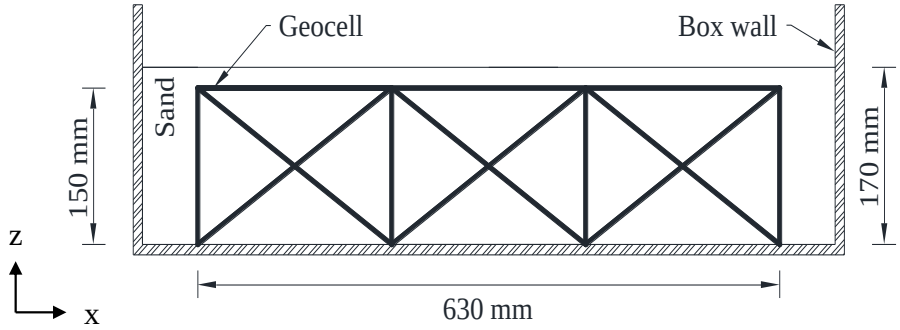

(b)

Fig. 1.8. Layout of geocells: (a) plan view and (b) vertical cross-section view

The F-T tests were performed subsequent to the soil compaction. The valve at the box bottom [Fig. 1.7(d)] remained closed during the freeze and thaw to simulate a closed F-T condition. The cooling plate was placed on the leveled surface of compacted soils. Four horizontal aluminum angles were added to connect the cooling plate and box walls, and insulation was then added to seal the box. The finished insulation to the box can be viewed in Fig. 1.4(b). In the freezing process, the chiller temperature was set to and maintained at -20°C and the soils were cooled from top to bottom. When temperature of the box bottom reached -10°C, the freezing process was terminated and the aluminum angles removed. Immediately after that, the thawing process commenced by setting the chiller temperature to 20°C. When the temperature of the box bottom

increased to the room temperature (approximately 15°C to 20°C), the thawing process was completed, which also represented the completion of one F-T cycle.

After the soils were subjected to certain freeze and thaw cycles (i.e., 0, 1, and 5 cycles), insulation panels and cooling plate were dismantled from the box. The F-T box was carefully slid along the rail tracks to the plate loading frame for static plate loading tests. The circular loading plate tied with the load cell was first placed on the soil surface, and then connected to the piston of the hydraulic cylinder. The load cell was a hydraulic load cell, which was connected to the pressure transducer of Omega® XP309 5KG5V and data readout of PASCO® 550 Universal Interface. The capacity of the load cell was about 109 kN with accuracy of ±0.25%. Three dial gages were placed on the three extensions of the loading plate [Fig. 1.6(c)] to measure the settlement of the soils. Static loads were applied in increments (62 or 124 kPa). At each increment of loads, the load was maintained for five minutes before next step of load was applied. When the applied load reached the maximum, it was unloaded to zero. Subsequently, sands were removed from the box and gravimetric moisture content for each layer of sands was determined.

1.5 Results and Discussion

Using the proposed device, results of both F-T tests and plate loading tests were obtained and are discussed in this section. The results of the F-T tests included evolution of temperature, temperature distributions in soils at different times, vertical temperature gradient, and changes in soil deformation (i.e., frost heave or thaw settlement). The results of the plate loading tests were mainly load-settlement curves. It is worth noting that the model test results may not represent the field scale or the prototype results. To translate the model test results to the prototype results, similitude relationship is normally adopted through applying scale factors. Based on the studies of scaling rule for the plate loading tests on geosynthetics-reinforced soils (Fakher and Jones,1996;

Kargar and Hosseini, 2018; Viswanadham and Konig, 2004; Yang et al., 2020; Yoo and Abbas, 2020), the scale factors are summarized in Table 1.5, in which λ is the geometric ratio between the prototype scale and the model scale.

To calibrate the design method of Giroud and Han (2004a, b) for geosynthetics reinforced unpaved roads, a plate load test with a 300-mm diameter loading plate is typically used, and this size of loading plate can be considered as the prototype size. Therefore, for the 150-mm diameter loading plate used in the model tests, the geometric scale factor is λ=2. Referring to Table 1.5, the scale factors of bearing capacity and displacement are λ=2 as well. However, the overarching goals of this study were to present the new device, and show the benefit of geocell in reducing heave and improving bearing capacity. These effects can be manifested by normalizing the results from the reinforced sands to those from the unreinforced sands. In this way, the scale factors will be cancelled when applied to the same parameters, and the normalized values will be equal between the model tests and the prototype tests. Therefore, the prototype results are not presented; but, the readers can easily obtain the prototype results (i.e., displacement and bearing capacity) by multiplying the corresponding model test results by a factor of 2.

Table 1.5. Scale factors

	Prototype	Model
Length	λ	1
Area	λ^2	1
Volume	λ^3	1
Density	1	1
Strain	1	1
Settlement	λ	1
Bearing capacity(F/L^2)	λ	1
Stress	λ	1
Force	λ^3	1
Stiffness (F/L^3)	1	1

1.5.1 Evolution of temperature

Fig. 1.9 depicts the time-dependent changes in temperatures of unreinforced and reinforced soils under one F-T cycle. The temperature curves for soils at heights of 50 mm and 100 mm above the bottom of box were the averaged readings of multiple thermocouples on the corresponding horizontal cross sections. Fig. 1.9(a) presents temperature evolution for unreinforced sands subjected to one F-T cycle, in which the subfreezing temperatures between 30^{th} and 44.6^{th} hour were interpolated. During this period, the data logger stopped working as a small amount of water wicked from soils through the thermocouple wires onto its electronic board. This was later prevented by gluing the plastic and wire at the one end of the cable. The target lowest temperature at the bottom of the box was -11°C. Overall, it took approximately 45 hours for the box bottom to reach this temperature, and approximately 3 days to complete one F-T cycle in the unreinforced soils. Fig. 1.9(a) also shows that the temperatures of soils at different heights changed with time in a similar fashion. They decreased linearly at the beginning of the freezing process, hitting a plateau at the freezing point before continuing the decrease in the subfreezing temperature.

The existence of the long plateau is the result of latent heat of fusion when water phase changed from liquid to ice. The plateau stretched out shorter for the soil nearer the cooling plate or soil at a shallower depth. This means that the soil at shallower depths was frozen earlier than at greater depths, indicating heat removal or freezing front was progressed downward as intended. During the thawing process, the temperature changes followed the opposite trends to the freezing process. The temperatures were linearly varied with time either above or below the freezing point. Similar to the plateau found in the freezing process, the plateau in the thawing process also stretched shorter at a shallow depth of soil, confirming the heating was progressed downward too.

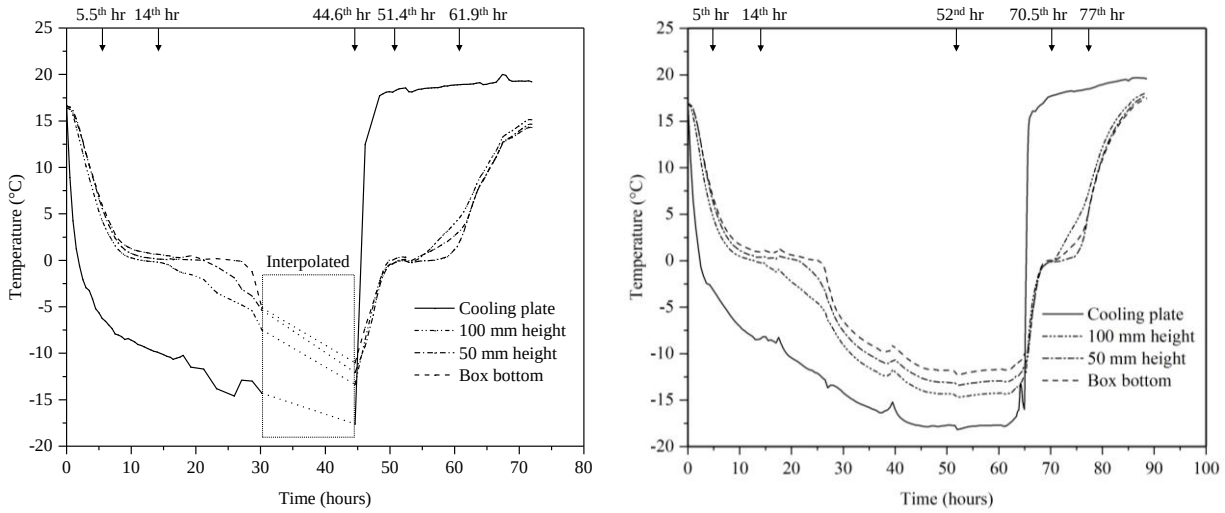

Fig. 1.9. Temperature evolution in: (a) unreinforced sands and (b) geocell-reinforced sands

Fig. 1.9(b) depicts the evolution of temperature of geocell-reinforced sands. The time to complete one F-T cycle was 3.7 days, which was longer than that for unreinforced soils. This is because after the temperature of the box bottom reached the lowest -10°C, the freezing process continued for additional 20 hours prior to the thawing. This allowed the steady state of the lowest temperature to be achieved and the corresponding heave to be investigated. Comparing Fig. 1.9(a) to 1.9(b) indicates that geocell-reinforced sands exhibited the similar temperature-time history to

the unreinforced sands, in particular both having almost identical duration of phase changes at the freezing point. This indicates that the inclusion of geocells had a negligible effect on the heat transfer during the freeze and thaw process, confirming the assumption made in the thermodynamic modeling.

1.5.2 Distribution of temperatures in soils

Evolution of temperatures presents the variations of temperatures over time, while the distribution of temperatures was obtained at specific times. This result was useful to evaluate if the proposed device could achieve the unidirectional heat transfer in soils in vertical direction. Fig. 1.10 shows the isotherms of the unreinforced sand at cross section a-a' [Fig. 1.7(d)] at the time of 5.5^{th}, 14^{th}, 44.6^{th}, 51.4^{th} and 61.9^{th} hour. Fig. 1.11 displays the isotherms of geocell-reinforced soils at the same cross section at 5^{th}, 14^{th}, 52^{nd}, 70.5^{th}, and 77^{th} hour. The time selected for both cases corresponded to five phases: above-zero freezing phase, freezing phase change, the lowest subfreezing temperature, thawing phase change, and above-zero thawing phase. Both Figs. 1.10 and 1.11 indicate that except the discrepancy near the boundaries, the soil temperatures were in general uniform on the horizontal cross sections of different heights, indicating the vertical freeze and thaw in soils. This result was in general comparable to the numerical result in the steady-state freezing phase.

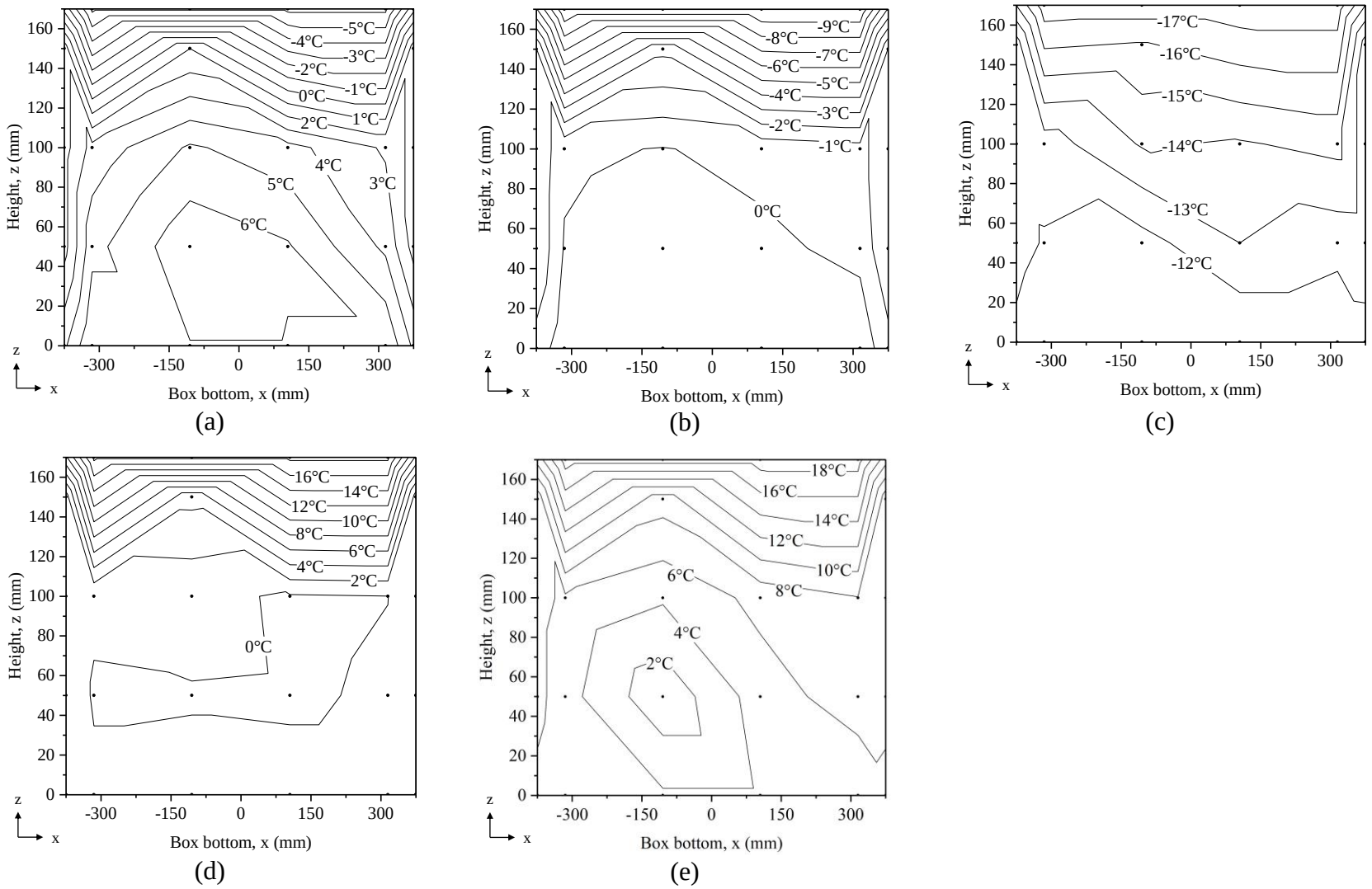

Fig. 1.10. Temperature profiles obtained at cross section a-a´ [Fig. 1.7(d)] for unreinforced sands at the time of: (a) 5.5th hour, (b) 14th hour, (c) 44.6th hour, (d) 51.4th hour, and (e) 61.9th hour

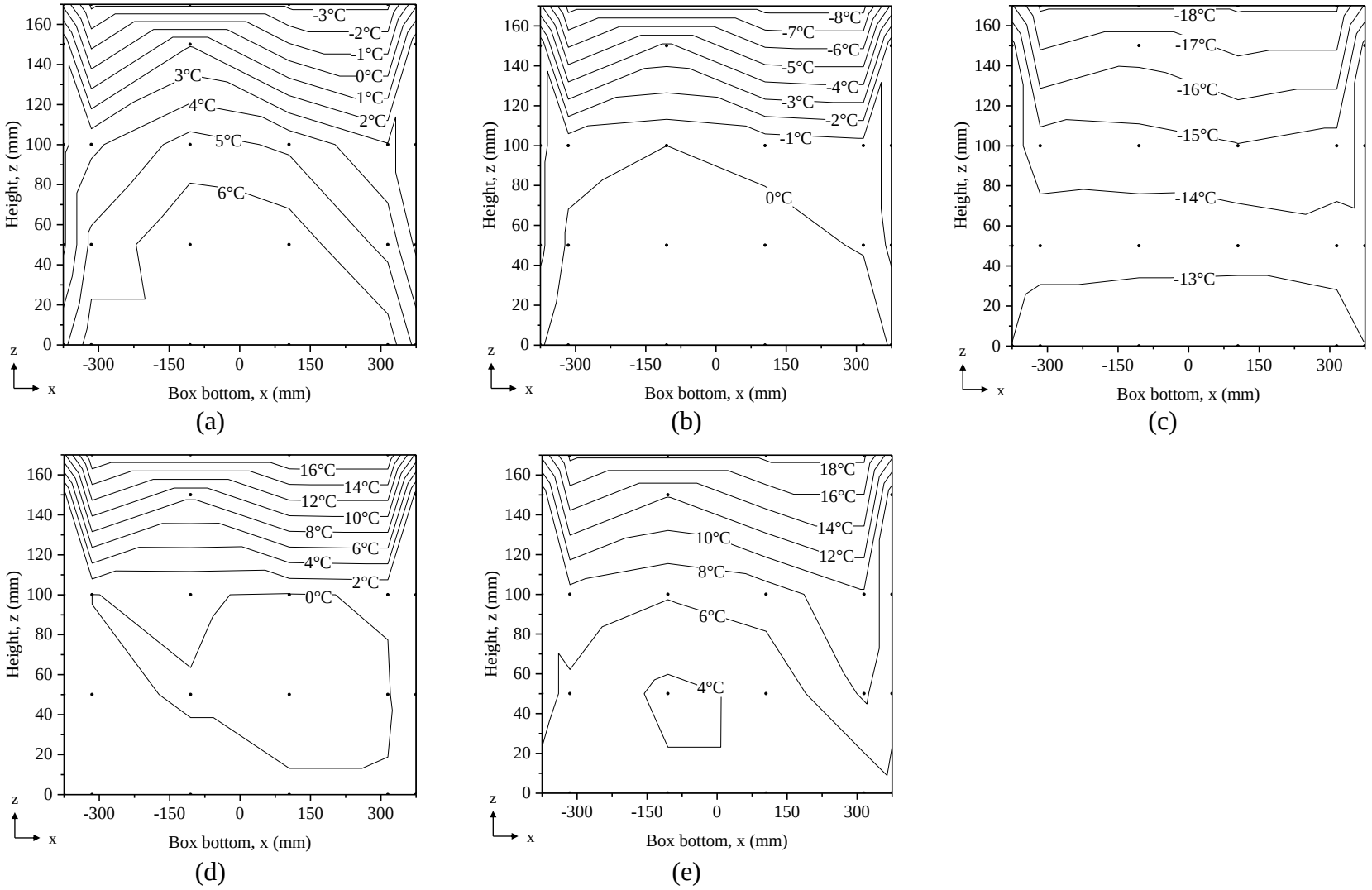

Fig. 1.11. Temperature profiles obtained at cross section a-a´ [Fig. 1.7(d)] for geocell-reinforced sands at the time of: (a) 5th hour, (b) 14th hour, (c) 52nd hour, (d) 70.5th hour, and (e) 77th hour

Figs. 1.10 and 1.11 only show temperature distribution on a vertical cross section. The distribution of temperature on the horizontal cross sections is shown in Figs. 1.12 and 1.13. The results were obtained at the different times on the horizontal cross sections of 50 mm and 100 mm high above the box bottom. The temperature difference on the same horizontal cross section was about 1 to 2°C, which was found not only in the steady-state phase but also in the transient phase. The relatively uniform temperature distribution confirms that the proposed device could achieve vertical heat transfer in soils.

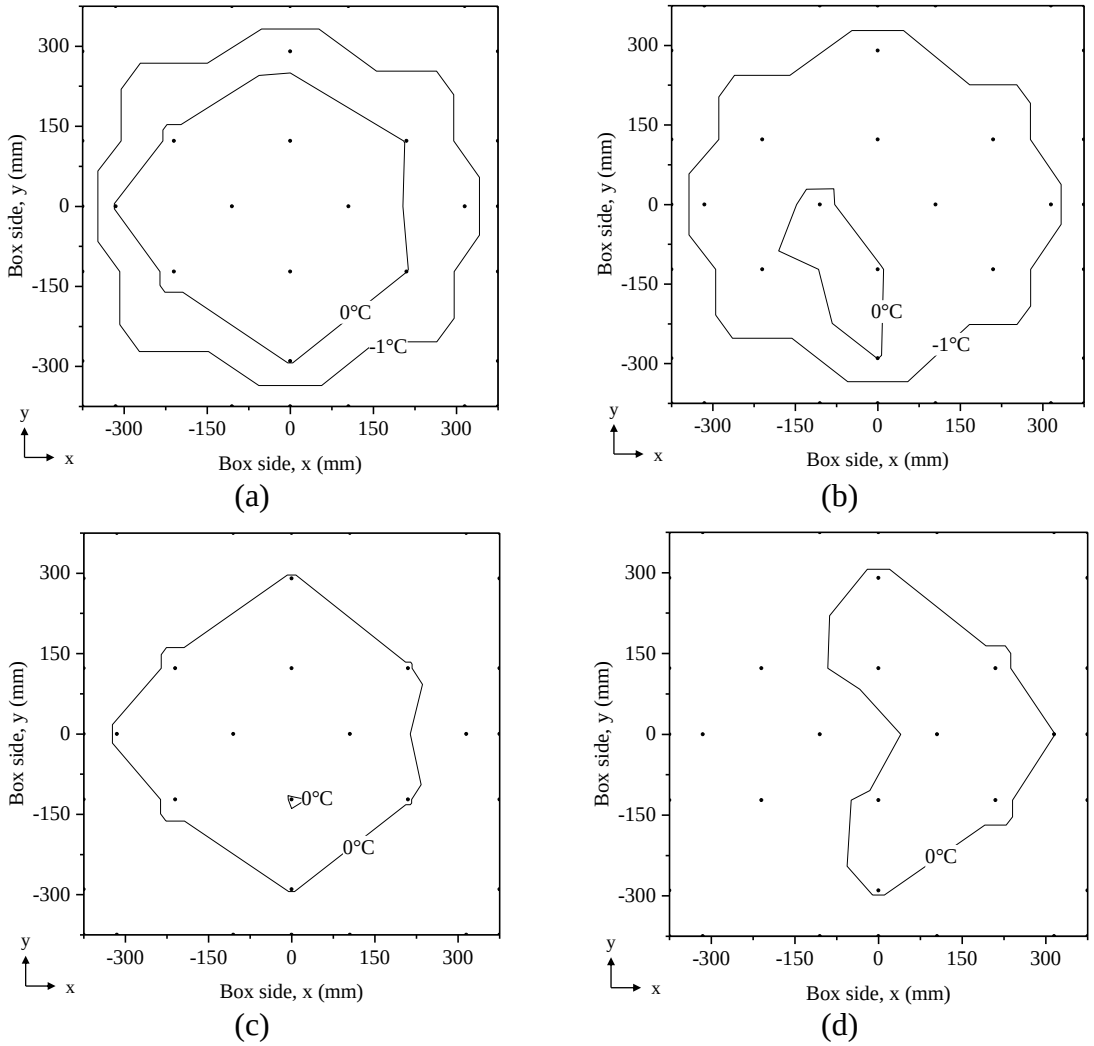

Fig. 1.12. Plan view of temperature distribution in unreinforced sands measured at: (a) 50 mm height, 14th hour, (b) 100 mm height, 14th hour, (c) 50 mm height, 51.4th hour, and (d) 100 mm height, 51.4th hour

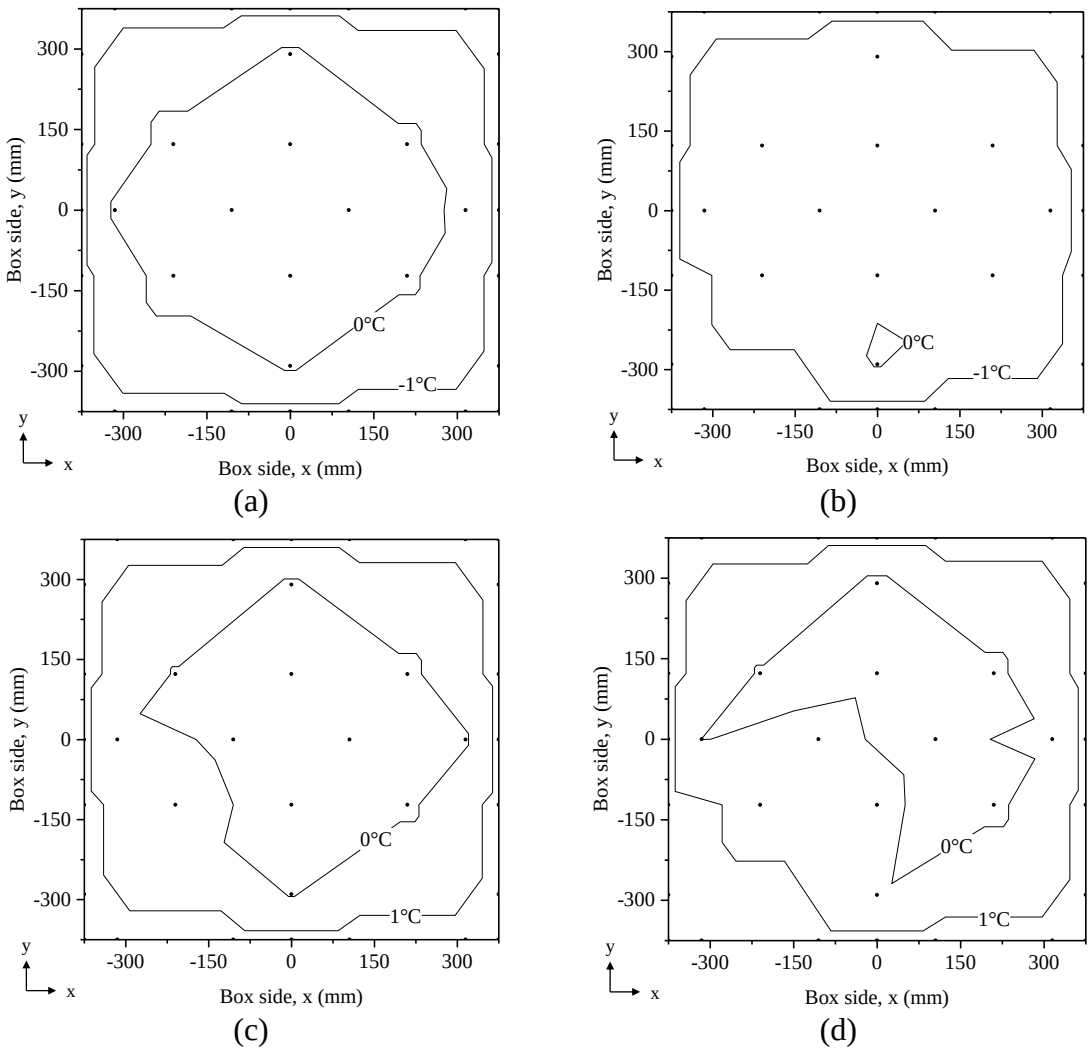

Fig. 1.13. Plan view of temperature distribution in geocell-reinforced sands obtained at: (a) 50 mm height, 14th hour, (b) 100 mm height, 14th hour, (c) 50 mm height, 70.5th hour, and (d) 100 mm height, 70.5th hour

1.5.3 Vertical temperature gradient

Fig. 1.14 shows the vertical temperature changes along line *b-b′* [Fig. 1.7(d)] when the lowest temperature of both unreinforced (44.6th hour) and reinforced (52nd hour) soils under one F-T cycle was attained. The heights of 0 and 170 mm in the vertical axis of Fig. 1.14 correspond to the soil-box bottom and soil-cooling plate interfaces, respectively. The temperature of the soils (middle three points) varied linearly with the height, which could be approximated with linear regression. The reciprocal of the slope of the regression line in Fig. 1.14 gives the vertical temperature gradient.

The temperatures of soils at the top and bottom boundaries can thus be determined by extrapolating the regression line to the boundaries. It is interesting to find that there was a distinct temperature discontinuity at the interface between the soils and the cooling plate or bottom aluminum plate. The temperature drop from the cooling plate to soil surface was 0.7°C and 1.2°C in the unreinforced and reinforced sands, respectively. The temperature discontinuity might be due to the interface thermal resistance at two different media of soil and aluminum in this study. It has been recognized that the existence of interface thermal resistance could introduce measurement errors to the thermal properties of the test material if the interface thermal resistance was not separated from the test material's thermal resistance. For example, it causes approximately 60% underestimate of thermal conductivity of porous media (Campbell et al., 2005) and over 300% overestimate for the thermal resistance of a material when the material has the nominal thermal resistance less than 0.1 m^2 °C /W (Clarke et al., 2015). In this study, the value of thermal contact resistance between aluminum and sands was estimated to be 0.4 m^2 °C/W based on back calculation in the thermodynamic model as discussed previously by fitting the experimental data. However, a direct measurement of this parameter requires a specially made equipment in laboratory. Unfortunately, only very limited research (Svec et al., 1983) has been conducted in this aspect, and therefore, more studies are warranted in the future.

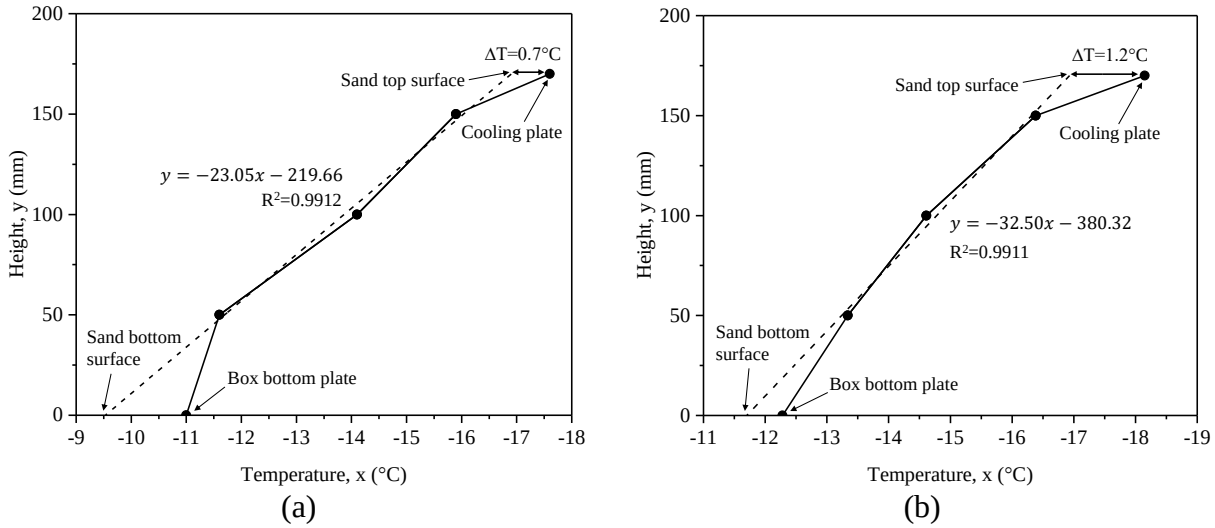

Fig. 1.14. Vertical temperature gradient obtained along line b-b′ [Fig. 1.7(d)]: (a) unreinforced sands at 44.6th hour, and (b) geocell-reinforced sands at 52nd hour

1.5.4 Vertical deformation due to freeze and thaw

The vertical deformation such as frost heave and thaw settlement is the main cause of the pavement failure in cold regions. Therefore, it is important to monitor the heave and settlement during the freeze and thaw process. Three dial gauges were used to monitor the frost heave and thaw settlement in the unreinforced sands while three LVDTs were used for the geocell-reinforced sands. Fig. 1.15(a) presents the evolution of heave of the unreinforced sands subjected to one F-T cycle. As previously mentioned, the data logger was off between 30th and 44.6th hour for the unreinforced soils, and therefore, both heave and temperature data at this period were interpolated in Fig. 1.15(a). The unreinforced sands reached their peak frost heave of 2.7 mm when the box bottom temperature decreased to -5°C, afterwards the heave was maintained constant (the first plateau) until the onset of the thawing process. As the thaw progressed, the heave turned to settlement, it reached another plateau with the residual heave of 0.6 mm when the box bottom temperature was 10°C or higher.

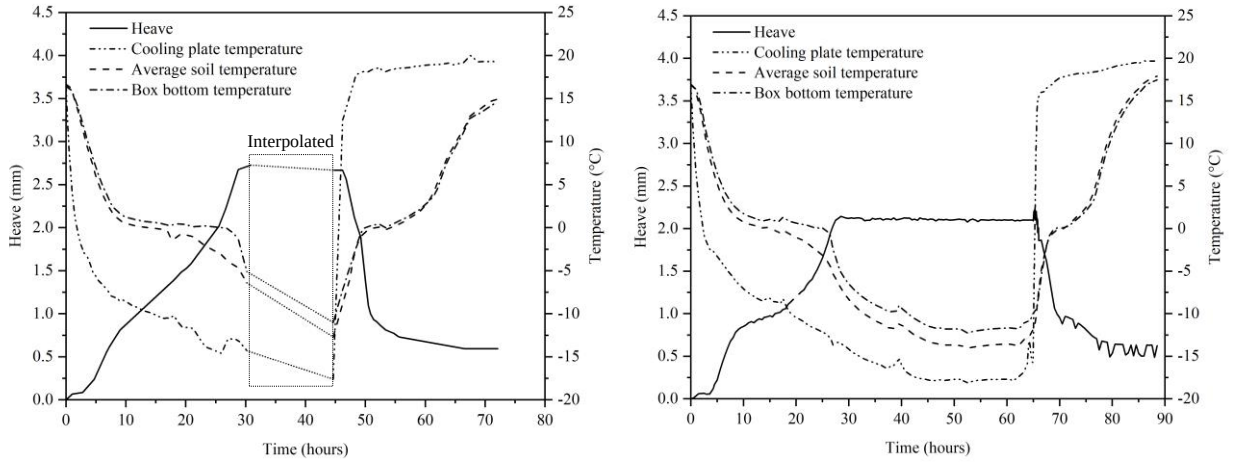

Fig. 1.15. Frost heave under one F-T cycle of: (a) unreinforced sands and (b) geocell-reinforced sands

Fig. 1.15(b) shows the heave for the geocell-reinforced soils subjected to one F-T cycle. The heave arrived at a maximum value of 2.1 mm when the box bottom temperature decreased to -5°C, and it remained stable for the remaining freezing period. Consistent with the unreinforced sands, the thaw settlement of geocell-reinforced sands was associated with the increase of soil temperature. When the box bottom temperature reached 10°C or higher, the thaw settlement ceased and reached a residual value of 0.6 mm.

The results of Figs. 1.15(a) and 1.15(b) indicate that the peak frost heave and residual thaw settlement of both unreinforced soils and geocell-reinforced soils were attained when the box bottom temperature reached -5°C and 10°C, respectively. Therefore, the temperature of -5°C and 10°C might be used as the temperature threshold to terminate the freezing and thawing processes, respectively. Moreover, the holding time of the lowest temperature appeared to be unnecessary as the heave plateau was maintained once the temperature thresholds were reached.

Fig. 1.16 depicts the cumulative peak heave, residual heave, and thaw settlement of unreinforced and reinforced sands under five F-T cycles. The results from one F-T cycle are also included in these figures. As the F-T cycle increased, the peak heave increased drastically at the

first cycle, but the heave increment became smaller in the subsequent cycles. In contrast, the residual heave increased continuously with the F-T cycle. Similar to the peak heave, the thaw settlement increased most considerably at the first cycle, followed by a gradual decrease. The forgoing result indicates that the most profound impact of cyclic F-T on sands occurred at the first cycle, implying that in the field the newly finished roads should not be open to traffic until after one F-T cycle.

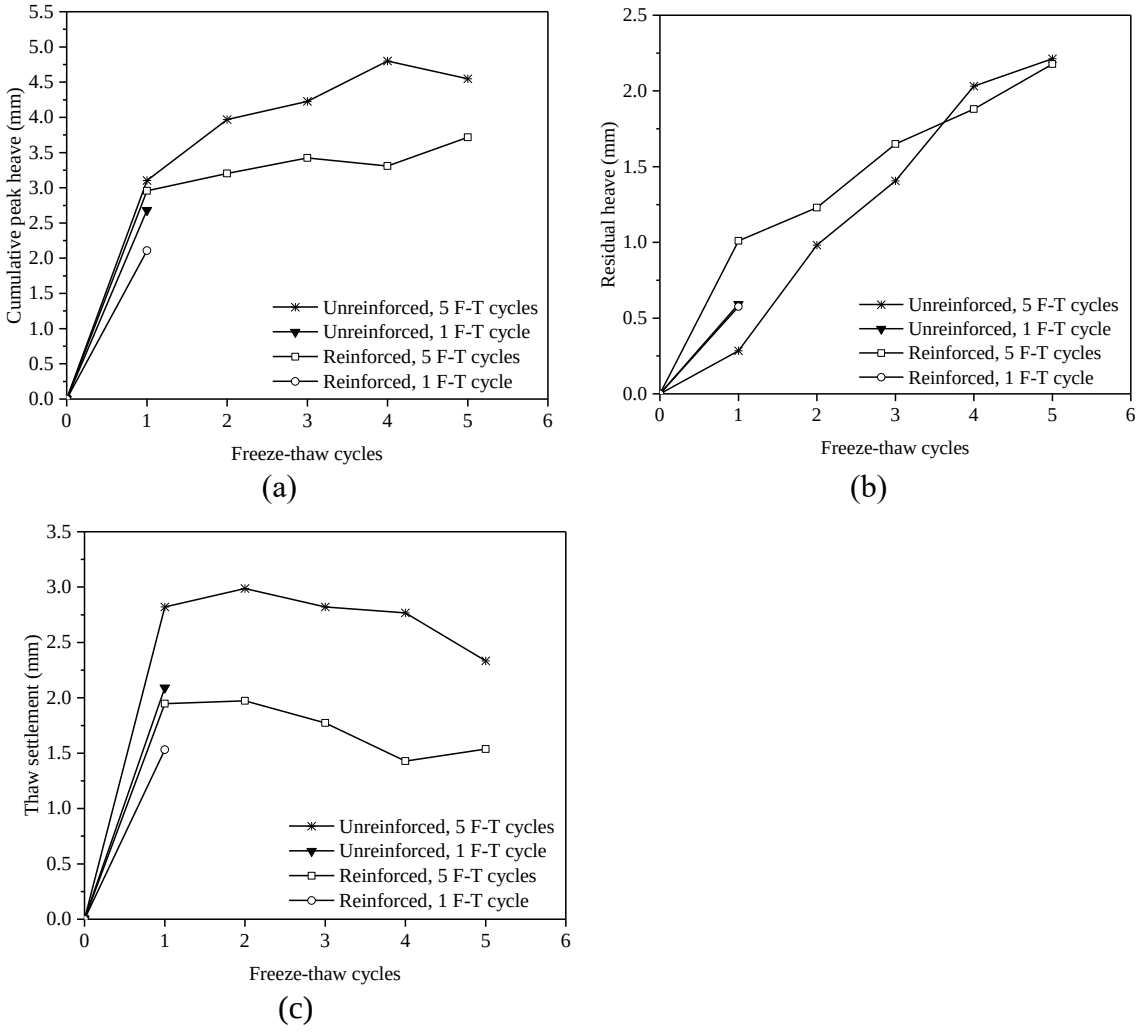

Fig. 1.16. Frost heave of unreinforced and reinforced sands after each F-T cycle: (a) peak heave, (b) residual heave, and (c) thaw settlement

It is noted that there existed some variability of the measured data at the first cycle: for example, peak heave from one test on reinforced sands even exceeded that from unreinforced sands. The variability of the measured data at the first cycle might be due to the variability in water distribution, contact between soil and cooling plate, soil compaction, etc. It might be also associated with the adjustment of the system (soil and F-T box) during the first cycle. However, the average value for the reinforced sands was still smaller than that for the unreinforced sands (2.5 mm vs. 2.9 mm). The thaw settlement was less variable, with the value for the reinforced sands being consistently smaller than that for the unreinforced sands (1.7 mm vs. 2.5 mm). In general, if the averaged results were compared, the geocells would reduce the peak heave and the thaw settlement by 14% and 32%, respectively after one F-T cycle. Moreover, the consistently lower peak heave and thaw settlement [Figs. 1.16(a) and 1.16(c)] from two to five F-T cycles also confirmed the benefits of the geocells. In general, after five F-T cycles, the geocells reduced the peak heave and the thaw settlement by 18%, and 34%, respectively. These values were generally comparable to those obtained at the first F-T cycle.

Using the measured heave data in conjunction with the initial void ratio of sands, the void ratio at peak and residual heaves was estimated and summarized in Table 1.6. Table 1.6 indicates that the measured maximum peak heave was about 4.8 mm. However, if we assume that the sands were fully saturated and water volumetric expansion by freezing was equal to a typical value of 9%, given the initial void ratio of 0.421 for unreinforced sands and 0.412 for reinforced sands (Table 1.6) and sand thickness of 170 mm, the maximum heaves were calculated to be 4.53 mm and 4.47 mm for unreinforced and reinforced sands, respectively. For the reinforced sands, the void ratio was calculated by excluding the volume of geocells. As a matter of fact, sands were not fully saturated but with a degree of saturation of 83%. In other words, the theoretical peak heave

would be less than the calculated values of 4.53 mm and 4.47 mm. However, the measured peak heave of the unreinforced sands exceeded this theoretical limit at the fourth and fifth F-T cycle [Fig. 1.16(a)] while that of the reinforced sands was within this limit throughout five F-T cycles. The possible reason is that a larger F-T cycle increased the likelihood of the internal structure rearrangement of the unreinforced sands, which caused the initial and residual void ratio to increase (see Table 1.6). This result also agreed with the finding from the previous study (Viklander 1998) that dense soils were loosened by F-T cycles. In contrast, the soil fabric alteration or internal structural reengagement in the reinforce sands was less profound due to the geocell reinforcing effect.

Table 1.6. Void ratio at cumulative peak and residual heaves

F-T cycle	Void ratio at peak heave				Void ratio at residual heave			
	Reinforced		Unreinforced		Reinforced		Unreinforced	
	1 cycle	5 cycles	1 cycle	5 cycles	1 cycle	5 cycles	1 cycle	5 cycles
0	0.412	0.412	0.421	0.421	0.421	0.412	0.421	0.421
1	0.430	0.437	0.444	0.447	0.417	0.421	0.426	0.424
2	-	0.439		0.454	-	0.422		0.429
3	-	0.441		0.456	-	0.426		0.433
4	-	0.440		0.461	-	0.428		0.438
5	-	0.444		0.459	-	0.431		0.439

1.5.5 Plate loading tests

Plate loading tests were performed following the F-T tests, and the results are presented in Fig. 1.17. From the load-displacement curves, bearing capacity and initial stiffness of soils were determined. The bearing capacity was determined corresponding to the largest curvature point on the curves. The stiffness of soils, also known as modulus of subgrade reaction, was defined as the initial slope of the curves. To elucidate the benefit of geocells, improvement factor, a ratio of

bearing capacity or stiffness between reinforced and unreinforced sands, was defined (Pokharel et al, 2010). The results of bearing capacity, stiffness, and improvement factor are summarized in Table 1.7.

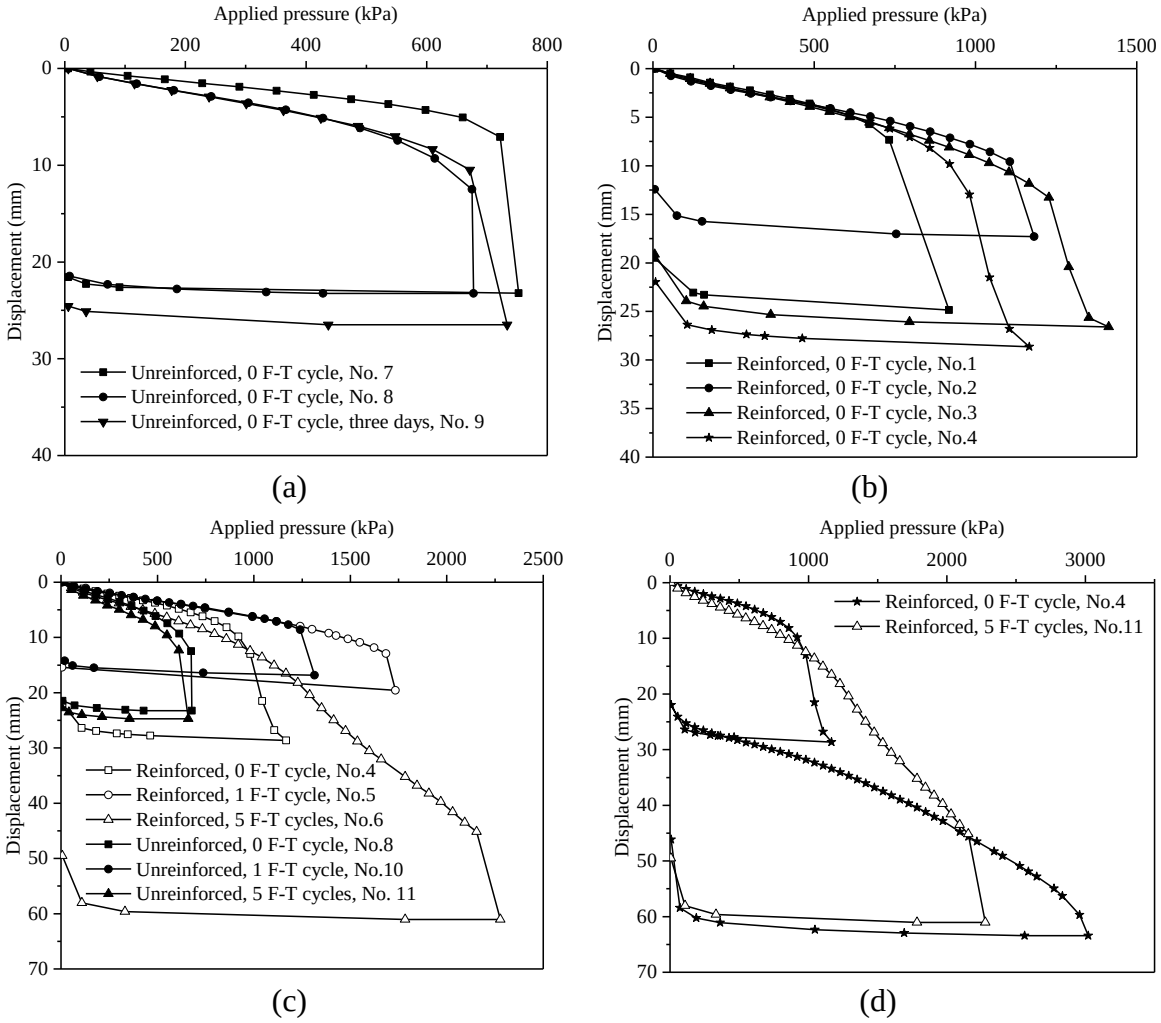

Fig. 1.17. Plate loading test results of: (a) unreinforced sands 0 F-T cycle, (b) reinforced sands 0 F-T cycle, (c) unreinforced and reinforced sands at different F-T cycles, and (d) failure modes of reinforced sands at 0 and 5 F-T cycles

Table 1.7. Bearing capacity and stiffness after different freeze-thaw cycles

	Bearing Capacity (kPa)			Stiffness (kPa/mm)		
No. of cycle	0	1	5	0	1	5
Unreinforced sands	690	1240	611	104	158	60
Reinforced sands	1013 (2959)*	1685 (NM**)	(2959)	127	159	84
Improvement factor	1.48	1.36	3.53	1.22	1.01	1.40

* The number outside and inside the parenthesis designates the first and second failure mode, respectively.
** Not measured.

Repeatability of the plate loading tests was conducted on triplicate unreinforced sand samples and four reinforced sand samples at zero F-T cycle. The results of the load-displacement curves are presented in Figs. 1.17(a) and 1.17(b). For the unreinforced sands, the bearing capacity from the triplicate tests was agreeable [Fig. 1.17(a)], confirming the repeatability of the tests. The bearing capacity for the four tests on the reinforced sands was less consistent [Fig. 1.17(b)], probably due to difficulty in reaching uniform compaction on the reinforced sands compared with the unreinforced sands. However, averaged values were used to minimize the effect of the variability. Furthermore, based on the improvement factor in Table 1.7, geocells provided approximately 48% and 22% increase in the bearing capacity and the stiffness of sands without F-T cycle.

After one F-T cycle, the bearing capacity of unreinforced and reinforced sands was increased by 80% and 66%, respectively [Fig. 1.17(c)]. The corresponding increase in the stiffness was by 52% and 25%, respectively. The reinforced sands attained approximately 36% higher bearing capacity but no difference in the stiffness than the unreinforced sands. The increase in bearing capacity after one F-T cycle was inconsistent to other results obtained for silts or clays in element tests (the size generally smaller than CBR mold) where the physical and mechanical properties of soils deteriorated remarkably after one to three F-T cycles (Viklander, 1998; Wang et al., 2007; Wong and Haug, 1991; Xie et al., 2015). A close examination of our experiments reveals that

water migration during the F-T might be the reason. For the no F-T case, the plate loading tests were run immediately after soil compaction. However, surface soils at this moment were weakest as the compaction generated excess pore water pressure near the surface and caused the water to perch on the soil surface [Fig. 1.18(a)]. We also ran a similar test, in which a waiting time of three days was set before the plate loading test. This test also observed the perched water on the surface and similar bearing capacity [Fig. 1.17(a)], implying the repeatability of the tests without F-T. The different water distribution along the depth was confirmed by the gravimetric moisture content measurement, in which the moisture content was approximately 13 % to 14% for the top soils (148 to 170 mm height), but 11% to 12% for the lower soils (0 to 50 mm height). When one F-T cycle was imposed, water was redistributed in sands and no perched water was observed on the surface [Fig. 1.18(b)].

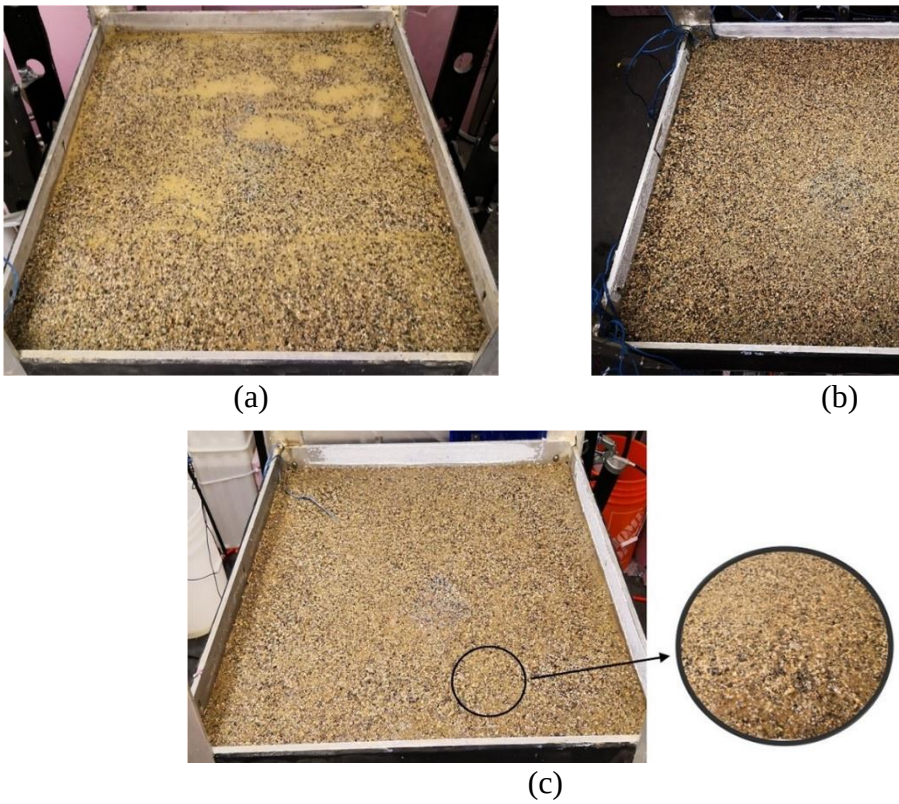

Fig. 1.18. Photographs of soil moisture on surface of unreinforced sands: (a) 0 F-T cycle, (b) 1 F-T cycle, and (c) 5 F-T cycles

In addition to the virtual observation, the water migration along the depth was quantified by the measured volumetric moisture content of the reinforced sands varied with F-T cycle (Fig. 1.19). Fig. 1.19 clearly displays that the most distinct change in the volumetric moisture content along the depth occurred during the first F-T cycle, when the volumetric moisture content of the top soils dropped rapidly but that of the lower soils increased. The above evidence of water redistribution along the depth might justify the increase in both bearing capacity and stiffness after the first F-T cycle.

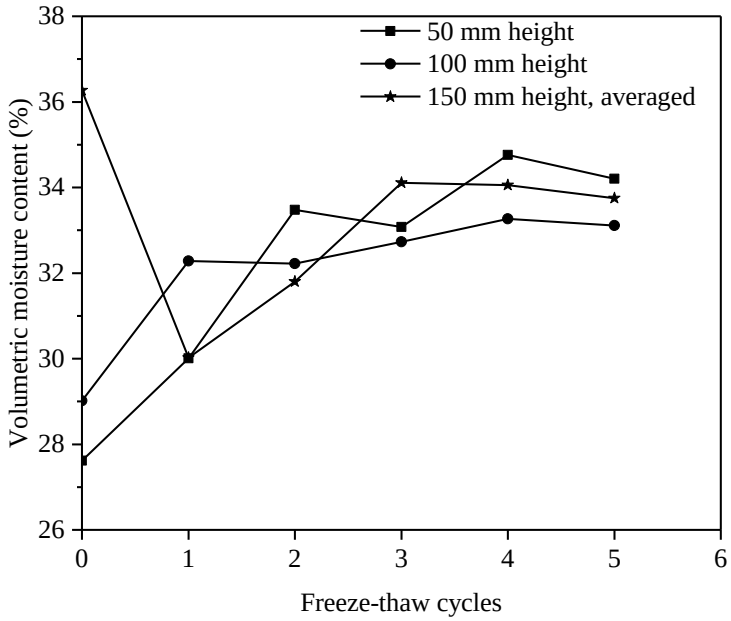

Fig. 1.19. Volumetric moisture content of reinforced sands subjected to 5 F-T cycles at heights of 50 mm, 100 mm, and 150 mm above the box bottom

After five F-T cycles, the stiffness of unreinforced and reinforced sands decreased by 42% and 34% respectively with respect to the value obtained in the initial condition (no F-T cycle). The corresponding decrease in the bearing capacity of the unreinforced and reinforced sands was 11% and 27%, respectively. The decrease in the stiffness and the bearing capacity of unreinforced sands after the five F-T cycles might be attributed to the combined effects of water redistribution and soil structure rearrangement. The continued cycled F-T action after the first cycle caused water to

move upward back to the surface, resulting in higher moisture in the top sands (gravimetric moisture content of 13.3% at 148 to 170 mm height) than in the lower sands (gravimetric moisture content of 11.8% at 0 to 50 mm height). As shown in Fig. 1.18(c), scatter perched water was observed on the surface of sands after five F-T cycles. More details of water changes at different heights were available in Fig. 1.19, in which the volumetric moisture content of the surface soils started to rise and gradually stabilized after a steep drop during the first cycle. Besides changing the moisture migration, the larger F-T cycles altered soil fabric and rearranged soil internal structure, which were also responsible for the weakened soil stiffness and bearing capacity. This is supported by the increased void ratio of soils (Table 1.6) and continuous development of the cumulative peak and residual heaves [Figs. 1.16(a) and 1.16(b)].

Another important observation from Fig. 1.17 is the creep-like behavior of reinforced sands after the five F-T cycles (i.e., large deformation required to mobilize the bearing capacity). This might be attributed to (a) the loading position in which the loading plate rested on the top of the geocell rib [Fig. 1.8(a)], and (b) the potential creep of geocells after cyclic F-T. For the plate loads applied above the rib, two failure mechanisms of the buckling of the geocell rib and the global bearing capacity failure may develop. This is elucidated in Fig. 1.17(d) for reinforced sands without F-T cycle, in which the first plunging failure was related to the buckling of the rib while the second failure corresponded to the global bearing capacity failure. However, for the reinforced sands experiencing five F-T cycles, the geocells might experience F-T creep, resulting in no buckling failure but only the global bearing capacity failure. The creep effect of F-T cycles on the geocells requires a further investigation to verify in the further study. Note that the unreinforced sands only involved the global bearing capacity failure.

The improvement factors in Table 1.7 indicate that after five F-T cycles, the geocells improved the stiffness of sands by 40% and the bearing capacity by 253%. Note that bearing capacity of reinforced sands obtained at the both failure mechanisms is given in Table 1.7. Considering the second failure mode, the geocells enhanced the bearing capacity by 329% at zero F-T cycle. Unfortunately, the bearing capacity at the second failure mode was not measured after one F-T cycle, and therefore, the improvement factor for bearing capacity at this failure mode was not available at this F-T cycle.

1.6 Conclusions

This paper presents the development of a model test device for investigating F-T performance of geocell-reinforced soils in a regular laboratory environment. A thermodynamic numerical model was constructed to assist with the design. With the proposed device, F-T tests in a closed system and plate loading tests were performed to verify the effectiveness of this device. The following conclusions are drawn from this study:

(1) The unique feature of this proposed device lies in the use of aluminum walls as a heat sink, which allows the device to be run in a regular laboratory environment while reducing the thickness of insulation. The F-T tests verified that the device could achieve vertical heat transfer in soils during the F-T cycles.

(2) The temperature evolution and isotherms of geocell-reinforced sands and unreinforced sands were similar, indicating that the addition of geocells to sands had an insignificant effect on altering the heat transfer in the sands.

(3) A temperature discontinuity was observed at the interface between soil and aluminum. This indicates the existence of the thermal contact resistance at soil-aluminum interface. In the absence

of direct measurement tool, the thermal contact resistance at sand-aluminum interface was back-calculated to be 0.4 m^2 °C /W by fitting the experimental results in the thermodynamic analyses.

(4) The threshold temperature for terminating freezing and thawing within each F-T cycle was found to be -5°C and 10°C, respectively. When the temperature of the box bottom reached the lowest subfreezing temperature, it is recommended to begin the thawing process immediately as the peak frost heave was not affected by the waiting time.

(5) For the 170-mm thick sands resting on a rigid base, the use of geocells reduced the peak frost heave and thaw settlement by about 18% and 34%, respectively after five F-T cycles. The residual heave of unreinforced and reinforced sands was found to increase with the F-T cycles (up to five cycles), indicating the compacted sands were loosened by the F-T action.

(6) During the five F-T cycles, the majority of peak heave and thaw settlement developed at the first cycle, with a small amount developed at the following cycle. This implies that in the field the newly finished roads should not be open to traffic until after one F-T cycle.

(7) For the loading plate resting above the geocell rib, the load-displacement curves revealed two failure mechanisms: buckling of geocell rib and global bearing capacity failure. However, after five F-T cycles, the buckling failure mode vanished, with only the presence of global failure mode. It is suspected that this was attributed to the F-T creep of geocells.

(8) After five F-T cycles, the bearing capacity and stiffness of both reinforced and unreinforced sands decreased as compared with the initial condition (zero F-T cycle). The reinforced sands had 40% higher in stiffness and 253% higher in bearing capacity than the unreinforced sands.

Chapter 2 Freeze-Thaw Behavior of Geocell-Reinforced Bases Considering Different Fines Contents

2.1 Abstract

Freeze-thaw (F-T) cycles are a major cause of pavement distress in seasonal frost regions, and the presence of fines in bases can accelerate the pavement degradation induced by cyclic freeze and thaw. Among countermeasures used to mitigate the F-T induced damages in pavements, geocell-reinforced bases can be an effective solution in mitigating F-T damages to cold region roads. However, there is almost no research dedicated to understanding the potential benefit of geocells and the underlying mechanisms in this regard. This study employed a custom-made model test device to investigate the F-T performance of geocell-reinforced sands considering different fines contents. The experimental results showed that the increase in fines content substantially increased the peak heave and thaw settlement and decreased the stiffness and ultimate bearing pressure. The application of geocells reduced the peak heave and thaw settlement by 11%-18% and 22%- 35%, respectively, but this benefit was negligible at high kaolin content (12%). The use of geocells increased the stiffness and ultimate bearing pressure by about 43%- 90% and 41%- 73%, respectively, after five F-T cycles. The findings of this study are relevant to the design of geocell-reinforced bases under F-T cycles and advance the understanding of the underlying mechanisms.

2.2 Introduction

In seasonal frost regions, freeze-thaw (F-T) cycles can lead to road distress because of the repetitive frost heave and thaw weakening. In general, base courses consist of F-T insusceptible materials such as gravels with limited fines contents. However, the maximum fines content allowed in the base courses varies in regions in practice. In North America, this number can range

from 5% to 8% (e.g., Alberta Transportation, 2020; ASTM D2940/D2940M; British Columbia Ministry of Transportation and Infrastructure, 2020). For geocell-reinforced bases, the requirement for infill quality can be lower than the aggregate bases due to their beneficial reinforcement effect. The use of geocells allows inferior materials to be used as infill, such as sands or granular materials with a higher fines content, e.g., 13% to 50% (Guo et al., 2018; Mengelt et al., 2006). Fines composition in base course materials is site-specific, mainly comprising silt, clay, or a mixture of them (e.g., Johnson, 2012; Li et al., 2019; Rosa et al., 2017; Syed et al., 2000). Both fines content and fines composition can affect the mechanical properties of base courses under freeze-thaw cycles.

Even for gravels and sands with almost no fines, their California Bearing Ratio (CBR) and resilient modulus (M_r) can decrease appreciably (up to 62% in CBR and 22% in M_r) after one or two freeze-thaw cycles (Babić et al., 2000; Huang et al., 2021; Ishikawa et al., 2019; Kawabata et al., 2016). It is anticipated that the presence of fines would increase F-T damage of base courses. Konrad and Lemieux (2005) found that frost susceptibility of base courses was increased with the increasing fines contents and kaolinite fraction. Based on experimental tests in a closed system, Wang et al. (2014) observed that the frost heave ratio (i.e., the ratio of frost heave to frozen depth) of coarse-grained soils more than doubled when the fines content increased from 5% to 20%. Liu et al. (2018) showed that among all the fines contents (6%, 8%, 10%, and 12%) investigated, the base course samples with 10% fines developed the largest frost heave under a low-temperature gradient. Babić et al. (2000) investigated the effect of mineralogical composition in fines on CBR of granular soils under F-T actions and found that the F-T induced reduction in CBR was more remarkable in clay-dominated fines than the crusher fines that were produced from stones.

The durability of roads in seasonal cold regions can be improved by using various engineering measures, which include the installation of an effective drainage system and a capillary barrier, replacement of frost-susceptible fines with granular materials, chemical stabilization of soils using cement or lime, and physical reinforcement of bases with geosynthetics (e.g., Christopher et al., 2000; Edil et al., 2002; Henry and Holtz, 2001; Hotineanu et al., 2015; Han and Jiang, 2013; Lai et al., 2012; Li et al., 2019; Li and Ashlock, 2017; Lin et al., 2017; Liu et al., 2018; Rosa et al., 2017; Roustaei et al., 2015; Wei et al., 2015; White and Vennapusa, 2013). In recent years, the beneficial use of geocell, a three-dimensional honeycomb geosynthetic, in improving the longevity of roadways in seasonal frost regions has been reported in several field observations (e.g., Edil et al., 2002; Henry et al., 2005; Pokharel et al., 2017). It has also been observed that geocell-reinforced bases that consisted of poor infill materials (i.e., locally available sands) still performed well after two-year F-T cycles (Pokharel et al., 2015, 2016). Although field observations provide useful evidence for the benefit of geocell reinforcement in seasonal frost roads, the field tests are highly scarce due to cost and logistic complexities. In comparison, laboratory model tests are an important supplement to the field tests as they are cost-effective while allowing for parametric study under controlled test conditions. In summary, there has been a significant lack of studies on the responses of geocell-reinforced bases to F-T cycles. No model tests on geocell-reinforced bases under F-T cycles are reported in other research labs. The proposed model device in the authors' lab allows comprehensively investigating into this problem. The previous study was focused on geocell-reinforced bases without fines. In practice, the application of geocells in roads allows for the use of poorer infill materials as bases, such as sands with fines, but no research has been concerned about F-T behavior of geocell-reinforced bases with fines. This paper aims to advance the understanding of this topic by investigating the effect of fines contents on the

effectiveness of geocell-reinforced bases in mitigating F-T damages. For this purpose, Huang et al. (2021) have developed a lab-scale model test device capable of conducting F-T and plate loading tests on geosynthetic-reinforced soils. Using this device, they performed a series of experimental tests on geocell-reinforced sands without fines under F-T cycles.

The objective of this study was to experimentally investigate the effect of fines content on the F-T performance of geocell-reinforced bases (i.e., sands) using the device developed by the authors (Huang et al., 2021). The cyclic F-T tests (up to five cycles) were run on the geocell-reinforced and unreinforced bases with different fines contents in a closed system, in which the time histories of temperature, volumetric moisture content, frost heave, and thaw settlement of soils were recorded. Following the F-T tests, static plate loading tests were carried out to measure how F-T cycles affected the bearing pressure and stiffness of the bases with varying fines contents. The outcomes of this experimental study would quantify the beneficial effect of geocell-reinforced bases with varying fines contents under F-T cycles and provide insights into the underlying mechanisms.

2.3 Experimental study

A total of 27 model tests were performed on unreinforced and geocell-reinforced sands with 0%, 5%, and 12% kaolin, each experiencing zero, one, and five F-T cycles. In general, each F-T cycle took approximately 2-3 days to be completed, with five F-T cycles taking 10-15 days. The difference in the F-T duration resulted from the combined effects of the freezing rate of soils with different fines contents and the variations of the ambient temperatures. For the soils with 5% kaolin, the ambient temperatures fluctuated over the course of tests spanning between spring and summer, while for the soils with 12% kaolin, the ambient temperatures were relatively stable during the testing because a tent equipped with an air conditioner was installed. The details of the

experimental program are given in Table 2.1. All laboratory model tests were performed in a closed system with no water supply. After the specified F-T cycles, the plate loading tests were conducted.

Table 2.1. Details of model test program

Test material	Reinforcement	Test No.	Number of F-T cycles
Sands with 0% kaolin [a]	Unreinforced	1-3	0
		4	1
		5	5
	Reinforced	6-9	0
		10-11	1
		12	5
Sands with 5% kaolin	Unreinforced	13-14	0
		15-16	1
		17	5
	Reinforced	18	0
		19-20	1
		21	5
Sands with 12% kaolin	Unreinforced	22	0
		23	1
		24	5
	Reinforced	25	0
		26	1
		27	5

[a] Results are extracted from Huang et al. (2021) except for Test No.11.

2.3.1 Test materials

Geocells used in this study were nano-polymeric alloy (NPA) Type-C geocells, donated by PRS Geo-Technologies®. The basic properties of the geocells are given in Table 2.2. A single geocell had perforated ribs of 150 mm in height and an opening of 245 mm × 210 mm when it was unfolded.

Table 2.2. Properties of geocells

Properties	Value	Test standard
Tensile strength, kN/m	19	ISO 10319
Seam weld splitting strength, kN/m	19	ISO 13426-1
Long-term plastic deformation, %	3	ASTM D6992
Brittle temperature, ºC	-70	ASTM E2254
Coefficient of soil-cell friction efficiency	0.95	ASTM D5321
Coefficient of thermal expansion (ppm/ºC)	135	ASTM E831

Sand and kaolin were mixed in different mixing ratios to produce base course materials with different fines contents. The sand was poorly graded sand according to the Unified Soil Classification System (USCS), the same base course material used in Huang et al. (2021), while the kaolin was commercial EPK kaolin manufactured by Edgar Minerals®. The specific gravity of the sand and the kaolin was 2.70 and 2.65, respectively. The national and provincial specifications of the US and Canada require the maximum of fines content in base courses be 5% to 8%, but this value in some regions (e.g., Maryland, Minnesota, etc.) can be higher, such as up to 12% to 14% (Cetin et al., 2014; Hatipoglu et al., 2008). Five percent of fines is considered the limit allowed by the standard specifications, while 12% represent the upper limit for the poor infill materials allowed by geocell-reinforced bases. Furthermore, per the Unified Soil Classification System (USCS), 5% and 12% are the percentages of fines to differentiate poorly graded sand (SP) from poorly graded sands with clay (SP-SC) and poorly graded sands with clay (SP-SC) from clayed sand (SC), respectively. In other words, they also imply the changes in soil types and properties. Therefore, this experimental study selected these three fines contents for evaluation. The grain size distribution curves and properties of the mixed soils are shown in Fig. 2.1 and Table 2.3, respectively. The addition of fines to the pure sand did not alter the soil's gradation. Per the USCS, the soils with 5% and 12% kaolin were classified as poorly graded sand with clay (SP-SC).

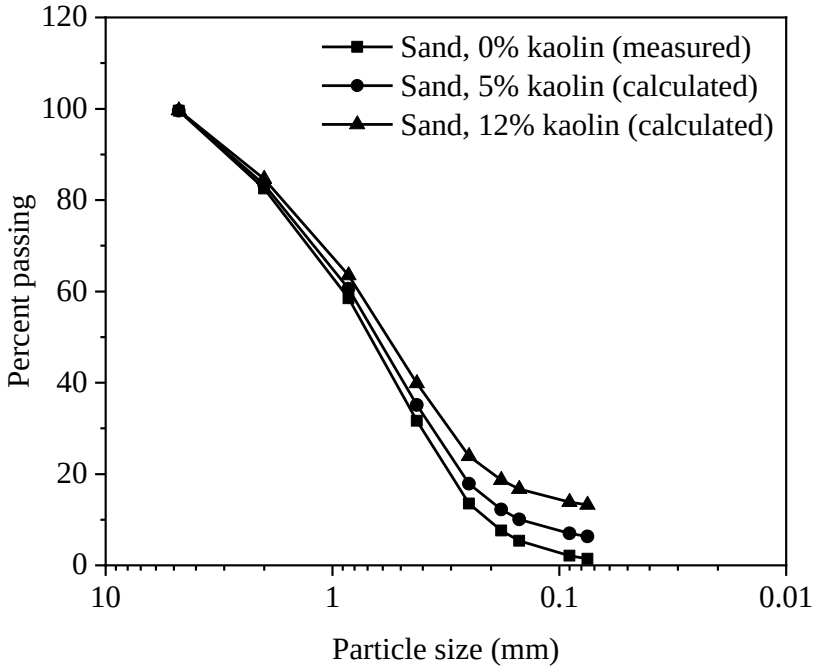

Fig. 2.1. Particle distribution of soils

Table 2.3. Properties of soils

Soil properties	Fines content			Test standard
	0%	5%	12%	
Mean particle size (D_{50}), mm	0.715	0.674	0.607	ASTM D6913
Uniformity coefficient	4.4	5.7	>50*	
Curvature coefficient	0.9	1.1	>10*	
Optimum moisture content, %	12.9	11.7	9.8	ASTM D698
Maximum dry density, g/cm^3	1.9	1.97	2.07	
Unsoaked CBR, %	37	49	65	ASTM D1883

*For fines passing No. 200 sieve>10%, D_{10} is taken as the mean particle size of kaolin (0.00136 mm) provided by the manufacturer.

2.3.2 Test Methods

Model tests were performed in a custom-made device capable of conducting unidirectional freeze-thaw tests and plate loading tests, as shown in Fig. 2.2 (Huang et al., 2021). The freeze-thaw tests were conducted on soils placed in an aluminum box with the dimensions of 750 mm

(length) × 750 mm (width) and an adjustable height up to 1000 mm. The cyclic cooling and heating of the soils were initiated by a 745 mm × 745 mm square cooling plate resting on the soil surface, and the temperature of the cooling plate was controlled by a chiller by circulating the cooling fluid through the cooling plate. The unique feature of this system is that the F-T tests can be run in a room temperature with thin insulation foams sealing the box. This is due to the use of thermally conductive aluminum walls as a heat sink to minimize the heat transfer between the ambient air and the soils inside during freezing. In the F-T tests on sands with 0% and 5% kaolin, it was observed that the air and soil temperature fluctuated in the summer. To control the ambient temperatures, a tent equipped with an air conditioner was added to the equipment in the subsequent F-T tests on sands with 12% kaolin. The plate loading tests were performed after completing F-T cycles and the removal of the insulation forms and cooling plate. During the loading tests, static loads were applied incrementally to the soils by a 150 mm diameter loading plate connected to a hydraulic cylinder with a maximum static load of 109 kN. The device can perform closed- or open-system F-T tests and static or dynamic plate loading tests. This study focused on F-T behaviors of unreinforced and geocell-reinforced soils in a closed system and under static plate loading.

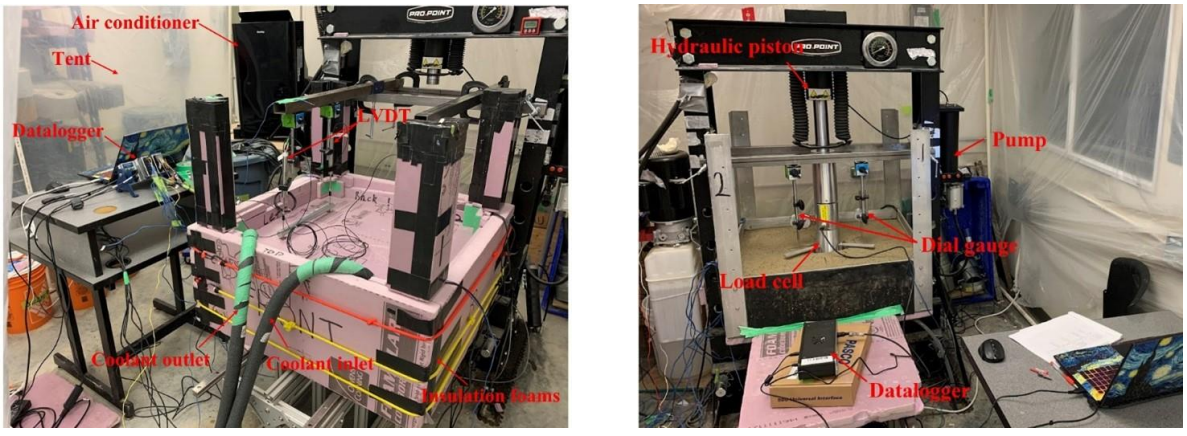

(a) (b)

Fig. 2.2. Photographs of: (a) freeze-thaw test and (b) plate loading test

The closed system can be used to simulate the intermittent F-T cycles in roads in most cold regions. This occurs during mild winter or at the early thawing spring, where base course materials experience intermittent freeze-thaw cycles at daytime and night. As the temperature rises, the ice lenses are gradually thawed, and the melted water is trapped in the thawing soil layers as the sublayers and snow-covered shoulders remain frozen (Johnson et al., 1975; Simonsen and Isacsson, 1999). The melted soils are then frozen as the temperature drops below the freezing point. The closed system can also simulate the seasonal F-T cycles that occur in the active layer underlain by permafrost. In this study, the base course materials (i.e., sand-kaolin mixtures) with and without geocell reinforcement were compacted to the maximum dry density and optimum moisture content (in Table 2.3) determined by the standard Proctor tests. The compaction was made in four lifts, with 50 mm each for the first three lifts and 20 mm for the last lift, which added up to 170 mm in total thickness. The added mass of soils for each lift of the compaction was calculated by multiplying the soil density by the volume of each lift. The target compaction level was achieved by controlling the added mass. At each lift, the soil surface was scratched to improve the bonding to the next layer and eliminate any layered effect in the soils. The test sections were intended to mimic an active layer overlain by a perennially frozen subgrade in the permafrost, and a rigid base in the model was used to simulate the frozen subgrade. For geocell-reinforced test sections, a typical layout of geocells is shown in Fig. 2.3, where a sketch of the vertical cross-section is also included.

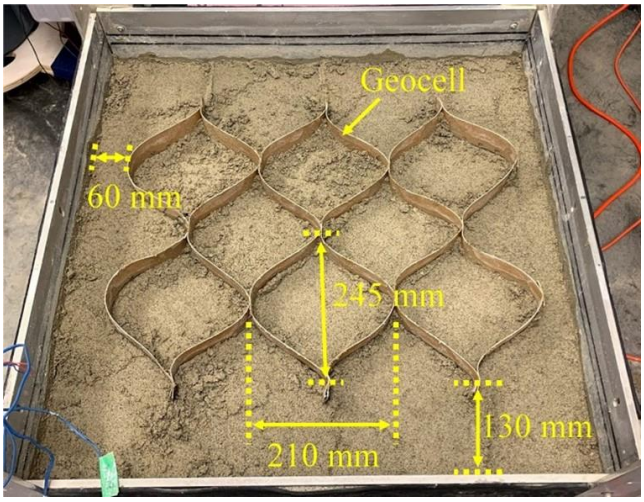

(a)

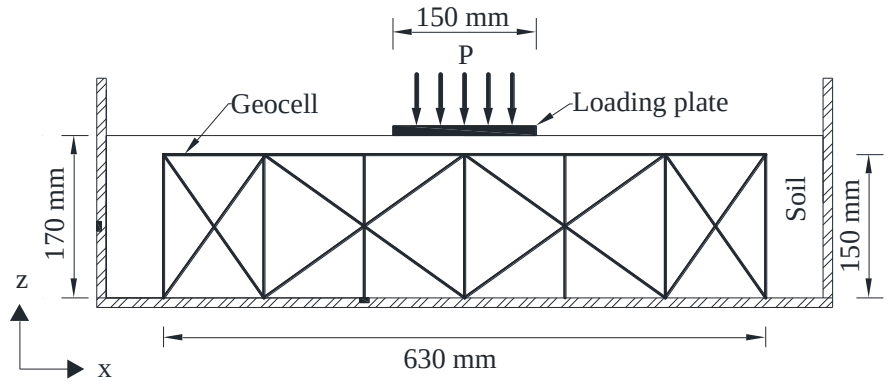

(b)

Fig. 2.3. The geocell layout of: (a) plan view and (b) vertical cross section

Fig. 2.4 shows the layout of T-type thermocouples (Omega®) and EC-5 moisture sensors (METER Environment®) in soils. Each sensor was located at three heights of 50 mm, 100 mm and 150 mm, while two more sensors were placed at the 150-mm height layer [A, B and C in Figs. 2.4(b) and 2.4(c)] to monitor soil temperature and volumetric moisture content during F-T cycles. Furthermore, three thermocouples were installed in the cooling plate, the box bottom, and the box walls. One more thermocouple was placed atop the box to monitor the ambient temperature. Three LVDTs (Omega®) were placed on the tips of screw columns fixed on the cooling plate to monitor the frost heave and thaw settlement, as shown in Fig 2.4(c). A data logger made by National Instruments® was used to take the readings of thermocouples and LVDTs at a frequency of 30

minutes, and another data logger (ZL6 model) made by METER Environment® was utilized to read EC-5 moisture sensors every 15 minutes. The accuracy of the thermocouples, LVDTs, and moisture sensors was 1ºC, 0.01 mm, and 3%, respectively.

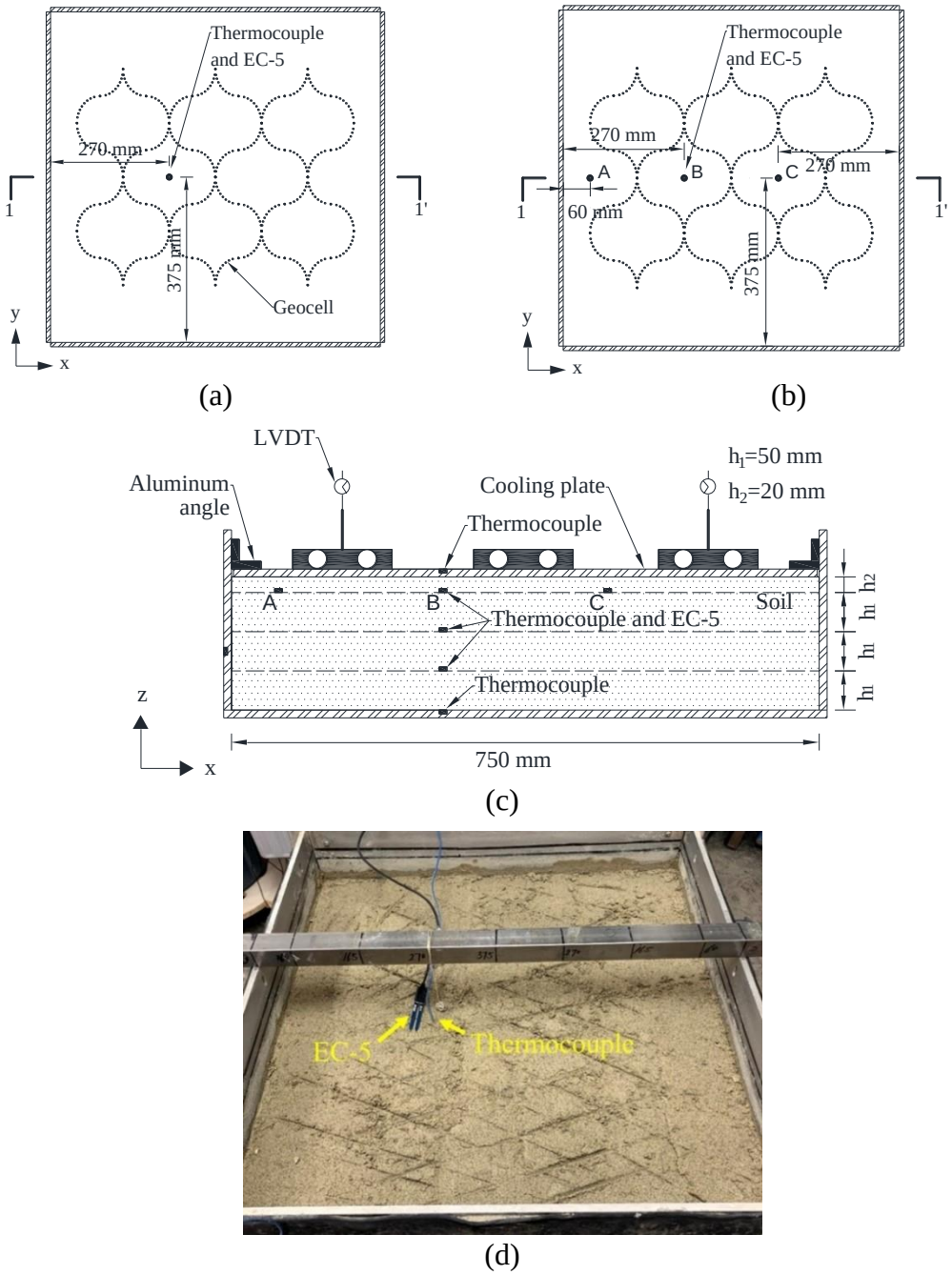

Fig. 2.4. Instrumentation plan: (a) plan view at the bottom, at the heights of 50 mm and 100 mm and at the cooling plate, (b) plan view at the height of 150 mm, (c) vertical cross-section at the cut 1-1' and (d) photograph of sensor installation

During freezing, the coolant in the chiller was cooled down to -20ºC, which, upon circulating through the cooling plate, imposed the unidirectional top-down freezing to the compacted soils. Freezing in sands and sand-clay mixtures was terminated once the box bottom's temperature reached -10ºC and -5ºC, respectively. A lower temperature of -10ºC was imposed on the sands because the tests on sands were the first few tests in which a lower range of temperature would allow evaluating a proper subfreezing temperature (i.e., -5ºC). Subsequently, thawing was started by increasing the coolant's temperature to 20ºC. When the temperature of the box bottom rose above 15ºC, thawing in all soils was completed, which concluded one F-T cycle. Upon the completion of F-T cycles at specified numbers (i.e., 0, 1, or 5), insulation foams and the cooling plate were removed from the box. The static plate loading tests were then performed by loading a 150-mm diameter plate on the soil surface at an increment of 62 kPa with a holding period of five minutes per increment. The load was increased until the soils reached plunging failure or the plate reached the movement limit of about 60-70 mm (i.e., when the steel strips [Fig. 2.2(b)] holding the displacement transducers touched the soil surface), whichever reached first. It was followed by unloading in decrements to zero. The load was measured by a load cell mounted on the plate connected to a data logger (PASCO® 550 Universal Interface). The displacement of the loading plate was measured by three dial gauges placed on three steel strips bolted at equidistance points on the perimeter of the loading plate. The accuracy of the load cell and dial gauges is 1 kPa and 0.025 mm, respectively.

2.4 Results and Discussion

The results of the experimental tests are organized in terms of F-T tests and plate loading tests. Central to the discussion are the effects of fines content on the F-T responses of base materials made of sands and the benefits of geocell in reducing F-T distress to soils.

2.4.1 Freeze-thaw test results

During the F-T tests, soil temperatures, surface deformation (i.e., heave and settlement), and soil volumetric moisture contents were monitored.

2.4.1.1 Temperature evolution

Fig. 2.5 depicts histories of temperatures in unreinforced and reinforced soils at heights of 50 mm, 100 mm, and 150 mm above the bottom of the box during one F-T cycle. The temperature evolution of the cooling plate and the box bottom are also included in each test. For all the unreinforced and reinforced soils, the pattern of temperature changes in the soils, in general, resembled that of the cooling plate except that a distinct transient plateau was apparent at the 50 mm height and the box bottom. This plateau was due to latent heat release during water phase changes. The ambient air temperature was also monitored throughout F-T cycles in each test except for the test on unreinforced soil with 0% kaolin. It can be seen that the fluctuations of ambient temperatures and soil temperatures were less noticeable in Figs. 2.5(c) and 2.5(f) than in Figs. 2.5(b), 2.5(d), and 2.5(e) because a better control of ambient temperatures was achieved in the former two tests by the addition of the tent with the air conditioner.

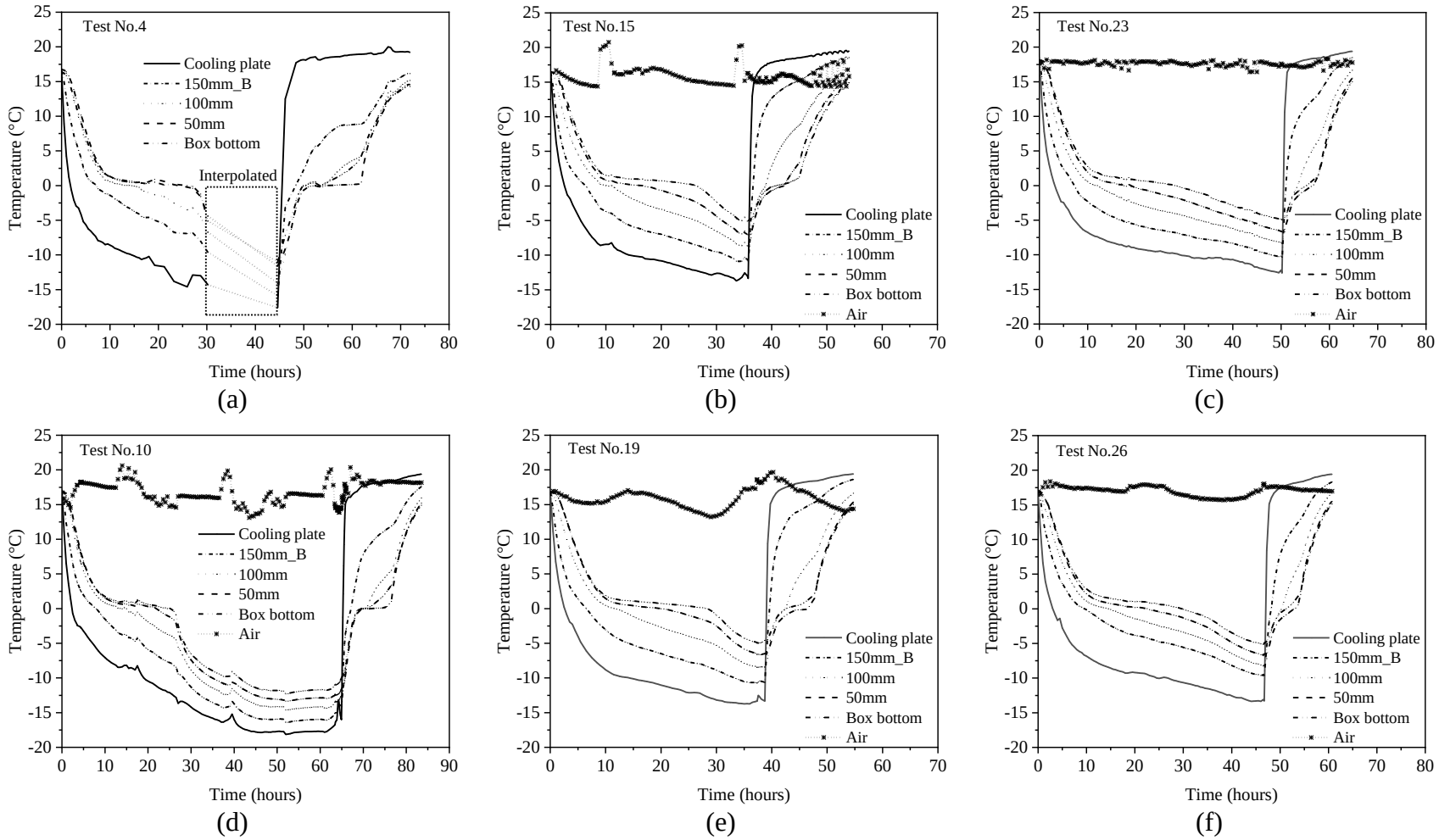

Fig. 2.5. Temperature evolution during one F-T cycle: (a), (b), and (c) unreinforced soils with 0%, 5%, and 12% kaolin, respectively, and (d), (e), and (f) reinforced soils with 0%, 5%, and 12% kaolin, respectively, in which (a) and (d) are modified from Huang et al. (2021)

Fig. 2.5 also shows that a higher kaolin content resulted in a longer freezing time or a slower freezing rate. For example, the freezing rate for temperatures of 0ºC to -4ºC at the 50-mm height of soil was 0.99ºC/hour, 0.34ºC/hour, and 0.20ºC/hour for the unreinforced soils with 0%, 5%, and 12% kaolin respectively, and the corresponding values in reinforced soils were 0.79ºC/hour, 0.37ºC/hour, and 0.27ºC/hour, respectively. It is noteworthy that the above result could not be correlated to the dry density (Table 2.3) because typically, soil with a higher fines content is associated with higher thermal conductivity (Mitchell and Soga, 2005). However, it might be explained by that an increase in fines content necessitated additional thermal energy to freeze the bound water in the fines (Andersland and Ladanyi, 2004). This observation agreed with the findings from a previous study (Zhang et al., 2020) that clays had a higher freezing rate than silts.

2.4.1.2 Soil movement during F-T cycles

The vertical deformation of soils under F-T cycles (i.e., frost heave, residual heave, and thaw settlement) that can contribute to the pavement distress, such as road bumps and surface cracks, was monitored. The rate of frost heave is an important parameter for assessing frost susceptibility of soils (e.g., ASTM D5918; Chamberlain, 1987; Tester and Gaskin, 1996). Therefore, it is necessary to evaluate the effect of geocell reinforcement on the alteration of soil potential movement due to cyclic freeze and thaw. Fig. 2.6 depicts the time-dependent heave of unreinforced and reinforced soils with different fines contents during one F-T cycle. The figure also includes the temperature changes in the cooling plate, soil, and box bottom. The heave and soil temperature values are the averaged readings of the three LVDTs and five thermocouples in the soils, respectively. In Fig. 2.6(a), data were missing between the 30^{th} and 44.6^{th} hour due to the dysfunction of the data logger. However, the heave at 28.8^{th}, 30^{th} and 44.6^{th} hour was almost equal, indicating that the peak frost heave was attained after 28.8^{th} hour; therefore, the missing

readings were believed not to affect the interpretation of the test results. The results of Figs. 2.6(a)-2.6(f) show that the deformation of all unreinforced and reinforced soils reached stable values once the box bottom temperature reached 0 to -3ºC and 3 to 9ºC during freezing and thawing, respectively. Further freezing or thawing would not change the frost heave or thaw settlement. This indicates that the box bottom temperature of -5ºC and 15ºC could be used as the terminal temperature for freezing and thawing, respectively.

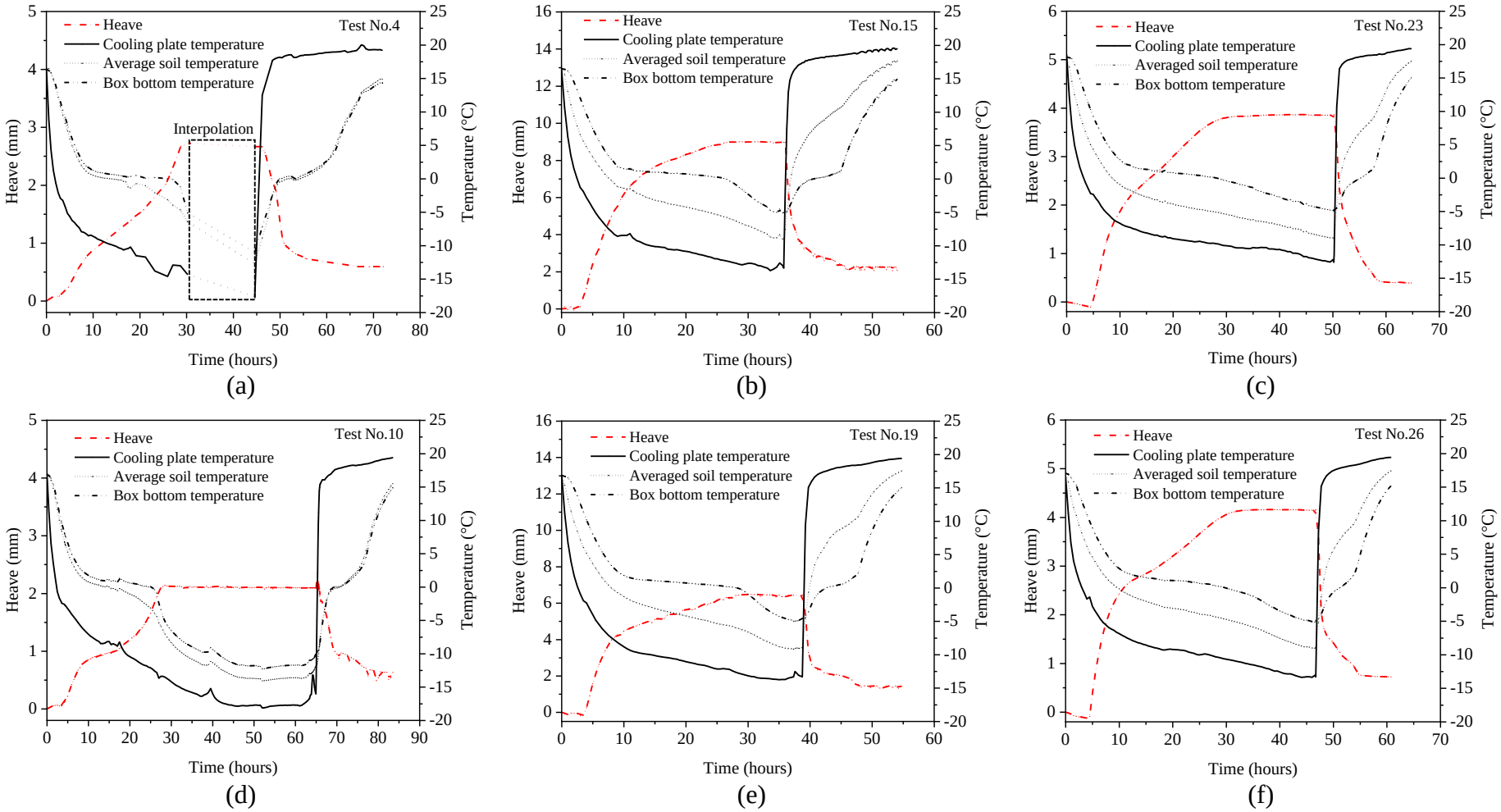

Fig. 2.6. Heave evolution during one F-T cycle: (a), (b), and (c) unreinforced soils with 0%, 5%, and 12% kaolin, respectively, and (d), (e), and (f) reinforced soils with 0%, 5%, and 12% kaolin, respectively, in which (a) and (d) are modified from Huang et al. (2021)

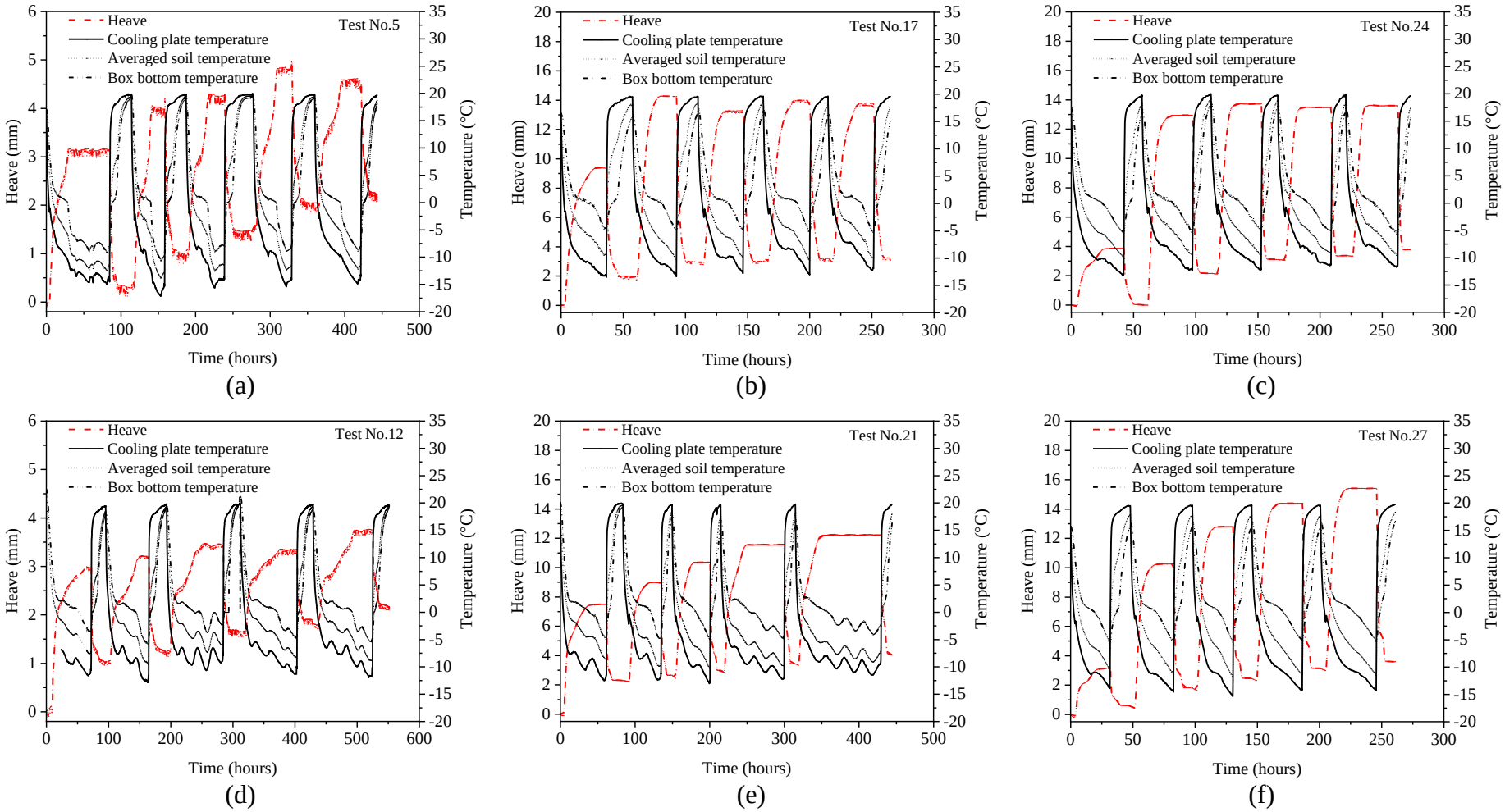

Fig. 2.7. Heave evolution during five F-T cycles: (a), (b), and (c) unreinforced soils with 0%, 5%, and 12% kaolin, respectively, and (d), (e), and (f) reinforced soils with 0%, 5%, and 12% kaolin, respectively

The heave evolution of soil under five F-T cycles is shown in Fig. 2.7. Figs. 2.8, 2.9, and 2.10 respectively present the peak heave, residual heave, and thaw settlement, respectively for F-T up to five cycles. The results of these deformations are discussed separately.

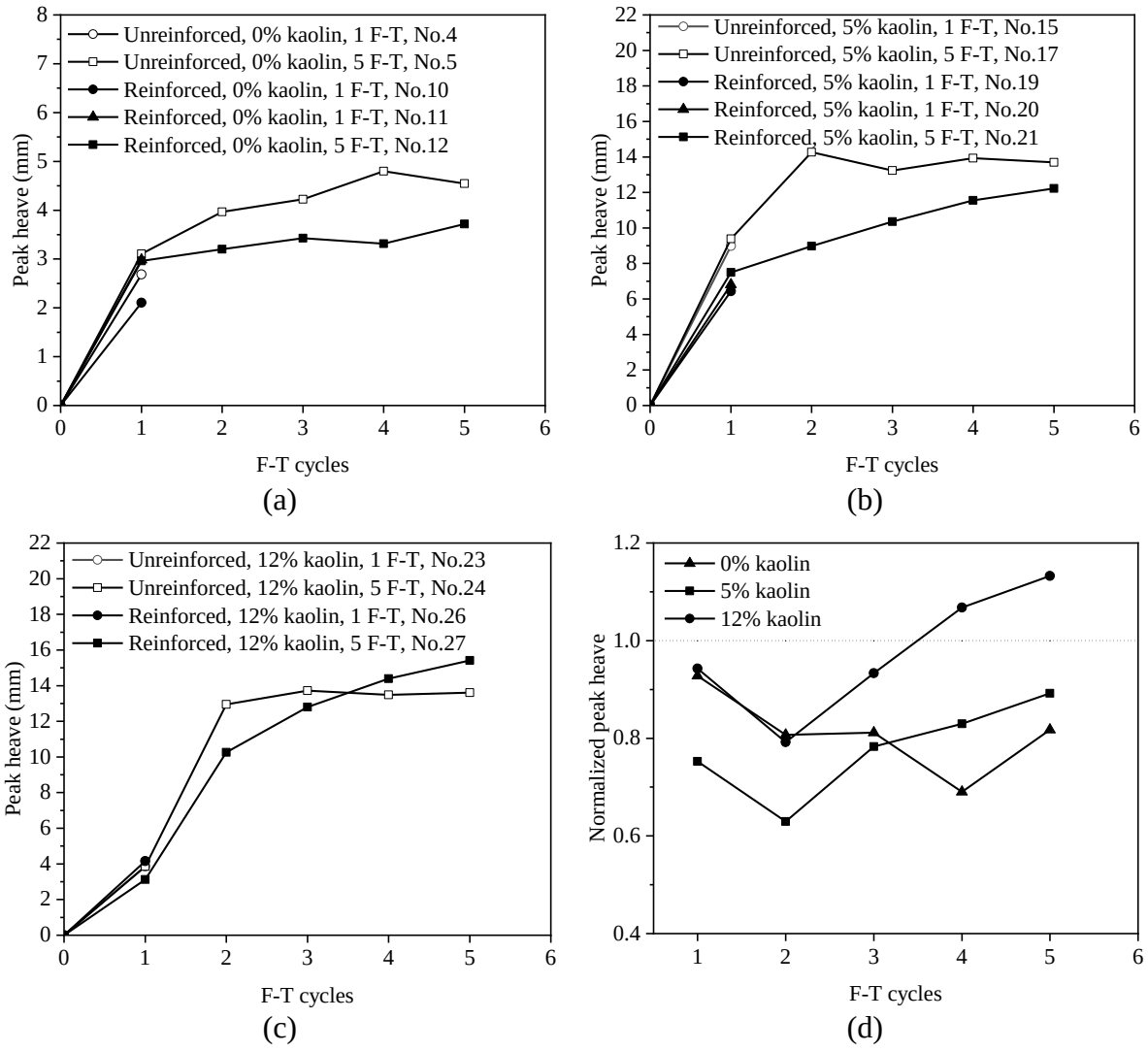

Fig. 2.8. Peak heave of unreinforced and reinforced soils after each F-T cycle: (a) 0% fines, (b) 5% fines, (c) 12% fines, and (d) normalized peak heave

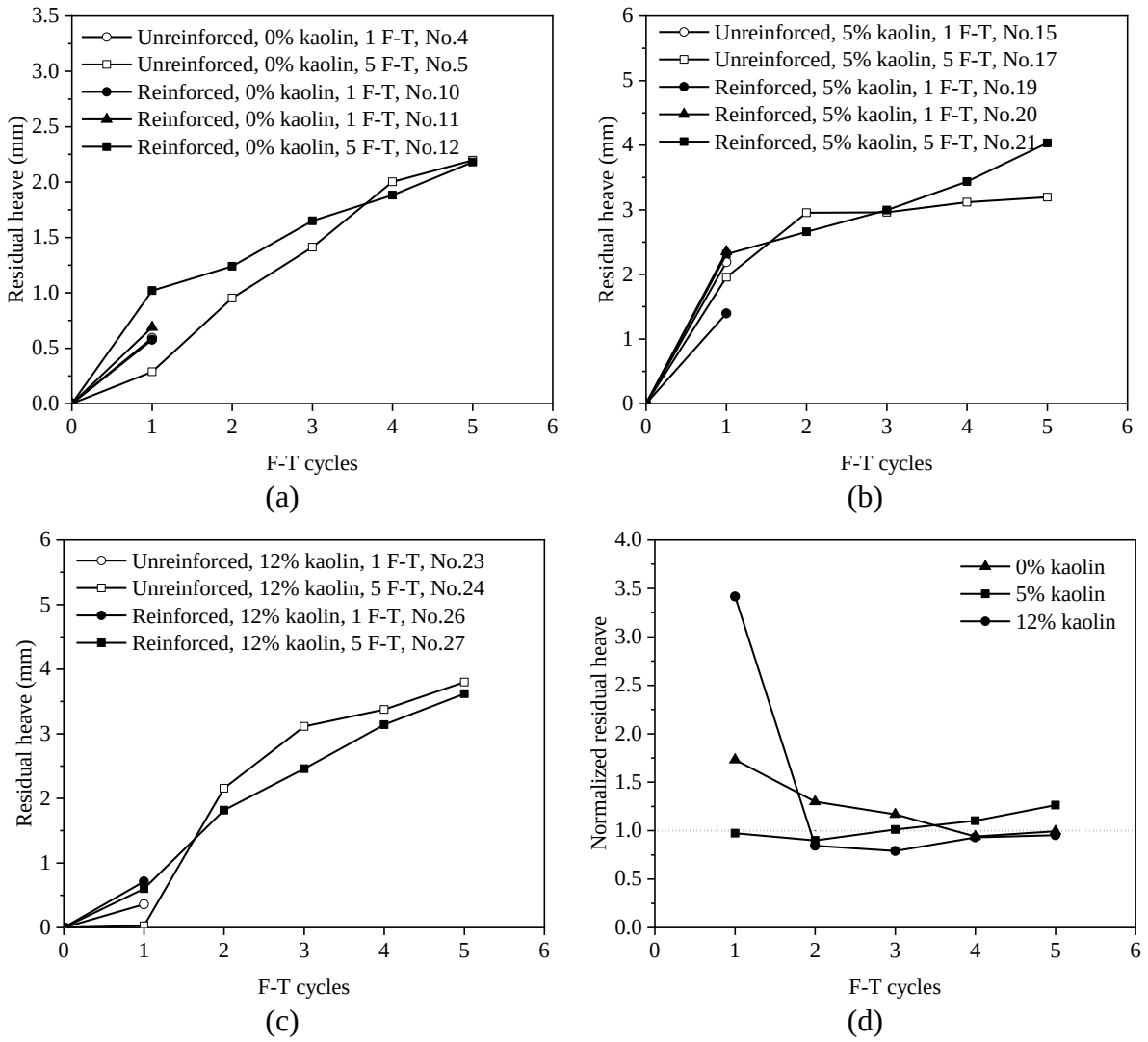

Fig. 2.9. Residual heave of unreinforced and reinforced soils after each F-T cycle: (a) 0% fines, (b) 5% fines, (c) 12% fines, and (d) normalized residual heave

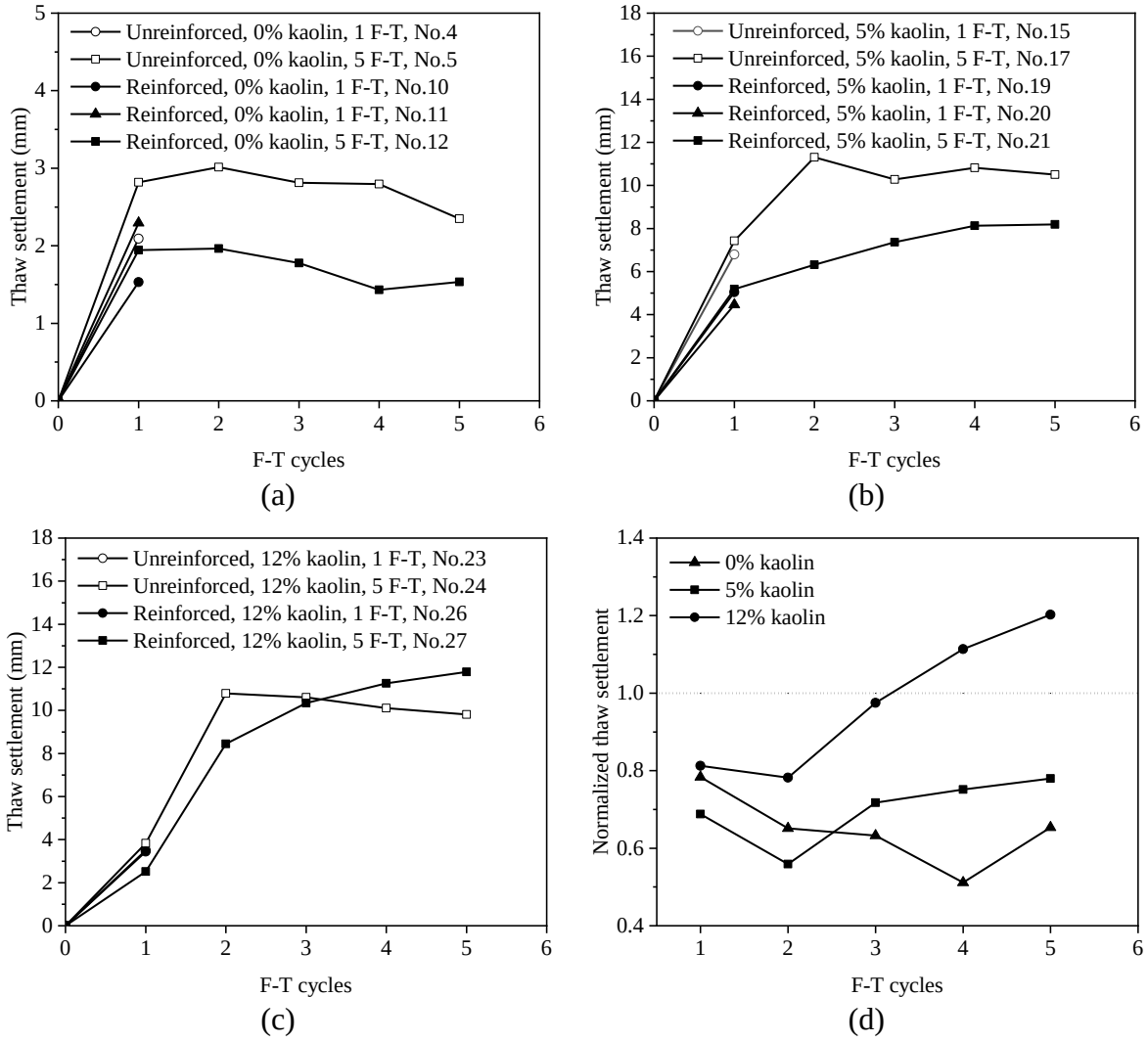

Fig. 2.10. Thaw settlement of unreinforced and reinforced soils after each F-T cycle: (a) 0% fines, (b) 5% fines, (c) 12% fines, and (d) normalized thaw settlement

Peak heave

Figs. 2.8(a)-2.8(c) shows variations of cumulative peak frost heave of the reinforced and unreinforced soils with fines content at each F-T cycle. The increase in kaolin from 0 to 5% substantially increased the peak heave by approximately 200% and 230% for unreinforced and reinforced soils, respectively, throughout five F-T cycles. This may be explained by differences in volumetric expansion of water-ice phase change and the formation of ice lenses in the soils. Observing the amount of peak heave indicates that the formation of ice lenses was generally

dominant. For example, the measured maximum peak heave was 14.3 mm for the unreinforced soil with 5% kaolin, which was 3.5 times the calculated maximum peak heave due to the volumetric expansion of water in the soil in the saturated state (e.g., 4.1 mm). The addition of clay fraction (e.g., from 0 to 5%) tended to increase soil frost susceptibility as an increase in fines content would increase soil suction. The cryogenic suction gradient combined with the capillary force was the driving force for water flow toward the freezing zone, leading to the formation of ice lenses and thus the frost heave. However, a further increase in kaolin from 5% to 12% did not increase the peak heave in the unreinforced soil. This might be attributed to the competing effect between a decrease in hydraulic conductivity and an increase in suction gradient, which resulted in the stable delivery of water to the freezing zone. A similar effect of fines was observed for reinforced soil except that continuing increase peak heave with F-T cycles was noticeable at 12% kaolin compared to 5% and 0% kaolin. The possible reason is associated with water distribution in the soils, which will be discussed later.

Fig. 2.8 also reveals the trend of the peak heave varied with the number of F-T cycles, in which the majority of peak heave was developed at the first or second F-T cycle. This result is consistent with the findings of others (Lu et al., 2021; Othman and Benson, 1993; Zhang et al., 2019). The soil with low kaolin content (i.e., 0%) experienced the most substantial peak heave at the first F-T cycle, while that with higher kaolin content (i.e., 12%) deferred it to the second F-T cycle. Fig. 2.8 also shows a "creep" peak heave after the first or second F-T cycle for the reinforced soils with 5% and 12% kaolin. This creep effect was likely attributed to the difference in initial water content and the presence of geocells that impeded the horizontal water migration and thus facilitated the development of localized ice lenses in the reinforced soils. This could be confirmed by the distribution of volumetric water content with height, as will be discussed in Section 2.4.1.3.

Fig. 2.8(d) plots normalized peak heave between reinforced and unreinforced soils at the same F-T cycles. The normalized value of less than 1.0 indicates the benefit of geocells in mitigating peak heave. It is noted that the normalized peak heave at the first F-T cycle was the average value of multiple tests. Fig. 2.8(d) clearly shows the reduction in the peak heave for the first three F-T cycles with geocell reinforcement. The most significant drop in peak heave due to geocell reinforcement occurred at the second F-T cycle, with a reduction up to 20%-37%. At higher F-T cycles (>2), the effectiveness of geocells in reducing the peak heave tended to diminish, showing higher rebounds of the normalized values for higher kaolin content. After five F-T cycles, the normalized peak heave was increased to 0.89 for 5% kaolin but more than 1.0 for 12% kaolin. By contrast, the geocell benefit remained effective with the increase in F-T cycles for 0% kaolin. The waning benefit of geocell reinforcement for the soils with higher kaolin content at larger F-T cycles was believed to be due to the creep effect resulting from the discrepancy of initial moisture distribution and the restraint of water horizontal flow, as discussed previously.

Residual heave and thaw settlement

Unlike the peak heave, residual heave of unreinforced and reinforced soils continuously increased with the increasing number of F-T cycles [Figs. 2.9(a)-2.9(c)]. In general, the trend and magnitude of the residual heave were similar for soils with and without geocell reinforcement, indicating a negligible effect of geocells on improvement in the residual heave. Fig. 2.9(d) shows variations of normalized residual heave (i.e., the residual heave of reinforced soil to that of unreinforced soil) with F-T cycles. The value above or equal to the unity indicated a negative or no beneficial effect of geocell reinforcement. These normalized values better reflected the limited effect of geocell reinforcement on residual heave, particularly at larger F-T cycles.

Fig. 2.10 depicts the changes in cumulative thaw settlement at each F-T cycle up to five cycles. Similar to the cumulative peak heave, the thaw settlement significantly increased at the first or second F-T cycle, followed by a small increase or decrease in the subsequent F-T cycles [Figs. 2.10(a)-2.10(c)]. Fig. 2.10(d) shows the normalized thaw settlement (i.e., thaw settlement of the reinforced soil to that of the unreinforced soil) with the increase in F-T cycles. The maximum reduction in thaw settlement due to geocells was approximately 50%, 45%, and 20% for the soil with 0%, 5%, and 12% kaolin, respectively. This, in general, occurred at the second F-T cycle for 5% and 12% kaolin, after which the effectiveness of geocells diminished, as observed in the peak heave (Fig. 2.8). At 12% kaolin, the thaw settlement of the reinforced soil even exceeded that of the unreinforced soil. This was due to the continuing development of peak heave, as discussed previously, because the thaw settlement was determined by subtracting the residual settlement from the peak heave, where residual settlement remained almost unchanged by geocell reinforcement.

Overall, the results of peak heave and thaw settlement indicated that the most significant damages of bases were developed after one or two F-T cycles depending on the percentage of fines in the base materials. The geocell reinforcement became less effective in mitigating F-T damages under larger F-T cycles (i.e., ≥3) at higher fines content (i.e., 12%).

2.4.1.3 Water distribution in soils during F-T cycles

During the freezing process, the presence of geocells reduced the efficiency of lateral water movement in soils, which more likely resulted in the formation of discrete, localized ice lenses within the cells (Zheng et al., 2020; Arenson et al., 2016). This could be revealed by examining volumetric moisture contents in soils with 5% and 12% kaolin. Fig. 2.11 displays volumetric moisture contents with soil height at different F-T cycles.

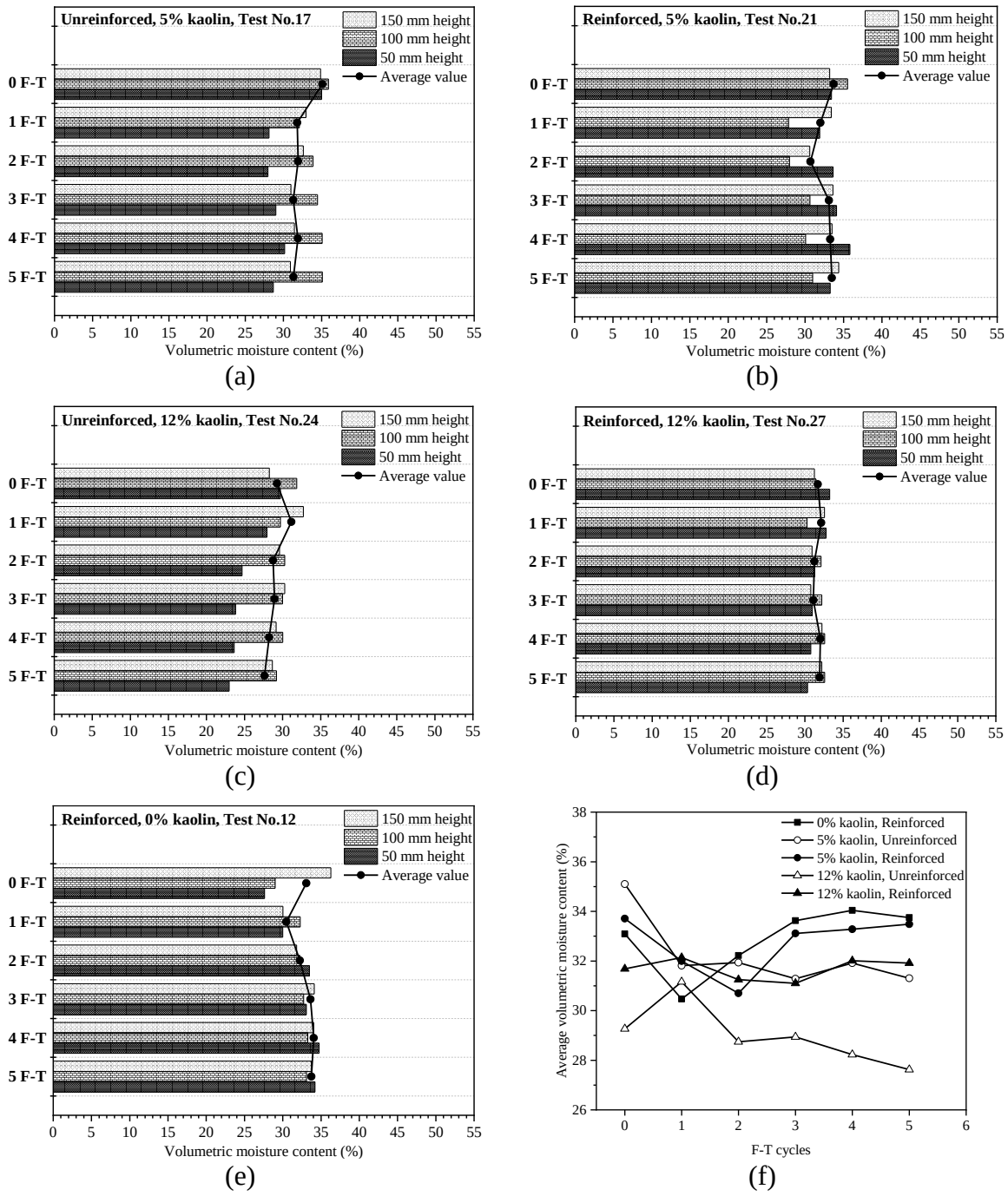

Fig. 2.11. Volumetric moisture contents during five F-T cycles: (a) and (b) unreinforced and reinforced soils with 5% kaolin, respectively, (c) and (d) unreinforced and reinforced soils with 12% kaolin, respectively, (d) reinforced soils with 0% kaolin and (f) average volumetric moisture content

It should be noted that the volumetric moisture content at the height of 150 mm was the averaged value of the three EC-5 moisture sensors located at different positions horizontally, as

shown in Figs. 2.4(b) and 2.4(c). Fig. 2.11 also plots the average value of all the EC-5 moisture sensors in the soils at different F-T cycles [i.e., the solid dots in each figure and Fig. 2.11(f)]. Figs. 2.11(a) and 2.11(b) show the volumetric moisture contents for unreinforced and reinforced soils with 5% kaolin, respectively, while Figs. 2.11(c) and 2.11(d) show the volumetric moisture contents for unreinforced and reinforced soils with 12% kaolin, respectively. At zero F-T cycle, the average moisture content was similar between unreinforced and reinforced soils with 5% kaolin; however, the average value was higher (about 2.5% higher) in the reinforced soil than in the unreinforced soil with 12% kaolin. As F-T cycles increased, a distinct reduction in the moisture content was noticed in the lower parts of soil (i.e., 50 mm or 100 mm height) for both unreinforced and reinforced soils, except for the reinforced soils with 12% kaolin. Unlike the unreinforced soils with 12% kaolin that saw the moisture content decreased by F-T cycles, the reinforced soils with the same kaolin content experienced almost no change in average moisture content at the three heights under F-T cycles. This virtually no loss of water by F-T cycles could provide a continuous supply for the formation of localized ice lenses at higher F-T cycles. This, along with the initial high moisture content in the reinforced soil with 12% kaolin, might have caused the creep developed at larger F-T cycles (i.e., $\geq$3), as observed in Figs. 2.8 and 2.10. The less loss in water in the reinforced soils during F-T cycles was attributed to the geocells that could cut or impede the horizontal movement of water in the lower permeable soils, i.e., the 12%-kaolin soils.

A comparison of volumetric moisture contents of the reinforced soils with different fines contents [i.e., Figs. 2.11(b), 2.11(d), and 2.11(e)] reveals that water in the top layer increased but in the bottom layer it decreased with increased F-T cycles for 5% and 12% kaolin; however, the reversed phenomenon was observed for 0% kaolin. This indicates the upward migration of water for the former two types of soils but the downward migration of water for the latter type of soil

driven by increased F-T cycles. This result can be verified by the visual observation of soil surface wetness through photographs taken before and after F-T cycles, as presented in supplementary material to this paper Figs. S.2.1 to S.2.6. These figures clearly illustrate that after one or five F-T cycles, the surface soil got wetter for 5% and 12% kaolin soils but became drier for 0% kaolin soil. This might explain why geocell reinforcement became less effective in reducing the peak heave (Fig. 2.8) and thaw settlement (Fig. 2.10) in the 5%- and 12%-kaolin soils than in the 0%-kaolin soils.

2.4.2 Plate loading tests

Plate loading tests were conducted right after the completion of F-T tests. The plate loading results are represented by the applied pressure-displacement curves in which stiffness, k, and ultimate bearing pressure, p_u, were determined. A proper interpretation strategy was implemented to determine the values of k and p_u. This section will first discuss the interpretation of test results, followed by the repeatability of the loading tests, and then the effects of geocells and fines content on the plate loading test results after being subjected to different F-T cycles.

2.4.2.1 Interpretation of test results

Two typical pressure-displacement curves measured in the plate loading tests are illustrated in Fig. 2.12. Both curves feature initial steep slopes under small loads, which are caused by sitting errors that occurred due to the incomplete contact between soil and loading plate, surface irregularities, etc. Like the adjustment of California Bearing Ratio test data (ASTM D1883), this initial portion of data necessitates correction for the sitting errors, as shown in Fig. 2.12. Basically, the initial portion of the curve is corrected by linearly extending the middle linear portion to intersect the vertical axis at a point (i.e., $0'$). The point will be used as a new origin. The stiffness of soils, k which is also known as the coefficient of subgrade reaction in foundation engineering,

is then defined as the initial slope of the corrected curve (Pokharel et al., 2010). The definition of ultimate bearing pressure, p_u, is dependent on the failure modes. If an abrupt or plunging failure is discernable, the ultimate bearing pressure is defined as the pressure at the failure shown in Fig. 2.12(a) (Pokharel et al., 2010). If the plunging load is not discernable as illustrated in Fig. 2.12(b), the ultimate bearing pressure is determined as the applied pressure having the maximum curvature-i.e., the largest variation of the two consecutive tangent slopes (Adams and Collin, 1997; Rajagopal et al., 2014).

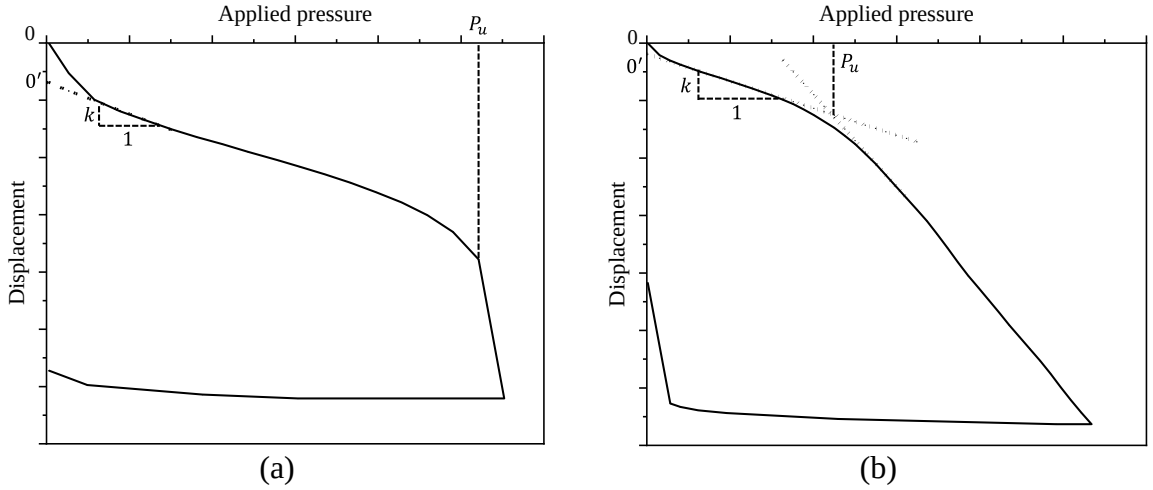

Fig. 2.12. Illustration of determination of stiffness and ultimate bearing pressure in the pressure-displacement curve: (a) plunging response and (b) hardening response

2.4.2.2 Repeatability of test results

Repeatability of the plate loading tests was examined on the unreinforced and reinforced soils with 0% and 5% kaolin under zero and one F-T cycle. The results are presented in Fig. 2.13. The results show that the addition of kaolin remarkably reduced the variability of pressure-displacement curves as compared with the soils without kaolin. The stiffness was more consistent than the ultimate bearing pressure. The application of F-T cycles helped reduce the variability of the test data for both 0%- and 5%-kaolin soils. Overall, the model tests on the soils with fines were repeatable under F-T cycles because the coefficient of variation of the measured values was

no more than 30% (Lee et al., 1983). The higher uncertainty of test results under lower F-T cycles was minimized by running more parallel tests [e.g., Fig. 2.13(b)].

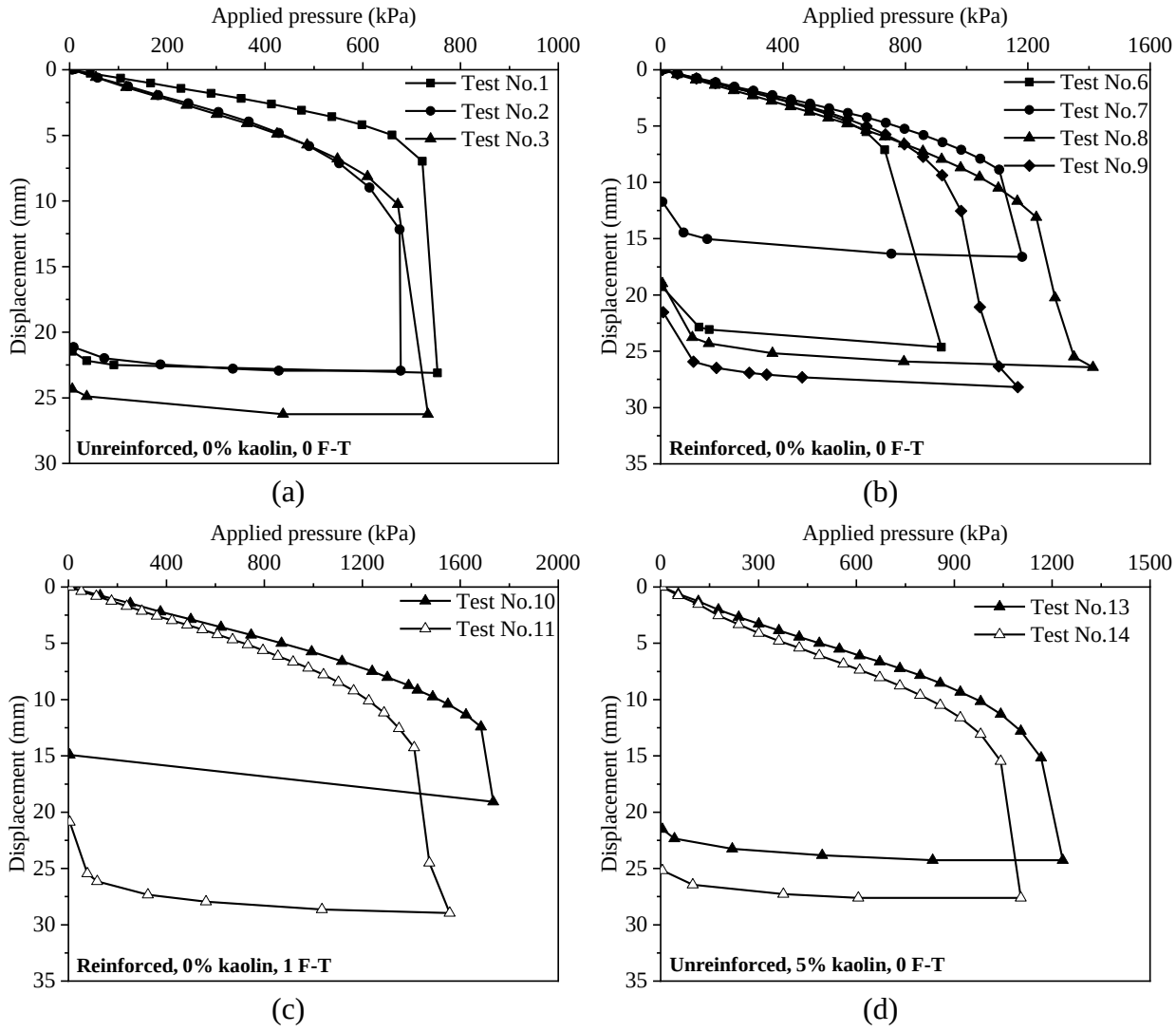

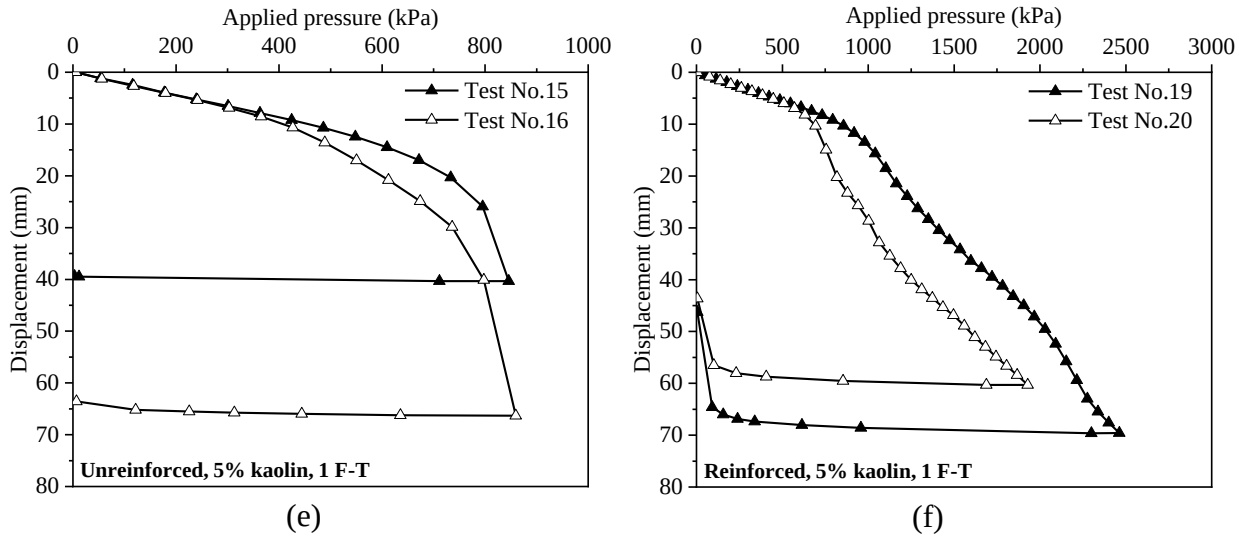

Fig. 2.13. Plate loading test results of: (a) unreinforced soils with 0% fines under 0 F-T cycle, (b) reinforced soils with 0% fines under 0 F-T cycle, (c) reinforced soils with 0% fines under 1 F-T cycle, (d) unreinforced soils with 5% fines under 0 F-T cycle, (e) unreinforced soils with 5% fines under 1 F-T cycle and (f) reinforced soils with 5% fines under 1 F-T cycle

2.4.2.3 Plate loading test results

Fig. 2.14 shows the pressure-displacement curves of unreinforced and reinforced sands with 0%, 5% and 12% kaolin after zero, one, and five F-T cycles. It can be clearly seen that most of the reinforced soils experienced hardening responses at the large deformation while the unreinforced soils underwent abrupt failure under incremental loads.

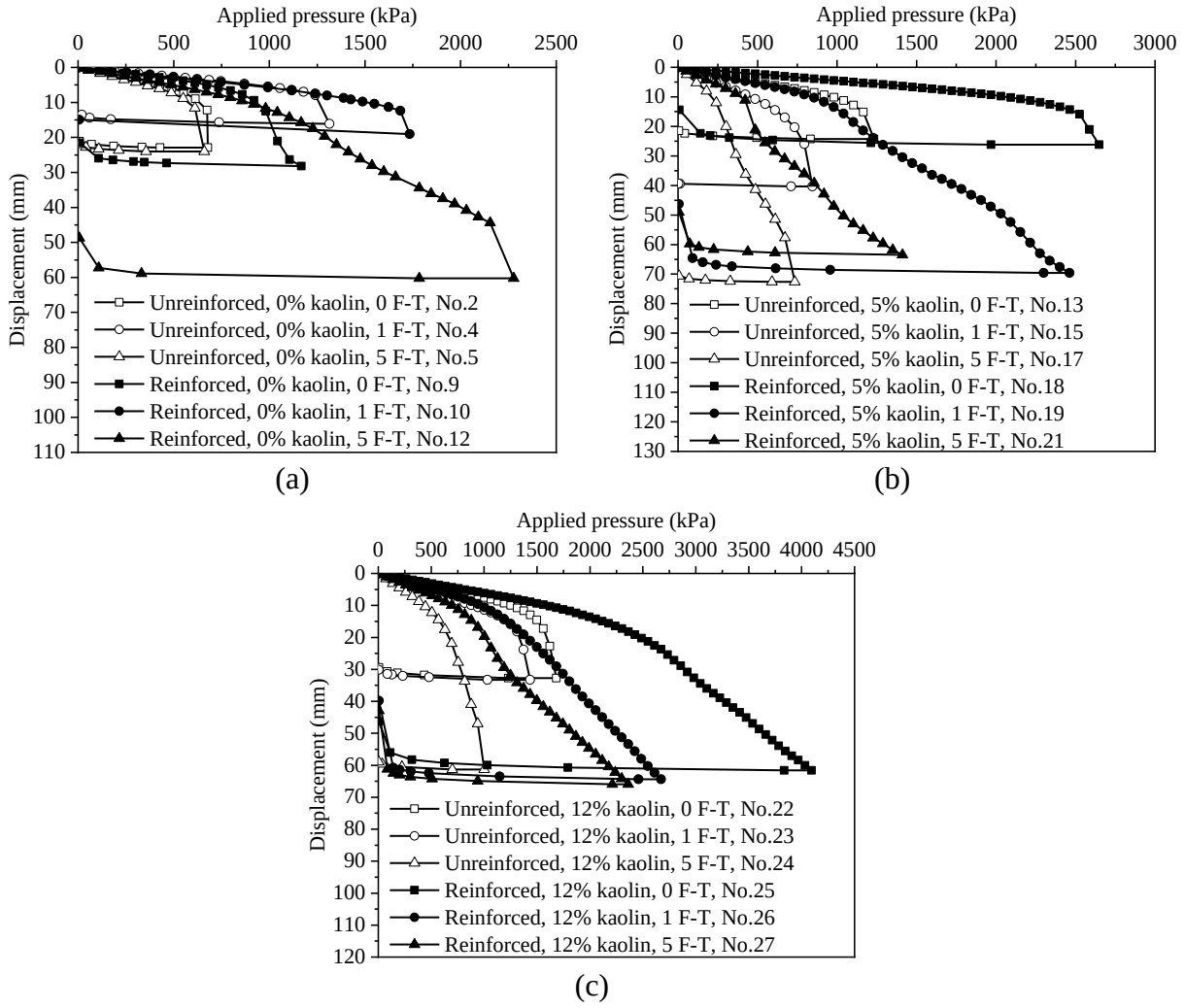

Fig. 2.14. Pressure-displacement curves of plate loading tests on unreinforced and reinforced soils with: (a) 0% fines, (b) 5% fines, and (c) 12% fines

Effect of fines content on stiffness and bearing capacity

The values of stiffness and ultimate bearing pressure determined from these curves in Figs 2.13-2.14 are illustrated in Figs. 2.15(a)-2.15(b), respectively. The averaged stiffness and ultimate bearing pressure were used in the parallel model tests. Figs. 2.15(c) and 2.15(d) is the plot of normalized stiffness and ultimate bearing pressure: i.e., the value after F-T cycles divided by the value prior to F-T cycles (or zero F-T cycle). For the soils with 0% kaolin, the values of k and p_u increased and then decreased with the increase in the number of F-T cycles. After the five F-T cycles, the values of k and p_u of the unreinforced soils were decreased by approximately 40% and

11%, respectively, with respect to the values prior to F-T. In contrast, for the reinforced soils, the value of k decreased by about 33%, and p_u remained almost unchanged with a slight increase of about 3%. By contrast, both unreinforced and reinforced soils with 5% and 12% kaolin underwent continuing decrease in k and p_u as F-T increased from 0 to 5 cycles, with most of the drop occurring after one F-T cycle. After five F-T cycles, the decrease in k was 54%-81% and that in p_u 61%-83%. In comparison, the addition of kaolin (from 0% to 5%) resulted in the increased loss in k and p_u caused by F-T cycles; however, a further increase in kaolin content from 5% to 12% did not cause a further decrease in k and p_u, as indicated in Figs. 2.15(e) and 2.15(f).

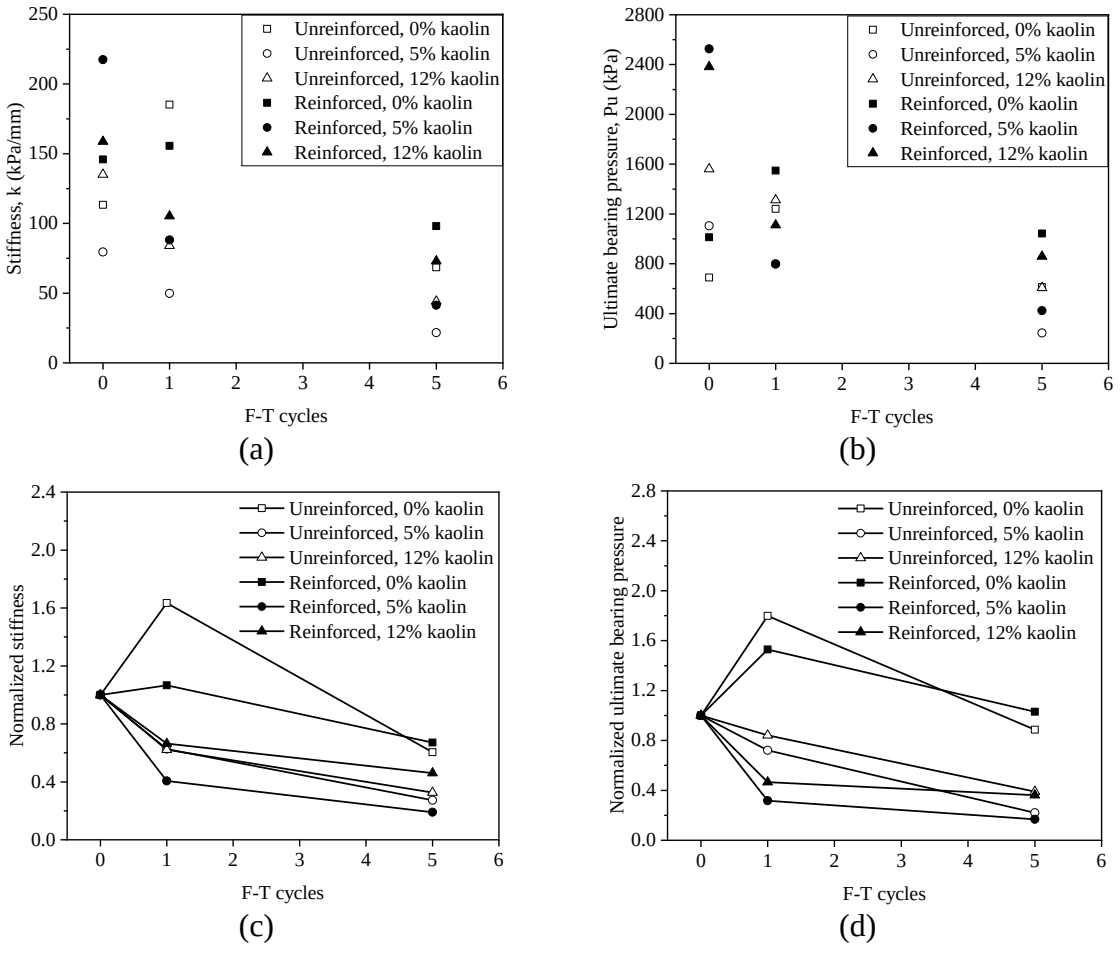

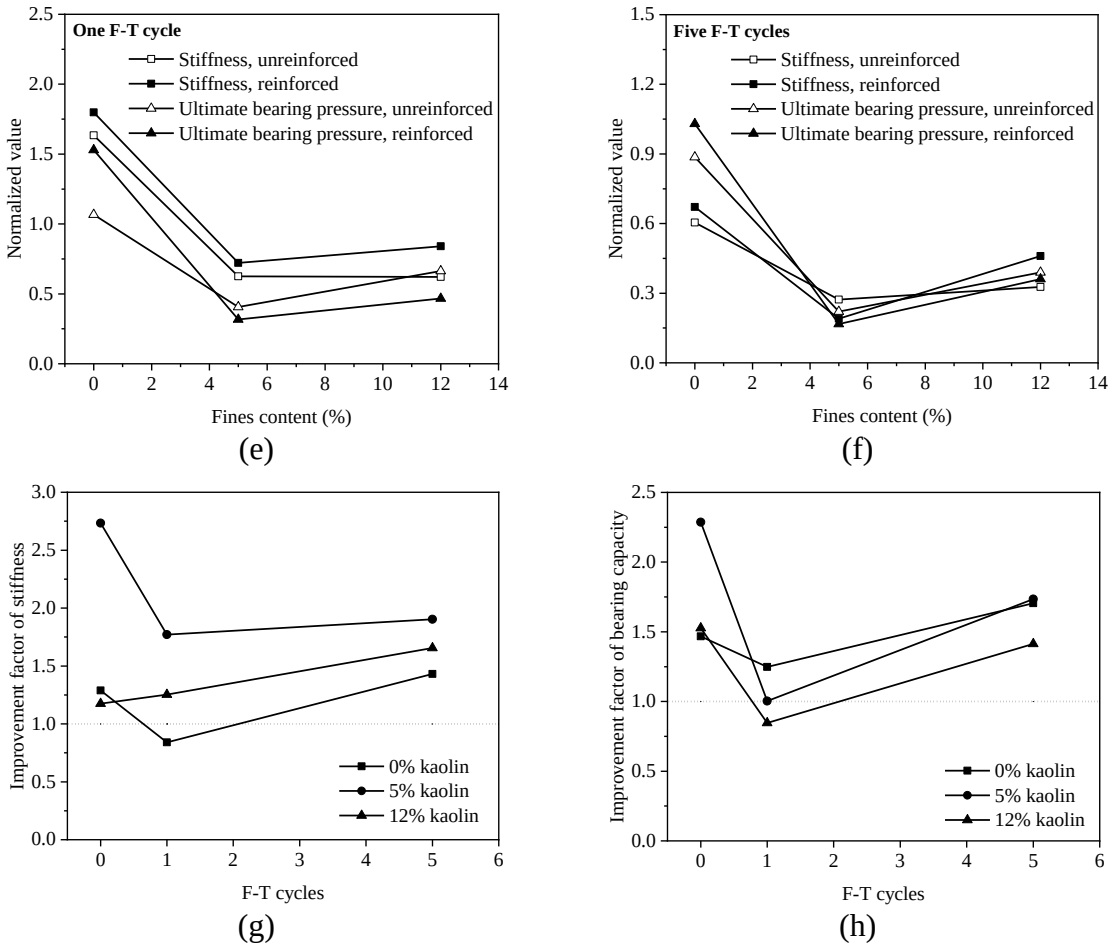

Fig. 2.15. Plate loading test results of unreinforced and reinforced soils with different fines contents under different F-T cycles: (a) stiffness, (b) ultimate bearing pressure, (c) normalized stiffness, (d) normalized ultimate bearing pressure, (e) normalized value after one F-T cycle, (f) normalized value after five F-T cycles, (g) improvement factor of stiffness and (h) improvement factor of bearing capacity

The different trends of k and p_u with F-T cycles for soils with and without kaolin were attributed to the combined effects of varying water redistribution and changes in internal structures of soils during F-T cycles. Water redistribution can be observed through supplementary material to this paper Figs. S.2.1-S.2.6. For 0%-kaolin soils (Figs. S.2.1 and S.2.2), the soil surface became drier after F-T cycles; however, for 5%- and 12%-kaolin soils (Figs. S.2.3-S.2.6), the soil surface became wetter after one and five F-T cycles. As discussed previously, the visible observation was consistent with the quantitative examination of water redistribution by the measured volumetric moisture contents during F-T tests in Fig. 2.11. The increase in moisture content of the surface

soil tended to decrease the stiffness and bearing capacity of the soils, and vice versa. In addition to water redistribution, the F-T induced changes to the soil internal structure contributed to the discrepancy in F-T responses of the soils with different fines contents. This can be assessed through the changes in void ratio with F-T cycles. Tables 2.4 and 2.5 show that the void ratio of the soils at the peak and residual heaves continued to develop with F-T cycles, revealing that the soils were loosened by repetitive F-T thermal loading. This phenomenon was similar to the softening of dense soils under mechanical loading. This loosening effect was more remarkable for soils with fines than without fines. For example, the increase in kaolin from 0% to 5% resulted in the most significant F-T induced loosening effect. In comparison, a further increase of kaolin from 5% to 12% did not correspond to a further increase in the cyclic F-T loosening of soils. This explains why the decrease in the stiffness and strength after five F-T cycles was most substantial for 5%-kaolin soils and least significant for 0%-kaolin soils. It also explains why the stiffness and strength of the 5%- and 12%-kaolin soils continued to decay with the increased F-T cycles. For the 0%-kaolin soils, the increase in the k and p_u after one F-T cycle might be due to the competing effect of water redistribution and changes in soil internal structure, where the water redistribution dictated.

Table 2.4. Void ratio of soils at the peak heave

No. of F-T cycle	Unreinforced soil			Reinforced soil		
	0% kaolin	5% kaolin	12% kaolin	0% kaolin	5% kaolin	12% kaolin
0	0.421	0.369	0.301	0.412	0.360	0.293
1	0.447	0.445	0.331	0.437	0.420	0.317
2	0.454	0.484	0.401	0.439	0.432	0.371
3	0.456	0.476	0.406	0.441	0.443	0.391
4	0.461	0.481	0.405	0.440	0.453	0.403
5	0.459	0.480	0.406	0.443	0.458	0.411

Table 2.5. Void ratio of soils at the residual heave

No. of F-T cycle	Unreinforced soil			Reinforced soil		
	0% kaolin	5% kaolin	12% kaolin	0% kaolin	5% kaolin	12% kaolin
0	0.421	0.369	0.301	0.412	0.360	0.293
1	0.423	0.385	0.302	0.421	0.379	0.298
2	0.429	0.393	0.318	0.422	0.382	0.307
3	0.433	0.393	0.325	0.426	0.384	0.312
4	0.438	0.394	0.327	0.428	0.388	0.317
5	0.439	0.395	0.330	0.430	0.393	0.321

Effect of geocell reinforcement on stiffness and bearing capacity

Figs. 2.15(g) and 2.15(h) shows improvement factors of stiffness and ultimate bearing pressure, which are a ratio of k (or p_u) of the reinforced soil to that of the unreinforced soil after the same F-T cycles. They are used to quantify the benefit of geocells in improving the F-T performance of soils. In general, the improvement factors decreased as F-T cycles increased from zero to one cycle, but they increased when the cycle number increased from one to five. This indicates that the initial geocell reinforcement was weakened by F-T cycles; however, the geocells could regain the beneficial effect at larger F-T cycles. After five F-T cycles, the geocell reinforcement increased the stiffness by about 43%, 90%, and 66% for the soils with 0%, 5% and 12% kaolin, respectively. The corresponding increase in ultimate bearing pressure was 71%, 73%, and 41%.

Figs. 2.15(g) and 2.15(h) also shows that the benefit of geocells was more evident in the 5%-kaolin soils than 0%- and 12%-kaolin soils. It has been reported that the benefit of geocells is less significant for the stronger infill materials (Han et al., 2010). One of the contributions of geocells is to provide an apparent cohesion for granular infill material (e.g., Bathurst and Karpurapu, 1993; Rajagopal et al., 1999) but the increase in fines in the infills can provide “true” cohesion, which

thus reduces such a beneficial effect of geocells (Pokharel et al., 2010). The result from this study did not seem to fully conform to the existing understanding. The reason for this discrepancy is unknown at this stage, which will be further investigated. However, the increase in the improvement factor at the larger F-T cycles confirmed that the benefit of geocells did play an effective role in the soils that were weakened by cyclic F-T thermal loading.

The findings of this research reinforced the previous field observations that the geocells were effective in mitigating the F-T damages and improving the bearing capacity of roads. Besides, this study provided additional implication that the inclusion of geocells was also beneficial for poorer base materials such as sands with fines and the benefit was most pronounced when the fines content ranged 0-5%.

2.5 Conclusions

This paper presents a series of model tests to investigate the freeze-thaw performance of geocell-reinforced base materials (sands) with different fines (kaolin) contents. The custom-made model test device was employed to conduct the model tests, which included the F-T tests and subsequent plate loading tests. The outcomes of this study were to improve the understanding of the benefit of geocells in improving the properties of base materials under F-T loading as well as how this benefit would be affected by varying fines contents in the base materials. The following conclusions are drawn from this study:

(1) The increase in fines content reduced the freezing rate during the subfreezing process and increased the duration to complete one F-T cycle (i.e., ranging from 40 to 65 hours). The inclusion of geocells in the soils did not affect the freezing rate and the duration of F-T cycle.

(2) The frost heave and thaw settlement were developed primarily at the first or second F-T cycle, and after that, they generally remained relatively stable. An increase in fines from 0% to 5%

substantially increased the peak heave and thaw settlement by approximately 200%-300% after five F-T cycles; however, a further increase in fines from 5% to 12% did not cause additional frost heave in the soils.

(3) The benefit of geocells was more remarkable in reducing frost heave and thaw settlement at lower F-T cycles for the soils with lower fines content. After two F-T cycles, the reduction in frost heave and thaw settlement was 37% and 44%, respectively, for soils with 5% kaolin, compared with 21% and 22% for soils with 12% kaolin.

(4) The reduction in frost heave and thaw settlement after five F-T cycles was approximately 11%-18% and 22%-35%, respectively when fines content was 0% and 5%. For a higher fines content of 12%, the geocells increased the frost heave and thaw settlement on the contrary. This was attributed to the relatively high initial moisture content in the prepared 12%-kaolin soils and decreasing horizontal water migration by geocells in lower permeable soils. An increase in the number of perforated holes in the geocell walls might help minimize this issue.

(5) The increase in fines content from 0% to 5% resulted in decreased stiffness and ultimate bearing pressure, and the reduction was more considerably at larger F-T cycles. However, a further decrease in the fines content from 5% to 12% instead increased the values of stiffness and ultimate bearing pressure.

(6) The use of geocells increased the stiffness by about 43%, 90% and 66% in the soils with 0%, 5% and 12% kaolin, respectively after five F-T cycles, and the ultimate bearing pressure by 71%, 73%, and 41%. The benefit of geocells in mitigating F-T damages was more noticeable for sands with 5% fines content at larger F-T cycles.

Notation

Basic SI units are given in parentheses.

CBR	California Bearing Ratio (dimensionless)
M_r	Resilient modulus (Pa)
D_{50}	Mean particle size (m)
D_{10}	Effective particle size (m)
k	Stiffness (Pa/m)
p_u	Ultimate bearing pressure (Pa)

Abbreviations

F-T	Freeze-thaw
NPA	Nano-polymeric alloy
USCS	Unified Soil Classification System
SP	Poorly graded sand
SP-SC	Poorly graded sand with clay
SC	Clayed sand
LVDT	Linear variable differential transformer

Chapter 3 Freeze-Thaw Impacts on Geocell-Stabilized Bases Considering Effects of Water Supply and Compaction

3.1 Abstract

Although geocells have been applied to stabilize road bases against the freeze-thaw (F-T) damage in practice, a scarcity of research has been conducted to assess their efficacy. This study aims to investigate quantitatively the F-T performance of geocell-stabilized bases, focusing on two influencing factors-i.e., water supply and degree of compaction in the bases. A series of model-scale experimental tests (19 tests) was conducted using an upgraded customized apparatus. The results showed that the inclusion of geocells was beneficial for reducing frost heave and thaw settlement as well as mechanical properties (i.e., stiffness and ultimate bearing capacity) of road bases. The benefit of geocells was more remarkable for the well compacted bases than for the poorly compacted bases. The benefit was more pronounced in the open system than in the closed system.

3.2 Introduction

Freeze-thaw (F-T) cycles are a major cause for distresses of roadways in seasonal frost regions. The repeated thermal action would mobilize water nonuniformly in soils via generating segregated ice lens and trapped meltwater, remold soil structure, and weaken pavement layers. To enhance the road durability, various engineering measures have been employed in practice, which can be grouped into two categories: reducing water access (e.g., use of effective drainage system, capillary barrier, and wicking fabrics) and improving soil properties (e.g., removal of frost-susceptible soils, cement/lime stabilization of bases or subgrades, and geosynthetics stabilization of base courses) (Christopher et al., 2000; Ghazavi and Roustaei, 2013; Henry and Holtz, 2001; Lai et al., 2012; Li et al., 2017; White and Vennapusa, 2013). Geocells, a type of three-dimensional

geosynthetic material, have demonstrated potential in enhancing the F-T resistance of roads in various projects across North America. For example, based on visual inspection on two test sections of flexible pavements in Alberta, Canada, Pokharel et al. (2017) found that the test section with geocell-stabilized bases outperformed that with cement-stabilized bases over three years of operation (i.e., three seasonal F-T cycles). Pokharel et al. (2016) reported several successful cases of using geocells to stabilize access roads across saturated soft Muskeg areas in British Columbia and Alberta, Canada, with no sign of distresses observed on the road surface after one to three years of services. Chatterjee et al. (2022) also reported the similar successful application in an access road over fully saturate subgrades across a wetland area in Quebec, Canada. The advantages of geocells observed in practical applications predominantly stem from visual assessments, rendering them largely qualitative in nature. In contrast to their real-world applications, there is a notable scarcity of research specifically addressing this topic. Consequently, a clear research gap exists regarding the factors influencing the performance of geocell-stabilized bases under F-T cycles and a quantitative evaluation of these factors' impacts.

To address the current research gap, the authors have developed a customized model test apparatus that can impose both thermal loading (simulating F-T cycles) and plate loading (simulating traffic loading) (Huang et al., 2021) so that a variety of influencing factors can be investigated directly. Utilizing this apparatus, an influencing factor-i.e., fines content in the base layer has been investigated (Huang et al., 2023). The present study is a continuous effort to elucidate the behavior of geocell-stabilized bases under F-T cycles through focusing on another two critical influencing factors: water supply and degree of compaction of the bases, which have not been investigated before.

The extent of F-T damage in roads is dependent on several influencing factors, including

thermal loading (e.g., temperature gradient, number of F-T cycles), pavement conditions (e.g., base course compaction and fines content, water supply, subgrade conditions, etc.), and traffic loading. Among these factors, water supply is deemed most influential as water is responsible for nonuniform heave and thaw in pavements, and thus the early distresses of the pavements. The source of water can be groundwater or infiltration through pavement surface during precipitation or snow melting. Numerous studies have investigated the impact of water supply on physical and mechanical properties of soils primarily through element tests. Li et al. (2019) demonstrated that frost heave of granular bases at the optimum moisture content in an open system (with external water supply) was up to 3.5 times higher than in a closed system (without external water supply) by performing a series of element tests. Lu et al. (2019a, b) revealed that soil samples in an open system "oversaturated" (a term used to describe the increase in moisture content that exceeds the initial saturated moisture content) after F-T cycles while those in a closed system exhibited greater water content at the top of the samples but less water content at the bottom of the samples. They also observed that after F-T cycles, soil modulus and strength decreased more significantly in the open system than in the closed system. Besides water access, degree of compaction of bases is also a crucial factor influencing the F-T performance of roads. According to Viklander (1998), with the progress of F-T cycles, loose soil became denser while dense soil became looser, and both converged toward a residual void ratio. However, Huang et al. (2022) reported that for cohesive soils, degree of compaction did not affect the variations of the strength of the soil with F-T cycles. They found the strength of the test soils at different compaction degrees exhibited a continuous decrease trend with increasing the number of F-T cycles. This was attributed to the increase in their surface porosity and pore sizes by the cyclic F-T. In general, previous studies have primarily focused on assessing the effects of water supply and degree of compaction on the F-T responses

of soils through element tests, i.e., triaxial tests, CBR tests, or permeability tests. To the best of authors' knowledge, there has no research conducted on geocell-stabilized bases considering these two factors through the model tests on a medium or large scale.

The objective of this study was to experimentally investigate the effects of water supply and degree of compaction on the F-T performance of geocell-stabilized bases. Utilizing the apparatus developed by Huang et al. (2021), a series of model tests were conducted by subjecting non-stabilized and geocell-stabilized bases to varying F-T cycles while considering effects of water supply and degree of compaction. After completion of the predefined F-T cycles, plate loading tests were performed. The findings from both the F-T tests and the plate loading tests are anticipated to enhance the understanding of geocells' contributions in mitigating F-T damage to base layers.

3.3 Experimental study

To achieve the research objective, a total of 19 model tests were conducted. The test program is given in Table 3.1. The designation for the specimens in the table would read in the order of the initial(s) of compaction degree (CD) and the number, closed system (CS) or open system (OS), non-stabilized (N) or stabilized (S), and freeze-thaw (F-T) and the number of F-T cycles. The tests are divided into three groups (A, B and C) based on the consideration of water supply and degree of compaction. Groups A and B explored F-T responses of the bases compacted to 100% of the maximum dry density (MDD) per ASTM standard Proctor's procedure in closed and open systems, respectively, while Group C tested the bases at 80% compaction (i.e., 80% of MDD) in a closed system. After the completion of the F-T tests, the plate loading tests were performed immediately.

Table 3.1. Details of model test program

No. of testing group	Water supply	Compaction degree	Reinforcement	Test No.	No. of F-T cycles	Specimen designation
A*	Closed system	100%	Non-stabilized	1-2	0	CD100/CS/N/FT0
				3-4	1	CD100/CS/N/FT1
				5	5	CD100/CS/N/FT5
			Stabilized	6	0	CD100/CS/S/FT0
				7-8	1	CD100/CS/S/FT1
				9	5	CD100/CS/S/FT5
B	Open system		Non-stabilized	10	1	CD100/OS/N/FT1
				11	5	CD100/OS/N/FT5
			Stabilized	12	1	CD100/OS/S/FT1
				13	4	CD100/OS/S/FT4
				14	5	CD100/OS/S/FT5
C	Closed system	80%	Non-stabilized	15-16	0	CD80/CS/N/FT1
				17	5	CD80/CS/N/FT5
			Stabilized	18	0	CD80/CS/S/FT1
				19	5	CD80/CS/S/FT5

*This group of results is extracted from Mian et al. (2023).

3.3.1 Test materials

The base material in this study was a mixture of 95% sand and 5% kaolin, the same material used in Huang et al. (2023). Note that instead of aggregates, sand was used as the base material for two reasons. Firstly, the three-dimensional confinement of geocells allows for the inferior granular infill. Secondly, sand, which is more prone to frost heave than aggregates, would better manifest the F-T effect. The fines content of 5%, adhering to the allowable maximum fines content of 5% to 8% in the specifications (e.g., AASHTO M147, 2004; Alberta Transportation, 2010; ASTM D2940/D2940M; British Columbia Ministry of Transportation and Infrastructure, 2020),

was chosen to enhance the F-T responses of the base in the model tests. The base material was classified as poorly graded sand with clay (SP-SC) according to the Unified Soil Classification System (USCS) with the mean particle size (d_{50}) of 0.674 mm, uniformity coefficient of 5.7, and curvature coefficient of 1.1. The specific gravity was 2.697, which was estimated based on combining the corresponding values of 2.70 for sand and 2.65 for kaolin. Fig. 3.1 shows the standard compaction curve of the base (ASTM D698), indicating that the maximum dry density (ρ_{dmax}) and the optimum moisture content (wo) were 1970 kg/m^3 and 11.7%, respectively. The unsoaked California Bearing Ratio (CBR) for the bases with the similar condition ($\rho_d = \rho_{dmax}$, w = 10.6%) was 49% (ASTM D1883).

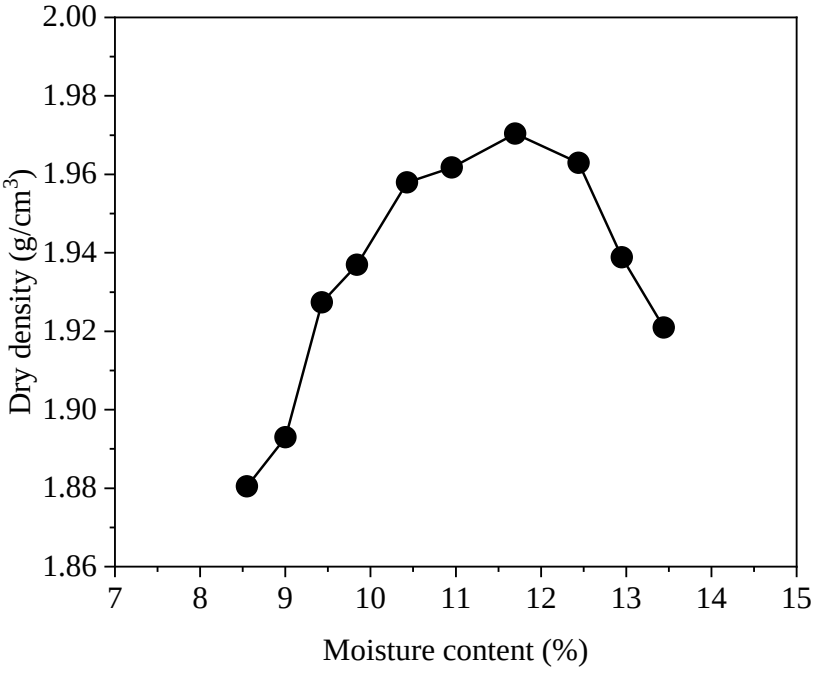

Fig. 3.1. Compaction curve of the bases based on Standard Proctor Tests

In alignment with previous studies by Huang et al. (2021, 2023), this study utilized Novel Polymeric Alloy (NPA) Type-C geocells, manufactured by PRS Geo-Technologies®. These geocells consist of perforated ribs with a thickness of 1.1 mm and a height of 150 mm. Upon unfolding, each cell displays an opening dimension of 245 mm × 210 mm. The basic properties

of the geocells are detailed in Huang et al. (2021).

3.3.2 Apparatus upgrade

The early version of customized model apparatus that only ran in a closed system (Huang et al., 2021 and 2023) has been upgraded to allow for both open and closed systems. Fig. 3.2 shows the upgraded setup, which includes an upgraded F-T box [Fig. 3.2(a)], an existing loading frame system [Fig. 3.2(b)], and an existing rail connection. The upgrading of the F-T box was accomplished by incorporating a water supply system. To enable the water supply with a consistent water table during the F-T process, a Mariotte's type container was set up and connected to the F-T box through the port at the box bottom [Fig. 3.2(c)]. A valve, referred to as Valve A, was installed near the port so the closed and open systems could be achieved by simply switching the valve off and on, respectively. The stable elevation of the water table in the bases was regulated by adjusting the air inlet position in the Mariotte's container [Fig. 3.2(c)]. Water replenishment in the container was possible through a separate input, controlled by Valve B. To enable uniform water exchange between the bases and the external source (i.e., Mariotte's container) during F-T process while retaining the bases inside the F-T box, porous polyethylene sheets (Scientific Commodities®), featuring 10-micron voids, were installed across the entirety of the box's bottom. The freezing and thawing of the bases were achieved by heating and cooling the base courses on the surface using a cooling plate, and the closed and open systems during the F-T tests were controlled by keeping Valve A close or open, respectively. After the completion of F-T cycles, a static plate loading test was performed, following the removal of the insulation foams and the cooling plate. Static loads were applied incrementally to the bases by using a 150-mm diameter loading plate fixed to a load cell. Loads were exerted by the loading plate and load cell, which was facilitated by a hydraulic jack and pump, as illustrated in Fig. 3.2(b).

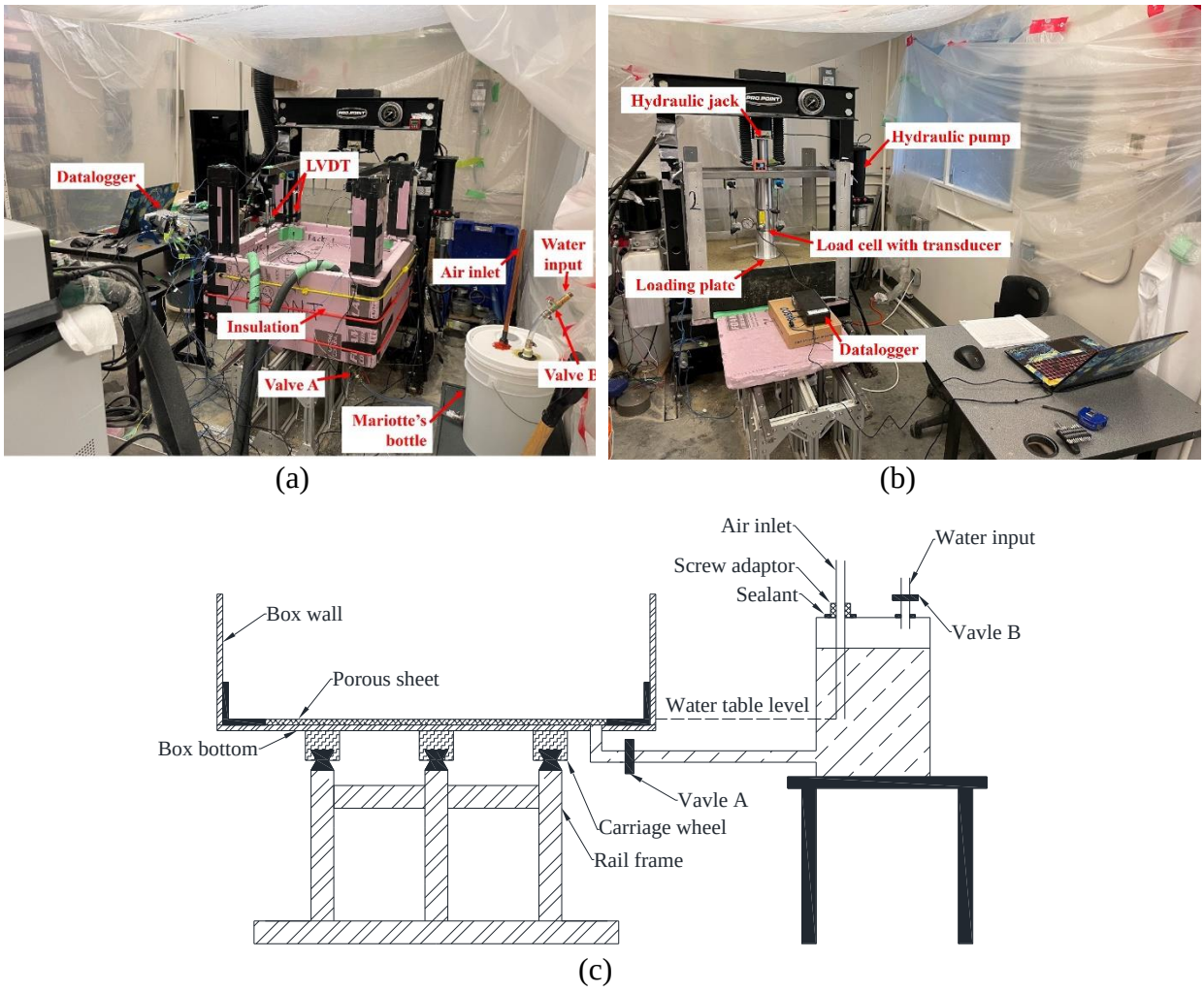

Fig. 3.2. The updated model setup: (a) photograph of freeze-thaw box with water supply system, (b) photograph of plate loading test component, and (c) design drawing of the freeze-thaw box with water supply system

3.3.3 Preparation of bases and instrumentation

During the preparation of the bases, Valve A was closed to facilitate the compaction of both non-stabilized and geocell-stabilized bases to either 80% or 100% of MDD (i.e., 1970 kg/m^3 or 1580 kg/m^3, respectively) with the optimum moisture content of 11.7%. The compaction was executed to achieve a total base thickness of 170 mm in four layers, 50 mm each for the first three layers and 20 mm for the fourth layer. The desired degree of compaction was attained by controlling the base mass added to each layer with predetermined thickness. Before the compaction of the subsequent base layer, the surface of each compacted layer was scratched, which

could enhance the interlayer bonding and minimize the effects of layering for improving the structural integrity of base stacks. In the case of geocell-stabilized bases, the geocell layout is shown in Fig. 3.3. The base compaction within these geocells followed the same protocol as that of the non-stabilized bases, ensuring consistency in the methodology.

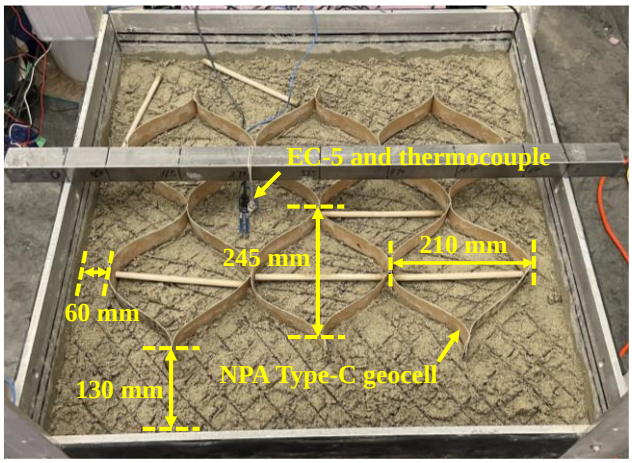

(a)

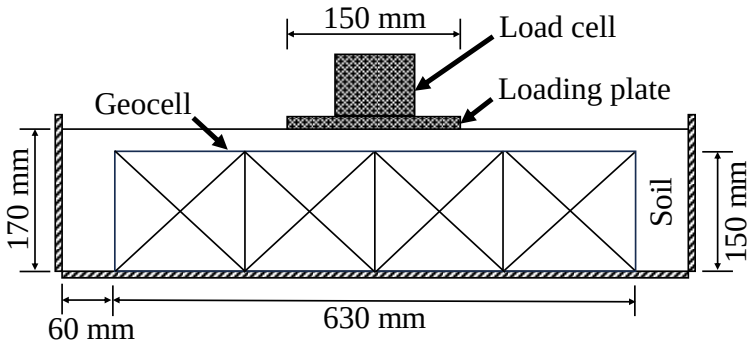

(b)

Fig. 3.3. Layout of geocells: (a) plan view and (b) vertical cross-section view

Fig. 3.4 shows the layout of the thermocouples and moisture sensors in the non-stabilized and geocell-stabilized bases, with their photographs given in Fig. 3.3(a). These sensors were embedded at three different heights within the bases to monitor the temperature and moisture content throughout F-T cycles. Additionally, four thermocouples were installed at various locations: on the cooling plate, atop the porous sheet, at the bottom of the box, and along the box wall to obtain comprehensive temperature data within this system. An extra thermocouple was

positioned above the box to track the variations of ambient temperature. To measure the heave and settlement of the bases during F-T cycles, three LVDTs (Omega® LD620-25) were placed on the heads of screw columns whose tips were fixed to the cooling plate, as shown in Fig. 3.2(a) and Fig. 3.4(c). A datalogger (National Instruments®) was utilized to take readings of the thermocouples and LVDTs at the sampling intervals of 30 minutes, and another datalogger (Meter Group ® ZL-6) was used to capture the data from EC-5 moisture sensors at a frequency of 15 minutes. The accuracies of the Type-C thermocouples, LVDTs, and EC-5 moisture sensors were 1°C, 0.01 mm, and 2%, respectively.

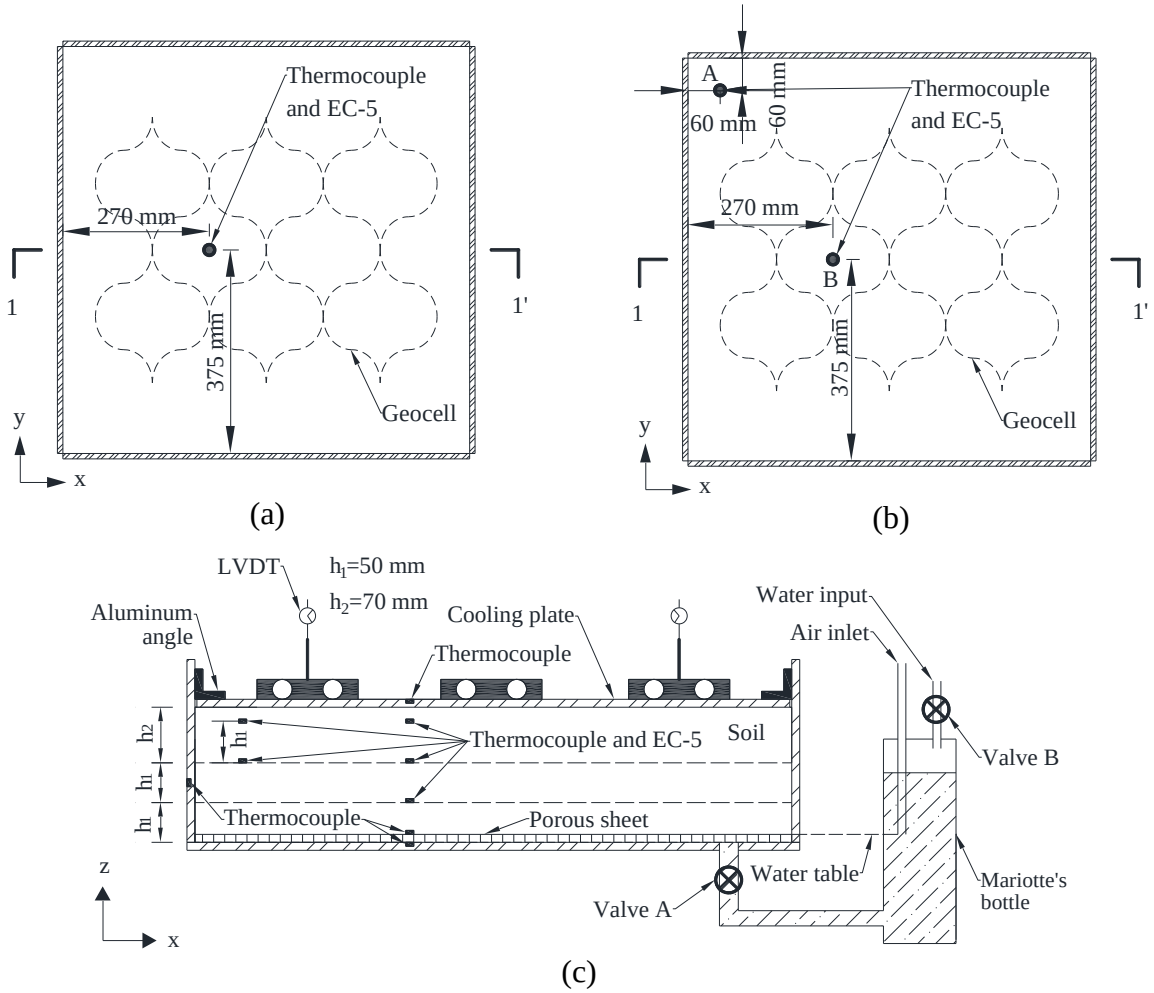

Fig. 3.4. Instrument arrangement: (a) plan view at 50 mm height and (b) plan view at 100 mm and 150 mm heights above the box bottom, and (c) vertical cross section at the cut 1-1′

EC-5 moisture sensors, as reported by Huang et al. (2023), were utilized to measure volumetric moisture contents by using a generic factory-calibration function. In this study, the volumetric moisture contents were further correlated to gravimetric moisture contents, a parameter that is more widely used in geotechnical engineering practice (Guo, 2017; Islam and Tarefder, 2015; Timm, et al., 2004). The correlation tests were conducted in accordance with Method A recommended by Meter Group®. Fig. 3.5 presents the results of these correlation tests.

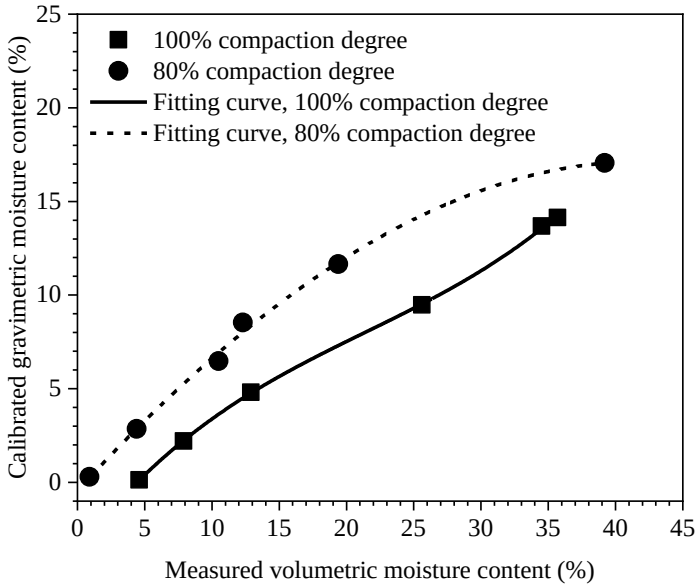

Fig. 3.5. Correlation of gravimetric and volumetric moisture content at different compaction degrees

The relationship between measured volumetric moisture contents and correlated gravimetric moisture contents was fit with the polynomial regression, expressed in Equation (3-1).

$$y = A \times x3 + B \times x2 + C \times x + D \quad (3\text{-}1)$$

where x is the measured volumetric moisture content of moisture sensors (%); y denotes the correlated gravimetric moisture content (%); A, B, C and D are the parameters derived from the fitting curves of the polynomial regression, as listed in Table 3.2.

Table 3.2. Parameters determined in the correlated tests

Compaction degree	Parameter value				
	A	B	C	D	Square R
100%	4.1703E-04	-2.6820E-02	9.2615E-01	-3.6109E+00	0.9998
80%	-3.2264E-05	-7.3000E-03	7.8186E-01	-4.3677E-01	0.9973

After the completion of the compaction, the bases were covered with a plastic sheet, and the condition was kept overnight to ensure hydraulic equilibrium. Afterwards, F-T tests were run. In the closed system (Groups A and C in Table 3.1), Valve A remained closed throughout F-T cycles, while in the open system (Group B in Table 3.1), Valve A was switched on, with the water table being kept at the top of the porous sheet (i.e., the bottom of the base courses) by adjusting the air inlet position in the Mariotte's container. During the freezing process, the temperature at the surface of the bases was set to -20°C via the cooling plate resting on it. The freezing process was completed once the box bottom reached -5°C. Prior to the thawing process in the open system, Valve A was then switched off. This was to mimic the worst scenario in the field that the melt water was trapped above the frozen layer. The thawing commenced by increasing the cooling plate temperature to 20°C. It was terminated when the temperature of the box bottom reached 15°C, thus concluding one F-T cycle. This testing procedure was repeated until the predefined number of F-T cycles was achieved. During the F-T cycles, evolution of the surface heave and settlement as well as temperature and moisture contents inside the bases was monitored.

Immediately after the completion of the freeze-thaw tests, a static plate loading test was conducted. During the test, Valve A remained closed for all groups. The loading plate was centrally positioned on the base surface, and the static loads were exerted at an increment of 62 kPa by the manual operation of the handle on the hydraulic pump. At each loading stage, the load was maintained for five minutes, during which both the applied pressure and the plate displacement

were recorded. The incremental loading continued until the bearing failure occurred, or the loading plate reached its travel limit of 70 mm. The loading was then decreased to zero, and the plate loading test was finished. The applied pressure on the loading plate was recorded by a pressure transducer (Omega® PX-309) mounted at the load cell and connected to a datalogger (PASCO® 550 Universal Interface). The displacement of the loading plate was measured with three mechanical dial gauges, placed on three steel bars that were bolted to the loading plate at equidistant points circumferentially [Fig. 3.2(a)]. The pressure transducer and dial gauges had measurable capacities of 34.5 MPa and 50.8 mm, respectively, with the corresponding resolutions of 1 kPa and 0.025 mm.

3.4 Results and discussions

The outcomes of freeze-thaw tests and plate loading tests conducted on the three groups of the non-stabilized and geocell-stabilized bases are presented in this section. The results pertaining to bases at 100% compaction in a closed system (Group A) were derived from Huang et al. (2023).

3.4.1 Freeze-thaw test results

The freeze-thaw test results encompass the evolutions of base surface movement and the changes in moisture content in the bases at each F-T cycle.

3.4.1.1 Evolution of base surface movement during F-T cycles

Fig. 3.6 depicts the time-history variations of the base surface movement for the three groups during F-T cycles as well as the temperatures in the bases, cooling plate, and box bottom. The base temperatures were the averaged readings of all thermocouples embedded in the bases [see Fig. 3.4(c)]. The changes in moisture contents at different heights for the corresponding tests under F-T cycles are shown in Fig. 3.7. The visual observations of the base surface before and after F-T cycles are also presented in Supplementary Figs. S.3.1 to S.3.3.

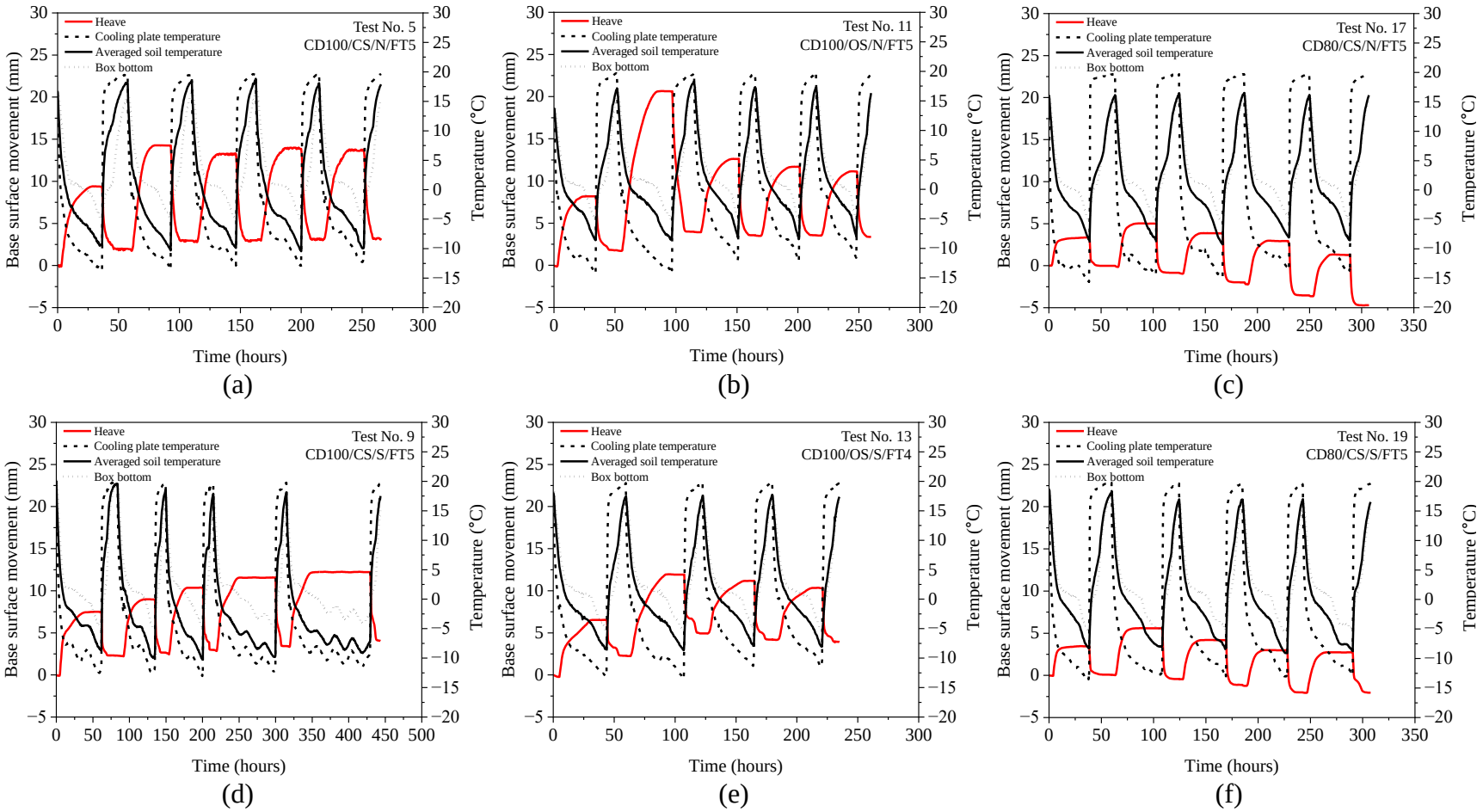

Fig. 3.6. Time-history variations of temperature during F-T cycles: (a) and (d) non-stabilized and stabilized bases (100% compaction degree) in a closed system, respectively, (b) and (e) non-stabilized and stabilized bases (100% compaction degree) in an open system, respectively, (c) and (f) non-stabilized and stabilized bases (80% compaction degree) in a closed system, respectively

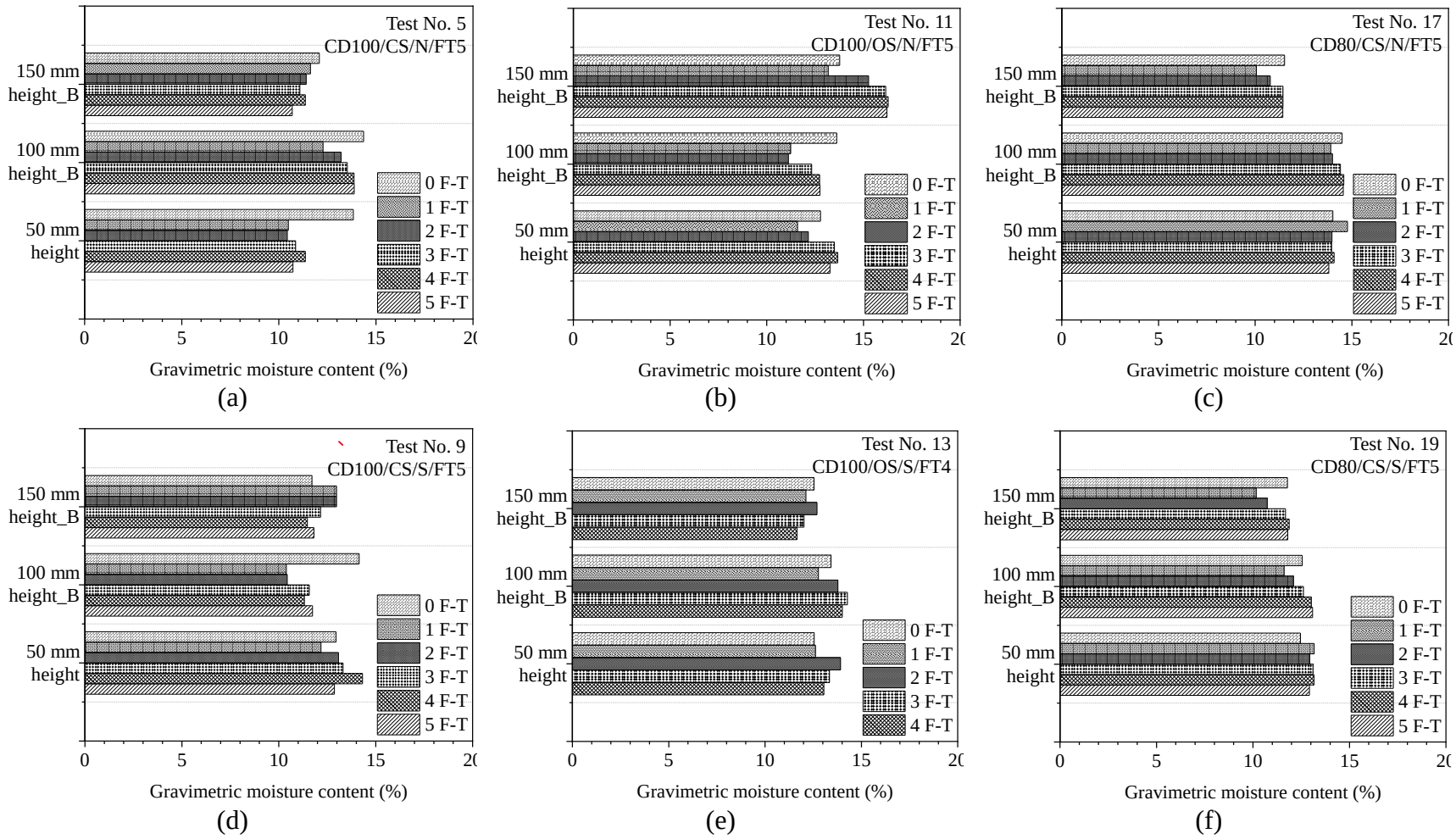

Fig. 3.7. Variations of moisture content with F-T cycles: (a) and (d) non-stabilized and stabilized bases (100% compaction degree) in a closed system, respectively, (b) and (e) non-stabilized and stabilized bases (100% compaction degree) in an open system, respectively, (c) and (f) non-stabilized and stabilized bases (80% compaction degree) in a closed system, respectively

It is worth noting that in Figs. 3.6 and 3.7, the results for the geocell-stabilized bases in an open system were represented by the specimen subjected to four F-T cycles (i.e., CD100/OS/S/FT4) instead of that subjected to five F-T cycles (i.e., CD100/OS/S/FT5). The F-T test on the former terminated earlier due to an unexpected interruption of the operation, which left the base materials in the box for six months. This caused the pore sheets to be contaminated by the fine particles from the base materials (i.e., soil clogging). The test on Specimen CD100/OS/S/FT5 resumed afterwards while the contaminated porous sheets were still used. The contamination or soil clogging was evidenced by 1.5% to 2.5% lower moisture contents measured in CD100/OS/S/FT5 in Fig. 3.8, alongside the visual inspection in Fig. S.3.4. Therefore, the result from CD100/OS/S/FT4 was more reliable. Fig. 3.6(a) and 3.6(d) indicates that for the well-compacted bases in a closed system, the cumulative heave of the non-stabilized bases reached a steady state after two F-T cycles, but that of the stabilized bases arrived at the steady state after four F-T cycles. Fig. 3.6(b) and 3.6(e) shows the heave for the same state of bases in an open system. The cumulative heave peaked after two F-T cycles but decreased afterwards. The decreased heave was not reasonable and the reasons for this are explained later. In comparison, the results from the first two F-T cycles from the closed and open systems indicated that the water supply enhance the cumulative heave. Fig. 3.6(c) and 3.6(f) presents the results of poorly compacted bases in a closed system, which also peaked after two F-T cycles and then slightly decreased in the following F-T cycles. Fig. 3.7 presents the moisture contents after each F-T cycle at different heights above the bottom. In general, water content distributions were rather scatter, barely showing distinct trends. Two observations could be taken. Firstly, in the closed system, poorly compacted bases [Fig. 3.7(c) and 3.7(f)] showed less variations of moisture contents with the increase in F-T cycles than the well compacted bases [Fig. 3.7(a) and 3.7(d)]. Secondly, in most cases, the moisture contents at

different heights were generally decreased after one F-T cycle, and then gradually increased after greater F-T cycles.

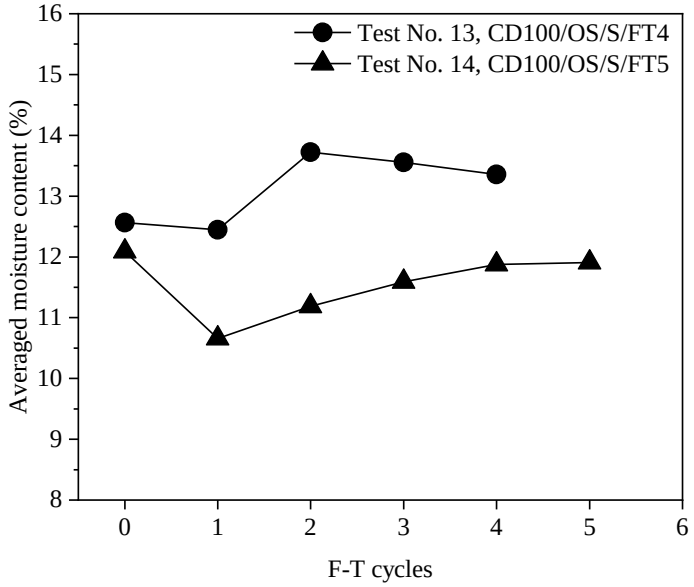

Fig. 3.8. Averaged gravimetric moisture content of geocell stabilized bases in an open system across four and five F-T cycles (Test No. 13 and 14)

To elucidate characteristics of the temperatures and surface movements, a closeup of the first F-T cycle was conducted for the three groups, as depicted in Fig. 3.9. The first F-T cycle was chosen because it initially altered the soil structures, typically representing the characteristic F-T behavior observed in the surface movement of newly compacted bases. Figs. 3.9(a)-(b) and 3.9(d)-(e) shows that for the base at 100% compaction (Group A and B), the temperature evolution pattern in the upper layer (at a height of 150 mm) resembled that of the cooling plate. However, a markedly slower rate of temperature changes in the upper base layer relative to the cooling plate was observed for the bases at 80% compaction (Group C) in Figs. 3.9(c) and 3.9(f). This discrepancy was attributed to larger interparticle voids in the bases with 80% compaction that would reduce the rate of the heat transfer between soil particles and the cooling plate during the freeze-thaw process. During the freezing process of all test groups, the base surface initially descended approximately 0.5 mm at the onset of freezing instead of heaving. This was due to the

cold shrinkage of soil particles. As the base temperatures fell below the freezing point, the base surface heaved with the temperature drop. The pattern of the frost heave could be categorized into three stages: fast frost heave, slow frost heave, and frost heave plateau. This phenomenon was also observed by Lu et al. (2018). The fast frost heave, occurring within three to five hours, resulted from the quick transformation of water to ice in the upper layers above the height of 100 mm. The subsequent 10 to 20 hours of slow frost heave corresponded to the phase change of water in the lower layers. After all the bases were fully frozen, the frost heave plateau was reached, a stage when the base structures were stabilized and no further ice was formed within the bases.

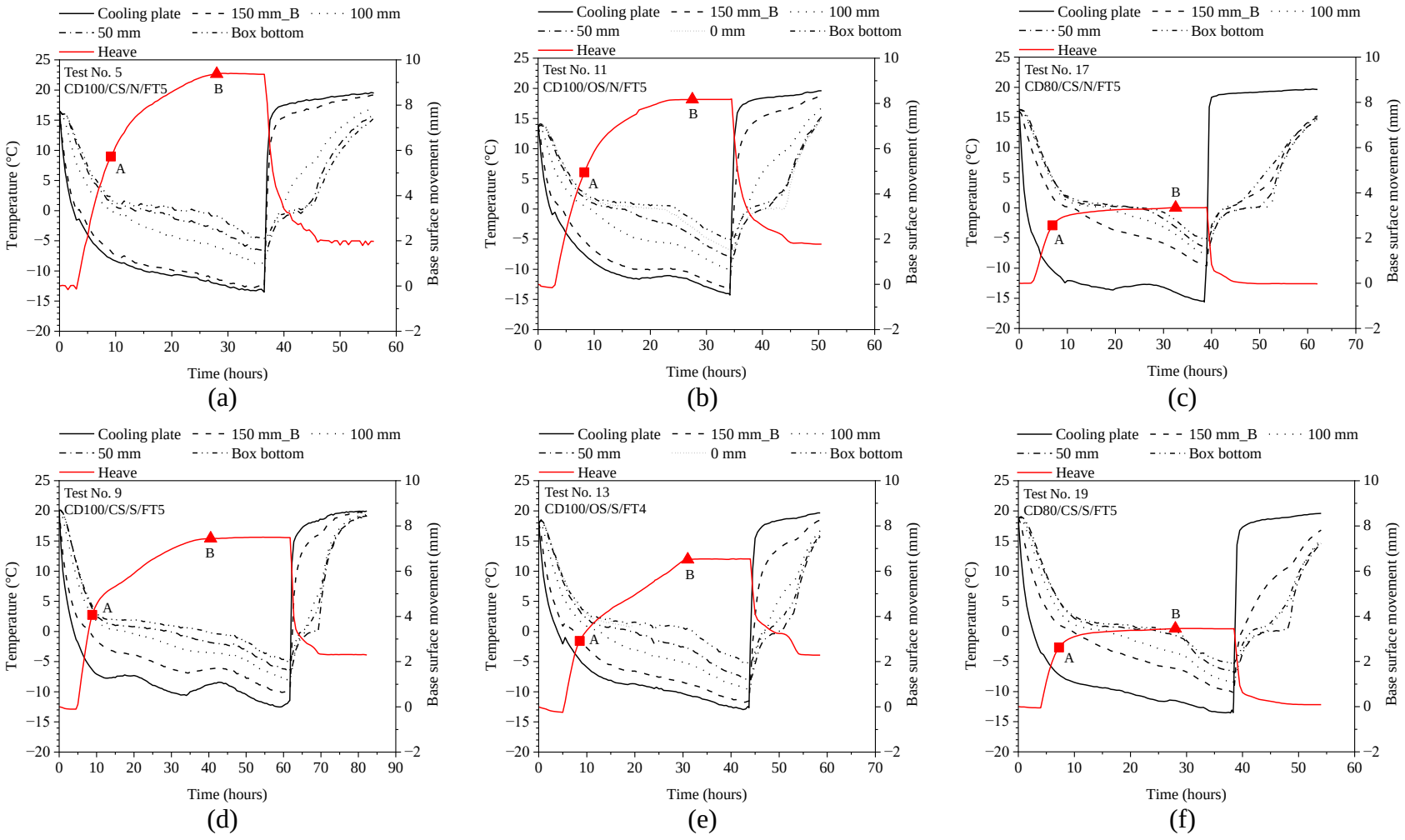

Fig. 3.9. Time-history variations of temperature during the second F-T cycle: (a) and (d) non-stabilized and stabilized bases (100% compaction degree) in a closed system, respectively, (b) and (e) non-stabilized and stabilized bases (100% compaction degree) in an open system, respectively, (c) and (f) non-stabilized and stabilized bases (80% compaction degree) in a closed system, respectively

To evaluate the effects of water supply and compaction on the contribution of the fast frost heave (Point A in Fig. 3.9) to the total movement of base surface (Point B in Fig. 3.9), the ratio of the fast frost heave to the peak heave at each F-T cycle was introduced. The higher this ratio, the higher contribution to the total heave from the upper layers (height > 100 mm). For the bases of 100% compaction, the average ratios of the non-stabilized bases and geocell-stabilized bases across first four F-T cycles were about 74% and 55%, respectively in a closed system, and the corresponding ratios in an open system were 59% and 47% during four F-T cycles. The lower ratio observed in the open system indicates that the presence of water supply at the base bottom promoted the formation of the ice in the lower base layers. Furthermore, the smaller ratio in the geocell-stabilized bases in both closed and open system suggested a greater contribution from the lower layers to frost heave as compared to the non-stabilized bases. This was possibly due to the discrepancy in the water redistribution after F-T cycles between the non-stabilized and geocell-stabilized bases. In the non-stabilized bases, the interstitial water could migrate relatively freely in both horizontal and vertical directions; whereas the pore water in the stabilized bases was partly impeded by the walls of geocells that were only partially perforated. This led to water accumulation at the geocell bottom. This facilitated the formation of localized ice lenses within geocell-enclosed bases. In contrast, for the bases with 80% compaction (Group C), the average ratios of the non-stabilized and geocell-stabilized bases were approximately 73% and 71%, respectively across the first four F-T cycles. This result indicated a predominant contribution to the total heave from the upper layers. The fast heave resulted from the freezing of the upper base layers above 150 mm height. Moreover, the frozen upper layers inhibited vertical expansion of the lower layers during the freezing process. This was particularly pronounced in the loose bases which were characterized by the reduced water amount and large inter-particle pores so that fewer

ice lenses were formed, and they subsequently filled the large pores in the loose bases. Meanwhile, Figs. 3.7(c) and (f) reveal that similar moisture content changes in both non-stabilized and geocell-stabilized bases, demonstrating minimal interference to interstitial water flow from geocell walls in the poorly compacted bases.

During the thawing process, all test groups exhibited a rapid settlement, followed by a slower settlement. The base surface movement stabilized when the box temperature reached 15°C, indicating a new equilibrium state achieved in the soil structures after each F-T cycle. To investigate the base surface movement across the full F-T cycles (four to five cycles), the peak heave, residual heave, and thaw settlement at each F-T cycle were determined, as shown in Figs. 3.10-3.12, respectively.

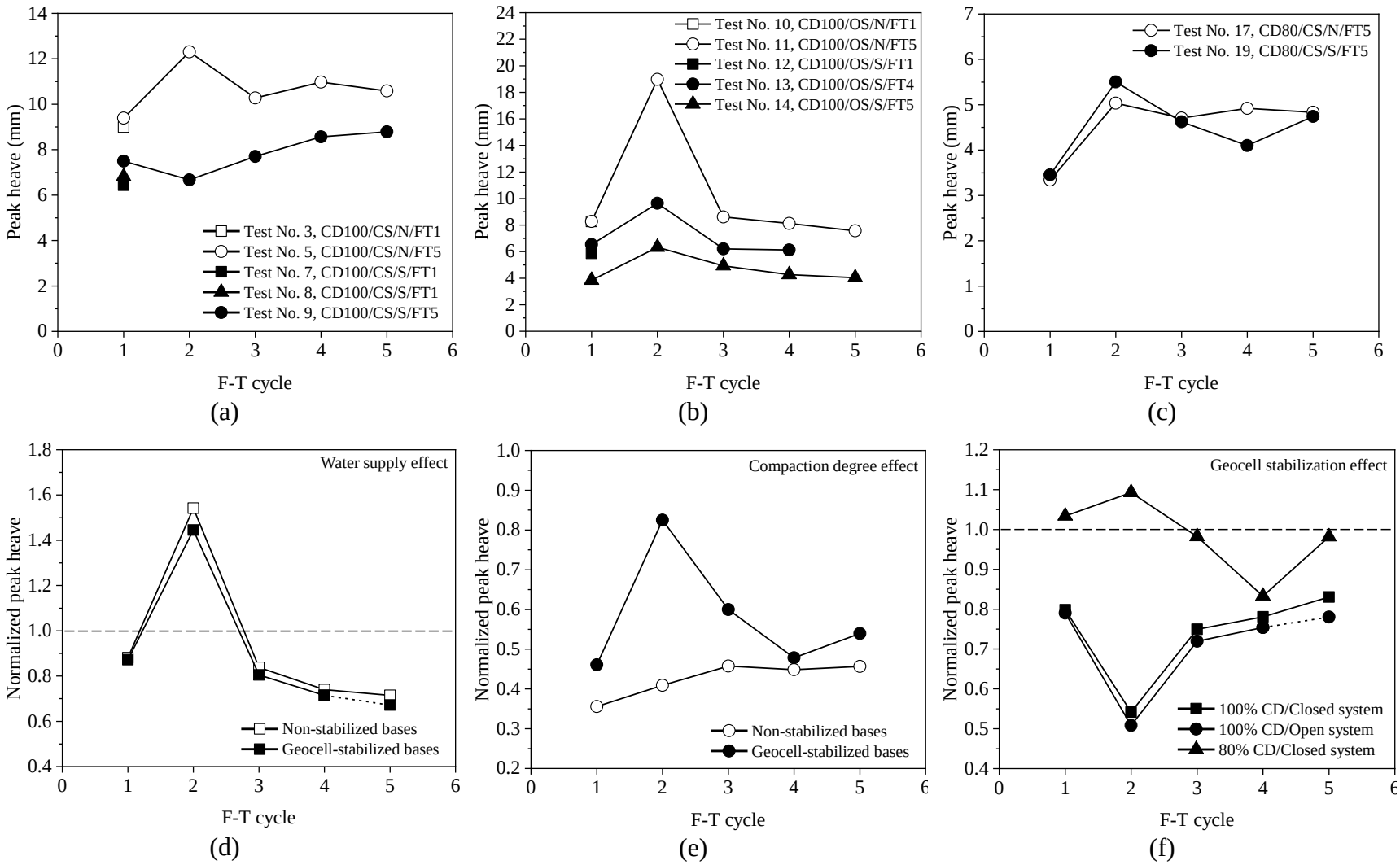

Fig. 3.10. Variations of peak heave at each F-T cycle: (a) in a closed system (100% compaction degree), (b) in an open system (100% compaction degree), (c) in a closed system (80% compaction degree), and (d), (e) and (f) normalized peak heave due to the effect of water supply, compaction degree and geocell stabilization, respectively

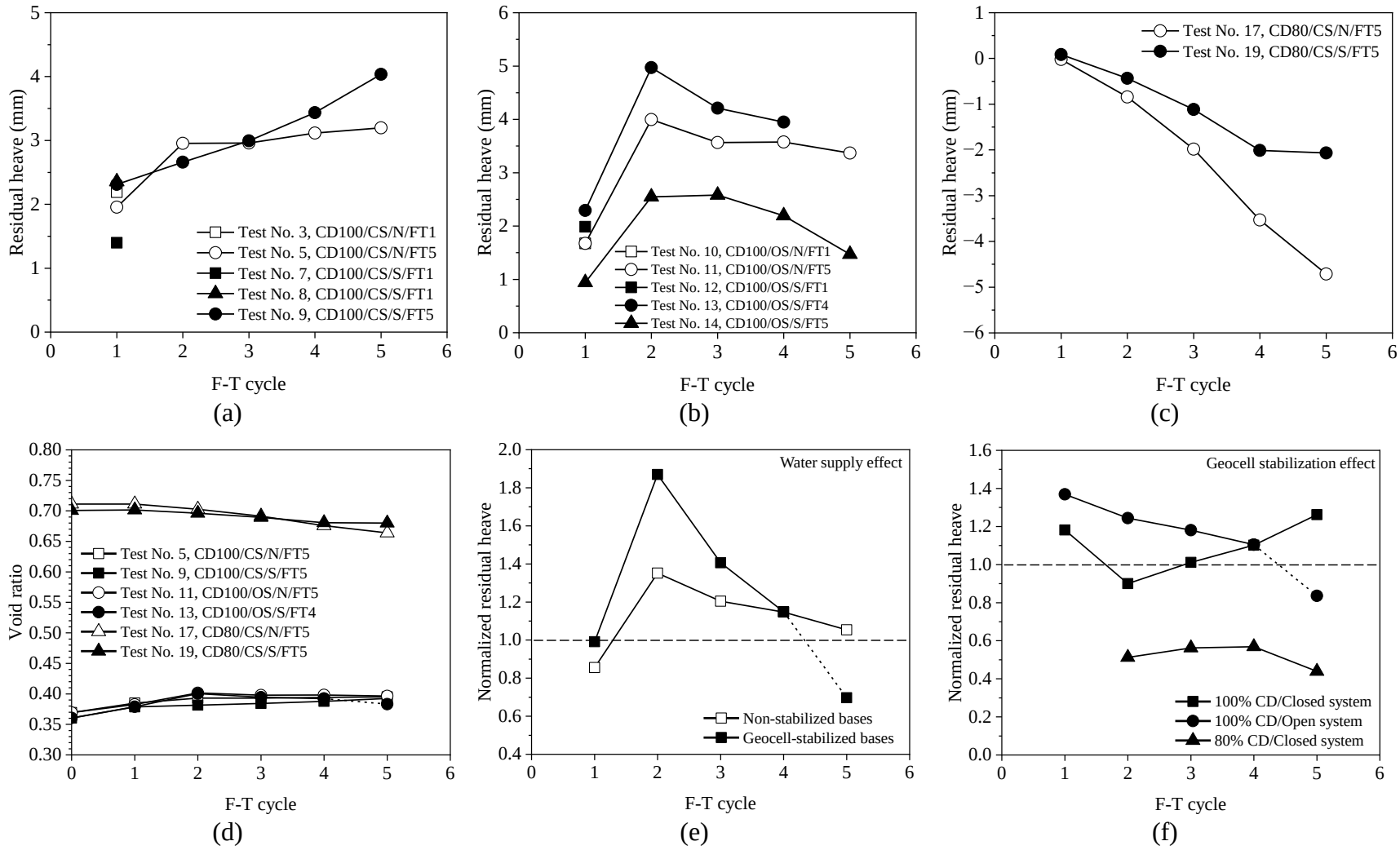

Fig. 3.11. Variations of residual heave after each F-T cycle: (a) in a closed system (100% compaction degree), (b) in an open system (100% compaction degree), (c) in a closed system (80% compaction degree), (d) void ratios, and (e) and (f) normalized residual heave due to the effect of water supply and geocell stabilization, respectively

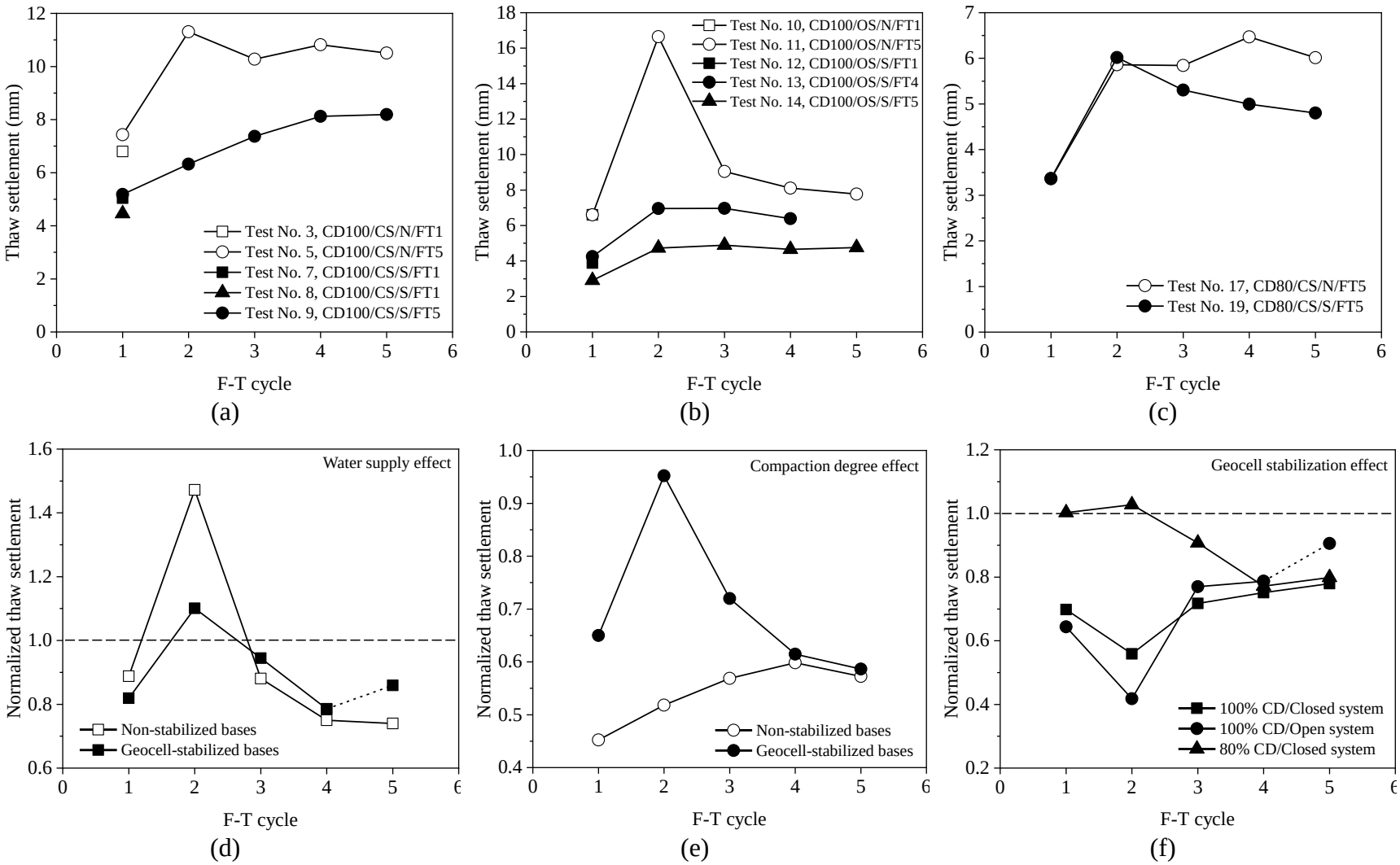

Fig. 3.12. Variations of thaw settlement at each F-T cycle: (a) in a closed system (100% compaction degree), (b) in an open system (100% compaction degree), (c) in a closed system (80% compaction degree), and (d), (e) and (f) normalized peak heave due to the effect of water supply, compaction degree and geocell stabilization, respectively

3.4.1.2 Peak heave

To examine the characteristics of the base surface movement induced by individual F-T cycles, the peak heave of each F-T cycle, rather than the cumulative peak heave in Huang et al. (2023), was introduced, with the definition as the difference between the maximum heave at a certain F-T cycle and the residual heave from its preceding cycle, therefore eliminating the influence of the residual heaves induced by previous F-T cycles. Figs. 3.10(a) to 3.10(c) displays the variations in the peak heave across each F-T cycle for the three test groups varying with water supply and compaction degree. The consistency of peak heaves at the first F-T cycle among the parallel tests in each test group underscored the repeatability of the freeze-thaw tests, with a notable exception for Test No. 14 in Fig. 3.10(b). In this test, the peak heaves at each F-T cycle were 21% to 41% smaller than those in the counterpart (Test No. 13). As discussed previously, it was due to the clogging in the pore sheets in Test No. 14. Nevertheless, the similar trend of the peak heaves between these two tests suggested the error caused by the clogging of pore sheets could be ruled out by simply shifting the curve upward to that of Test No. 13.

Effect of water supply

To quantify the effect of the water supply, a normalized peak heave was defined, which is a ratio of the peak heave in an open system to that in a closed system for the dense bases at the same number of F-T cycles. The result is presented in Fig. 3.10(d). The normalized values greater than 1.0 represents a negative effect of water supply during the freeze processes.

Both non-stabilized and geocell-stabilized bases exhibited a similar trend of peak heave over the five F-T cycles: an increase with increasing F-T cycles and peaked at the second F-T cycle, followed by a continuous decrease for the further F-T cycles. It was also observed that except at the second F-T cycle, for other cycles, the normalized peak heaves were all below 1.0. For the

first cycle, the peak heave in the open system was 12%-13% lower than that in a closed system. This was because for the bases in the open system, the hydraulic equilibrium process resulted in the initial moisture content exceeding the optimum moisture content, thereby increasing the thermal conductivity. During the first freezing process, the bases in the open system underwent more rapid freezing (see Fig. 3.9), leading to reduced water migration and the formation of thinner ice lenses. The faster freezing rate, predominately leading to in-situ freezing, could be the reason that the frost heave in the open system was smaller than that in the closed system during the first F-T cycle (Liu et al., 2018).

Before the start of freezing, the pores in the dense bases were relatively small and disconnected. After the first F-T cycle, the soil structure was altered, which could open up the pores and increase the chance of the pore connectivity, therefore facilitating water movement and ice lens growth in the subsequent F-T cycles (Hohmann-Porebska, 2002; Lu et al., 2019a; Shen et al., 2022). This was manifest with the normalized peak heave increasing and reaching the maximum values of 1.54 and 1.45 at the second F-T cycle for the non-stabilized and geocell-stabilized bases, respectively. This could be verified by the more water uptake in the open system than in the closed system: i.e., 0.8% and 1.2% increase in the averaged moisture contents in the former as compared to the corresponding 0.2% and 0.3% increase in the closed system as well as the perched water observed over the cooling plate after the second F-T cycle [Supplementary Fig. S.3.5]. The considerably lower values of the normalized peak heave (<1.0) in the following cycles were attributed to the boundary restraint from the top cooling plate. This restraint, as illustrated in Supplementary Fig. S.3.6, resulted from the ices formed and filled the gaps between plate edge and box walls, while the ices were due to the perched water from previous F-T cycles. This suggested that the heave results for the open system were only reliable for the first two F-T cycles, and the heave was

underestimated for the F-T cycles than two.

Effect of compaction degree

Fig. 3.10(e) presents the normalized peak heave considering the effect of compaction degree, i.e., a ratio of the peak heave measured in the bases of 80% compaction to that in the bases of 100% compaction. The values were all less than 1.0, indicating that the decrease in compaction for the bases reduced the frost heave. For the non-stabilized bases, the peak heave of loose and dense bases increased at the first two F-T cycles to 0.45 and stabilized from the third F-T cycle onwards. In contrast, for the geocell-stabilized bases, the normalized values remarkably increased from 0.46 to 0.82 in the first two F-T cycles, before decreasing in following F-T cycles. In general, the geocell-stabilized bases had higher normalized peak heave than the non-stabilized bases. This suggested that the geocell stabilization was less effective in minimizing the peak heave of the loose bases, although 80% compaction may not be practical in construction. This was attributed to that in the loose bases, the tensile force of geocells was not effectively mobilized due to the low compaction degree (Dash, 2010), leading to minimal geocell-base interaction and less benefit for resisting base volumetric increase by the frost. As the cyclic F-T action continued, the loose bases became denser, allowing the geocell stabilization to be mobilized. Therefore, the peak heave decreased in following F-T cycles, resulting in a reduction in the normalized values. This dynamic process would be elaborated in the residual heave section.

Effect of geocell stabilization

The effect of the geocell stabilization was quantified by the similar normalized peak heave (a ratio of the peak heave with geocell stabilization to that without the stabilization), as depicted in Fig. 3.10(f). In the bases with 100% compaction (Group A and B), the use of the geocells significantly reduced the peak heave. The maximum reduction in the peak heave was 46% and

49% in the closed and open system, respectively, occurring at the second F-T cycle. However, as the number of F-T cycles increased, the normalized peak heave gradually rose, indicating a diminishing effectiveness of geocell stabilization. This was possibly due to dynamic changes in base structures and water redistribution over F-T cycles. Specifically, the initially dense state of the bases became gradually looser after the first two F-T cycles. In the non-stabilized bases, the void ratio increased from 0.369 to 0.393 in a closed system and to 0.401 in an open system, and the increases in the geocell-stabilized bases were from 0.360 to 0.382 and to 0.400 in the closed and open system, respectively [Fig. 3.11(d)]. As discussed previously, the decreased compaction tended to weaken the geocell stabilization efficacy in mitigating frost heave. For the bases of 80% compaction in a closed system (Group C), the normalized peak heave was approximate to 1.0 throughout the F-T cycles, suggesting that the benefits of the geocell reinforcement were minimal in the loose bases compared to the dense bases, as discussed in the above section.

3.4.1.3 Residual heave and thaw settlement

Figs. 3.11(a), 3.11(b), and 3.11(c) depict the residual heave, which represents permanent heave after each thawing process, in both non-stabilized and geocell-stabilized bases of the three test groups. Void ratios of the bases after each thawing stage, calculated from the residual heave, are presented in Fig. 3.11(d). The value for the geocell-stabilized bases in an open system at the 5^{th} F-T cycle was extrapolated based on the trend of Test No.14, as previously discussed. For the non-stabilized dense bases, the void ratios increased during the first two F-T cycles, and then stabilized for the greater F-T cycles. This corresponded to the uniform residual heave observed after the second F-T cycle in Figs. 3.11(a) (Test No. 5) and 3.11(b) (Test No.11). Conversely, for the geocell-stabilized dense bases, the void ratios in the closed system continuously increased throughout the F-T cycles while in the open system, they increased to 0.40 at the second F-T cycle

and decreased in the following cycles. Notably, after five F-T cycles, the void ratios in all test dense bases tended to converge to a value of 0.39. This convergence, consistent with the observation by Viklander (1998), showed that cyclic F-T actions gradually loosened dense bases until a new equilibrium was reached. In contrast, for the loose bases, the void ratios decreased with increasing F-T cycles starting the second cycle. This suggests that the initial loose bases became denser under the cyclic F-T actions.

Fig. 3.11(e) illustrates the normalized residual heave of the three test groups, highlighting the impacts of water supply. After the first F-T cycle, the residual heave was decreased by 14% in non-stabilized bases and 1% in geocell-stabilized bases in an open system, indicating a minimal effect of water supply on the residual heave during the first F-T cycle. However, After the second F-T cycle, the influence of water supply became evident, with the residual heave increasing by approximately 35% and 87% in the non-stabilized and geocell-stabilized bases, respectively. This coincided with the maximum peak heave at the same cycle [Fig. 3.10(d)]. During the subsequent F-T cycles, excess external water entered the bases, drawn by the F-T induced suction and accumulated on the base surface, as depicted in Supplementary Fig. S.3.5. The increased pore pressure weakened the interparticle contacts, preventing them from returning to their original positions and resulting in greater residual than that in the closed system. However, in the following freezing stages, the development of ice seal between cooling plate and the box walls in the open system (in Fig. S.3.6) restrained the peak heave. This restraint led to a reduction in residual heave and a consequent decrease in normalized residual heave related to the water supply.

Fig. 3.11(f) displays the effect of the geocell stabilization on the residual heave (or permanent heave). The normalized values (i.e., residual heave with geocell stabilization divided by that without geocell stabilization) were generally greater than 1.0 for the well compacted bases, but

they were much lower than 1.0 for the poorly compacted bases. This suggested that geocells provided no benefit in mitigating the residual heave for well compacted bases but could reduce the residual heave by 50% to 60% for poorly compacted bases. This result was opposite to the peak heave observed previously.

Figs. 3.12(a), 3.12(b), and 3.12(c) present the thaw settlement, defined as the difference between the cumulative peak heave and the residual heave in each F-T cycle, in both non-stabilized and stabilized bases for the three test groups. Like the peak heave, the thaw settlement notably increased during the first and second F-T cycles, before stabilizing or diminishing in the further number of F-T cycles. An exception was noted in the geocell-stabilized bases in a closed system (Test No. 9), which exhibited a steady increase in thaw settlement up to the fourth F-T cycle. Figs. 3.12(d) to 3.12(f) shows the normalized thaw settlement with increasing F-T cycles to elucidate the effects of water supply, compaction, and geocell stabilization, respectively. The variations in the normalized thaw settlement closely followed those of the peak heave, as the thaw settlement is calculated by deducting the residual heave from the cumulative peak heave, where the residual heave was comparatively smaller, except in the case of loose bases, which underwent subsidence as F-T cycles progressed. In general, the following observations can be made: 1) the water supply increased thaw settlement of bases [Fig. 3.12(d)]. Note that the thaw settlement for the open system at F-T cycles greater than 2 was not discussed as the measured peak heave was unreliable. 2) The increase in degree of compaction of the bases whether they are stabilized with geocells reduced the thaw settlement [Fig. 3.12(e)]. 3) The inclusion of the geocells reduced the thaw settlement by 10% to 60%, which was more effective for well compacted bases [Fig. 3.12(f)].

3.4.2 Plate loading test results

Plate loading tests were performed on the three testing groups immediately following the

completion of the freeze-thaw tests. The plate loading test results are represented by the applied pressure-displacement curves, from which the stiffness and ultimate bearing pressure of the non-stabilized and geocell-stabilized bases could be determined. Fig. 3.13 shows the corrected curves in which the sitting errors had been eliminated in the accordance with the result adjustment used in California Bearing Ratio tests (ASTM D1883). The repeatability of the plate loading test results had been verified in Huang et al. (2023).

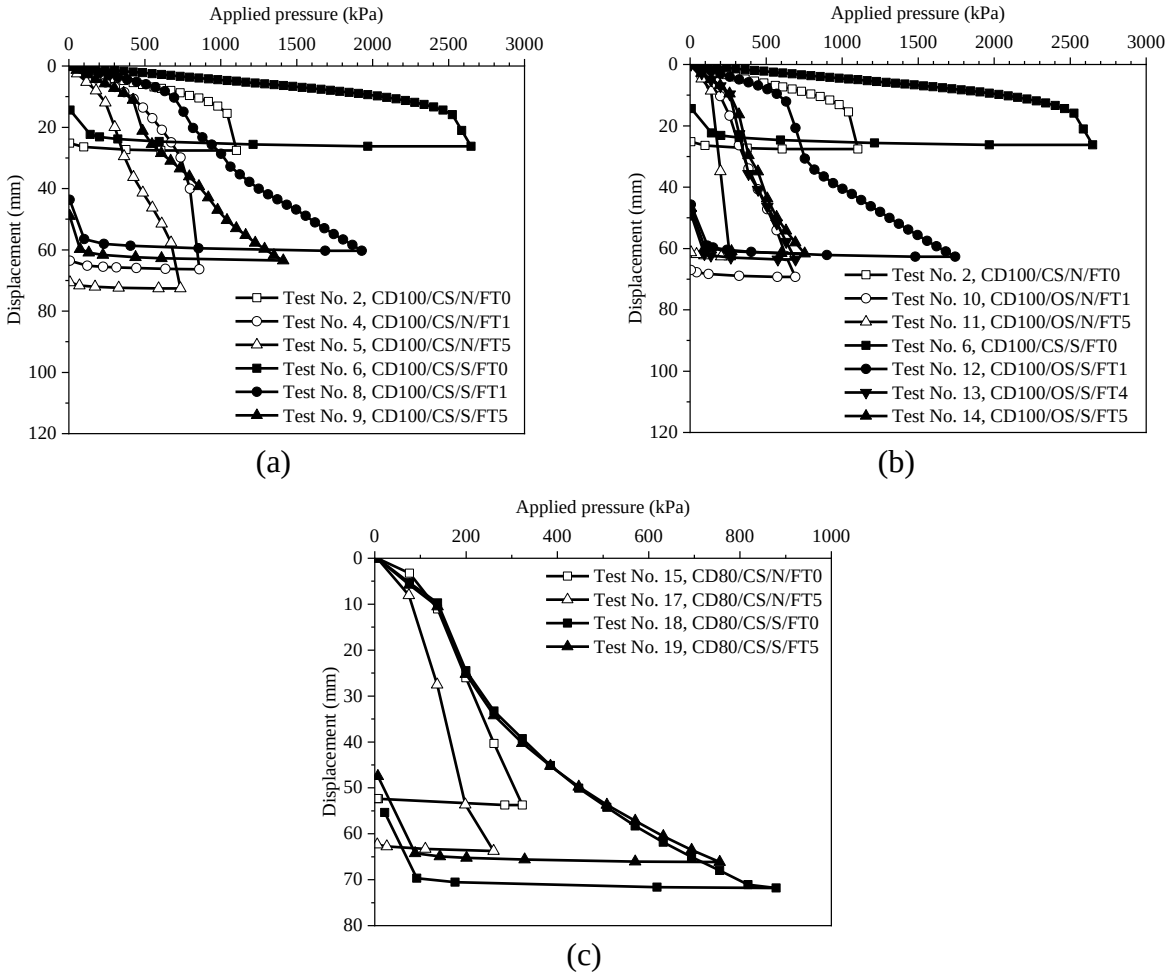

Fig. 3.13. Plate loading test results for bases with: (a) 100% compaction in a closed system, (b) 100% compaction in an open system, and (c) 80% compaction in a closed system

During the plate loading tests, a distinct difference in response was observed between the non-stabilized bases and geocell-stabilized bases, with the former experiencing an abrupt failure under incremental loads while the latter exhibiting a hardening response at a large displacement. The

stiffness, known as a modulus of subgrade reaction, is defined as the slope of the initial portion of the corrected pressure-displacement curves (Pokharel et al., 2010). The ultimate bearing pressure is determined as either the pressure at the bearing failure or the pressure corresponding to the maximum curvature in the cases where the abrupt failure is not evident (Adams and Collin, 1997; Pokharel et al., 2010; Rajagopal et al., 2014). The values of stiffness and ultimate bearing pressure obtained from the corrected curves are depicted in Fig. 3.14(a) and 3.14(b), respectively. The average values for the stiffness and ultimate bearing pressure were used in the parallel model tests (i.e., Test No. 1 and 2; Test No. 3 and 4; Test No. 15 and 16).

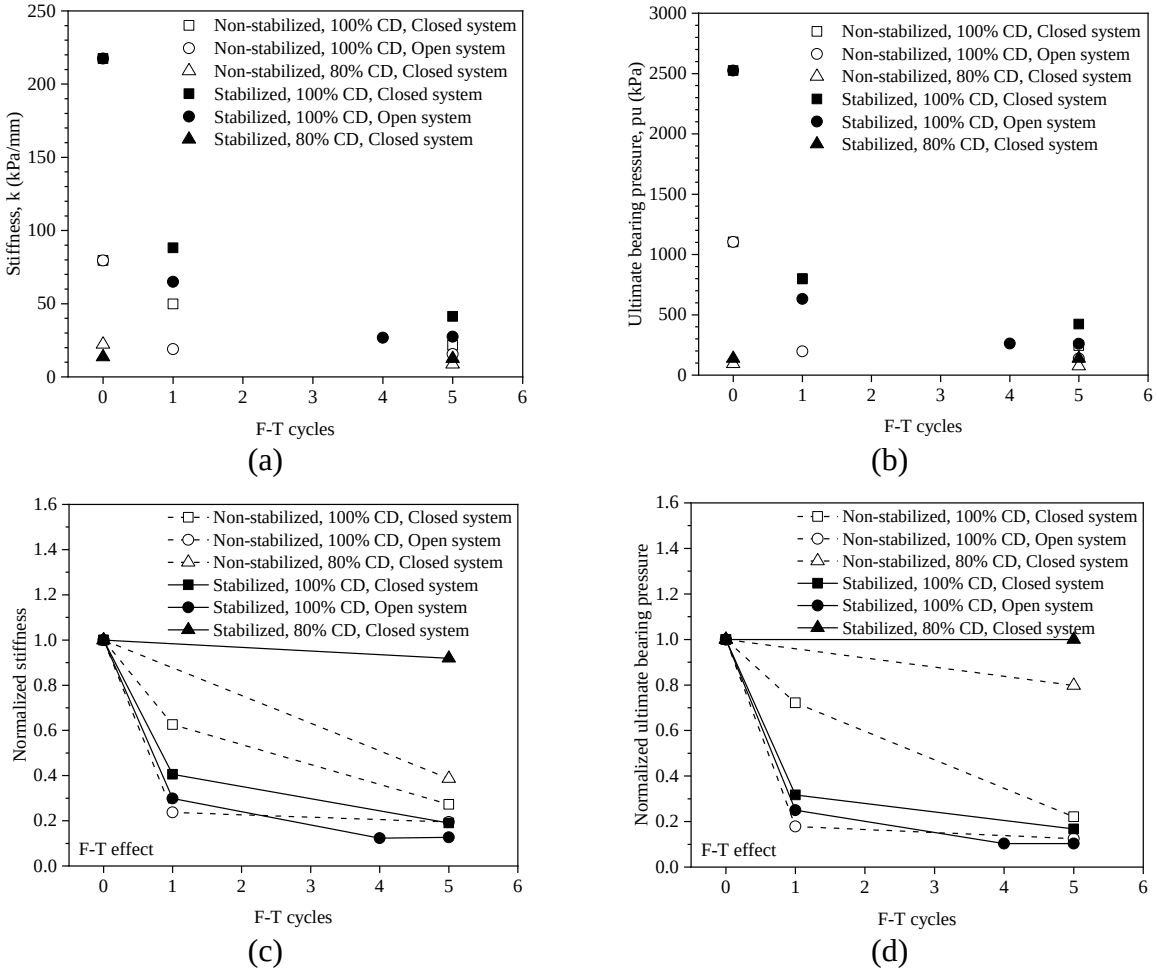

Fig. 3.14. Plate loading test results: (a) and (b) stiffness and ultimate bearing pressure, respectively, and (c) and (d) normalized stiffness and ultimate bearing pressure due to F-T cycles, respectively

3.4.2.1 Effect of F-T cycles

To quantify the effects of F-T cycles on mechanical responses, normalized stiffness and ultimate bearing pressure (i.e., the values obtained at zero F-T cycle divided by the corresponding values at different F-T cycles) are presented in Fig. 3.14(c) and 3.14(d). The bases with 100% compaction exhibited a markable drop in both stiffness and ultimate bearing pressure after the first F-T cycle, with a greater reduction in the open system than in the closed system. For instance, the stiffness in non-stabilized and geocell-stabilized bases in the closed system decreased by approximately 37% and 59%, respectively after the first F-T cycle, compared to the reductions of 76% and 70% in the open system. Similarly, the ultimate bearing pressure in the non-stabilized and geocell-stabilized bases was reduced by about 28% and 68%, respectively, in the closed system, as compared to the corresponding decrease by 82% and 75% in the open system. After five F-T cycles, the stiffness and ultimate bearing pressure were decreased by 73% to 83% in the closed system and 81% to 90% in the open system. The above result along with the result for the maximum frost heave observed previously suggested that road bases were most susceptible to damage during the first two F-T cycles, necessitating additional inspection and maintenance for newly constructed roadways during these initial F-T seasons. For the bases with 80% compaction (Group C), despite the densification effect by F-T cycles, stiffness and ultimate bearing pressure were reduced by about 61% and 20%, respectively. This phenomenon was also observed in other studies (e.g., Huang et al., 2022; Qi et al., 2008). It is likely because the densification was relatively moderate and the decay in mechanical properties was more governed by the F-T induced alteration of soil fabrics, such as the aggregation of fine particles, the orientation of coarse particles, and the development of cracks (Shen et al., 2022). In contrast, the geocell-stabilized bases of 80% compaction maintained the stiffness and ultimate bearing pressure almost unchanged after five F-T cycles.

This demonstrated the effectiveness of the geocell stabilization in mitigating the F-T induced deterioration of mechanical properties in the poorly compacted bases.

3.4.2.2 Effect of water supply

Fig. 3.15(a) presents the normalized stiffness and ultimate bearing pressure considering water supply effect: i.e., the values obtained in the open system divided by the corresponding values obtained in the closed system. In general, the water supply generally degraded the stiffness and ultimate bearing pressure under cyclic F-T condition, even though the results obtained from the open system were less reliable after five F-T cycles. The discussion herein only focuses on the results from F-T cycles ≤ 2. The figure shows that the stiffness and ultimate bearing pressure of the geocell-stabilized bases was approximately 26% and 21% less in the open system than in the closed system, respectively. The corresponding values (62% and 75%) were more pronounced for the non-stabilized bases.

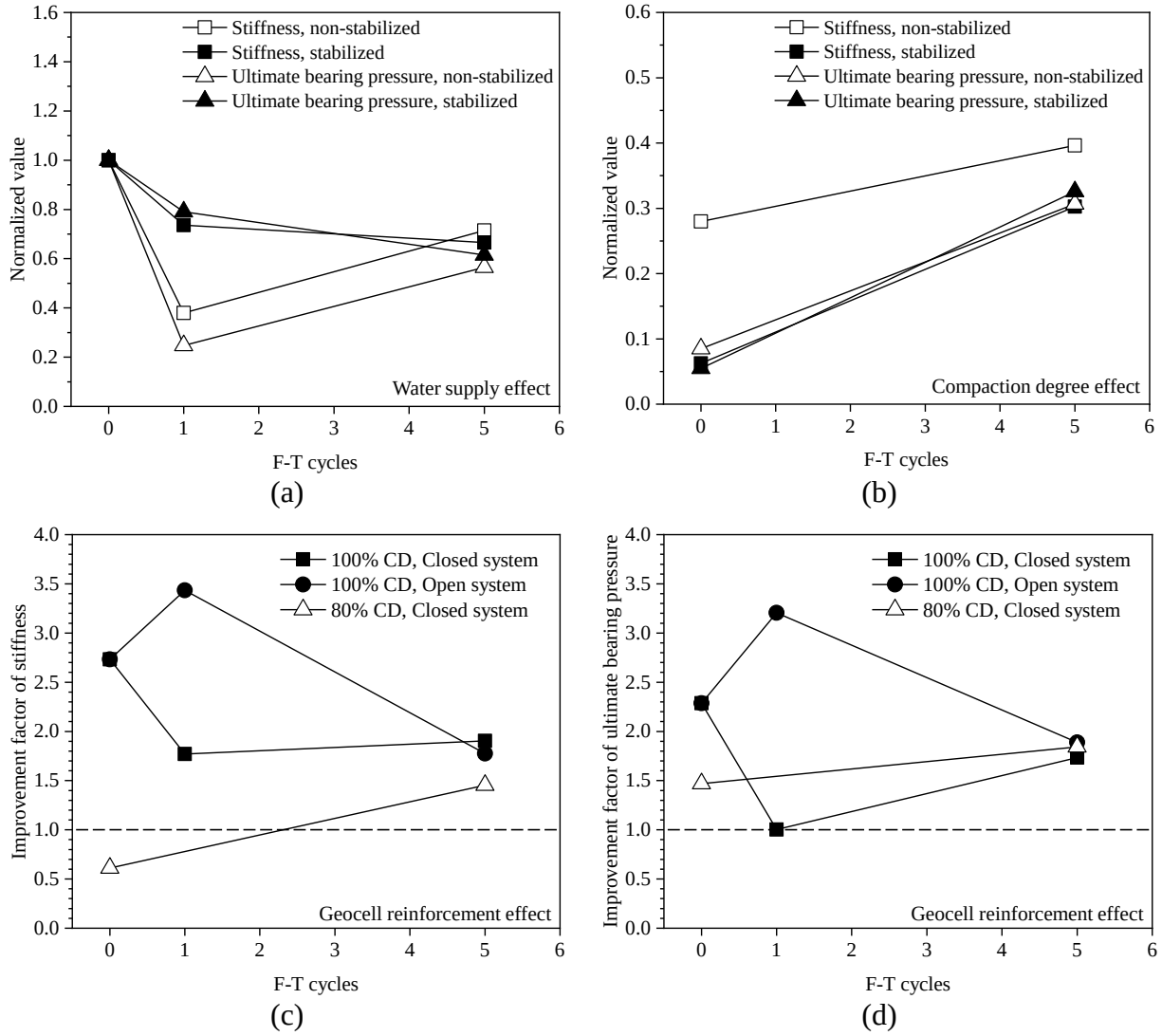

Fig. 3.15. Plate loading test results: (a) and (b) normalized stiffness and ultimate bearing pressure due to water supply and compaction degree, respectively, and (c) and (d) improvement factors of stiffness and ultimate bearing pressure due to geocell stabilization, respectively

3.4.2.3 Effect of compaction degree

Fig 3.15(b) delineates the normalized stiffness and ultimate bearing pressure considering the compaction effect: i.e., the values obtained from 80% compaction (poorly compacted) divided by the corresponding values obtained from 100% compaction (well compacted), with the results obtained from Groups A and C in Table 1. Before F-T cycles, the values of stiffness and ultimate bearing pressure of poorly compacted bases were only 5% to 9% of those for well compacted bases,

except for the stiffness of the poorly compacted non-stabilized bases that was 28% of that for the corresponding well compacted bases. After the F-T cycles, the percentages increased markedly. This revealed that the mechanical properties of the poorly compacted bases were affected less than the well compacted bases by the F-T cycles. This could be attributed to the densification of loose bases and the loosening of dense bases under cyclic F-T conditions, as discussed previously.

3.4.2.4 Effect of geocell stabilization

Figs. 3.15(c) and 3.15(d) display the improvement factors of stiffness and ultimate bearing pressure: i.e., the values obtained for the geocell-stabilized bases divided by the corresponding values obtained for the non-stabilized bases. The improvement factors greater than 1.0 demonstrate the beneficial effect by the inclusion of geocells into the bases under cyclic F-T conditions. Some observations can be taken from Fig. 3.15(c) and 3.15(d). Firstly, in general, the improve factors were greater than 1.0, confirming the beneficial effect of geocell stabilization. Secondly, the geocells' benefit was more remarkable for the well compacted bases than for the poorly compacted bases. However, as the F-T cycles increased, such a benefit weakened for the former and enhanced for the latter. Thirdly, with increasing F-T cycles, the geocells' benefit reduced in the closed system but increased in the open system (not accounting for the results obtained after five F-T cycles). Lastly, after five F-T cycles, the improvement factors for the stiffness were 1.4 to 1.9, and those for the ultimate bearing capacity ranged from 1.8 to 2.1. This corresponded to 40%-90% improvement for the stiffness and 80% to 110% improvement for the ultimate bearing pressure.

3.5 Conclusions

This study presents a series of model tests to investigate the freeze-thaw (F-T) performance of geocell-stabilized bases (i.e., sands), considering effects of water supply and compaction degree.

The model tests, including freeze-thaw tests and plate loading tests, were conducted in an upgraded customized model test device. The outcomes of the model tests would enhance the understanding of the geocell stabilization of road bases under cyclic F-T conditions. The following conclusions are drawn from this study:

(1) The base surface movement during the freezing could be categorized into four stages: cold shrinkage, fast frost heave, slow frost heave, and frost heave plateau. The fast frost heave was primarily due to freezing in the upper part of the bases while the slow frost heave was associated with the lower part of the bases. In the well compacted bases (100% compaction), the geocell-stabilized bases showed a greater amount of the slow frost heave than the non-stabilized bases. In the poorly compacted bases (80% compaction), the fast heave governed in both non-stabilized and stabilized bases.

(2) The water supply increased the peak heave of the non-stabilized and geocell-stabilized bases by about 54% and 45%, respectively during the second F-T cycle, revealing the adverse effect of water supply on the F-T performance of road bases.

(3) Efficacy of geocells in mitigating frost heave and thaw settlement varied with degree of compaction. In general, geocells were more effective in reducing peak frost heave and thaw settlement in the well compacted bases than in the poorly compacted bases. The opposite was found in reducing residual heave.

(4) With increasing the F-T cycles, void ratios of well and poorly compacted bases showed divergent trends: an increase for the former and a decrease for the latter. This indicated that F-T processes would densify the loose bases but weaken the dense bases.

(5) The mechanical properties (i.e., stiffness and ultimate bearing pressure) were decreased after the F-T cycles. The reductions were more pronounced in the open system than in the closed system.

In terms of the mechanical properties, the poorly compacted bases were affected less than the well compacted bases at greater F-T cycles.

(6) The inclusion of geocells was found to be beneficial for mitigating F-T damage to the mechanical properties of road bases. The benefit of geocells was more remarkable for the well compacted bases than for the poorly compacted bases. however, as the F-T cycles increased, such a benefit weakened for the well compacted bases but enhanced for the poorly compacted bases. The geocells' benefit was more pronounced in the open system than in the closed system.

Chapter 4 Freeze-thaw effects on mechanical behavior of geocell-reinforced sands from element and model tests

4.1 Abstract

Freeze-thaw (F-T) cycles are a major cause of pavement distress in seasonal frost regions. It has been demonstrated in practical applications that geocell-reinforced roads are effective in resisting F-T damage. However, this beneficial effect has not been quantified, and the underlying mechanisms are not well appreciated either. To address these questions, this study carried out two types of laboratory-scale tests, namely element tests (single geocell) and model tests (multiple geocells) to investigate the mechanical properties (stiffness and ultimate bearing pressure) of geocell-reinforced sands subjected to various freeze-thaw cycles. The experimental results showed that although the poorly graded sands used in this study were classified as frost insusceptible, both mechanical properties (stiffness and ultimate bearing pressure) of the sands were reduced up to 20% after five F-T cycles. The mechanical properties of both unreinforced and reinforced sands were decreased with the increased F-T cycles. At different F-T cycles, geocells improved the mechanical properties by 30%-110%. The test results showed high variability at a small number of F-T cycles in the element tests, but the variability diminished at a higher number of F-T cycles. The discrepancy of test results between element tests and model tests might be due to scale difference that resulted in different soil conditions prepared and thus different water distributions inside the soils.

4.2 Introduction

Roads and other earth structures are often prone to performance degradation in seasonal weather regions, in which the repetitive freeze-thaw (F-T) action is a major threat. The F-T induced distress of roads occurs in the form of frost heave and thaw weakening. During the frost process, frost

front advances downwards in soils, causing formation of ice lenses in localized zones. The ice lenses can grow when water supply is available and capillary action can develop to move water towards the frost front (Andersland and Ladanyi, 2004; Fredlund et al., 2012). The volumetric expansion of water and growth of ice lenses result in frost heave, roughness, and cracks of pavements. During the thawing process, the melted water can be trapped in the thawed soil layer if the thawing is top down, leading to an appreciable drop in the bearing capacity of road sections (Simonsen and Isacsson, 1999). In general, the vulnerability of roads to F-T depends on the source of water, frost susceptibility of soils, frost depth, and F-T frequency. In a closed system where water supply does not occur, the heave is attributed to 9% swell of water when it is solidified. However, the heave is more severe when the water supply is available. In frost susceptible area, a road section with ground water at a depth shallower than 3 m below the ground surface is considered as frost susceptible and frost treatment action is needed (Christopher et al., 2006). Although subgrades containing fines are considered susceptible to frost, and sensitive to F-T damage, research found that frost insusceptible gravels and sands could also be damaged by F-T action (Kawabata et al., 2016; Corte, 1962). Roads experiencing seasonal F-T changes are often improved to enhance their durability using a variety of techniques, which include placement of frost-susceptible fines, effective drainage system, geosynthetics reinforcement, soil stabilization by mixture of cement or lime additives (Christopher et al., 2000; Edil et al., 2002; Helstrom et al., 2006; Lai et al., 2012; Li et al., 2017). Geocells, a honeycomb-like interconnected cells, can provide three-dimensional reinforcement to soils, and geocell-reinforced bases are reported to be an effective solution to increasing longevity of roadways based on the field monitoring in the seasonal F-T regions of Canada and the US (Henry et al., 2005; Pokharel et al., 2017). However, these field observations are qualitative and site specific, highly limited to the local soil conditions

and temperature variations. In comparison to field experiments, laboratory model tests are relatively efficient and cost-effective, and enable application of well-controlled test conditions. This allows for better investigating the benefits of geocells and the underlying mechanisms. However, limited model tests have been performed on geocell-reinforced soils subjected to F-T cycles, probably due to a lack of proper test device. To investigate the F-T behavior of unreinforced and reinforced soils, a newly designed lab-scale model test device has been developed by the authors (Huang et al., 2021). This device could impose top-down F-T cycles and subsequently apply plate loads on geocell-reinforced soils.

The objective of this study was to investigate the mechanical behavior of geocell-reinforced sands under the cyclic F-T effect in a series of lab-scale tests, including element tests and model tests. The element tests involved subjecting single-geocell-reinforced sands and unreinforced sands to various F-T cycles before testing their bearing pressures, while the model tests included testing the bearing pressure of multiple-geocells-reinforced sands and unreinforced sands after various F-T cycles. The results from both element tests and model tests are compared and the possible underlying mechanisms are discussed.

4.3 Experimental study

The experiment consisted of element tests and model tests. The element tests included three groups of CBR tests for unreinforced sands and 14 plate loading tests on single-geocell-reinforced sands after the soil samples experienced zero, one, and five F-T cycles. The model tests included 11 plate loading tests on multiple-geocell-reinforced sands and unreinforced sands after subjected to the same numbers of F-T cycles as in the element tests. All the laboratory tests were performed in a closed system.

4.3.1 Materials

This paper is to investigate the mechanical response of base courses subjected to F-T cycles. The specifications of base courses in road constructions require fines content less than 8% (ASTM D2940). Therefore, sands were used as testing materials in this study. The sands used were poorly graded sands (SP) according to the Unified Classification System (USCS). The particle distribution curves of the sands are shown in Fig. 4.1. The sands had mean particle size (D_{50}) of 0.760 mm, coefficient of uniformity of 4.48, and coefficient of curvature of 0.80. The specific gravity of the soils was 2.7. Based on the standard Proctor compaction test (ASTM D698), the maximum dry density and the optimum moisture content were determined to be 1.9 g/cm^3 and 12.9%, respectively.

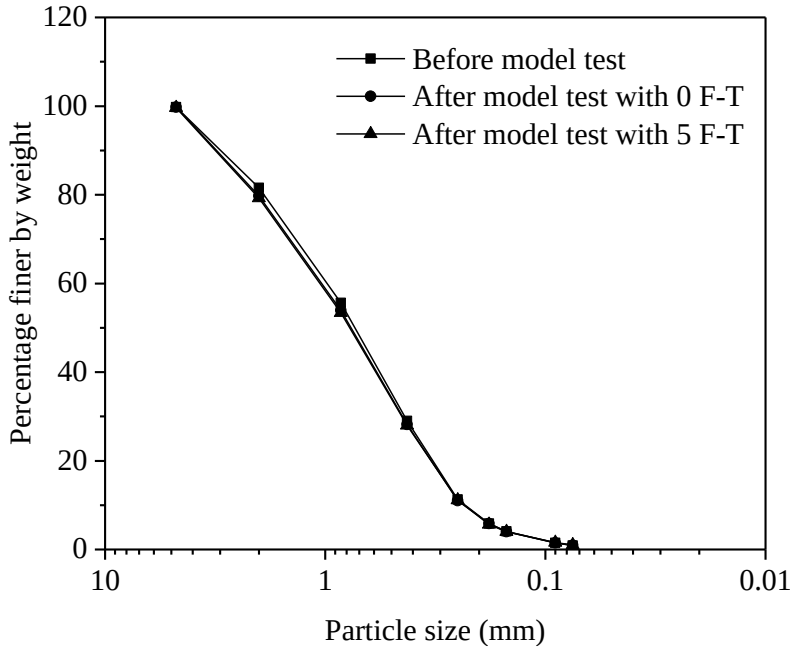

Fig. 4.1. Particle size distribution of sands

Geocells were nano-polymeric alloy (NPA) Type-C geocells, donated by PRS Geo-Technologies®. A geocell had an opening of 245 mm × 210 mm (245 mm in the major axis and 210 mm in the minor axis). The geocell ribs were perforated, with 150 mm height and 1.1 mm

thickness. The nominal tensile strength of geocell sheets and nominal splitting strength of welded seam were 19 kN/m.

4.3.2 Test methods

Both element tests and model tests involved zero, one, and five F-T cycles prior to CBR tests and plate loading tests. At present, the changes in mechanical behavior of unreinforced and reinforced sands under the freeze-thaw cycles were only investigated up to five F-T cycles. The influence of greater F-T cycles will be investigated in the future. The details of these test programs are given in Table 4.1 and 4.2.

Table 4.1. Details of the element test program

Mechanical loading	Test No.	Test material	Number of F-T cycles	Imposed coldest temperature (°C)
CBR loading	1-3	Unreinforced sands	0	NA
	4-6		1	-10
	7-9		5	-10
Plate loading	1-2	Unconfined four geocells-reinforced sands	0	NA
	3-6	Unconfined single geocell-reinforced sands	0	NA
	7-10		1	-10
	11		1	-20
	12-14		5	-10

NA=not applied.

Table 4.2. Details of the model test program

Test No.	Test material	Number of F-T cycles
1-4		0
5	Geocell-reinforced sands	1
6		5
7-9		0
10	Unreinforced sands	1
11		5

4.3.2.1 Element test for unreinforced sands

The element test for unreinforced sands was performed on a CBR sample, which was subjected to various F-T cycles, followed by CBR penetration test. The details of the test program are summarized in Table 4.1. Two numbers of F-T cycles (1 and 5) were considered, and triplicate samples were used for each number of F-T cycles. Therefore, a total of nine samples were prepared in this test.

A CBR sample measuring 116 mm in height and 152 mm in diameter was prepared as per ASTM D1883. The sands were compacted to the dry density of 1.84 g/cm^3 (within 95% of the maximum dry density) and the optimum moisture content. A T-type thermocouple with accuracy of ±1°C was embedded in the center of the sample to monitor changes in temperature during F-T. The sample temperature was recorded automatically by a National Instruments® data logger at an interval of 10 minutes. To prevent water loss, all the CBR samples were sealed with plastic films throughout the F-T process. The sealed CBR samples were then placed in a freezer [Fig. 4.2(a)] until the temperature in the samples reached -10°C. Immediately after that, the samples were moved to a constant room temperature to start thawing. Once the sample temperature was up to 10°C, thawing was terminated, and one F-T cycle was completed. After the samples experienced a given number of F-T cycles, CBR tests were performed as shown in Fig. 4.3(a).

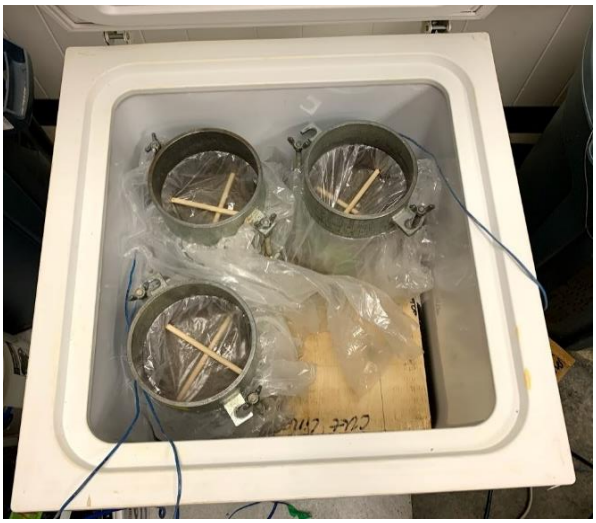

(a)

(b)

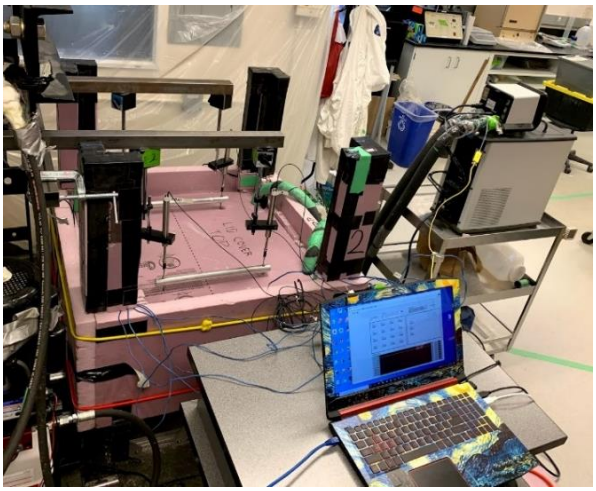

(c)

Fig. 4.2. Photographs of F-T process for: (a) element test-unreinforced sand, (b) element test-reinforced sands, and (c) model tests

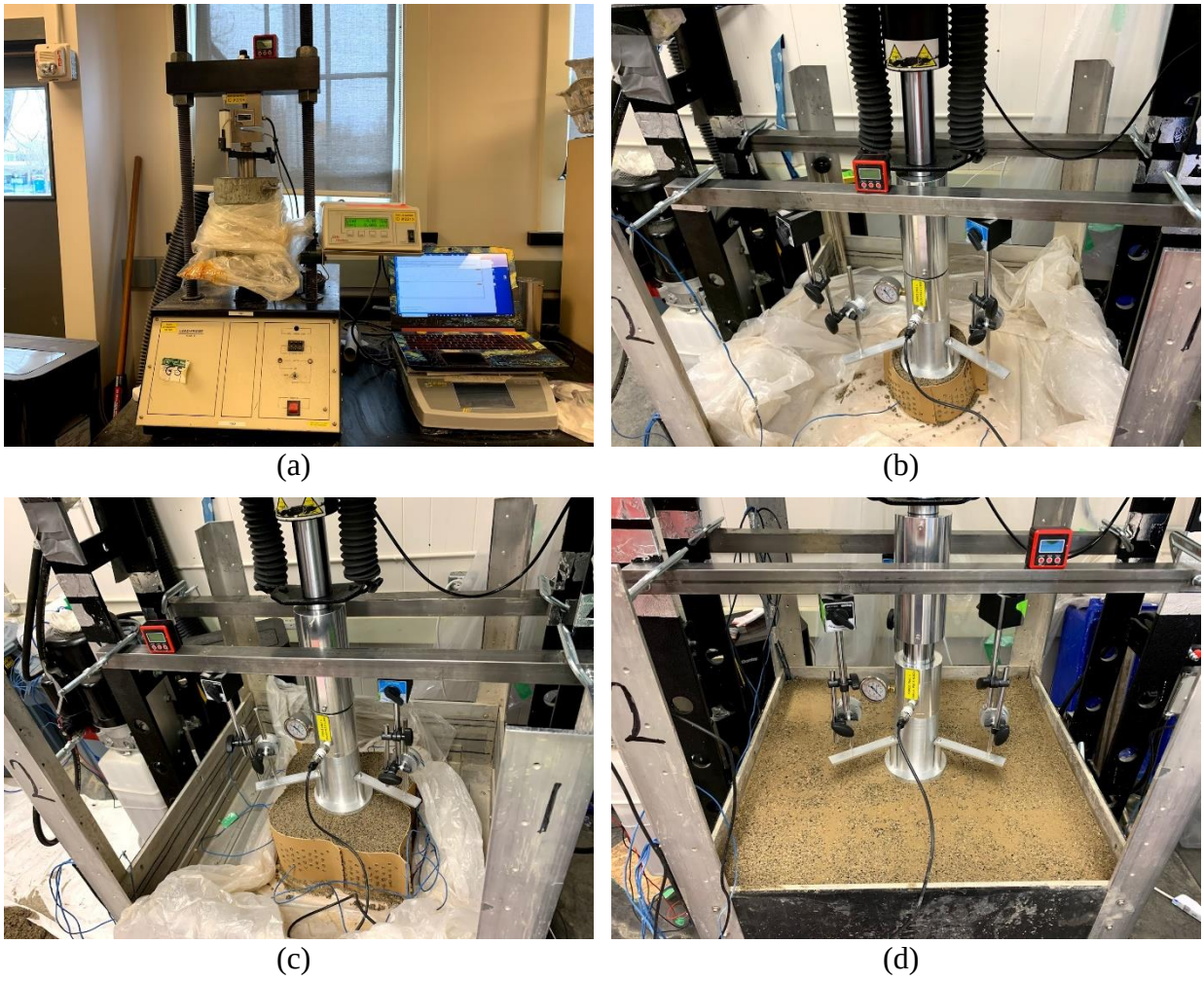

(a) (b)

(c) (d)

Fig. 4.3. Photographs of plate loading test: (a) CBR test, (b) element test involving unconfined single geocell, (c) element test involving unconfined four geocells, and (d) model test involving multiple geocells confined by soils

4.3.2.2 Element test for reinforced sands

This test was run on 12 samples of single-geocell-encased sands [Fig. 4.3(b)] that underwent zero, one, and five F-T cycles. For comparison of the boundary effects of multiple-geocell and single-geocell reinforced sands under initial loading, two four-geocell-encased-sand samples [Fig. 4.3(c)] were prepared for plate loading test only (without F-T). In the cases of single-geocell reinforced sands subjected to one F-T cycle, additional test was run to investigate if a lower subfreezing temperature (i.e., -20°C) would affect the mechanical behavior of the reinforced soils. In other words, the test was to ensure if the subfreezing temperature of -10°C was adequate. The

details of the test program are given in Table 4.1. The dimensions of the single-cell-reinforced sample were the same as those of an opened geocell (i.e., 245 mm × 210 mm in plan × 150 mm height).

The single-cell-reinforced samples were compacted in three 50-mm lifts to the maximum dry density and the optimum moisture content. Similarly, a T-type thermocouple was embedded in the sample, placed at the center of the first layer surface to monitor the soil temperature. All the samples were sealed by plastic films throughout F-T to prevent water loss, as shown in Fig. 4.2(b). The sealed samples were frozen to -10°C or -20°C (temperatures in soils) in a freezer, immediately followed by thaw to a soil temperature of 10°C. This completed one F-T cycle. Following the F-T cycles, the single-cell-reinforced samples were transported to the developed model test device (Huang et al., 2021) for plate loading tests, as shown in Fig. 4.3(b).

A circular loading plate (150 mm in diameter) connected with a load cell was placed centrally on top of the test sample. Piston of hydraulic cylinder was manually lowered down until it was tied to the load cell. The load was automatically read by a data logger PASCO® 550 Universal Interface. The displacement was measured by three dial gauges mounted on three extensions that were evenly bolted to the loading plate (i.e., every two neighboring extensions form an angle of 120º). The load cell and dial gauges had precision of 1 kPa and 0.025 mm, respectively. Load was applied in an increment of 62 kPa and maintained for five minutes at each loading stage. In the meantime, the displacement was recorded. The load was terminated when the soil reached bearing failure or the loading plate movement reached its limit (i.e., when the extensions touched the soil surface), and then the soil was unloaded in decrement to zero.

4.3.2.3 Model test

The model test was performed in the newly designed model test device capable of conducting both F-T tests and plate loading tests. It consisted of a F-T test to freeze and heat the soils to the same numbers of F-T cycles as the element test (i.e., 0, 1, and 5), followed by a plate loading test. The device consists of a F-T component, a plate loading component, and a rail connecting component. Details of this device were described in Huang et al. (2021). The F-T component is composed of a square aluminum box with interior width of 750 mm, a cooling plate, insulation layers, and a chiller connected to the cooling plate. During the F-T test, the cooling plate is placed on top of compacted soils in the box to cool or heat the soils, thus imposing one-dimensional thermal loads to the soils. The plate loading component has been described in Section 4.3.2.2. The rail connecting component is utilized to connect the F-T component and plate loading component so that soil preparation and F-T tests can be performed outside the loading frame.

Eleven model tests were conducted on multiple-geocell-reinforced sands and unreinforced sands. The details of the model test program are given in Table 4.2. The layout of multiple geocells was such that the geocells would fully occupy inside the box, and in this case, eight interconnected geocells were used. The soils were filled and compacted to the maximum dry density and the optimum moisture content determined by the standard proctor test in four lifts to a height of 170 mm. The first three lifts were 50 mm per lift while the last lift was 20 mm thick. Different from the element tests in which the loading plate was placed directly on the surface of geocell-sand matrix, the model tests used the top 20-mm thick layer as protection cover over the geocell-sand matrix, and the plate exerted loads on top of the cover. The use of this cover is consistent with the general design practice in roads as it can improve the mechanical performance of geocell-reinforced bases (Dash, 2001; Pokharel et al., 2010). To monitor soil temperature, T-type

thermocouples were installed on top of each lift and embedded in the box bottom and the cooling plate. The detailed instrumentation can be referred to Huang et al. (2021).

During the freezing process, the chiller was set to a constant temperature of -20°C. It circulated coolants to cool the cooling plate, which thus froze the soils inside the insulated box top-down. Once the box bottom reached a subfreezing temperature of -10°C, the chiller was switched to heating by setting the temperature to 20°C, which resulted in top-down thawing of the soils. When the box bottom temperature reached 20°C, the thawing process was terminated, which concluded one F-T cycle. To monitor the F-T induced movement of soils, three Omega® linear variable differential transformers (LVDTs) with a measurement limit of 50 mm and an accuracy of 0.01 mm were placed on three screw columns that were tied down to the cooling plate [see in Fig. 4.2(c)]. National Instruments® data logger was used to acquire the readings of T-type thermocouples and LVDTs every 30 minutes throughout the F-T process.

After the F-T tests, insulation foams were removed, and the box was carefully moved to the loading frame through the rails for plate loading tests, as shown in Fig. 4.3(d). The loading procedure was the same as described in the element test for reinforced sands. After the completion of the plate load tests, soils at different locations were sampled for gravitational moisture content tests. For the reinforced sands under five F-T cycles, besides the gravitational moisture contents, volumetric moisture contents were also monitored during F-T by moisture sensors embedded in different locations of the soils.

4.4 Results and discussion

The results from the element tests and model tests were presented and compared. As described previously, during the F-T process, element test samples experienced three-dimensional heat transfer, while sands in the model tests underwent one-dimensional heat exchange. Past studies

(Othman and Benson, 1992, 1993; Wang et al., 2007) revealed that the dimensional effect was negligible on the morphological and mechanical responses of soil samples with 114-125 mm height and 61.8 to 102 mm diameter. In this study, we assume the element tests and model tests would not be affected the dimensional effect either. Therefore, the results between the two types of tests are comparable.

Scale rules may be used to relate the model test results to prototype results (Kargar and Mir Mohammad Hosseini, 2018; Viswanadham and König, 2004). Table 4.3 lists the scale factors of that may be of use to translate model test results to the prototype scale. Since the present study is focused on the relative changes in soil properties due to F-T cycles, a normalized value of soil parameters (CBR, stiffness and ultimate bearing pressure) after certain F-T cycles in relation to before F-T cycle is adopted to quantify the F-T impact. This normalized value is identical between the model scale and the prototype scale as the scale factors are cancelled out.

Table 4.3. Scale factors

	Prototype	Model
Length	1	$1/\lambda^*$
Area	1	$1/\lambda^2$
Volume	1	$1/\lambda^3$
Density	1	1
Strain	1	1
Settlement	1	$1/\lambda$
Bearing capacity(F/L^2)	1	$1/\lambda$
Stress	1	$1/\lambda$
Force	1	$1/\lambda^3$
Stiffness (F/L^3)	1	1

*λ is the geometric ratio between the prototype scale and model scale.

4.4.1 Effect of F-T cycles on CBR of unreinforced sands

California bearing ratio (CBR) is the percentage of the stress at the penetration of 0.1 inch or 0.2 inch to the standard stress at the corresponding penetration. This parameter can be used to characterize mechanical properties of pavement materials. Soil stiffness can be estimated given a CBR value (Barker and Alexander, 2012), as shown in Equation (4-1).

$$k = 53.438CBR^{0.5719} \quad (4\text{-}1)$$

where, k is the stiffness, also known as modulus of subgrade reaction, psi/in.

Fig. 4.4 shows variations of CBR values with F-T cycles in the element tests for unreinforced sands. In the figure, the CBR value for a specific number of F-T cycles represents an averaged value of triplicate samples, and the normalized CBR is the ratio of CBR after a certain number of F-T cycles to that at zero F-T cycle. The normalized value can better indicate the degradation of soil strength by F-T cycles.

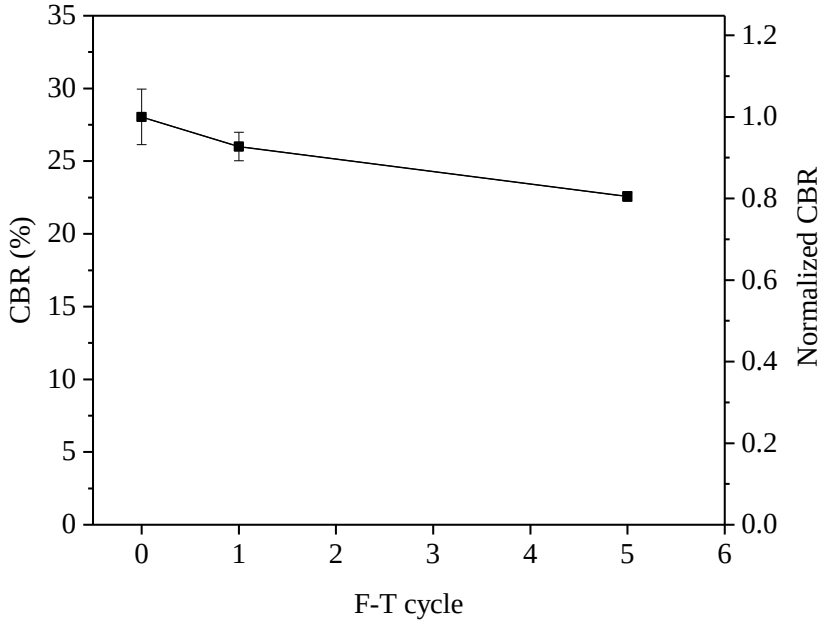

Fig. 4.4. Variations of CBR of sands with F-T cycles in which normalized CBR is ratio of CBR after F-T cycles to CBR before F-T cycles

It is shown from Fig. 4.4 that sand strength slightly decreased with the increasing number of F-T cycles and after one and five F-T cycles, CBR was reduced by about 7% and 20%, respectively. This indicates that although the poorly graded sands are not susceptible to frost, F-T cycles could still pose an adverse effect on the soil strength. This is in agreement with the findings by Kawabata et al. (2016). This might be due to the loosening effect of F-T cycles on dense sands. During the freezing process, the frost front advanced inwards in the sands, accompanied with the freezing of the pore water in sands as well as migration of pore water towards the frost front (i.e., from center to exterior). For the dense sands, the phase change from water to ice caused the pores to expand. During the thawing process, pore ice was melted and soil particles might not fall exactly back into initial positions (Simonsen et al., 2002). This resulted in a net increase in void ratio and rearrangement of soil structure (Viklander, 1998). It is expected that the reduction in CBR would become progressively smaller and stable after a certain number of F-T cycles (Xie et al., 2015). A larger number of F-T cycles will be warranted in the future study for all the element and model tests.

4.4.2 Effect of F-T cycles on single-geocell reinforced sands

Fig. 4.5 presents the load-displacement curves for single-geocell-reinforced sands from the element test after exposed to different F-T cycles. It also contains the load-displacement curves for four-geocell-reinforced sands, which experienced no F-T cycle. From the load (in pressure)-displacement curves, stiffness and ultimate bearing pressure were determined. The stiffness (in kPa/mm) herein is equivalent to the modulus of subgrade reaction that is commonly obtained from a plate loading test (DeMerchant et al., 2002; Huang et al., 2021; Pokharel et al., 2010). For the single-geocell-reinforced sand samples, the stiffness was defined as the slope of the second linear segment of the load-displacement curves instead of the initial slope of the curves. The reason will

be discussed later. Note that since the slope is taken as the ratio of incremental applied pressure to incremental displacement, the stiffness herein is similar to coefficient of subgrade reaction. The ultimate bearing pressure was taken as an inflection point of the curves excluding the first linear segment.

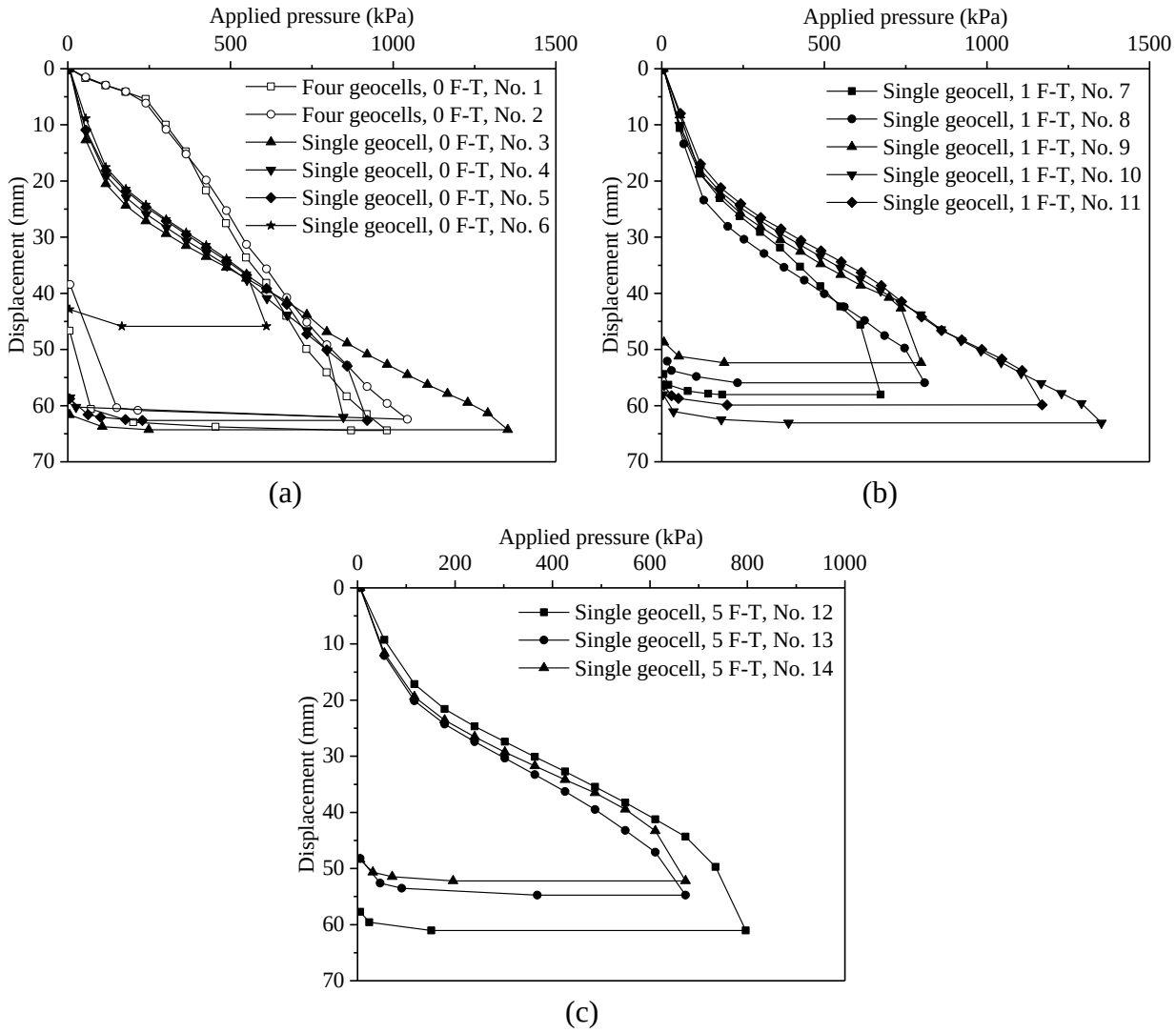

Fig. 4.5. Load-displacement curves from element tests after: (a) 0 F-T cycle, (b) 1 F-T cycle and (c) 5 F-T cycles

For all the element tests involving single-geocell-reinforced samples, an appreciable displacement was developed when a small pressure (<200 kPa) was applied. This was primarily due to the optimization of the geocell shape from initially elliptical shape to circular shape in

response to the initial loading. Fig. 4.6 illustrates the shape change of single geocell under the initial loading in the element tests. This occurred as the single geocell was unconfined and the boundary of the sample (245 mm × 210 mm) was relatively close to the loading plate edge (150 mm diameter). The boundary effect was significant as the initial rapid increase in displacement was not observed in the four-geocell-reinforced sample [Fig. 4.5(a)]. Once the geocell was adjusted to an optimal circular shape, a new linear displacement response was developed under a further load increment. Since the development of the initial displacement was due to the shape adjustment, the stiffness was not taken from this segment but from the second linear segment. It is expected that the circular geocell shape could mobilize the geocell reinforcement to sands at the initial loading without F-T cycles. However, the mechanical response to the F-T cycles for circular-shape single-geocell-reinforced sands is still uncertain and it will be investigated in the future.

(a) (b)

Fig. 4.6. Single geocell shape in element test: (a) before initial loading and (b) after initial loading

Parallel samples (approximately 3 to 5 samples per test) were prepared to verify the repeatability of the element tests. Fig. 4.5 shows that the curves were in general overlapped, with

only some variations in the ending points. This indicated that the element tests were relatively repeatable. In all the element tests for single-geocell-reinforced sands, the subfreezing temperature was -10°C except test No. 11 in which the lowest temperature was set to -20°C. It was found that a lower temperature (< -10°C) resulted in a negligible effect on the mechanical responses of single-cell reinforced sands.

Fig. 4.7(a) shows variations of the stiffness of single-geocell-reinforced sands with F-T cycles. The stiffness of the samples after one and five F-T cycles was decreased by 2% and 17%, respectively. Fig. 4.7(b) displays that the ultimate bearing pressure was increased slightly by 3% after one F-T cycle, but decreased by about 25% after five F-T cycles. Fig. 4.7 also presents error bars for the test results. It is interesting to find that variability of the stiffness and ultimate bearing pressure was reduced significantly after five F-T cycles. Similar finding was also observed for CBR values of unreinforced sands in Fig. 4.4. The cause of the waning variability of stiffness and strength results at higher F-T cycles might be attributed to the rearrangement of soil internal structures to a more stable state under the increased number of F-T cycles. The rearrangement of soil microstructure under F-T actions was mentioned in previous study (Viklander, 1998), indicating that initially loose or dense soils ended up with a similar residual void ratio after certain numbers of F-T cycles. As the mechanical variation of sands was reduced significantly with a larger number of F-T cycles, the programs of model tests can be arranged according to this phenomenon. Several parallel tests with small number of F-T cycles (i.e., 0 and 1 F-T cycle) are performed and the averaged results are adopted to reduce the variation, while with larger number of F-T cycles (i.e., 5 F-T cycles), only one test can be run as the variation is not significant after such F-T actions.

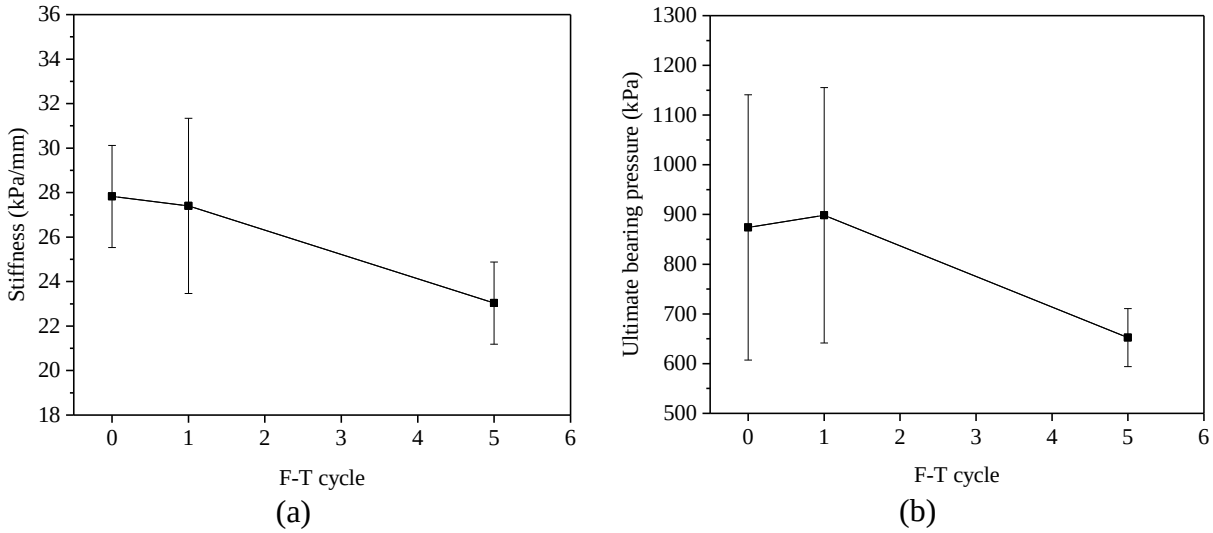

Fig. 4.7. F-T effects on: (a) stiffness and (b) ultimate bearing pressure from element tests

4.4.3 Effect of F-T cycles on mechanical behavior of multiple-geocell-reinforced sands

The mechanical behavior of multiple-geocell-reinforced sands measured in the model tests referred to the load-displacement curves, where the stiffness and ultimate bearing pressure were identified. Fig. 4.8 depicts the typical load-displacement curves for different F-T cycles. The change in soil volume in response to F-T cycles was not monitored during the element tests due to the constraints of operating LVDTs in the freezers, while this data was measured in the model tests, and the detailed results can be referred to Huang et al. (2021). Here some of the results are reanalyzed and interpreted such that results from both element and model tests are comparable. For example, the ultimate bearing pressure for reinforced sands under five F-T cycles was reanalyzed and the first inflection point was selected as the ultimate bearing pressure instead of the second inflection point used by Huang et al. (2021). The relationship between stiffness and F-T cycles presented in Fig. 4.9 was not investigated in Huang et al. (2021).

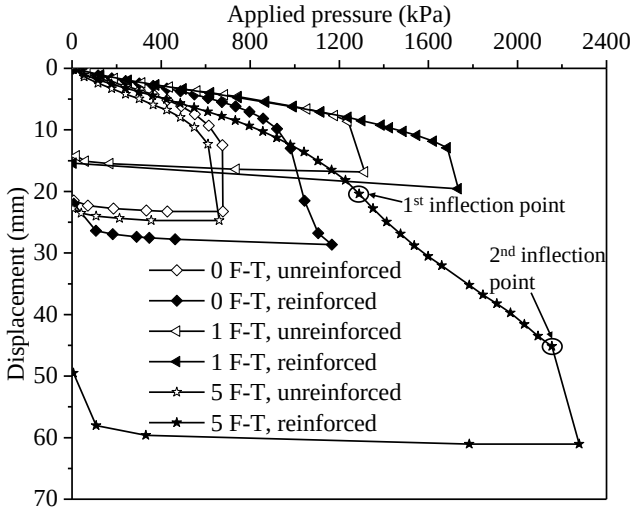

Fig. 4.8. Load-displacement curves from model tests [modified from Mian et al. (2021)]

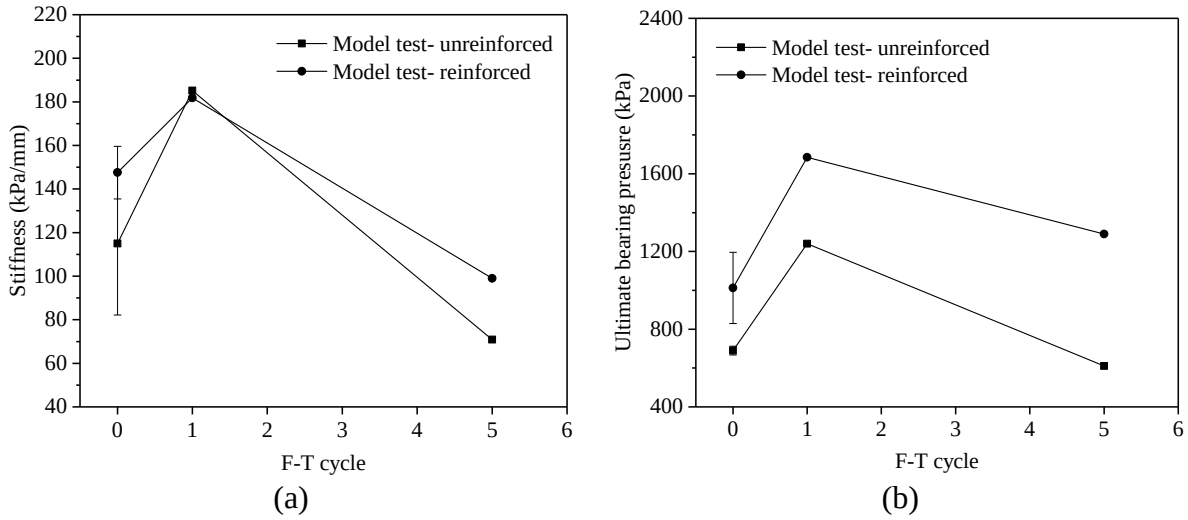

Fig. 4.9. Variations of (a) stiffness and (b) ultimate bearing pressure with F-T cycles from model tests

Fig. 4.9 presents variations of stiffness and ultimate bearing pressures with F-T cycles. At no F-T condition, the multiple-geocell reinforcement increased the stiffness and ultimate bearing pressure by about 28% and 47%, respectively. Both the stiffness and ultimate bearing pressure increased apparently after one F-T cycle, followed by a drastic decrease after five F-T cycles. The positive effect of F-T at one cycle to the mechanical properties of soils in the model tests is counterintuitive. It is inconsistent to the results from the element tests and previous studies (Wang

et al., 2007; Wong and Haug, 1991; Xie et al., 2015). Huang et al. (2021) attributed it to the combined effects of water redistribution and the rearrangement of soil internal structure change. Here we reanalyze it with the element test in the following section to provide a further insight. It is also noted that sieve analyses were performed before and after thermal loading (F-T cycles) and mechanical loading (plate loading test) to investigate if the soil particles were damaged during these loading processes. The results plotted in Fig. 4.1 show that both thermal loading and mechanical loading did not alter the particle sizes. For the effect of thermal loading, particle size distribution was measured only for a larger number of F-T cycles (five cycles) not for a smaller number of F-T cycles (one F-T cycle) as the five F-T cycles did not cause any changes to particle size.

4.4.4 Comparison of test results between element tests and model tests

The observations of failure modes in the element tests and model tests are illustrated in Fig. 4.10. For all the element tests involving single geocell reinforcement, the failure was due to the breakage of the welded seam at the bottom [see Fig. 4.10(a)]. Similar phenomenon was also observed by others (Pokharel et al., 2010). In contrast to single-geocell-reinforced sands, multiple-geocell-reinforced sands exhibited buckling of geocell ribs, as shown in Figs. 4.10(b) and 4.10(c). This was due to the loading plate that was placed on top of the geocell ribs. After the completion of plate loading test on four-geocell-reinforced sands, it was observed that the geocells were lifted up by about 10 mm from the bottom and sands directly below the loading plate were pushed sideway, causing a heave of 15 mm at the surface. The lift of multiple geocells (about 5 mm) and the heave of sand surface around the loading plate were also observed in the model tests. The combined effects of buckling of geocell ribs and escape of sands from geocell confinement might contribute to the bearing failure of the multiple-geocell reinforced sands.

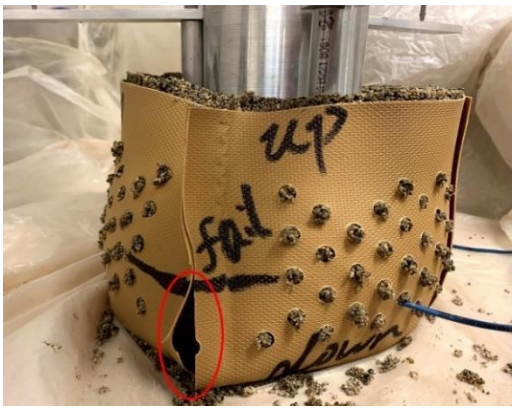

(a)

(b)

(c)

Fig. 4.10. Observed failure modes of geocells: (a) element test-single geocell, (b) element test-four geocells and (c) model test

To quantitively compare the F-T effects on the mechanical behavior of soils from both element tests and model tests, normalized values, i.e., results after F-T cycles normalized by before F-T cycles, were used for analyses. Fig. 4.11 presents normalized stiffness and ultimate bearing pressure measured from the element tests and model tests. Normalized CBR values were plotted in both stiffness and bearing pressure graphs as the CBR is a normalized value determined based on the prescribed penetration, which could represent both secant stiffness and strength. It is evident that both stiffness and ultimate bearing pressure decreased with increased F-T cycles in the element tests. The beneficial effect of F-T at one cycle observed in the model tests was not seen in the element tests. The discrepancy is due to the different distribution of moisture contents with F-T cycles in the element tests and model tests. Fig. 4.12 shows the distribution of

gravitational moisture content after different F-T cycles. Figs. 4.12(a) and 4.12(b) present the distribution of pore water in the element tests. It is clearly shown that the distribution of pore water in sands increased along the depth and water migrated top-down with the increased number of F-T cycles. However, in the model tests, the distribution of pore water was opposite, with the moisture content decreasing along the depth, as shown in Figs. 4.12(c) and 4.12(d). The trend of water migration was not consistently seen from Figs. 4.12(c) and 4.12(d), while the measured volumetric moisture content results showed the consistent top-down water migration after one F-T cycle but bottom-up migration after five F-T cycles (Huang et al., 2021). This might explain the increase in stiffness and bearing pressure after one F-T cycle, followed by the decrease after five F-T cycles. Overall, scale difference between element tests and model tests might contribute to difference in soil conditions prepared, leading to the discrepancy of water distribution and migration driven by F-T action. As discussed in the element tests, the higher variability of the mechanical properties was found at a smaller number of F-T cycles. This alluded to that the beneficial effect at one F-T cycle in the model test might require more tests to verify as the present test for one F-T cycle did not contain parallel samples.

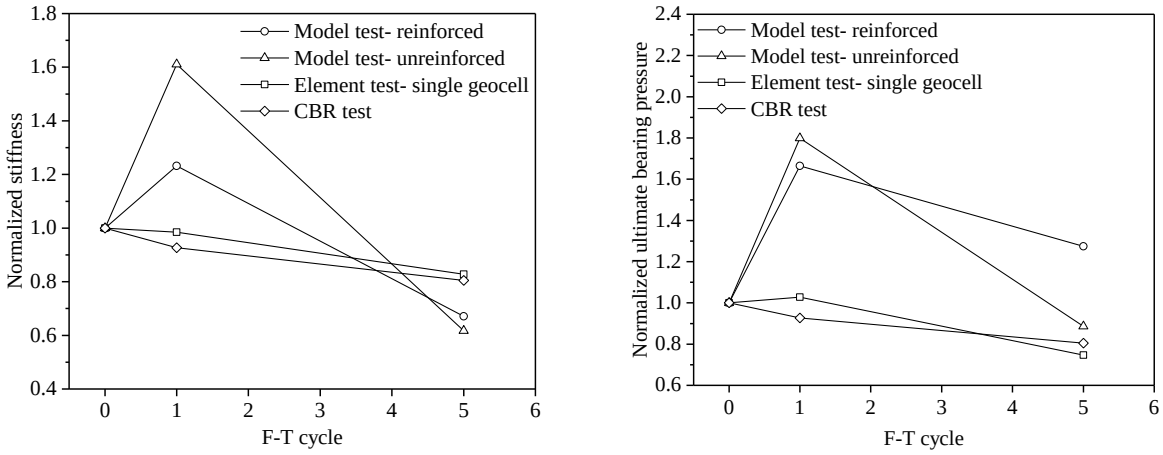

(a) (b)

Fig. 4.11. Comparisons of test results between element and model tests: (a) normalized stiffness and (b) normalized ultimate bearing pressure

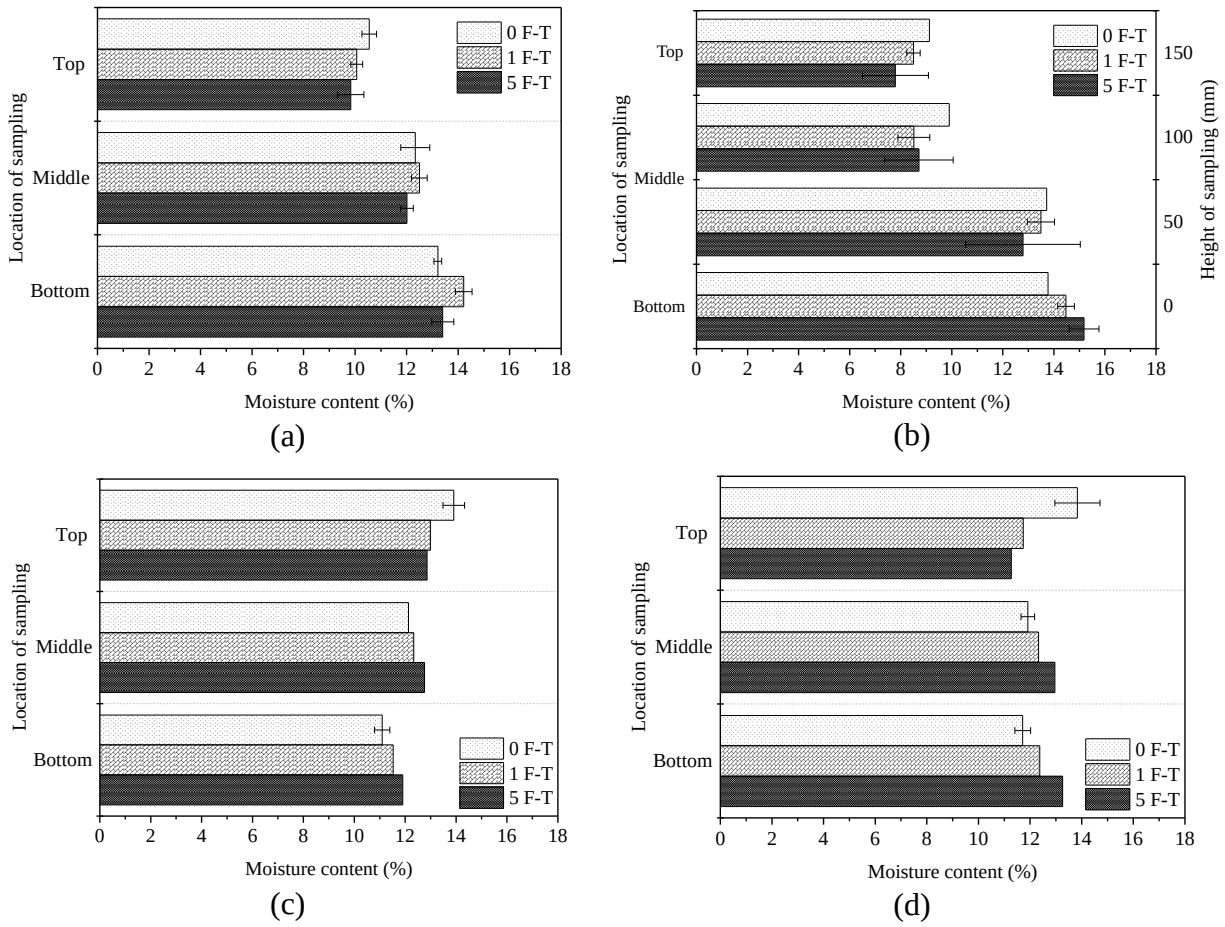

Fig. 4.12. Averaged moisture contents at different locations of specimen: (a) element test- unreinforced (CBR), (b) element test- single geocell, (c) model test- unreinforced and (d) model test- reinforced

In this study, the mechanical behavior of reinforced sands was varied with increased number of F-T cycles, but the F-T effects on geocell materials are unknown. Previous studies reveal that the F-T cycles had a negligible effect on mechanical and physical properties of geosynthetics materials (Allen, 1983; Calhoun, 1972; Wang and Xu, 2008). However, limited research is concerned on the F-T response of geocell welded seam, which represents the weakest location in the element tests involving single-geocell-reinforced samples. The strength of geocell seams may be also varied with F-T cycles as thermal stress can develop at the welded seam due to the different coefficient of thermal expansion between geocell seam and geocell ribs. The role of variations of

geocell seam with F-T cycles in the mechanical behavior of geocell-reinforced soils warrants a further study.

4.5 Conclusions

This paper presents experimental studies to investigate the F-T effects on the mechanical behavior of geocell-reinforced sands in element tests and model tests. The mechanical properties of the sands including stiffness and ultimate bearing pressure were evaluated through plate loading tests after the sands were exposed to different F-T cycles. The results from the element tests and model tests were analyzed and compared. The following conclusions are drawn from this study:

(1) Although sands are not frost susceptible, their CBR values decreased with F-T cycles. After five F-T cycles, CBR values decreased by about 20%. A similar amount of reduction was also found in stiffness and ultimate bearing pressure of single-geocell-reinforced sands after exposed to five F-T cycles.

(2) In the element tests, variability of the test results was reduced with the increased F-T cycles. This might be attributed to the rearrangement of soil internal structure to a more stable state by F-T action. This rearrangement would alter the sands from the initial dense state to a looser state. This indicates that to improve the reliability of the test results, more parallel samples are needed for a smaller number of F-T cycles.

(3) From the model tests, geocells were found to increase the mechanical properties of sands by 30%-110%. Unlike the continuous decrease in mechanical properties by F-T cycles in the element tests, the model tests found an increase in the mechanical properties after one F-T cycle, followed by dramatical decrease after five F-T cycles. The unexpected beneficial effect of one F-T cycle was attributed to temporary water redistribution and rearrangement of soil internal structure.

(4) The discrepancy of the test results might be due to the scale difference that contributed to difference in soil conditions prepared, thus the difference in water distribution in the soils. The higher variability of the mechanical properties at a smaller number of F-T cycles in the element tests alluded to that the beneficial effect at one F-T cycle in the model tests might require more parallel tests to verify as the present test for one F-T cycle was restrictive to only one sample.

Chapter 5 Freeze-thaw performance of geocell-Stabilized flexible pavement in Surgeon County, Alberta: Instrumentation

5.1 Abstract

Geosynthetics have been widely used to enhance the performance of roadways in seasonal frost regions, but their effectiveness against freeze-thaw-induced deterioration in pavements, particularly in full-scale road sections, is seldom documented. This project aims to fill this gap through construction of three full-scale asphalt pavement sections with the road bases stabilized by geocomposite, Novel Polymeric Alloy (NPA) 4-inch Type-D geocells and NPA 6-inch Type-D geocells at the existing pavements in Sturgeon County, Alberta. Each section was fully instrumented with thermocouples, moisture sensors, and earth pressure cells for both short-term field testing and long-term monitoring. Dynamic cone penetration (DCP) tests were conducted on compacted subbases and base courses of each section in the summer of 2022. Plate loading tests and trafficking tests were performed on each section before the pavement was frozen in ground at the beginning of November 2022, and will be carried out after each seasonal F-T cycle in two to three following years. This report describes the instrumentation of soil sensors, weather station and data acquisition system, and presents the first stage of the experimental results involving the results of plate loading tests, trafficking tests, and long-term monitoring. Some lessons learned from the instrumentation and preliminary observations on the performance of the three test sections are discussed.

5.2 Introduction

5.2.1 Background

In seasonal frost regions, roads are vulnerable to freeze-thaw (F-T) cycles, which can induce the repetitive action of frost heave and thaw weakening. This process can result in water

movement in the soil, formation of segregated ice lens, expansion of soil volume, generation of non-uniform melted pore water, and consolidation of soil, all of which contribute to changes in void ratio and soil structure (soil fabric and bonding) and thus are responsible for road destabilization (Kawabata et al., 2016; Simonsen and Isacsson, 1999; Viklander, 1998).

A variety of engineering countermeasures have been implemented in practice to mitigate F-T damages and improve durability of roads. These include installation of effective drainage systems, replacement of frost-susceptible fines, chemical stabilization of road bases with binders (e.g., cement, lime, etc.), and physical stabilization of road bases with geosynthetics. Geocells, a three-dimensional geosynthetic featuring honeycomb-like interconnected cells, have been reported to benefit the durability of roadways against the F-T cycles at limited project sites (Edil et al., 2002; Henry et al., 2005; Pokharel et al., 2017). However, the beneficial effect of geocells as a base stabilization for paved or unpaved roads subjected to seasonal F-T action has not be quantified at the full scale of roads.

This research project aims to add to the limited evidence of the F-T performance of the geocells-stabilized bases through the testing and monitoring of well-instrumented road sections. The experimental data would allow for quantifying the efficacy of the geocell stabilization as a mitigation solution for F-T damages and illuminating the underlying mechanisms. Fig. 5.1(a) shows the project site (circled in the map), which are located at the intersection of Township Rd 544 and Range Rd 260 on a stretch of rehabilitated highway in Sturgeon County, Alberta. Fig. 5.1(b) presents the three test sections at this project site, which are asphalt surface over the base courses stabilized by three types of geosynthetics, respectively: a layer of 4-inch Type-D Novel Polymetric Alloy (NPA) geocells, a layer of 6-inch Type-C NPA geocells, and a layer of geogrid-geotextile composite (known as geocomposite), as shown in Fig. 5.1(b). The geocell and

geocomposite sections were designed by Stratum Logics and MPE Engineering Ltd., respectively. The construction was done by TBL Construction Ltd., starting in June 2022 and ending in October 2022. The instrumentation and field testing and monitoring were implemented by the team of the University of Victoria and Stratum Logics.

(a)

(b)

Fig. 5.1. The satellite map of: (a) the site location and (b) the three test sections

5.2.2 Subsurface condition

Geotechnical investigation was conducted for the old road at the same site by J.R. Paine & Associates Ltd during July - September 2019 with complementary investigation in 2018 Sturgeon County Local Roads Reconstruction Program. Twenty (20) soil borings to a depth of no less than 3.8 m below the existing grade were performed, with one located at Range Road 260 and the other 19 at Township Road 544. The generalized top-down soil profile consisted of asphalt surface, gravels, clay backfill, and native clay, as shown in Fig. 5.2. No ground water was observed in all the boreholes except for three boreholes where free water was accumulated at the depth of 3.5 to 3.7 m.

Graphical lithology	USCS	Soil description	Thickness (mm)
	ASPH	COLD MIX	80 to 100
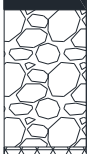	G	GRAVEL: trace to moderate clay fill, or sandy	200 to 420
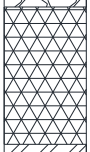	FILL	CLAY BACKFILL: silty, sandy, medium plasticity	500 to 1100
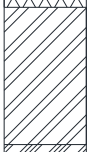	CH	CLAY: silty, medium plasticity	900 to 2000
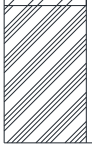	CL	CLAY TILL: silty, low to high plasticity	N/A

Fig. 5.2. Soil profile at the project site

5.2.3 Experimental objectives

The objective of this project was to assess the F-T performance of the geocell-stabilized road bases through full-scale testing and monitoring. To achieve this objective, the following tasks were carried out.

1) conduct instrumentation of various types of sensors in the pavement section.

2) perform the short-term tests after seasonal F-T cycles.

3) monitor the long-term performance of the instrumented test section during the seasonal F-T cycles.

4) quantify the effectiveness of geocell stabilization in improving the F-T performance.

5.2.4 Report composition

This report is organized as follows. Sections 5.3 and 5.4 present construction of the road test sections and the corresponding instrumentation, respectively. Sections 5.5 and 5.6 describe the field testing and monitoring procedure and the corresponding results, respectively. Section 5.7 summarizes the preliminary observations and recommendations.

5.3 Pavement structure and construction

5.3.1 Pavement structure

A stretch of the old highway was fully removed up to the depth below native subgrade and then reconstructed with a two-lane flexible pavement. Fig. 5.3(a) indicates the pavement structure, consisting of top-down: (A) 90 mm thick asphalt concrete pavement (ACP) layer, (B) 300 or 350 mm base courses, (C) 300 mm subbase, and (D) 1000 mm pit run backfill underlain by the native subgrade (i.e., CH or CL in Fig. 5.2). The ACP included two layers: i.e., 50 mm for the lower layer and 40 mm for the upper layer. The base course layer in the geocomposite section was 50 mm thicker than in the geocell sections. The width of asphalt surface was 9 m, while the geosynthetic

layer was approximately 10 m in width as shown in Figs. 5.3(b) and 5.3(c). The pavement surface was sloped 3% from the centerline to the shoulders. The shoulders on both sides were constructed in a slope of 3(H):1(V) before joining the drainage ditches.

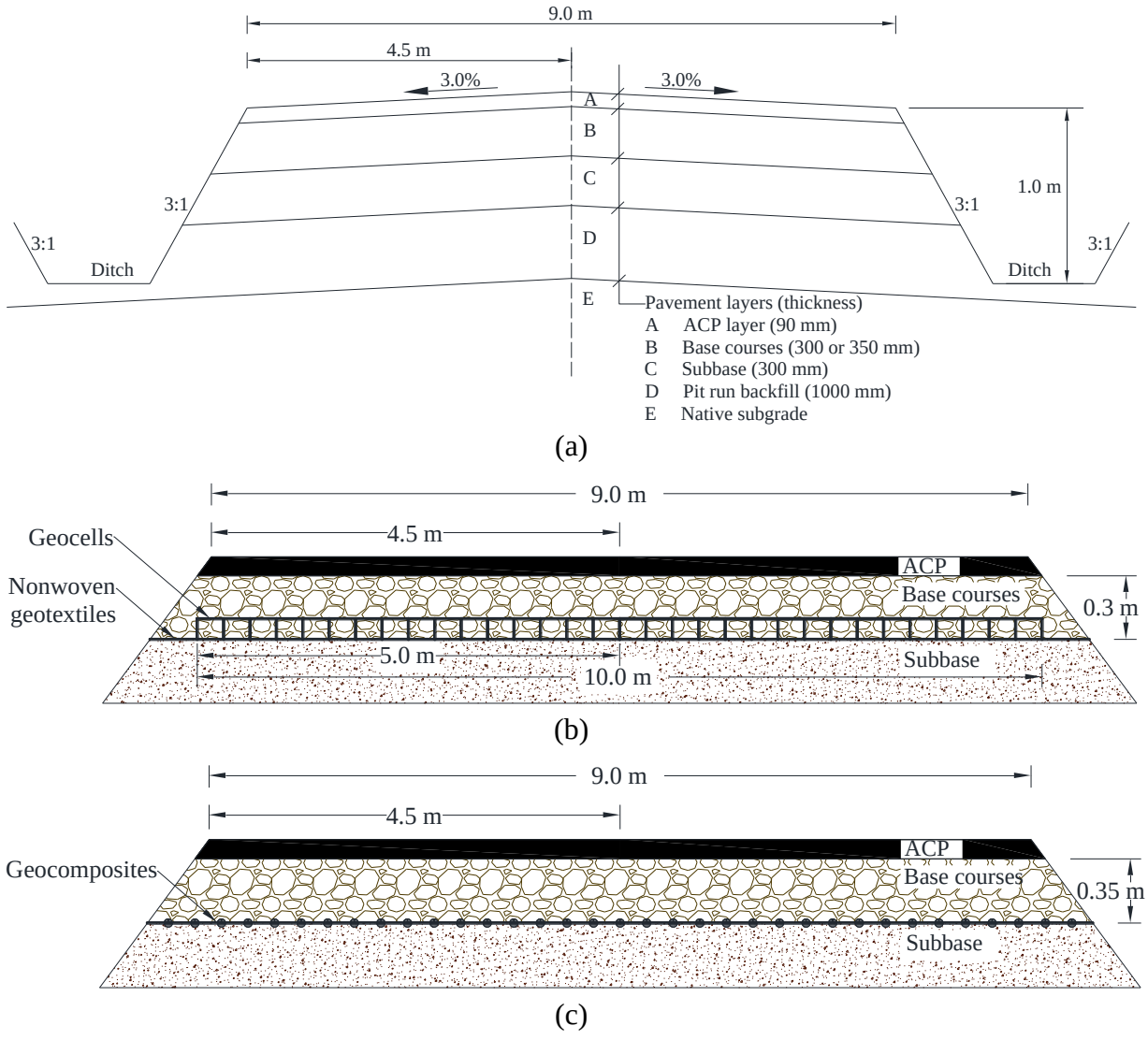

Fig. 5.3. The pavement structures

5.3.2 Materials of geosynthetics and pavement layers

5.3.2.1 Geosynthetics materials

Geocells used in this project were Novel Polymeric Alloy (NPA) 6-inch Type-C and 4-inch Type-D geocells manufactured by PRS Geo-Technologies. The 4-inch and 6-inch represent the

height of the corresponding geocells. Geocomposite used in this project is a composite geosynthetic, made by welding a layer of nonwoven geotextile within the structure of a biaxial geogrid layer. The 30/30 represents the nominal tensile strength of the geogrid portion is not less than 30 kN/m at both the machine direction and cross machine direction. Tables 5.1 and 5.2 summarize the basic properties of geocells and geocomposite, respectively.

Table 5.1. Properties of NPA geocells

Properties	Values		Test standard
	Type-C	Type-D	
Seam weld splitting strength, kN/m	19	22	ISO-13426-1
Tensile strength, kN/m	19	22	ISO-10319
Long-term permanent deformation at 65°C, %	3	3	ASTM D6992
Dynamic modulus, MPa			ASTM E2254
+30°C	775	800	
+45°C	675	700	
+60°C	525	650	
Coefficient of soil-cell friction efficiency	0.95	0.95	ASTM D5321
Brittle temperature, °C	-70	-70	ASTM E2254
Coefficient of thermal expansion, ppm/°C	135	135	ASTM E831
Distance between weld seams, mm	330	330	
Cell wall height, mm	150	100	
Opening cell dimension, mm × mm	245 × 210	245 × 210	

Table 5.2. Properties of geocomposites

Properties	Value			Test standard
	Geogrid	Geotextile	Composite	
Nonimal tensile strength (md/cmd)*, kN/m	30/30	7.5/11.0	-	ASTM D4595
Elongation at nominal tensile strength (md/cmd), %	8/8	70	-	ASTM D4632
Tensile strength at, kN/m				ASTM D4632
1% elongation (md/cmd)	6/6	-	-	
2% elongation (md/cmd)	12/12	-	-	
5% elongation (md/cmd)	24/24	-	-	
Grab tensile strength (md), kN	-	-	0.55	ASTM D4632
Trapezoidal tear strength, kN	-	-	0.26	ASTM D4533
Puncture force, kN	-	1.67		ISO 12236
Index puncture, kN	-	-	0.26	ASTM D4833
Aperture size (md × cmd), mm × mm	32 × 32	-	-	
Displacement at static puncture, mm	-	30	-	ISO 12236
Characteristic opening size, μm	-	90	-	ASTM D4751

*md is machine direction; cmd is cross machine direction.

5.3.2.2 Pavement layer materials

ACP was prepared with the mix formula of 70% coarse aggregate, 10% blend sand and 20% recycled asphalt pavement (RAP). Basic properties of base courses, subbase, and pitrun at each section were determined according to the related ASTM standards. The materials were collected near the locations where sensors were embedded in the road sections as illustrated in Fig. 5.1(b). Specifically, the subbase and base course materials at 6-inch geocell and geocomposite sections were collected near the joint of these two sections, while the materials at 4-inch geocell section were collected 10 m away from the border of the two geocell sections.

Fig. 5.4 presents the particle size distribution of these materials. It can be seen that the subbase was essentially sands with significant amounts of gravels and fines; base courses and pitrun were gravels, both having similar amounts of sands and fines. Pitrun is typically unsorted granular by-products from a quarry, and there were oversized gravels encountered in this study. Table 5.3

indicates that the subbase in 4-inch geocell section contained more than twice the percentage of fines than in the 6-inch geocell or geocomposite sections, which resulted in drastically lower CBR values. In contrast, the base course materials were relatively consistent between the sections in terms of grain size distribution (Fig. 5.4). Due to this consistency, the further tests (e.g., CBR) were performed on the base courses taken from only one location: i.e., at the joint of 6-inch geocell and geocomposite sections. Additional test results of these materials can be found in Table 5.3.

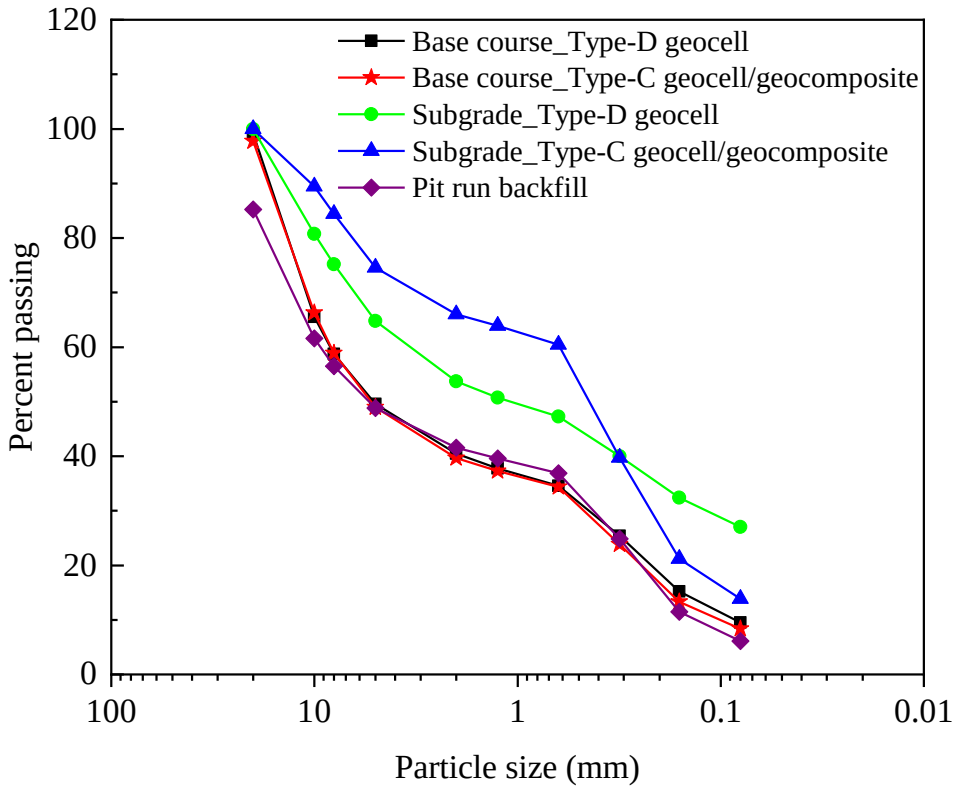

Fig. 5.4. Particle distribution of soils

Table 5.3. Soil properties of each pavement layer

Properties	Base courses	Subbase		Pit run backfill	Test standard
		Type-D geocell	Type-C geocell & geocomposite		
Mean particle size (mm)	5.142	1.115	0.471	5.465	
Uniformity coefficient	96.63	46.26	7.79	68.12	ASTM D6913
Curvature coefficient	0.31	0.05	1.09	0.16	
Fines content (%)	9.5	27.1	13.9	6.1	ASTM C117
Optimum moisture content (%)	4.4	11.2	7.7	6.7[a]	ASTM D698
Maximum dry density (g/cm^3)	2.14	1.95	2.11	2.18[a]	AASHTO T224[*]
Unsoaked CBR (%)	110.0	3.6	81.3	-[b]	ASTM D1883
Soaked CBR (%)	101.7	4.9	77.3	-[b]	

[a] The moisture content and dry density are corrected according to AASHTO T224 due to more than 5% oversize gravels retained on 19 mm sieve.
[b] CBR tests need modified soil gradation due to oversize gravels retained on 19 mm sieve.

5.3.3 Pavement construction

The pavement rehabilitation covered Township Rd 544 between Eloit St and Highway 2, and the northern portion of Range Rd 260 between Township Rd 544 in Sturgeon County, as shown in Fig. 5.1. The 4-inch geocell section was 200 m long, extending from Township Rd 544 STA 1+30 to STA 1+230. The 6-inch geocell section was 1,150 m long, starting from Township Rd 544 STA 1+230 to STA 1+880, Range Rd 260 STA 2+020 to STA 2+420, and Township Rd 544 STA 3+030 to STA 3+130. One end of the 6-inch section was joined by the geocomposite section, which ran for 2,710 m long, terminating at Township Rd STA 5+840.

Fig. 5.5 includes photographers taken during the construction of the two geocell sections. In these sections, the compacted subbase was overlaid by a layer of nonwoven geotextiles prior to placement of the geocells. The nonwoven geotextiles served as a separation layer to prevent the intrusion of fine particles from the subbase to the base courses. The geocell matrix was then added on top of the nonwoven geotextiles and stretched manually and fixed by nails inserted in the soil.

Once the cells were fully opened, the base course materials were filled and compacted by road rollers to a thickness of 300 mm with ≥ 95% of maximum dry density and the optimum water content (Table 5.3). In the geocomposite section, a layer of geocomposite was laid down on the surface of the compacted subbase prior to the addition of the base courses as shown in Fig. 5.6. The base course materials were compacted in the same manner as those in the geocell section, but with a greater thickness (i.e., 350 mm). Fig. 5.7 shows the placement of asphalt concrete pavement (ACP) surface in two layers. As indicated in Fig. 5.7(b), 0.5 m wide ACP shoulder was left at each side.

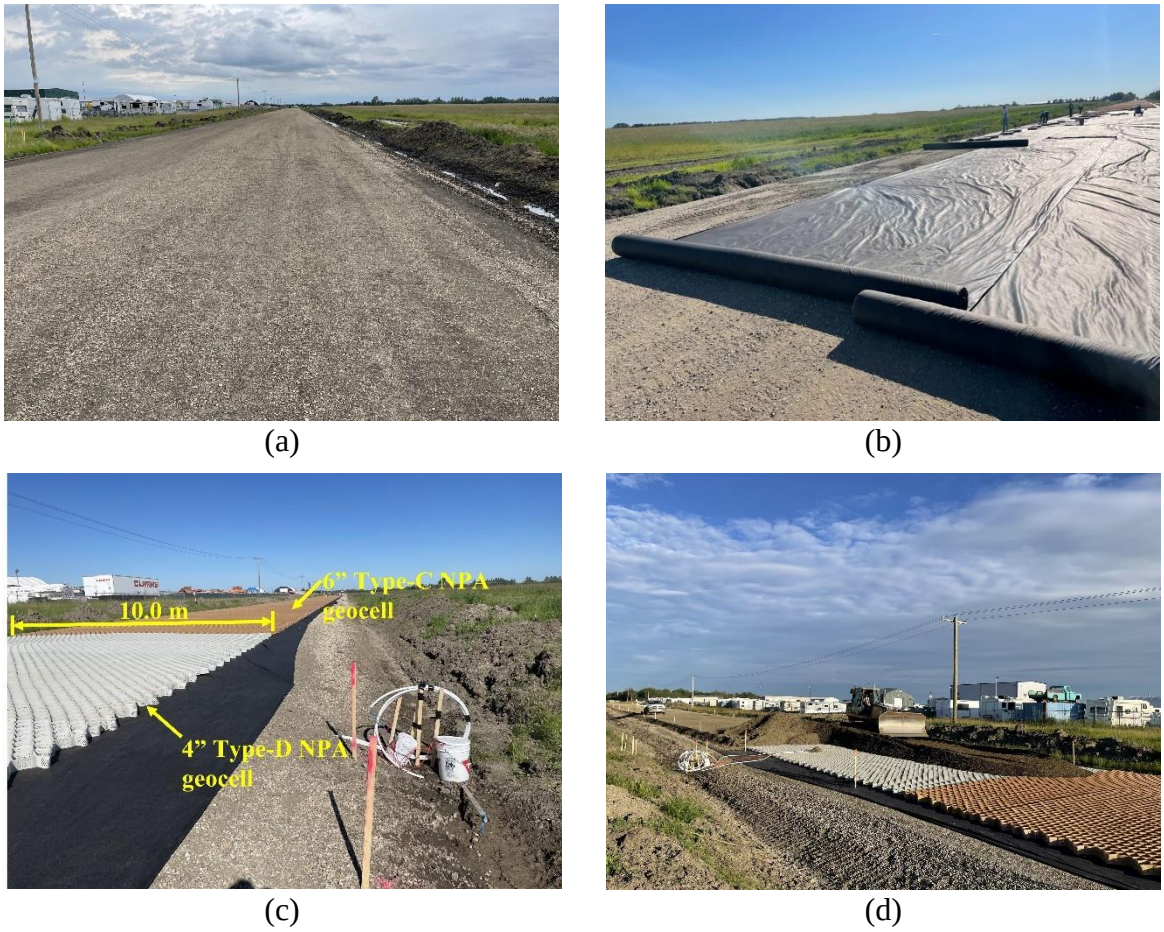

(a) (b) (c) (d)

Fig. 5.5. The construction process of geocell-stabilized sections in: (a) compacted subbase, (b) placing nonwoven geotextile, (c) installing geocell, and (d) adding base courses

(a)

(b)

(c)

Fig. 5.6. The construction process of geocomposite-stabilized section: (a) compacted subbase, (b) laying out geocomposite, and (c) placing base courses

(a)

(b)

Fig. 5.7. Asphalt concrete pavement: (a) the lower layer and (b) the finished layer

5.4 Instrumentation

Sensors embedded in the test sections included LPTPC12-S earth pressure cells (RST Instruments®), Type-T thermocouples (Omega®, the blue PVC insulation peel, and Thermo-Kinetics®, the brown Teflon insulation peel), and EC-5 moisture sensors (Meter Group®), as shown in Fig. 5.8(a). A weather station (made by Campbell Scientific®) was installed at the site, which included a TE525M tipping rain gauge and a Type 109 thermistor to monitor the precipitation and air temperatures on site, respectively. A remote data acquisition system (also manufactured by Campbell Scientific®) was set up to collect the data from the sensors and weather station. These data points could be remotely viewed or downloaded via the commercial software PC400 in computers. As shown in Fig. 5.8(b), the system consisted of a datalogger (i.e., CR1000X with the extension module AM16/32B multiplexer), a remote communication system (i.e., a C2446 antenna and a CELL205 cellular module), and a power supply unit (comprising a BP26 12-V rechargeable battery and a SP50-L 50-W solar panel). The datalogger, cellular module, and rechargeable batter were housed in a fiberglass case, which was enclosed in a wooden container.

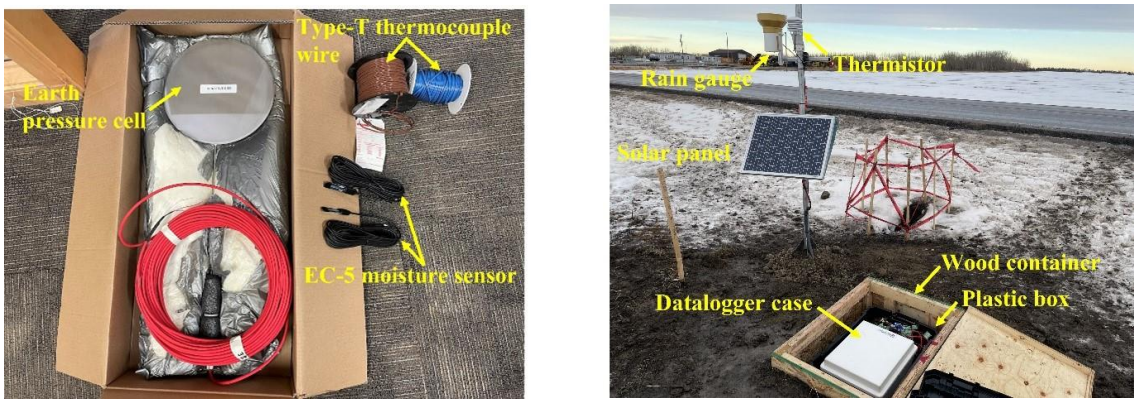

(a) (b)

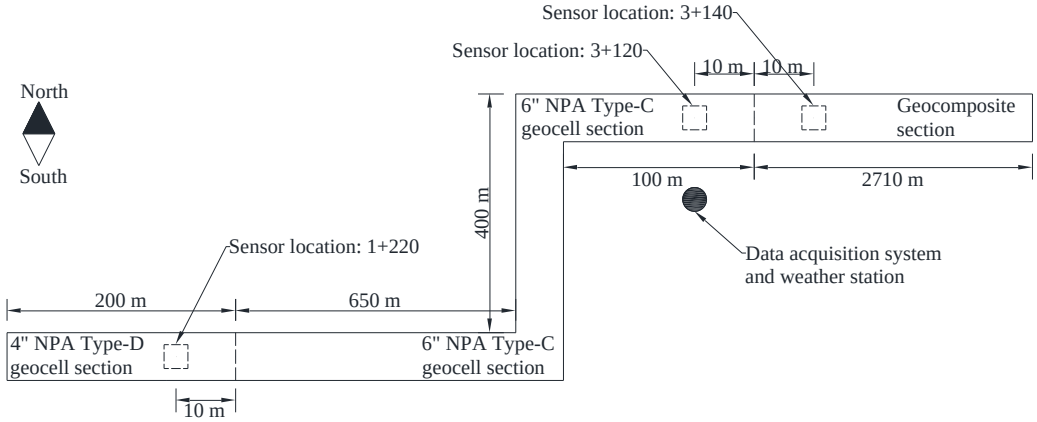

(c)

Fig. 5.8. (a) photographs of sensors, (b) weather station and remote sensing system, and (c) sensor locations

5.4.1 Sensor locations

Fig. 5.8(c) illustrate the instrumentation locations for each test section and the location of the weather station and the data acquisition system. The sensors were installed at a distance of 10 m from the joints between two neighboring sections to avoid the boundary effects while minimizing the lengths of sensor cables. The data acquisition system along with the weather station was installed close to the border of 6-inch geocell and geocomposite sections; therefore, the remote sensing for the long-term monitoring would only be performed at these two sections. However, the short-term measurement would be undertaken for all the three sensor locations as the datalogger can be manually connected to the sensor cables when the field tests such as plate loading tests and trafficking tests are conducted. All sensors were embedded in the south-bound lane as

shown in Fig. 5.9(a). Horizontally, earth pressure cells, thermocouples, and moisture sensors were spaced at distances of 1200 mm and 500 mm to avoid interference between each other while utilizing different measurements at the same location.

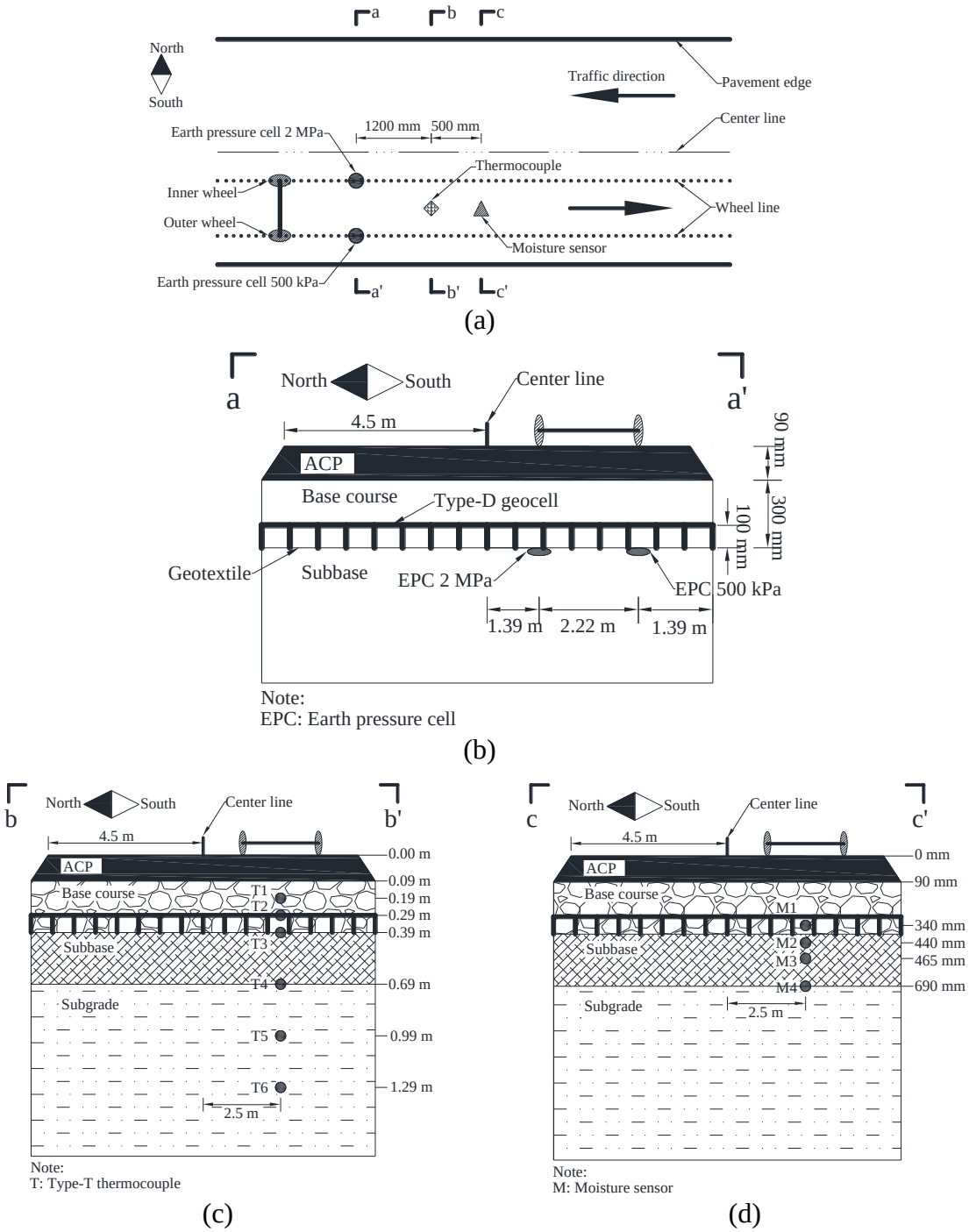

Fig. 5.9. Sketch of sensor location in 4-inch Type-D geocell section of: (a) top view, (b) earth pressure cells, (c) thermocouples and (d) moisture sensors

Fig. 5.9 presents the instrumentation plan for the 4-inch geocell section, where two earth pressure cells with different measurement capacities were placed at the interface of subbases and base courses as shown in Fig. 5.9(b). The larger measurement capacity cell (2 MPa) was installed below the inner wheel path and the smaller capacity one (500 kPa) was installed below the outer wheel path. The two cells were at a distance of 2.22 m, which was equivalent to the common axle width of a trailer in Alberta. Figs. 5.9(c) and 5.9(d) respectively present the layout of six Type-T thermocouples and four EC-5 moisture sensors vertically embedded in base courses and subbases. Two thermocouples were placed in the base courses and the other four in the subbase. One moisture sensor was placed in the base courses while the remaining three moisture sensors were located in the subbase. It is worth pointing out that the temperature and moisture sensors in the subbase were installed by drilling a hole in the subbase while those in the base courses were placed during the construction of the base courses. The vertical positions of the sensors were surveyed in reference to the surface of the subbase so the depths with respect to the asphalt surface could be determined.

Fig. 5.10 shows the plan view of the sensor layout for 6-inch geocell and geocomposite sections. The earth pressure cells and thermocouples in these two sections were arranged in the same manner as those in the 4-inch geocell section (see Figs. 5.9, 5.11, and 5.12). However, the arrangement of moisture sensors was slightly different, with one more moisture sensor placed at the pavement edge in the 6-inch geocell and geocomposite sections than in the 4-inch geocell section.

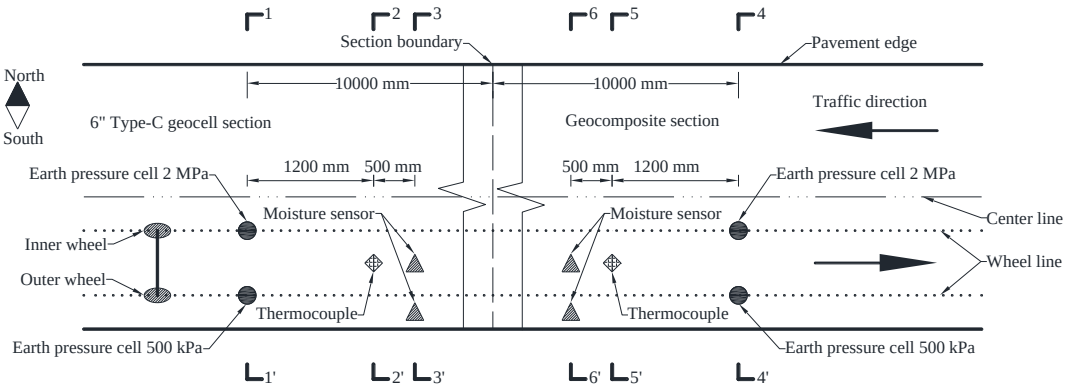

Fig. 5.10. Plan view of sensor arrangement in the Type-C geocell and geocomposite sections

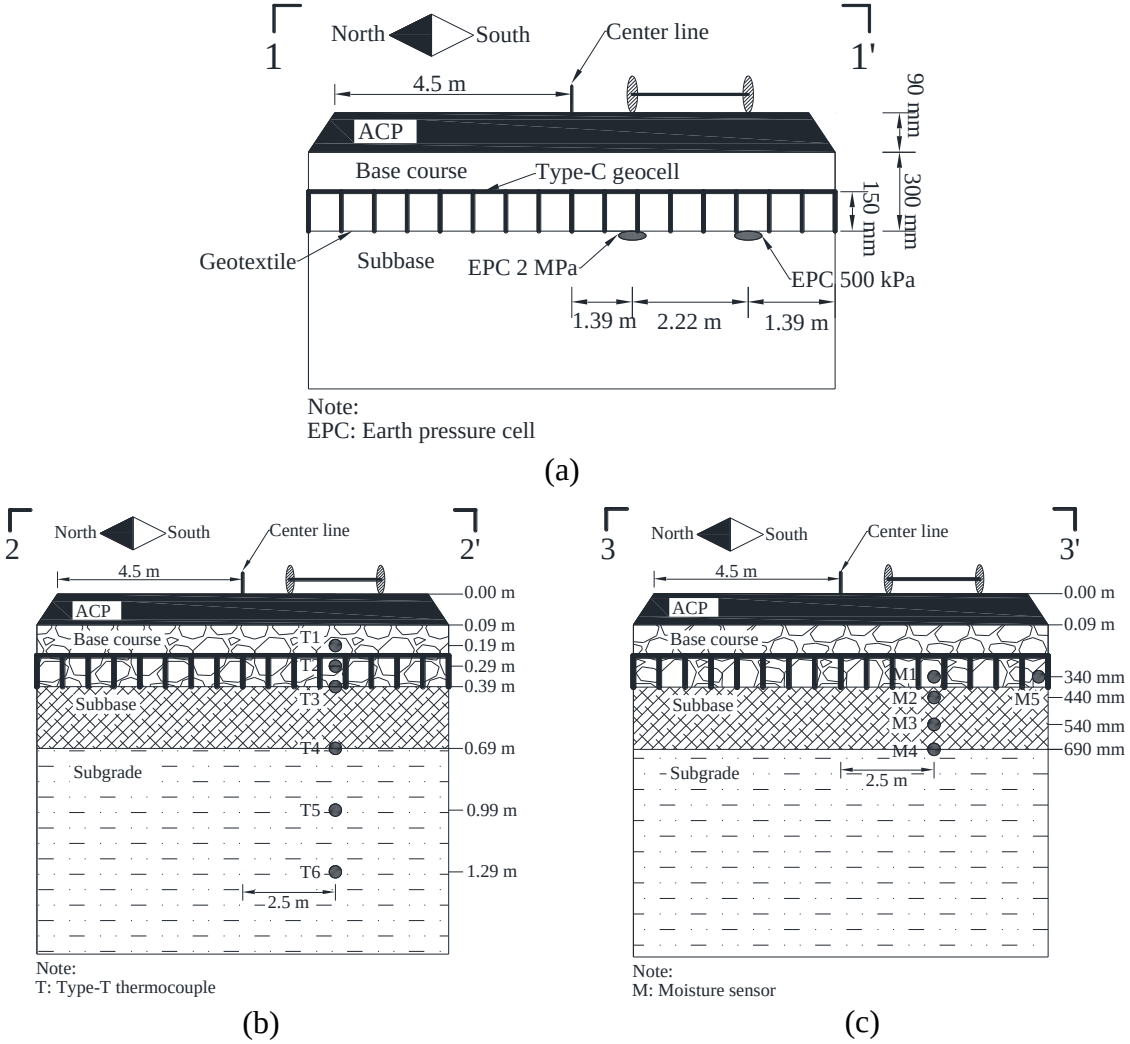

Fig. 5.11. Arrangement of sensors in the 6-inch Type-C geocell section: (a) earth pressure cells, (b) thermocouples, and (c) moisture sensors

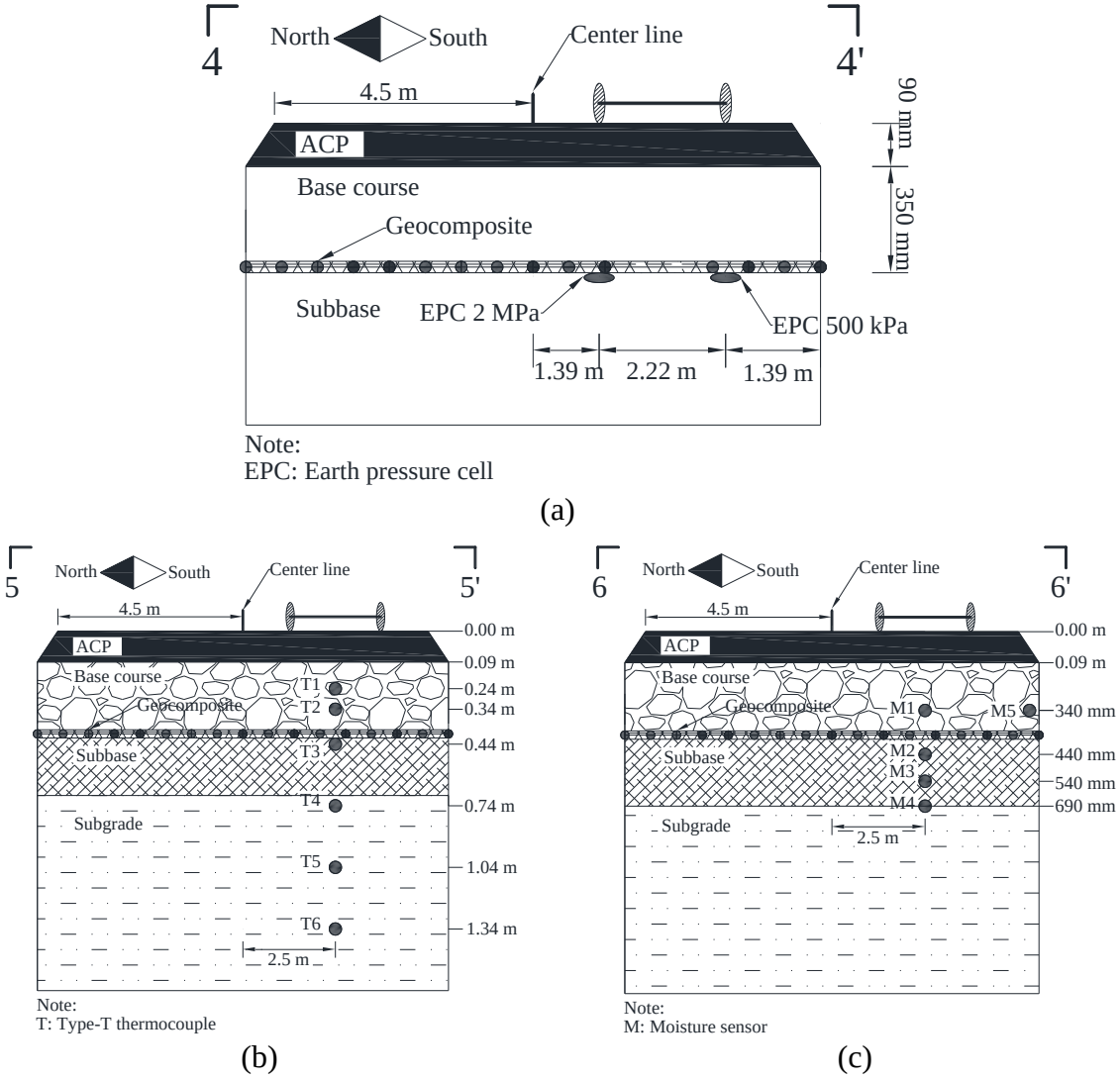

Fig. 5.12. Arrangement of sensors in the geocomposite section: (a) earth pressure cells, (b) thermocouples, and (c) moisture sensors

5.4.2 Installation of earth pressure cells

Earth pressure cells (model LPTPC12-S manufactured by RST Instruments®) used in this project were a strain gauge type of earth pressure transducer with 4-20 mA signal output, with the dimensions of 317 mm in diameter and 10 mm in thickness. The accuracy of the measurement was 0.15% full scale (i.e., 2 MPa and 0.5 MPa) and operating temperature ranged between -29°C and 65°C.

Fig. 5.13 illustrates the installation process for earth pressure cells on the subbase. After construction of the subbase, two cavities (400 diameter × 40 mm depth) and one trench (at least 75 mm depth) were created on the subbase surface to accommodate the cells and the connecting cables. Prior to placing the cells, a 20-mm thick air-dry sand pad was prepared for each cavity with the surface being leveled. During the installation of the cell, the sensitive side of the cell was faced upwards and carefully covered with a 10-mm thickness of the same sand. The sand was compacted to the same density of the subbase. The placement of sand avoided the direct contact of the cells and the gravels in the base course to protect the sensors from damage of sharp gravels. The cables were protected with PVC tubes before being placed in the trench.

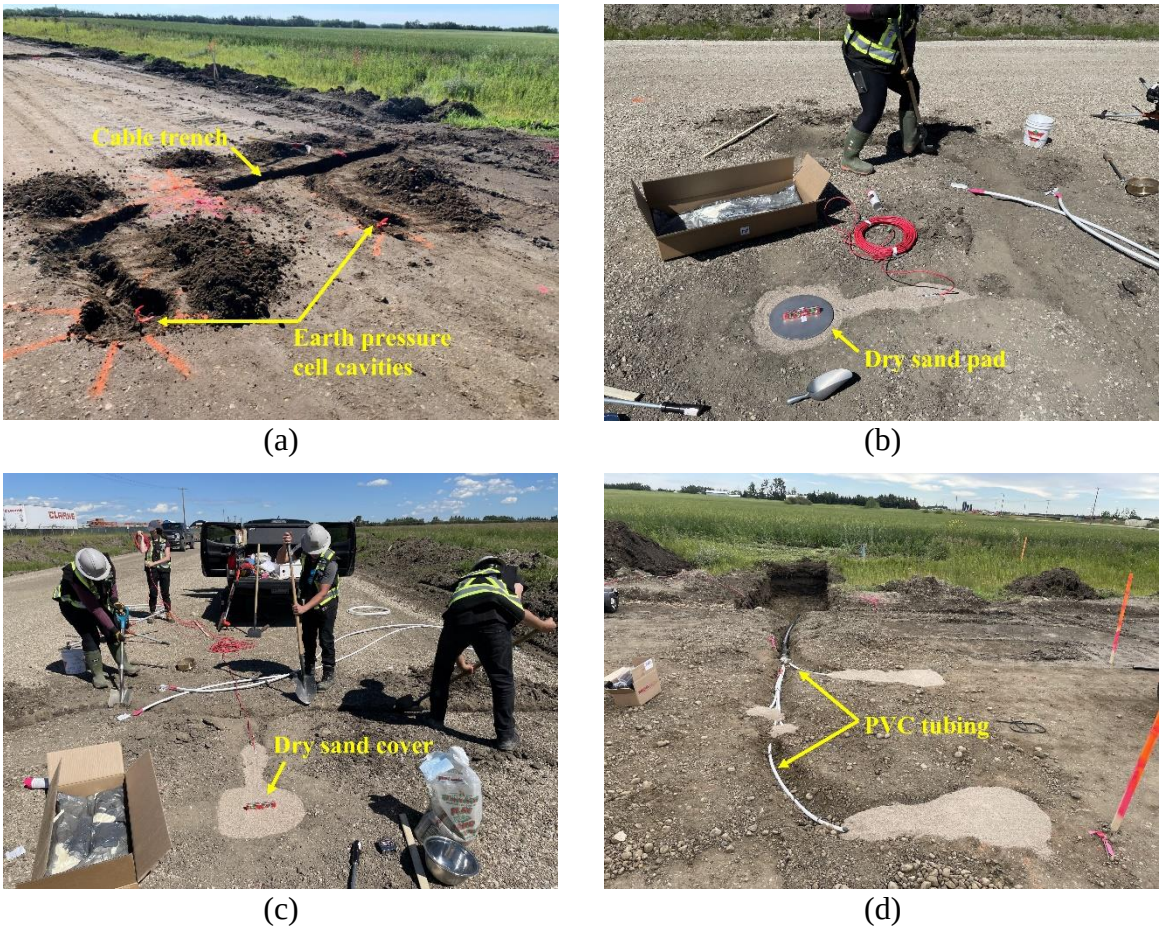

Fig. 5.13. Installation of earth pressure cells: (a) creating cavities and trench, (b) placing sensors, (c) covering sensors with sand, and (d) adding cable protected by PVC

5.4.3 Installation of thermocouples

Type-T thermocouples made by Omega® (blue PVC insulation peel) and Thermo-Kinetics® (brown Teflon insulation peel) were used to measure the temperature changes. There are various types of commercial thermocouples (e.g., Type-K, Type-J, Type-E and Type-N), while Type-T thermocouples are the most accurate among the products with an accuracy of ±1℃ or ±0.75%, whichever is greater. The operating temperature of the Omega® thermocouples was in the range of -20℃ to 100℃ and that of Thermo-Kinetics® thermocouples between -50℃ to 200℃.

Figs. 5.14 and 5.15 show the installation process of thermocouples in the subbase and base courses, respectively. For those in the subbase, four thermocouples were attached to a rigid hollow PVC tube at the spacing of 300 mm. A hole was drilled to a depth of 0.9 m below the subbase surface, in which the PVC tube with thermocouples was inserted and then in-situ soils were filled and compacted. The inside of the PVC tube was also filled up with soils of the subbase to minimize the influence of air on the soil temperature readings as shown in Fig. 5.14(d). For the two thermocouples in the base courses, they were installed in different ways between the geocell sections and the geocomposite section. In the geocell sections, two thermocouples were attached to small PVC pipes tied to the geocell ribs. In the geocomposite section, the same PVC tubes holding the thermocouples in the subbase were used to hold the two thermocouples in the base courses as shown in Fig. 5.15(c). The PVC tubes were used primarily due to the need for protecting thermocouple wires from being damaged during the construction of the base course layer.

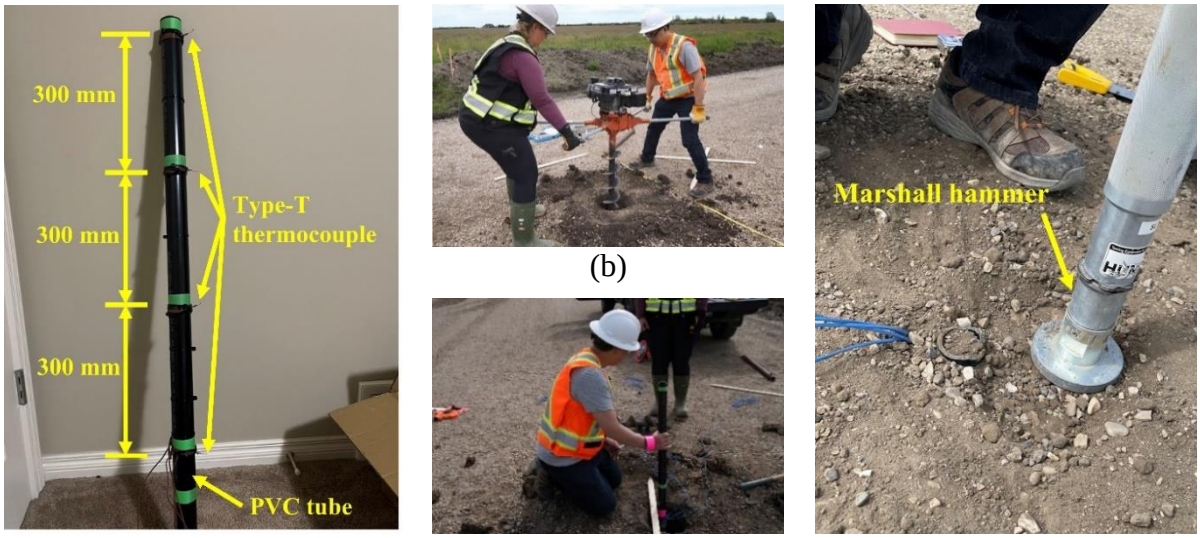

(a) (b) (c) (d)

Fig. 5.14. Installation of thermocouples in the subbase: (a) attaching sensors to PVC tube, (b) augering a borehole, (c) inserting the PVC tube with sensors, and (d) filling the borehole and PVC pipe

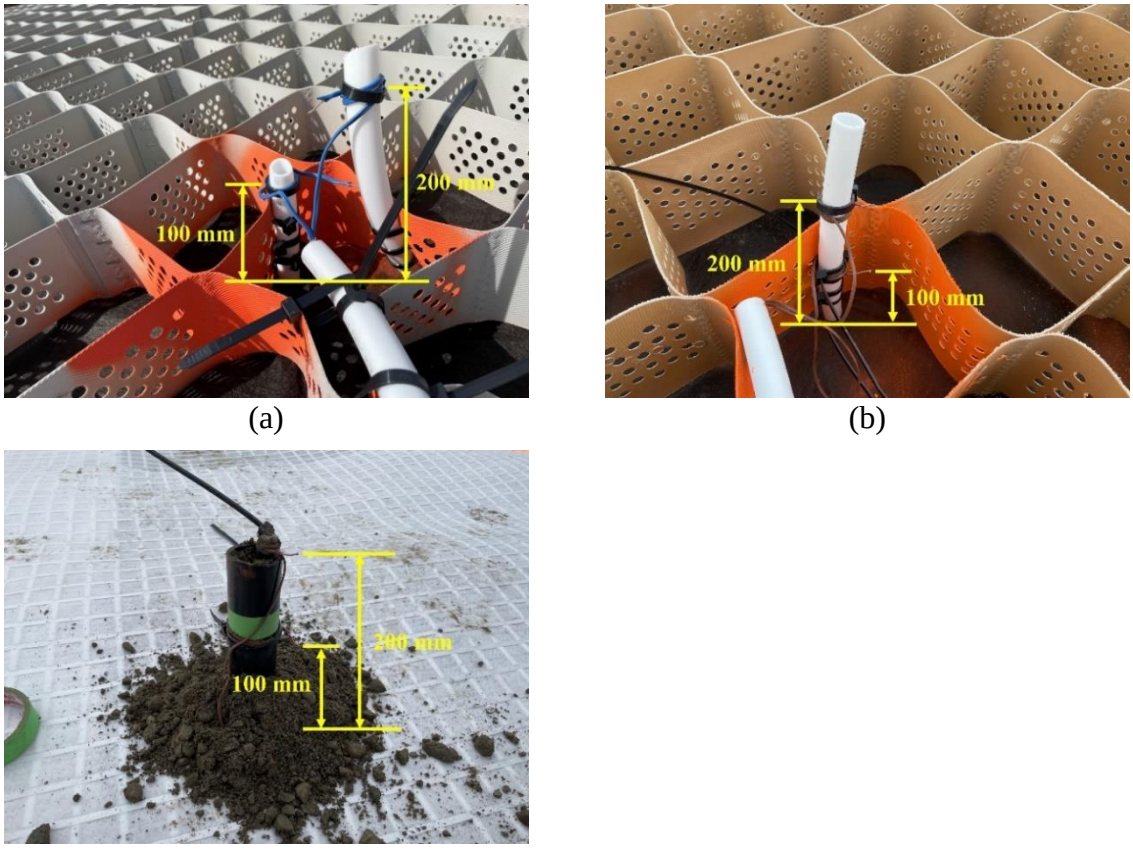

(a) (b) (c)

Fig. 5.15. Installation of thermocouples in the base courses at: (a) 4-inch Type-D geocell, (b) 6-inch Type-C geocell, and (c) geocomposite

5.4.4 Installation of moisture sensors

EC-5 moisture sensors supplied by Meter Group were used to determine the volumetric water content (VWC) in soils by measuring the dielectric constant of soils with outputting voltage signals. The measurement accuracy was ± 0.02 m^3/m^3 in porous medium and ± 0.03 m^3/m^3 in mineral soils, and the operating temperature ranged from -40°C and 60°C.

Figs. 5.16 and 5.17 indicate the moisture sensor installation in the subbase and base courses, respectively. To install the moisture sensors in the subbase, a hole was augered to a depth of 300 mm below the subbase surface, which was then backfilled to the designed depths of moisture sensors. As shown in Fig. 5.16(a), the moisture sensor was laid down horizontally at each depth in the hole and was covered with backfill. After that, the backfill was compacted to the same density of the subbase. The backfill material was taken directly from the subbase material by removing the gravels (i.e., particle size greater than 4.75 mm). After the compaction, soil surface was scratched to eliminate the layered effect and improve the bonding to the next backfill layer. For the instrumentation in the base courses, the backfill used was the base course materials after removing the gravels. In the geocell sections, EC-5 moisture sensor was placed inside the geocell as indicated in Fig. 5.17(a), with the sensor positioned by referring to the cell wall top. In the geocomposite section, the sensor positioning was controlled in reference to a long nail driven into the subbase with a stickup of al least 50 mm above the subbase surface. The backfill was compacted to the same density as the base courses.

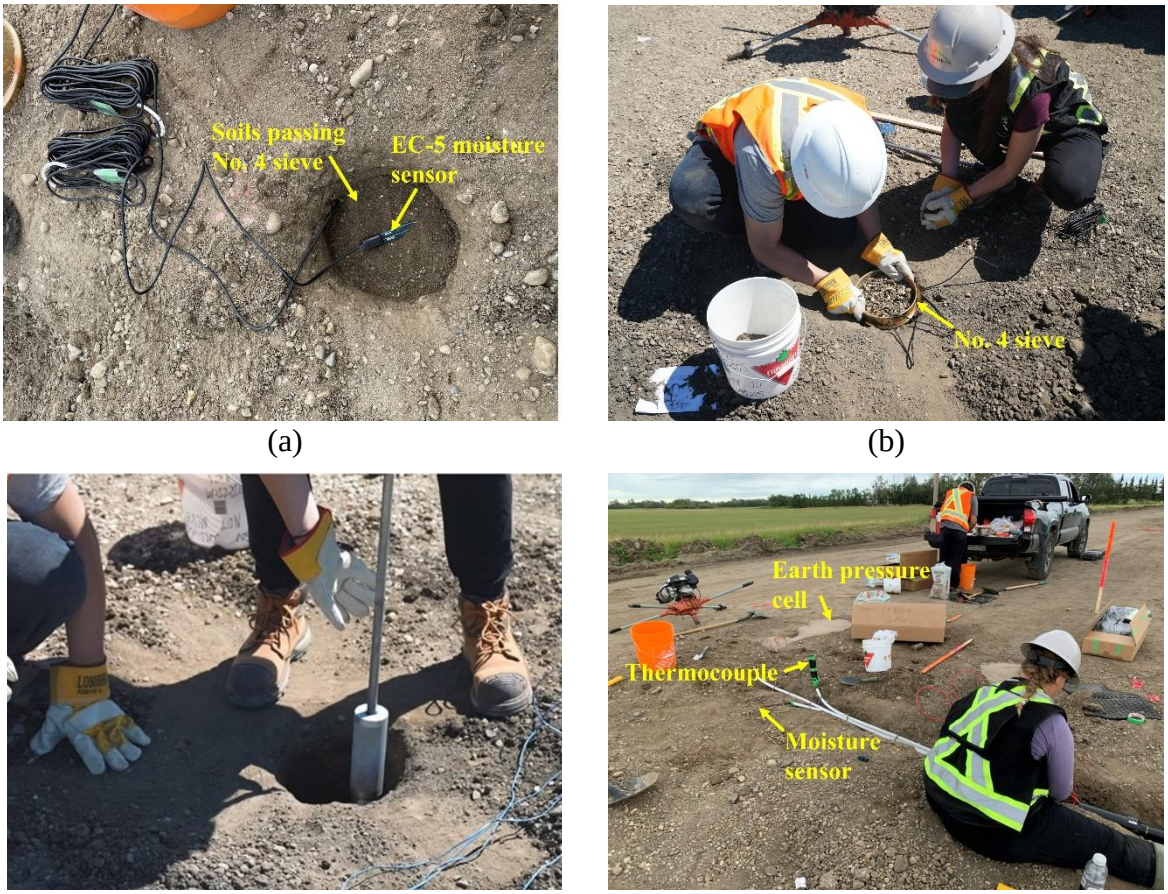

(a) (b)

(c) (d)

Fig. 5.16. Installation of moisture sensors in the subbase at: (a) moisture sensor placement, (b) sieving the backfill, (c) compaction, and (d) cable tubing placement

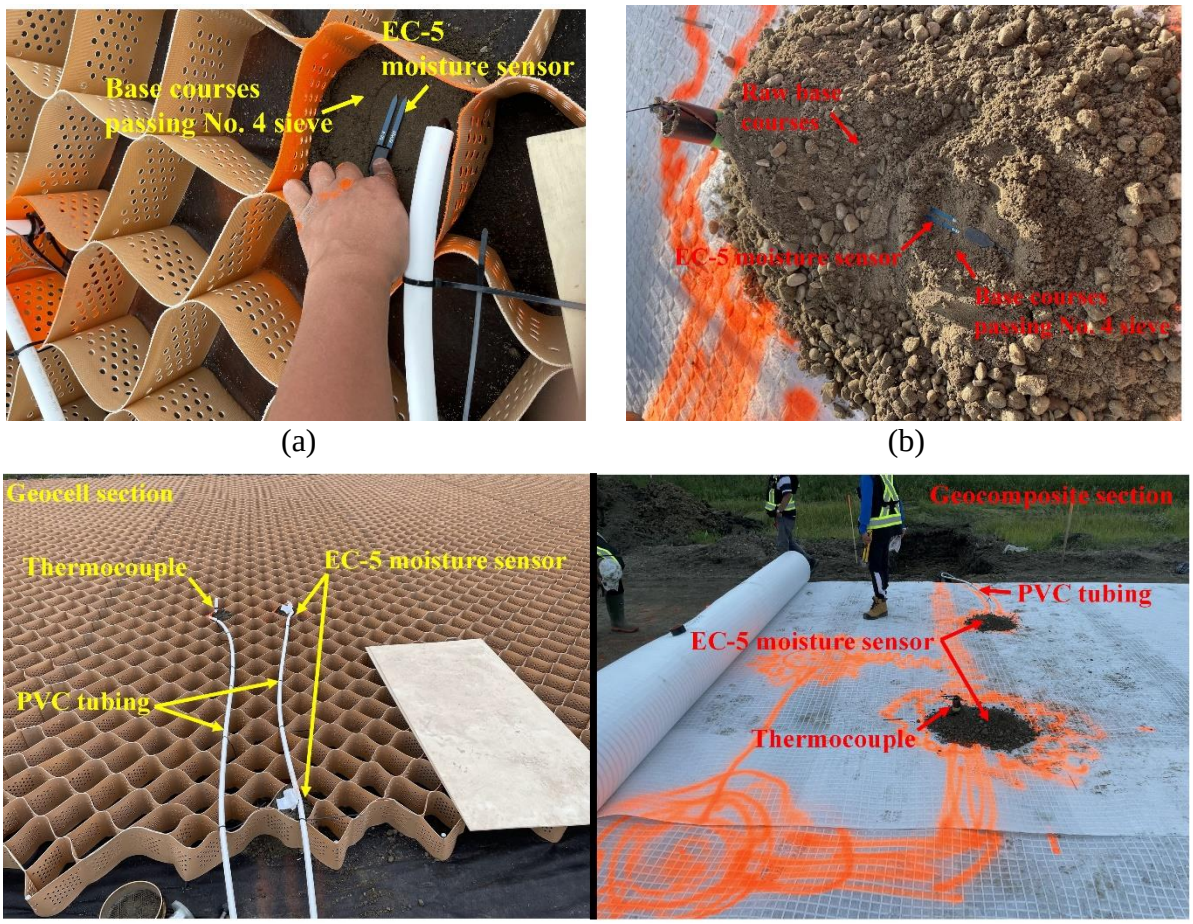

Fig. 5.17. Installation of moisture sensors in the base courses at: (a) geocell sections, (b) geocomposite section, and (c) cable tubing placement

5.4.5 Wire extension and cable access terminal

All the wires and cables were collected at the terminals located beyond the drainage ditches that were excavated after completion of the road construction and instrumentation. As such, the wires and cables should be buried sufficiently deep to avoid the damages from the excavation of the ditches and snow plowing over pavement shoulder during winters. As described in Fig. 5.8(b) in Section 5.4.1, a data acquisition system was set up near the boundary between the 6-inch geocell and geocomposite sections. The original cables of thermocouples and moisture sensors were not long enough to reach the datalogger location; therefore, wire extension was needed. This section introduces the extension of sensor cables and the installation of cable access terminal.

5.4.5.1 Wire extension

Thermocouple wire extension

A Type-T thermocouple was made of two conductors containing copper (reddish brown) and copper-nickel alloy (white), respectively. The wire extension should consist of the same metal-based conductors, and the waterproof and electrically insulated measurements were also needed at splicing points. Fig. 5.18 illustrates the process for performing the wire extension.

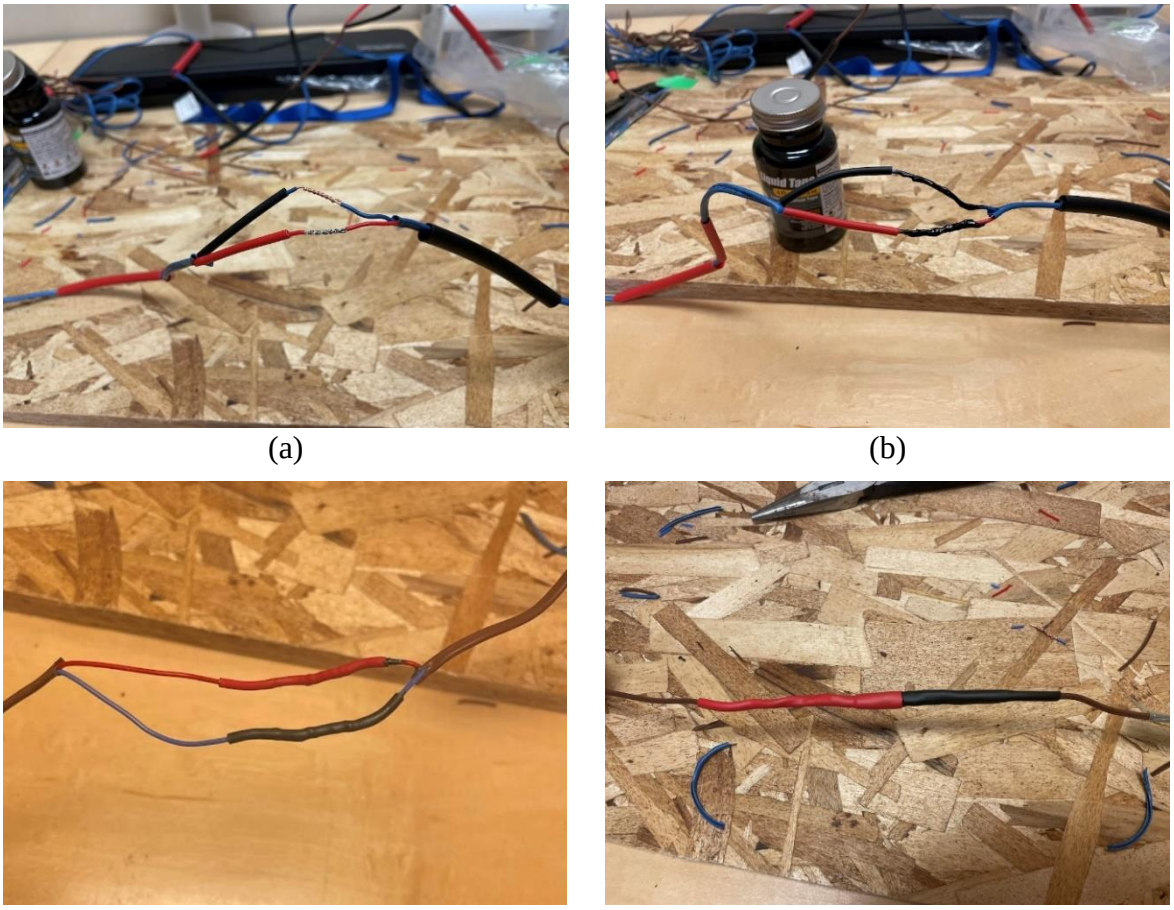

(a) (b)

(c) (d)

Fig. 5.18. Wire extension of thermocouples: (a) lead splicing, (b) liquid electrical tape cover, (c) shrinking tube protection of leads, and (d) shrinking tube protection of cable

The conductors were spliced tightly, and the bare splicing wires were covered with *Gardner Bender*® liquid electrical tape, which could serve as the waterproof and electrical insulation coating under the operating temperature of -34℃ to 93℃. When the liquid tape was hardened after one-

night curing, heat-shrinking tubes were applied as an insulation cover for both the conductors and the wires. This would make the splicing points durable under the attack of mechanical abrasion, water infiltration, and electrical circuit. The heat-shrinking tubes was composed of polyolefin with the operating temperature from -55℃ to 135℃.

EC-5 moisture sensor wire extension

Cable connector for an EC-5 moisture sensor was the 3.5-mm stereo plug, which called for commercial 3.5-mm male to female audio cables as the wire extension. The plug connection was ruled out due to its susceptibility to damage or disconnection during construction. Instead, the extended wires were spliced with the original wires in the same way as the connection for the thermocouple wire extension. Similarly, the same conductors between the extended and original wires were used when the material for the extension was selected. As shown in Fig. 5.19, an EC-5 sensor cable comprised three conductors: ground line (bare lead), data transducer line (orange) and power supply line (brown). The same lines should be joined between the extension and the original cables. The corresponding extended wire was 7.62 m (25 ft) and 30.48 m (100 ft) long for the 6-inch geocell and geocomposite sections, respectively. Calibrations of voltage outputs and volumetric moisture content were conducted after the installation of extended wires. Details can be found in section 5.6.4.2.

Fig. 5.20 presents the photographs of wiring the extension of EC-5 moisture sensors. Like the thermocouple extension, the splicing points were covered with the liquid electrical tape, further coated with the shrinking tubes for both the conductors and the wires.

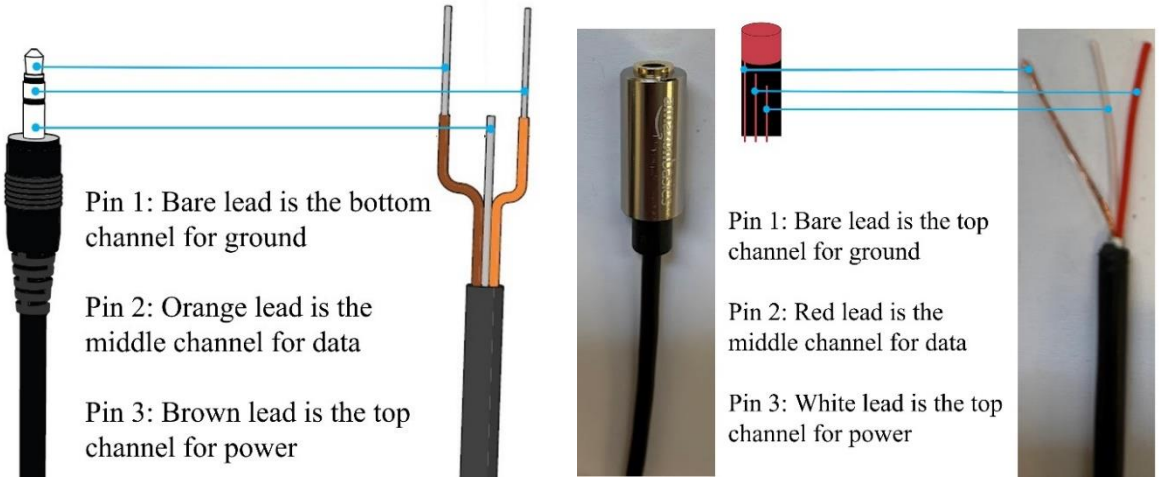

(a) (b)

Fig. 5.19. Diagram of wire connection between (a) EC-5 original cable and (b) extension cable

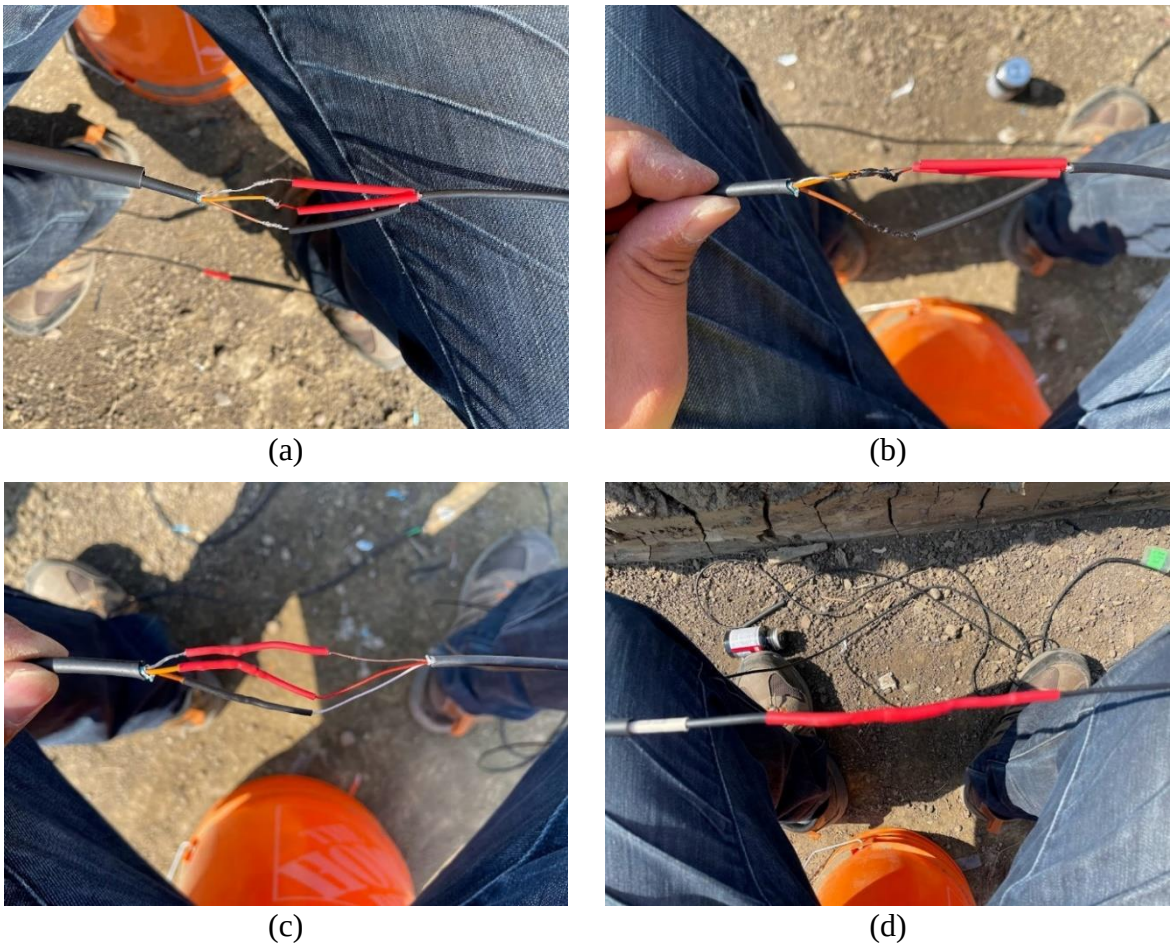

(a) (b)

(c) (d)

Fig. 5.20. Connection of wire extension: (a) lead splicing, (b) liquid electrical tape cover, (c) shrinking tube protection of leads, and (d) shrinking tube protection of cable

5.4.5.2 Cable access terminal

Two cable access terminals were established with one for the 4-inch geocell section while the other for the 6-inch geocell and geocomposite sections. Fig. 5.21 shows the installation of the cable access terminal for the 4-inch geocell section. A trench was excavated to a depth of about 0.5 m below the ditch bottom, spanning from the pavement edge to the ditch outside slope. Sensor cables, protected by PVC tubes, were buried in the trench, with the ends terminated at a three-way terminal tower, which could be accessed through the three openings. Silicone sealants were added to seal the connection between the terminal tower and the PVC tubes from water infiltration, and the three openings were sealed with the screw caps.

(a) (b)

Fig. 5.21. The cable access terminal for the 4-inch geocell section: (a) trench excavation and (b) terminal tower installation

The long-term monitoring for the seasonal frost impacts is implemented only for the 6-inch geocell and geocomposite sections. To facilitate the data collection, a data acquisition and wireless communication system was set up near the joints of these two sections. To avoid the negative impact of water, the system was located at a distance of 7 m from the edge of the pavement, slightly beyond the far end side of the ditch. To enable the cable to reach the data acquisition system, a

trench was dug to a depth of 0.5 m below the ditch bottom where the wire extension embedded in the PVC tubes was laid down, as shown in Fig. 5.22.

Fig. 5.22. Trench excavation for connecting cables in 6-inch geocell and geocomposite sections

In 6-inch geocell and geocomposite sections, access boxes were installed to house the splicing points before the sensor cables were connected to the data acquisition system. Fig. 5.23 shows some photographs of the installation of the access boxes on site. About 1 m long of each cable was kept inside the access boxes at these splicing joints and placed [Fig. 5.23(a)], for some contingent considerations: e.g. reducing the stress concentration of the cable, and supplying cables in case of any damage at this weak spot. After that, these boxes were capped and sealed with electrical tapes for waterproof purpose, as shown in Fig. 5.23(b). The boxes were then buried at the depth of 20 to 30 cm below the pavement surface. Their locations were surveyed for the future

positioning use after the pavement construction was finished. A layer of sand was added to surround the boxes to direct any accumulated water away from the boxes. Flexible electrical pipes, instead of the rigid PVC tubes, were used as the cable conduit between the access boxes and the data acquisition unit because the flexible pipes were easier for installation to span the 25-m distance.

(a) (b)

Fig. 5.23. Access boxes: (a) extra cables and (b) box closure

Unlike the typical above-grade setup, the data acquisition system was buried in ground to protect it from damages of wild animals or theft. Fig. 5.24 presents the system housed in a plastic box, which sat on a rigid steel plate and was tied by four steel chains welded to the steel plate. Seven holes were made in the outer wall of the plastic box to allow for the connection with the electrical pipes. A wooden box was added to enclose the plastic box for protection. The box was placed in a pit with 1000 mm length × 500 mm width × 400 mm depth, and then backfilled with soils.

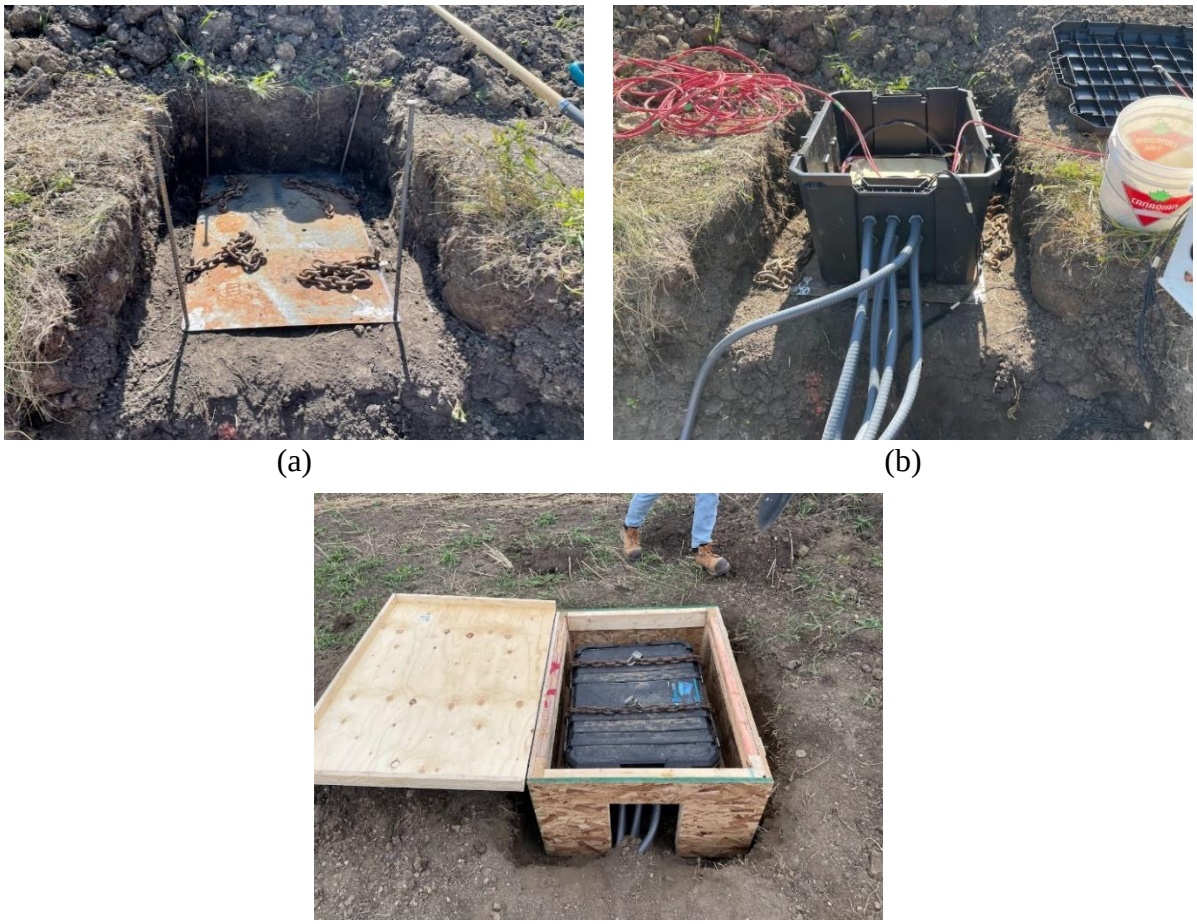

(a) (b)

(c)

Fig. 5.24. The installation of the data logger box: (a) steel plate base, (b) plastic box and (c) wood box

5.4.6 Weather station and data acquisition system setup

5.4.6.1 Weather station

A weather station was mounted on a pole, approximately 0.8 m away from the data acquisition system. The data acquisition system was a wireless system including a datalogger and a cellular unit that were placed inside the plastic box as well as the power supply unit (i.e., solar panel) and an antenna that were mounted on the pole along with the weather sensors.

Fig. 5.25 presents the installation process of the weather station. A 2-7/8 inch diameter helical screw pile was drilled to a toe depth of 3.3 m (10 ft). A square pile cap with the width of 203 mm (8 inches) was screwed and welded to the pile head. Another identical cap was welded to one end

of the steel pole. The two cap plates were then welded as shown in Fig. 5.25(b). The pole was a 4 m long galvanized hollow steel section with the outside and inside diameter of 48 mm and 41 mm, respectively (1.500 schedule 40 size). Figs. 5.25(c) and 5.25(d) present the photograph and sketch of each component installed on the pole. Weather sensors, comprising a TE525M tipping rain gauge and a Type 109 temperature probe, were mounted on the pole along with a 41303-5A solar radiation shield and an antenna. The height of the sensors and parts on the pole [Fig. 5.25(d)] was determined with the consideration of external forces of wind, rainfall, and snow cover. The measurement accuracy of the rain gauge and temperature probe is ±1% at rate of 25 mm/h and ± 0.2°C, respectively. Their corresponding operating temperatures are 0°C to 50°C and -50°C to 70°C, respectively. The solar panel was faced to south with an inclination angle of 53º (the latitude of Edmonton) to maximize the solar harvest and the snow removal according to a local study by Northern Alberta Institute of Technology (Matthews and Sandercock, 2016). The cables for the weather sensors, solar panel, and antenna were also protected by electrical pipes, which were buried in ground and connected to the data acquisition system.

(a)

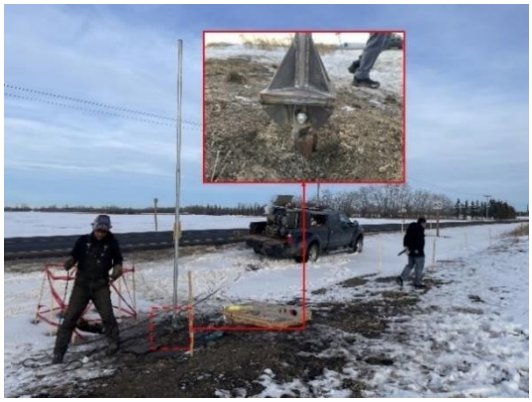

(b)

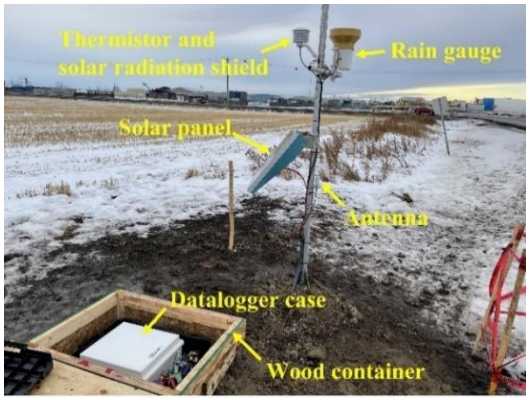

(c)

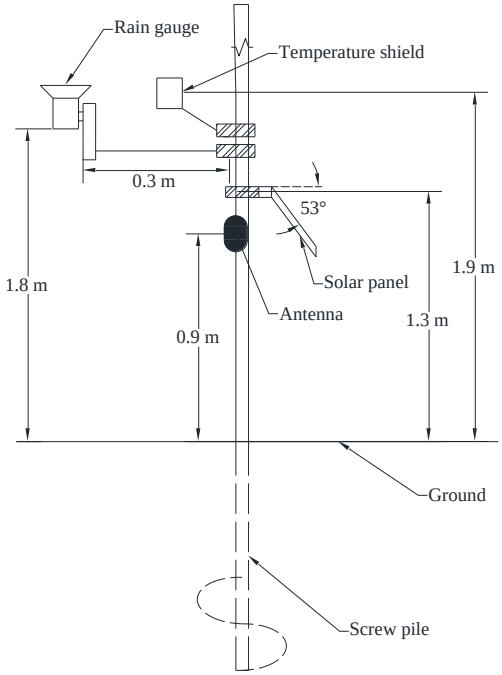

(d)

Fig. 5.25. Weather station installation of: (a) helical screw pile, (b) steel pole, (c) weather station photograph and (d) sketch

5.4.6.2 Data acquisition system

Fig. 5.26 illustrates the data acquisition system housed in a white fiber glass box, placed inside the plastic box. All soil sensors and weather sensors were connected to the CR1000X data logger and AM 16/32B multiplexer. The maximum sampling rate of the CR1000X datalogger is 100 Hz. The antenna was connected to the CELL205 cellular modem to achieve the remote communication. A custom-made computer program PC400 was used to read and download data remotely, as shown in Fig. 5.26(b).

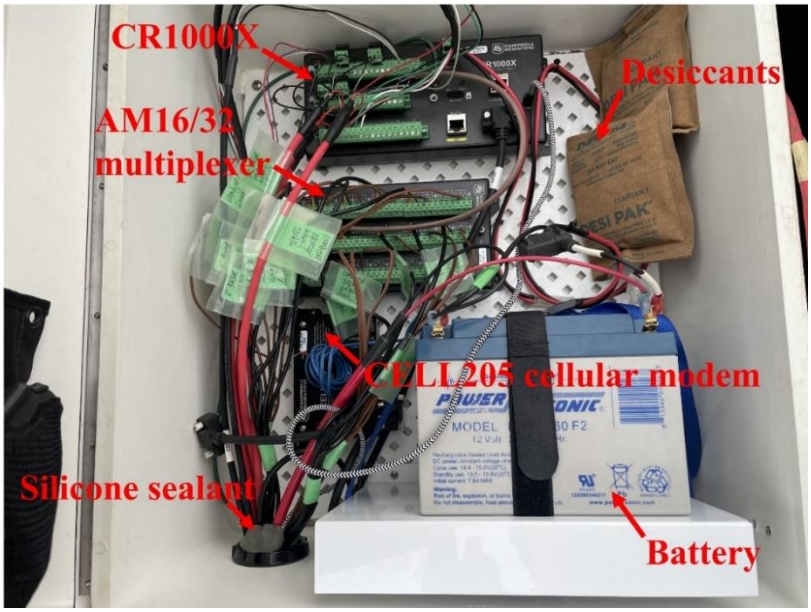

(a)

RecNum	51784742	TP4149_kPa	5.63	EC_5_mV(15)	NAN	TC_T(14)	NAN
TimeStamp	18 14:40:29	EC_5_mV(1)	559.34	EC_5_mV(16)	NAN	TC_T(15)	6.79
PTemp	7.70	EC_5_mV(2)	575.61	TC_T(1)	-0.21	TC_T(16)	NAN
Batt_V	13.66	EC_5_mV(3)	555.43	TC_T(2)	2.50	Rain_mm	0.00
Press_Cell_V(1	457.24	EC_5_mV(4)	568.41	TC_T(3)	5.43	T_Air	12.76
Press_Cell_V(2	444.83	EC_5_mV(5)	617.72	TC_T(4)	6.35		
Press_Cell_V(3	414.57	EC_5_mV(6)	NAN	TC_T(5)	8.80		
Press_Cell_V(4	408.60	EC_5_mV(7)	652.88	TC_T(6)	10.29		
Press_Cell_mA	4.57	EC_5_mV(8)	681.78	TC_T(7)	NAN		
Press_Cell_mA	4.45	EC_5_mV(9)	677.92	TC_T(8)	-0.45		
Press_Cell_mA	4.15	EC_5_mV(10)	657.36	TC_T(9)	1.75		
Press_Cell_mA	4.09	EC_5_mV(11)	693.39	TC_T(10)	4.33		
TP4144_kPa	9.41	EC_5_mV(12)	NAN	TC_T(11)	5.76		
TP4145_kPa	5.10	EC_5_mV(13)	NAN	TC_T(12)	8.29		
TP4148_kPa	12.39	EC_5_mV(14)	NAN	TC_T(13)	10.88		

(b)

Fig. 5.26. Data acquisition system: (a) data logger modules and (b) PC400 software panel

5.5 Testing methodology

Testing in this project mainly involve short-term tests and long-term monitoring. The short-term tests include: (1) dynamic cone penetration (DCP) tests on compacted layers of subbases and base courses, (2) static plate loading tests and (3) trafficking tests on the finished surface for three test sections. The DCP test provides a measure of in-situ resistance of a material to penetration and the results can be correlated to CBR. The static plate loading tests and trafficking tests can be used to measure response of the road section to loading, thus, reflecting the effectiveness of geosynthetic stabilization.

The long-term monitoring includes recording the variations of temperatures and water contents in the road sections during the seasonal freeze-thaw cycles and earth pressure at the subbase-base interface induced by the real traffic. These data would help quantifying the beneficial effect brought by geocell stabilization.

This section covers both short-term tests and long-term monitoring, but more focus was put on the procedures of the short-term tests.

5.5.1 Dynamic cone penetration tests

DCP tests were performed according to the standard ASTM D6951 right after the compaction of subbase or base courses. The tests were performed near the sensor locations in each test section. Based on the DCP results, CBR values for the subbase and base courses could be correlated. Figs. 5.27(a) and 5.27(b) are the photographs of DCP tests performed on the subbase and base courses, respectively.

(a) (b)

Fig. 5.27. Dynamic cone penetration at: (a) subbase and (b) base course

5.5.2 Static plate loading tests

Three types of static plate loading tests with various numbers of loading cycles and maximum applied pressures were conducted in each geosynthetic-stabilized section to investigate their mechanical behaviors under static loading. The first type of plate loading tests was performed in accordance with ASTM D1195/1195M-21, in which two loading cycles with the maximum applied pressure of 500 kPa and 420 kPa at the 1st and 2nd cycle, were imposed respectively. The second type of plate loading tests followed an incremental loading procedure (Huang et al., 2023; Pokharel et al., 2010): specifically, the load was increased in increments of 10 kPa, 200 kPa, 400 kPa, 800 kPa and 900 kPa, followed by the decrements of 450 kPa, 225 kPa and 10 kPa. The third type of plate loading tests is documented in PRS report and McCartney et al. (2010). It was conducted under 10 loading cycles with increments of 10 kPa, 250 kPa and 552 kPa and decrements of 125 kPa and 10 kPa at each cycle.

Figs. 5.28(a) and 5.28(b) presents the schematic view and photograph of the setup of the plate loading tests. The test system was HUMBOLDT HD-4601 plate bearing tester, which could exert a maximum load of 200 kN over a 300-mm loading plate. The loading plate was located exactly over the 2 MPa earth pressure cell. The plate was not in direct contact with the asphalt surface but

rested on a thin layer of sand in between. The addition of sand layer was to create a leveled loading surface and avoid damage to the existing asphalt surface. The load was provided by a hydraulic jack sitting on the center of the loading plate and restrained by a truck bottom frame, which served as the reaction beam. The jack was connected to a hydraulic pump with high-pressure hose. A Dwyer® DPG-111 digital pressure gauge was mounted on the pump to measure the applied pressure. Three mechanical dial gauges were placed on the loading plate with the angular spacing of 120º to obtain accurate measurement of the displacement. Preloading of 10 kPa was applied for 30 seconds prior to each plate loading tests. While preloading, the vertical movement was recorded. After that, the tests commenced by applying the predetermined incremental plate loads. At each increment of loads, the load was maintained until the displacement rate was less than 0.03 mm/min for three minutes before the next loading step was applied. At each incremental loading stage, the applied pressure and displacement were recorded, and the readings of the earth pressure cell were also taken with the sampling rate of 50 Hz at the same time. The capacity of digital pressure gauge and mechanical dial gauge was 34.5 MPa (5000 psi) and 25 mm, respectively. The corresponding accuracy was 0.25% of the full-scale value and 0.01 mm.

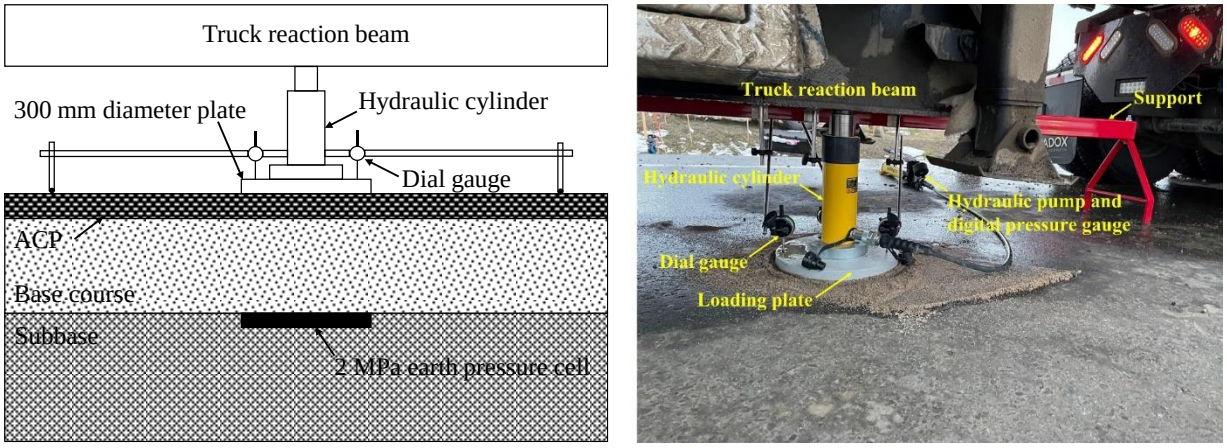

(a) (b)

Fig. 5.28. Setup of plate loading tests: (a) schematic and (b) photograph

5.5.3 Trafficking tests

After the completion of the plate loading tests at each section, trafficking tests were conducted to investigate the dynamic responses of geosynthetic-stabilized pavement under traffic loading (Timm and Priest, 2004; White et al., 2010). A 40-ton trailer with eight axles ran two passes in a forward-backward direction for each section, as shown in Fig. 5.29. The trailer wheels were set to pass over the locations of two earth pressure cells. As described previously, the axle width was approximately equal to the distance of the two earth pressure cells, and therefore, each earth pressure cell was able to measure the pressure induced by the wheel passing over. The forward and backward speeds were controlled at 5 km/h and 2 to 3 km/h, respectively. During the trafficking tests, the datalogger (Campbell Scientific® CR1000X) for the earth pressure cells acquired the data at a sampling rate of 100 Hz to produce the time-history of stress over the subbase.

Fig. 5.29. Photograph of trafficking test on site

5.6 Results and discussions

The results from the field tests including short-term tests such as DCP tests, plate loading tests, and trafficking tests before freeze; and the long-term monitoring of soil temperature and water content changes from December 2022 to April 2023.

The DCP tests were performed on subbases and base courses in summer 2022. The plate loading tests and trafficking tests were conducted on 3rd and 4th November 2022 when the air temperatures were -9℃ to -5℃ and -9℃ to 4℃, respectively. Before performing the plate loading tests, the soil temperatures in 6-inch geocell and geocomposite sections were measured at the sunrise on November 3, 2022. The soil temperature profiles along depth are shown in Fig. 5.30. The temperatures at any depth were above 2℃ and they increased with depth. This indicates that soils were still unfrozen in ground while the field tests were performed at air temperatures below 0℃.

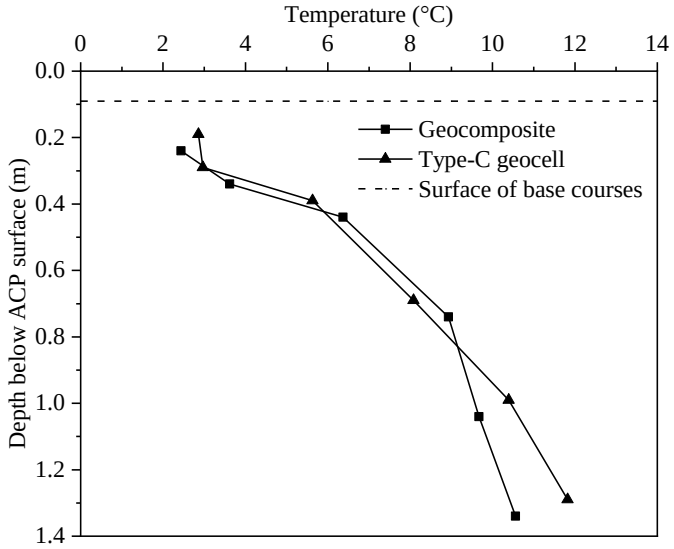

Fig. 5.30. Temperature profiles at 6" geocell and geocomposite sections

5.6.1 Dynamic cone penetration tests

After the compaction of base courses and subbases, dynamic cone penetration (DCP) tests were conducted near the sensor location. CBR values were then estimated based on the correlation with the DCP results, as derived from the Equations (5-1) - (5-3).

For all soils except for CL soils with CBR<10 and CH soils

$$CBR = \frac{292}{DCP^{1.12}},\ \text{DCP in mm/blow} \quad (5\text{-}1)$$

For CL soils with CBR<10

$$CBR = \frac{1}{(0.017019 \times DCP)^2}, \text{ DCP in mm/blow} \quad (5\text{-}2)$$

For CH soils

$$CBR = \frac{1}{0.002871 \times DCP}, \text{ DCP in mm/blow} \quad (5\text{-}3)$$

The CBR results could be further correlated to resilient modulus. Table 5.4 synthetizes such empirically correlative equations. In this study, AASHTO MEPDG method was adopted for its application in wide ranges of soil types. The parameters for each geosynthetics-stabilized section are listed in Table 5.5. The equivalent resilient modulus of each soil layers is tabulated in Table 5.6.

Table 5.4. Relation between CBR and resilient modulus, Mr (MPa)

References	Resilient modulus, MPa	Note
Heukelom and Klomp, 1962 & Giroud and Han, 2004a	M_r=10.35*CBR	Fine-grained subbase with CBR<10
Green and Hall, 1975	M_r=37.29*CBR$^{0.711}$	Base, subbase and subbase materials
AASHTO, 1993 & Giroud and Han, 2004a	M_r=36*CBR$^{0.3}$	Granular base/subbase course materials
AASHTO MEPDG	M_r=17.62*CBR$^{0.64}$	A wide range of soil types

Table 5.5. Parameters of road test sections

Layer materials	Layer No.	Layer thickness (mm)	Resilient modulus (MPa)		
			Type-D geocell	Type-C geocell	Geocomposite
Base course	1	50	184.4	146.9	156.9
	2	50	261.1	164.0	173.2
	3	50	287.1	183.4	178.7
	4	50	277.6	152.6	169.4
	5	50	256.0 [a]	138.2	167.2
	6	50	216.4	141.3	159.5
	7	50	-	-	175.1 [b]
Subbase	8	50	101.2	79.0	103.1
	9	50	135.3	129.8	186.2
	10	50	115.5	235.6	246.8
	11	50	93.3	297.7	270.7
	12	50	89.8	284.1	264.2
	13	50	99.2	229.9	288.7

[a] Shadow represents the soil layers reinforced by geocells.
[b] Dash line represents the location of geosynthetics.

Table 5.6. Equivalent resilient modulus of each layer

Layer materials	Layer thickness (mm)	Resilient modulus (MPa)		
		Geocomposite	Type-C geocell	Type-C geocell
Base course	300 or 350[a]	168.2	153.0	241.3
Subbase	300	199.6	167.4	103.7

[a] Thickness of base course is 300 mm in Type-D and Type-C geocell sections and 350 mm in geocomposite section.

5.6.2 Static plate loading tests

As introduced in Section 5.5, three types of static plate loading tests were conducted: 1) standard tests with two loading cycles; 2) monotonic tests with one loading cycle, and 3) cyclic tests with 10 cycles. The results of static plate loading tests are characterized with curves of the applied pressure and displacement.

5.6.2.1 Standard tests with two loading cycles

Fig. 5.31 presents the results of standard tests with two loading cycles on the three test sections. From the pressure-displacement curves, the strain modulus for the first and second cycles (i.e., E_{v1} and E_{v2}) was determined, taken as the secant between the points of $0.3\sigma_{0max}$ and $0.7\sigma_{0max}$ (σ_{0max} was the maximum stress at each cycle). In practice, E_{v2} is a more common indicator of the road stiffness because the influence of plastic deformation is reduced after the 1st loading cycle. Another useful parameter is the stiffness ratio (E_{v2}/E_{v1}) that can be linked to the soil degree of compaction, with a higher ratio representing a lower compaction degree. According to the European Commission, this ratio is recommended to be no greater than 2.2 to 2.5. Fig. 5.31(d) shows the load transfer ratio, a ratio of the applied pressure at the loading surface to the measured stress by the earth pressure cell at the base-subbase interface. It is apparent that the geocomposite section had the higher load transfer ratio than the Type-C geocell section, and the Type-D geocell section had the lowest ratio. This was attributed to the modulus difference between base courses and subbases. The modulus ratio between bases and subbases was 0.79, 0.81, and 2.06 for the geocomposite, Type-C geocell, and Type-D geocell test sections, respectively. The lower base-subbase modulus ratio would cause more load transferred to the subbase and vice versa. This explains why a higher load transfer ratio, but a lower ratio was found in the geocomposite section and the Type-D geocell section, respectively. Applying a theory for calculating stress distribution in a three-layer elastic medium (Poulos and Davis, 1974), the load transfer ratio was calculated to be 15.5%, 18.4%, and 10.9% for the geocomposite, Type-C geocell, and Type-D geocell sections, respectively. These values are close to the measured (15.5%, 14.5%, and 12.2%), except for the Type C geocell section. The exact reason for this discrepancy remains to be further investigated; the authors suscept the DCP might not fully represent the confinement effect provided by the

geocell considering the small diameter of DCP cone could only mobilize a limited region of soil radially (e.g., within 5 times cone diameter). For a 20 mm diameter cone, the radial influencing zone of soil was less than 100 mm, which is less the geocell opening of 330 mm.

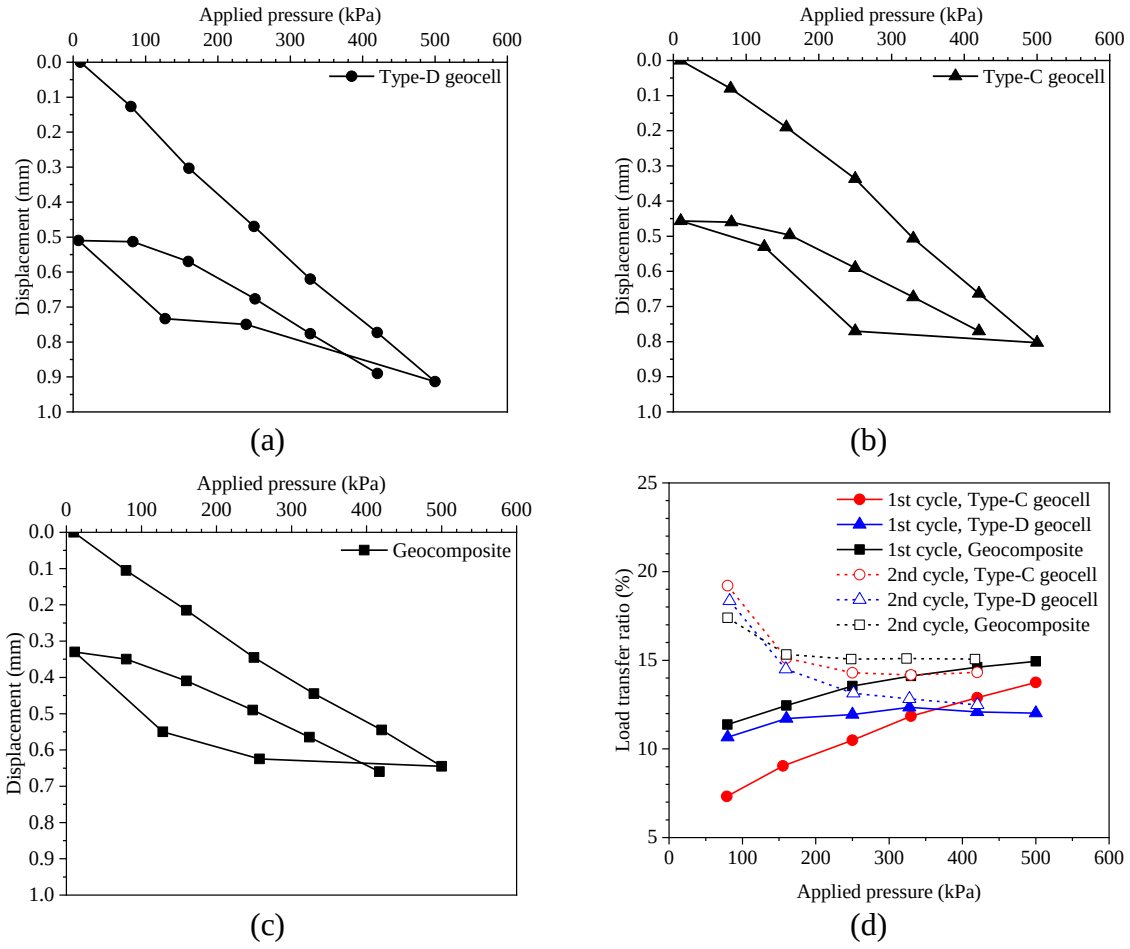

Fig. 5.31. Results of standard tests with two loading cycles: (a) 4-inch Type-D geocell section, (b) 6-inch Type-C geocell section, (c) geocomposite section, and (d) load transfer ratio

Fig. 5.32 shows the stiffness ratio (E_{v2}/E_{v1}) and E_{v2} at three types of geosynthetic-stabilized sections. The 6-inch Type-C geocell-stabilized section exhibited the highest stiffness ratio, indicating the lowest level of compaction among three test sections. This seemed to correlate well with the relative difference of the estimated resilient modulus (M_r) of the base courses among the three test sections. In contrast, the geocomposite section had the lowest stiffness ratio among the

three test sections, which did not correlate with the relative difference of M_r. The possible reason was that the resilient modulus was measured right after the base courses were compacted; however, the stiffness ratio was determined after the asphalt layer was completed. As shown in Fig. 5.33, the asphalt surface of the geocomposite section was completed before that of 6-inch Type-C geocell section. When compacting the asphalt layer of the 6-inch Type-C geocell section, the roller would cross the joint line and enter the neighboring geocomposite section, which resulted in the over compaction of the geocomposite section near the joint. This over-compacted area covered the spot that was approximately 2 m from the border and where the sensors were located, and the plate loading tests were performed.

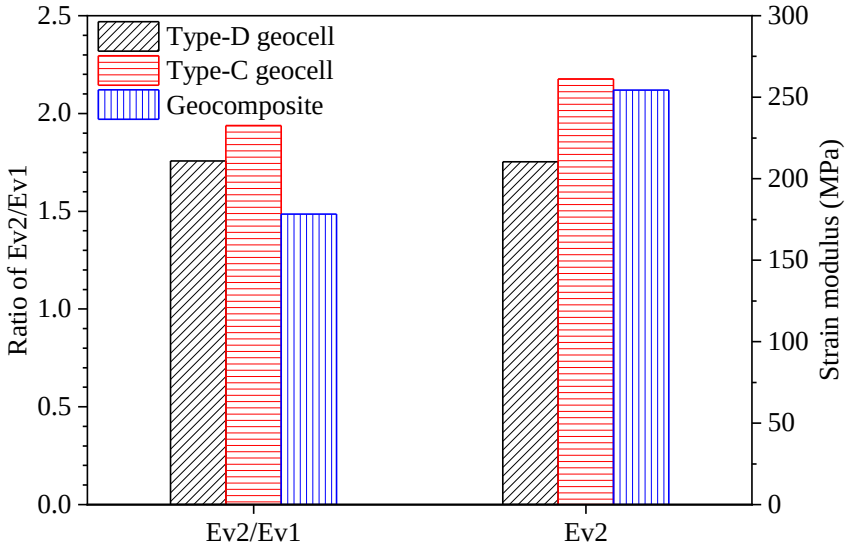

Fig. 5.32. The calculated strain modulus

Fig. 5.33. Photograph of the location of earth pressure cells in geocomposite section

Fig. 5.32 also presents the modulus for the second loading cycle (Ev2). This parameter is an equivalent modulus of the pavement section within the load influencing depth. Although it had the lowest compaction, the Type-C geocell section showed the highest modulus among the three test sections. In comparison, the Type-D geocell section had the lowest modulus. The likely cause was that geocell confinement provided additional stiffness in the base courses, rendering the overall stiffness equal or slightly greater than the geocomposite section that had a thicker base course. The lower modulus for the Type-D geocell might result from the weaker subbases than the other sections as indicated in Table 5.6.

5.6.2.2 Monotonic loading tests with one cycle

Figs. 5.34(a) to 5.34(c) displays the results of monotonic plate loading tests on the three test sections, representing the plate movement against applied load. The distributed stress over the subbase was measured by the earth pressure cells at each loading stage. This result along with the applied pressure on the asphalt surface is given in Fig. 5.34(d).

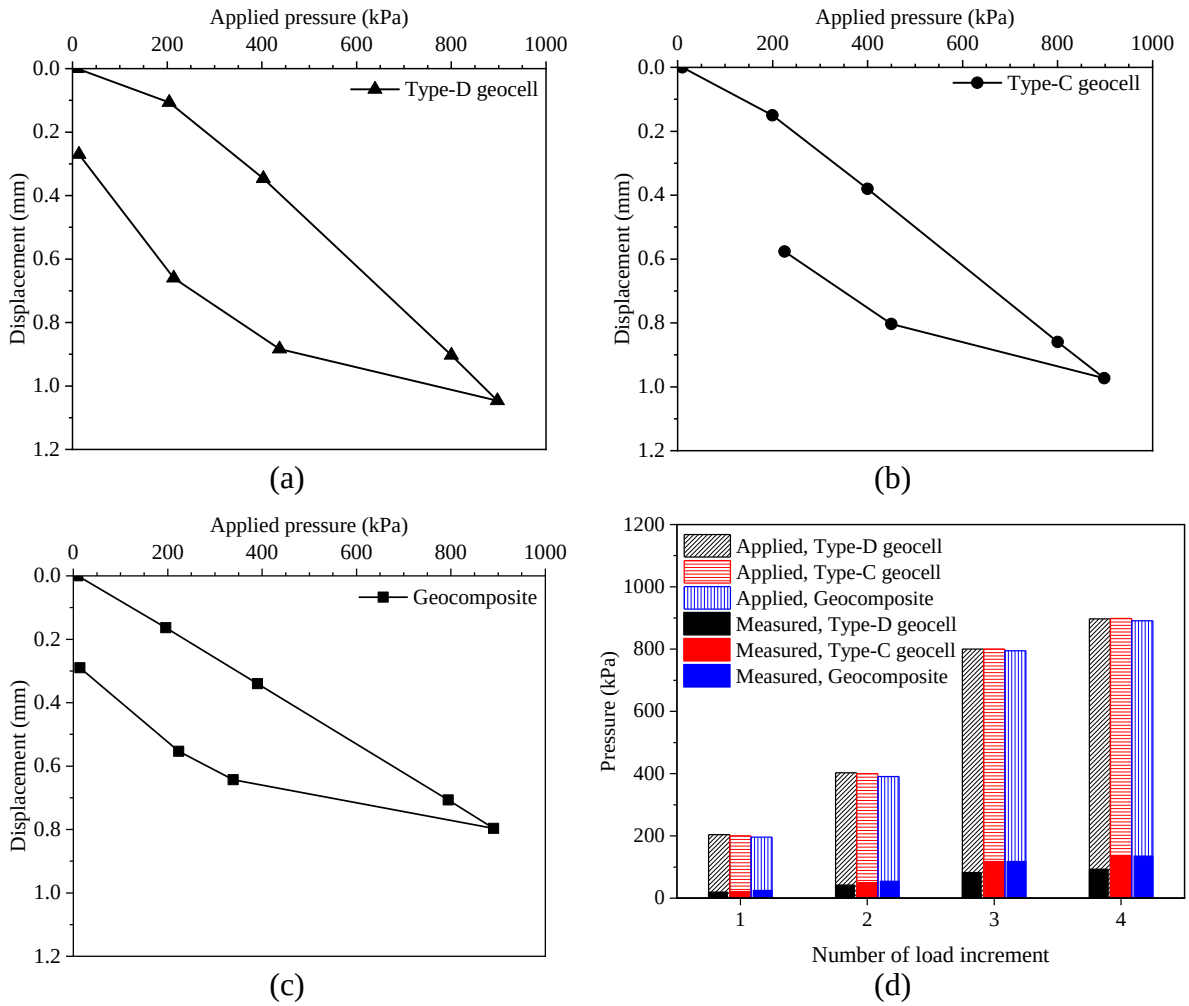

Fig. 5.34. Load-settlement curves: (a) 4-inch Type-D geocell section, (b) 6-inch Type-C geocell section, (c) geocomposite section, and (d) measured pressure at the base-subbase interface

Fig. 5.34(d) indicates a small percentage of load transferred to the subbases. To normalize the effect of base course thickness and to quantify and estimate the effectiveness of geosynthetics-stabilized base courses in distributing applied pressure over subbases, an equivalent stress distribution angle, θ, was defined for multiple layers, as illustrated in Fig. 5.35(a). For a multi-layer section, the distribution angle can vary from layer to layer-e.g., θ_1 in ACP and θ_2 in base course, due to differing modulus of the layers (see Table 5.6). The equivalent value is adopted for the ease of comparison between different test sections, which is determined in Equations (5-4).

$$tan\theta = \frac{b}{2h}\left(\sqrt{\frac{p_0}{p_1}} - 1\right) \quad (5\text{-}4)$$

Where, θ is the equivalent stress distribution angle, º.

b is the diameter of the loading plate, mm.

h is the depth between the pavement surface and the subbase surface, mm.

p_0 is the applied pressure by the loading plate, kPa.

p_1 is the measured stress by the earth pressure cell, kPa.

Fig. 5.35(b) presents the calculated equivalent distribution angle for the three test sections. As the applied load increased, the value of θ decreased slightly and then stabilized for the Type-D geocell section but that for the Type-C geocell and geocomposite sections decreased more markedly and did not stabilize. As the applied load increased, the deeper soils were engaged to resist the load. The decrease in θ for Type-C geocell and geocomposite sections demonstrated a stiffer deep soil in the subbases engaged in these sections. This agreed with the modulus profile in Table 5.5. Fig. 5.35(b) also shows the relative difference of θ between the test sections, which in the increasing order was geocomposite section, Type-C geocell section, and Type-D geocell section. This result was consistent to the relative difference of load transfer ratio as discussed previously.

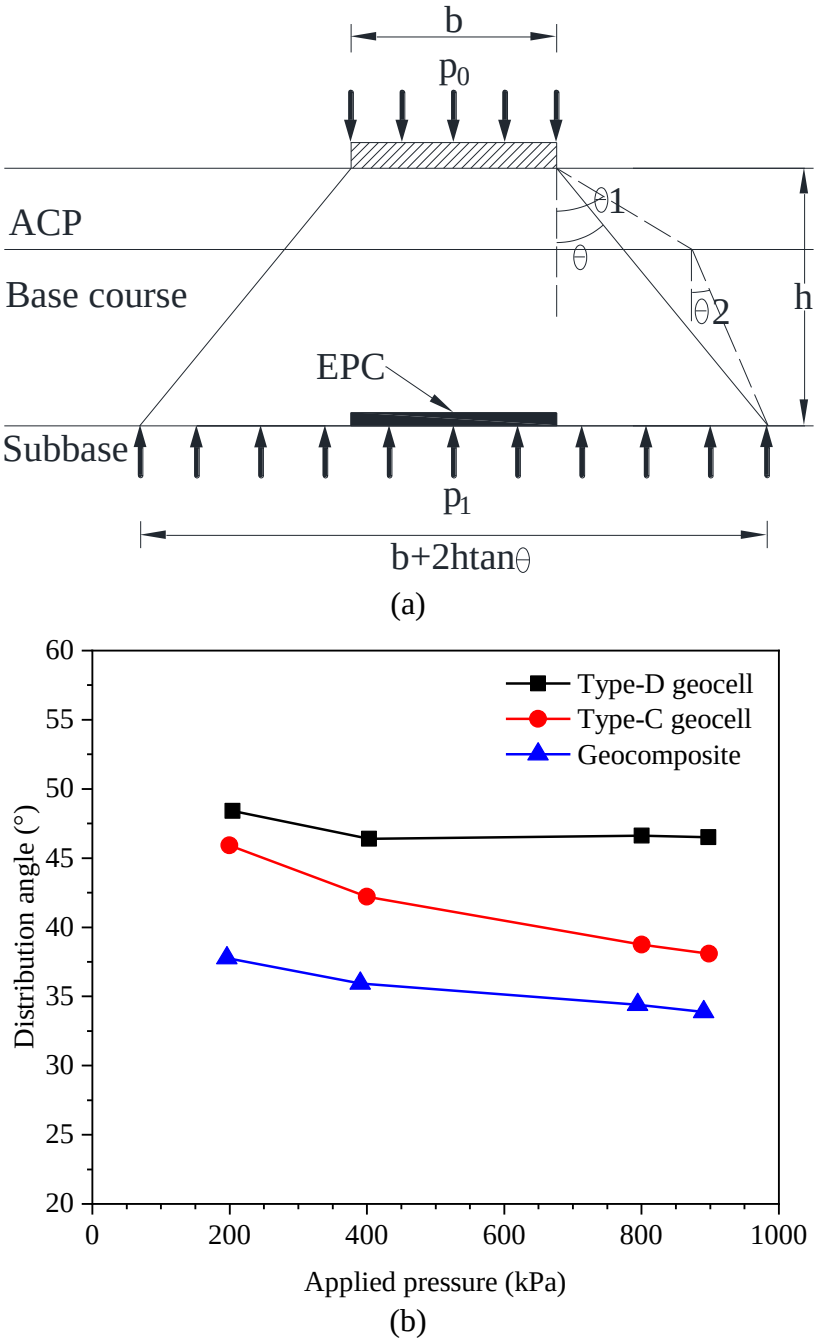

Fig. 5.35. Equivalent distribution angle: (a) definition and (b) results

5.6.2.3 Cyclic loading tests with 10 cycles

The applied pressure-displacement curves of cyclic tests with 10 loading cycles of the three test sections are presented in Figs. 5.36(a) to 5.36(c), respectively. At each loading cycle, the earth pressure at the base-subbase interface was measured. Fig. 5.37 shows the load transfer ratio and

distribution angles. In general, the geocomposite section underwent less movement than the other two geocell sections (Fig. 5.36). This result was comparable with the one-cycle loading test (Fig. 5.34) but different with the two-cycle loading test (Fig. 5.31). The load transfer to the base-subbase interface in general was comparable to the one-cycle loading test (Fig. 5.34) and the two-cycle loading (Fig. 5.31).

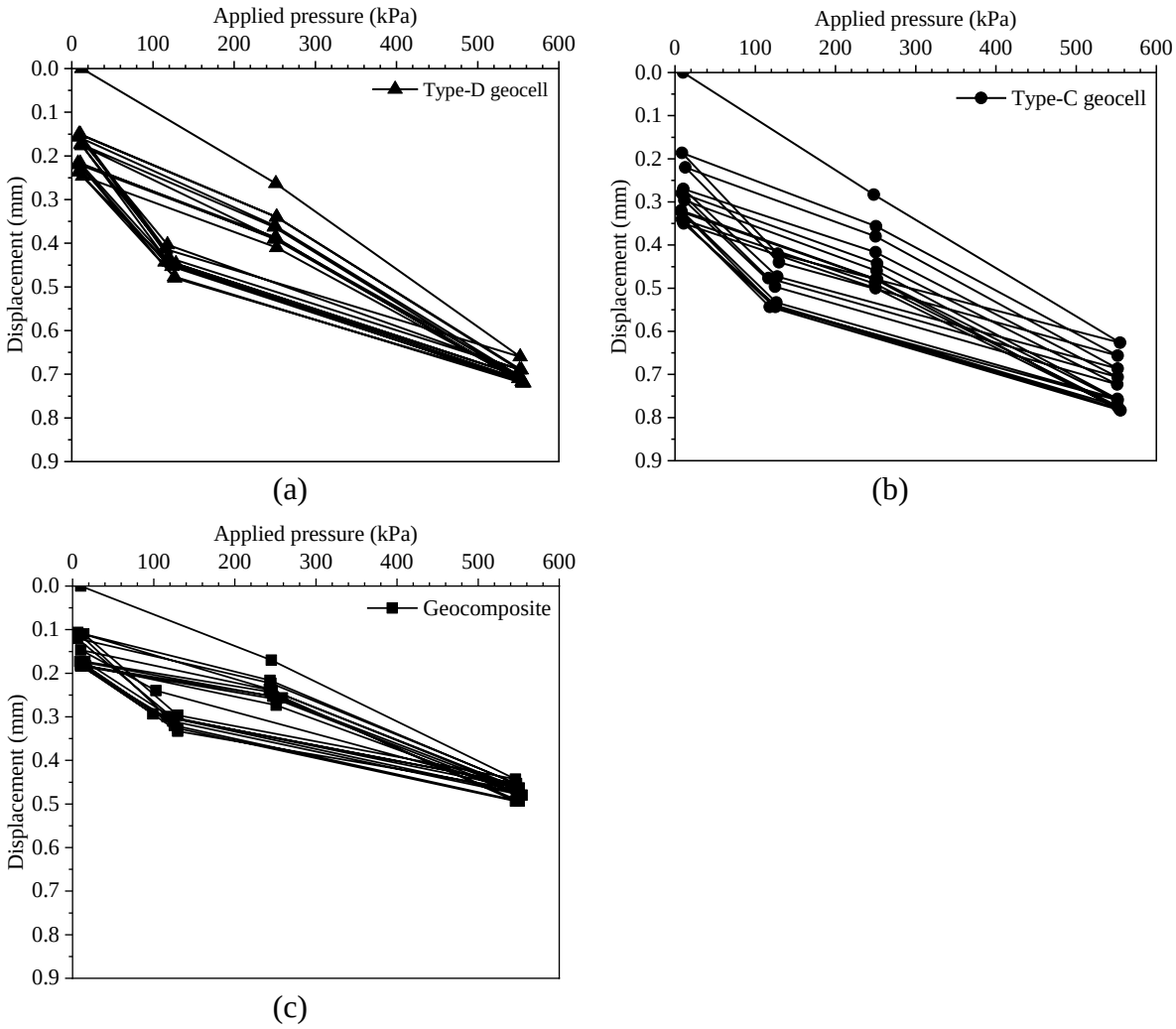

Fig. 5.36. Load-settlement curves based on the ten-cycle loading tests: (a) 4-inch Type-D geocell section, (b) 6-inch Type-C geocell section, and (c) geocomposite section

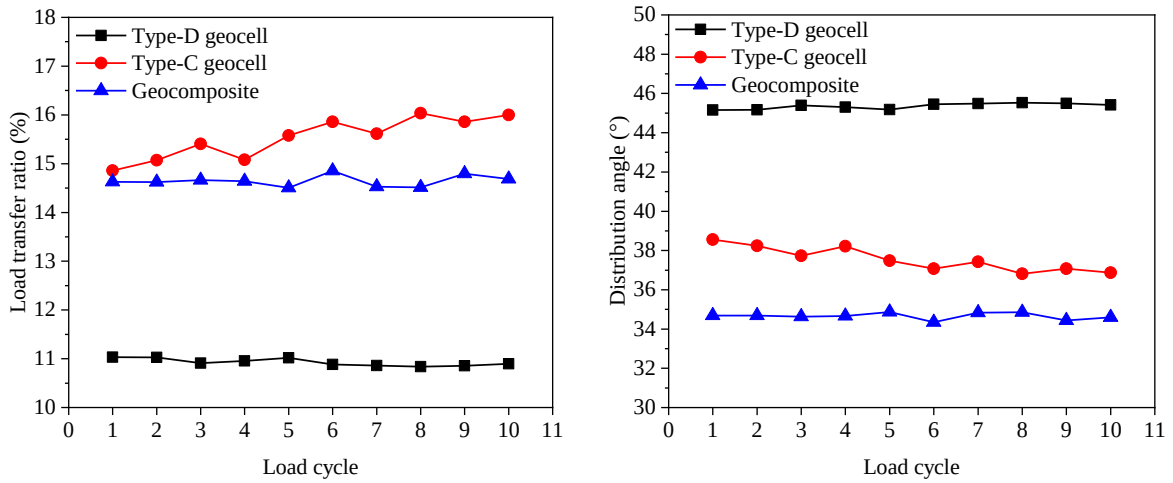

Fig. 5.37. Results of 10-cycle loading test: (a) load transfer ratio and (b) distribution angle

From Fig. 5.37, the peak displacement and plastic displacement were also calculated. The plastic displacement is equivalent to the residual settlement after unloading. Fig. 5.38 compares the peak displacement and plastic displacement at each loading cycle. The figure indicates that the cumulative peak and plastic displacements increased with the loading cycles. The increasing rate was most remarkable in the Type-C geocell section than in the other sections. The geocomposite section experienced the least deformation while the Type-C the greatest deformation.

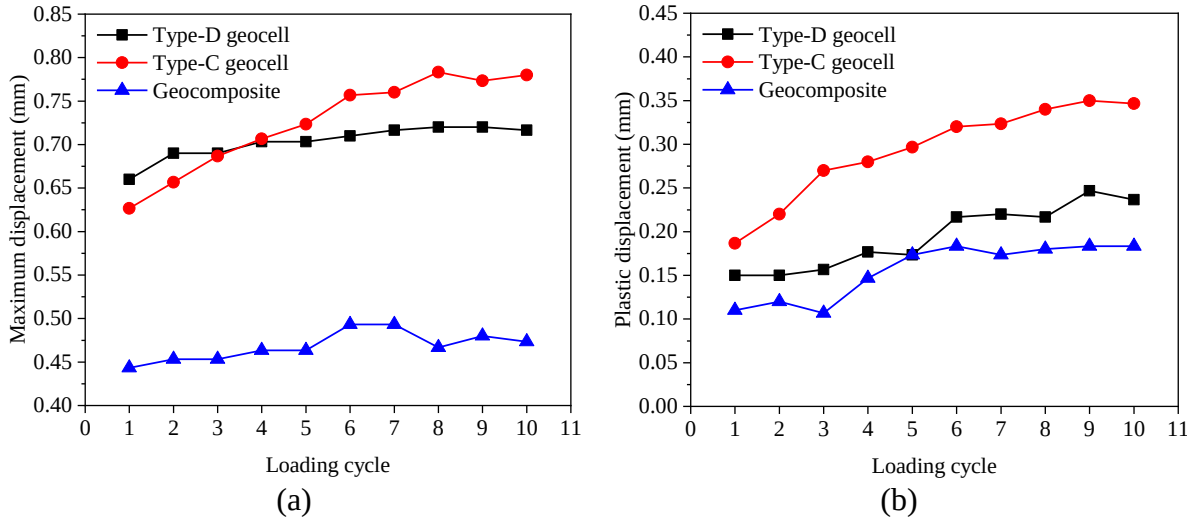

Fig. 5.38. Displacement measured from the 10-cycle loading tests: (a) maximum displacement and (b) plastic displacement

5.6.3 Trafficking tests

Fig. 5.39 presents the measured vertical stress as the wheels of the trailer passed over the asphalt surface where the earth pressure cells were located. The peak values were registered as the eight axles passed over the locations of the earth pressure cells. The forward pass that was run at a higher speed (5 km/h) resulted in higher earth pressure readings than the backward pass running at a lower speed (2-3 km/h). For both passes, the 4th to 8th wheels produced relatively stable readings of the earth pressures. The magnitude of the earth pressure (i.e., 50-60 kPa) was comparable to the earth pressure (50-70 kPa) measured during the two-cycle and 10-cycle plate loading tests where the maximum applied pressure was 500 kPa.

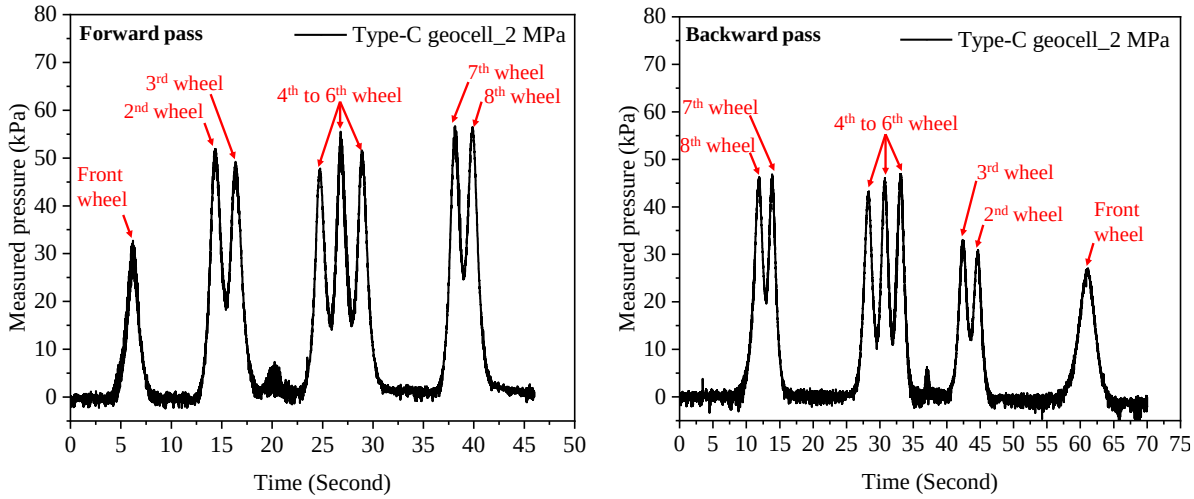

Fig. 5.39. Typical time-history response of trafficking tests: (a) forward pass and (b) backward pass

Figs. 5.40 to 5.43 show the trafficking response of the three test sections recorded by 2 MPa and 500 kPa earth pressure cells at 1st forward, 1st backward, 2nd forward and 2nd backward pass, respectively. In general, the load transfer ratio from the trafficking tests was more agreeable with that of the two-cycle plate loading test-i.e., the geocomposite section had the largest load transfer ratio while the 4-inch Type-D geocell section the lowest load transfer ratio. It is worth pointing

out that although the exact value of the load transfer ratio could not be determined, the relative comparison is possible as the tire pressure exerted on the pavement was the same between the three test sections.

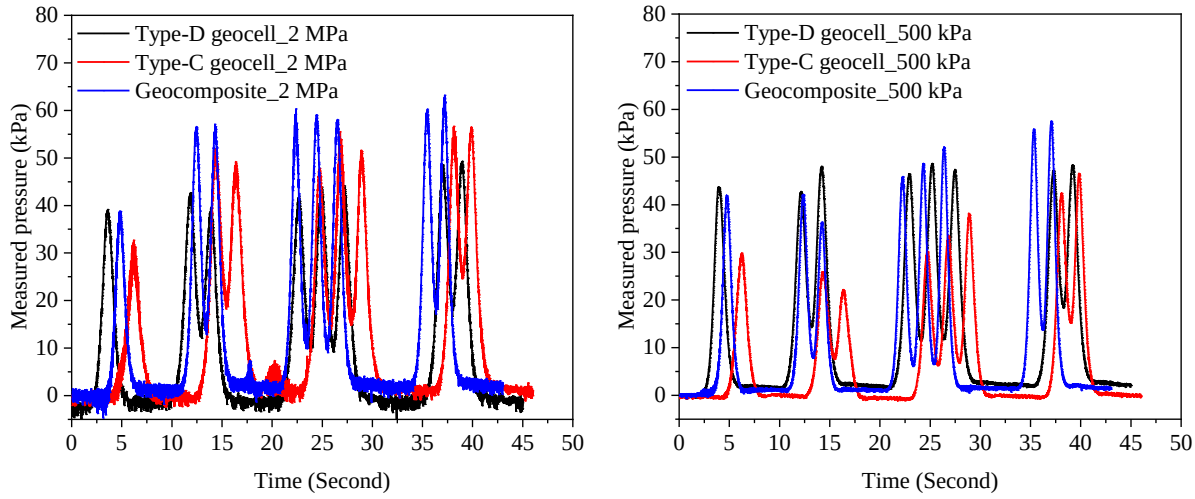

Fig. 5.40. The trafficking response at 1st forward pass in: (a) 2 MPa earth pressure cell and (b) 500 kPa earth pressure cell

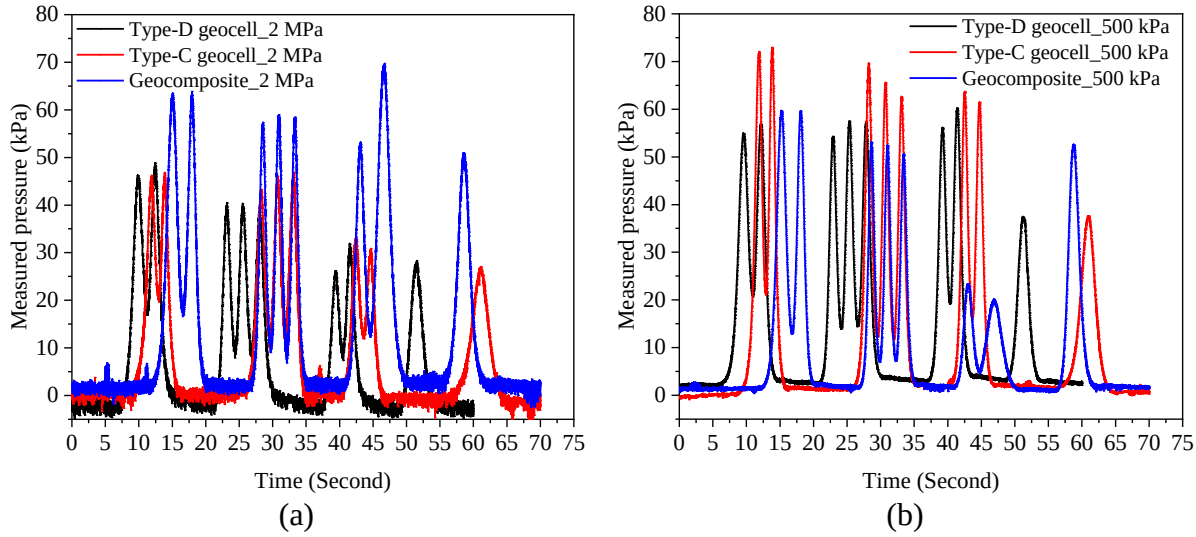

Fig. 5.41. The trafficking response at 1st backward pass in: (a) 2 MPa earth pressure cell and (b) 500 kPa earth pressure cell

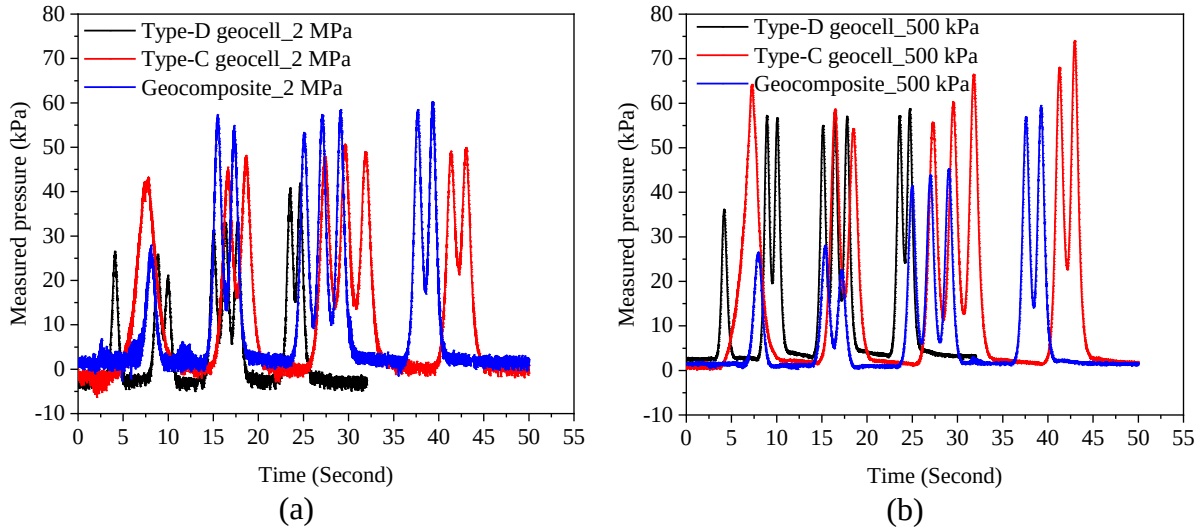

Fig. 5.42. The trafficking response at 2nd forward pass in: (a) 2 MPa earth pressure cell and (b) 500 kPa earth pressure cell

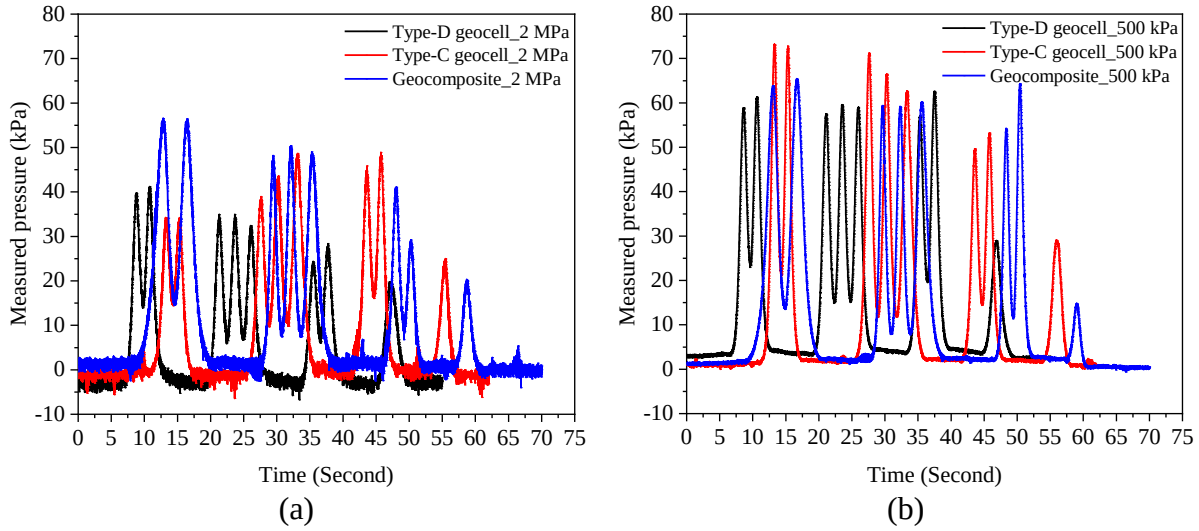

Fig. 5.43. The trafficking response at 2nd backward pass in: (a) 2 MPa earth pressure cell and (b) 500 kPa earth pressure cell

Due to the variation of the responses for each pass, the peak pressure recorded by two earth pressure cells was determined for comparison as shown in Fig. 5.44. The average peak values were also calculated in the figure. As with the results of one-cycle plate loading tests with the maximum applied pressure of 900 kPa in Fig. 5.34(d), the peak pressure transferred to subbase was similar between the Type-C geocell and geocomposite sections-i.e., 50.7 kPa and 50.4 kPa,

respectively. The 4-inch Type-D geocell section registered a lower average peak value than the other two sections.

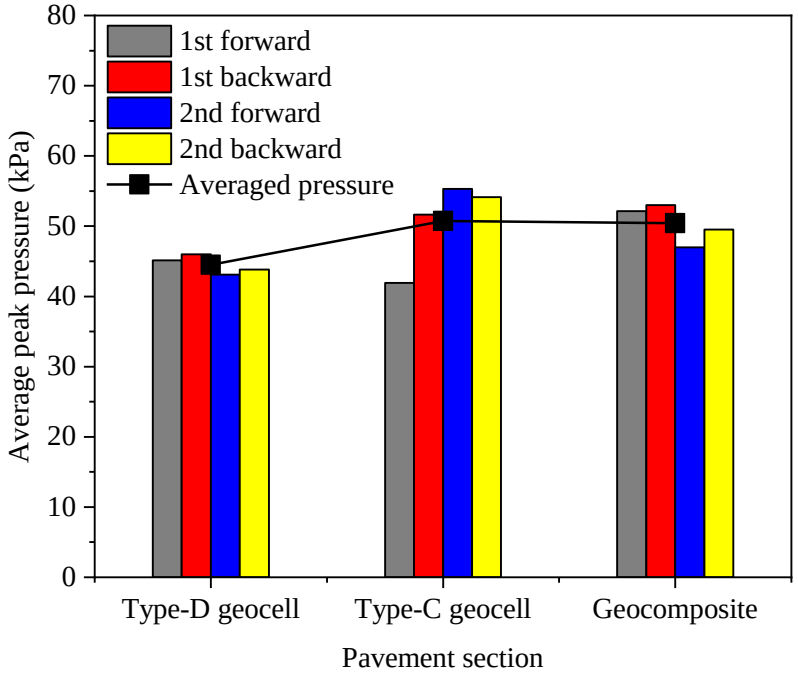

Fig. 5.44. Averaged peak pressure recorded by earth pressure cells

5.6.4 Long-term monitoring

The readings of soil temperature and soil moisture content were taken manually from 2022-09-17 to 2022-11-03. The long-term monitoring started in the 6-inch Type-C geocell and geocomposite sections in the afternoon on 2022-01-25 right after the setup of the data acquisition system and the weather station. Soil temperature and water content as well as air temperature probe and rainfall were monitored every second and the averaged value was recorded every hour. The readings of earth pressure cells were monitored and recorded with the initial sampling rate of 20 Hz. However, the readings of all sensors were missing between 2022-12-29 and 2023-02-16 as the data acquisition system experienced dysfunction during this period. This was due to the large sampling rate set for the earth pressure cells; thereafter, the rate was reset to 10 Hz.

The ground was fully frozen during the period of monitoring, and limited traffic was received by the road; therefore, no vertical stress was recorded by earth pressure cells. This section focuses the monitoring of soil temperature and water content between 2022-09-17 and 2023-04-15. Once the earth pressure cells take readings, the load transfer results will be updated in the future.

5.6.4.1 Evolution of temperatures in soils

Fig. 5.45 shows the temperature evolution at the different depths in soils. The ground freeze progressed from surface downwards, and the temperatures of soils near the ground surface experienced more fluctuation than the deeper soil. The temperatures in the pavement sections started to decrease since November of 2022 and the frozen depth reached 1.3 m in December of 2022. In the spring, the soil temperatures for all depths monitored gradually rose with time, starting in mid-February 2023 and ending approximately in mid-April 2023. Like the freezing, the thawing also progressed in a top-down manner.

Fig. 5.46 presents the temperature profiles at different times. It is clear that the soil temperature at the deep layer was always higher than the top layer in winter, especially at the depth of 1.3 m where the soil temperature kept stable at -5℃ during the whole winter while the temperature at the base courses (the top two sensors) was even as low as -17℃. This result indicates that the frozen depth at the site was greater than 1.3 m.

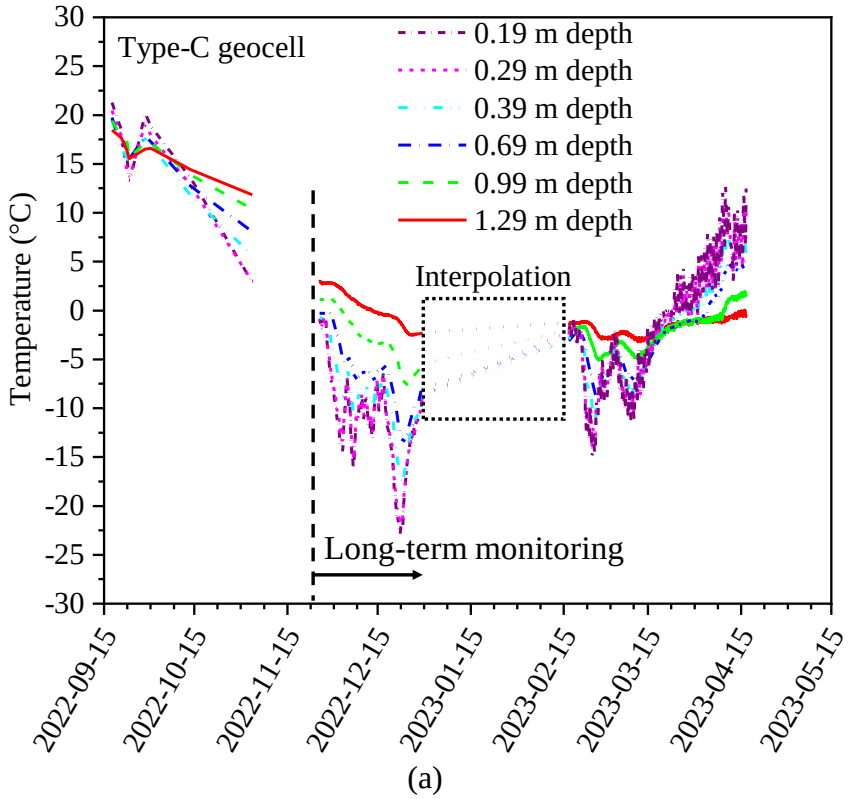

(a)

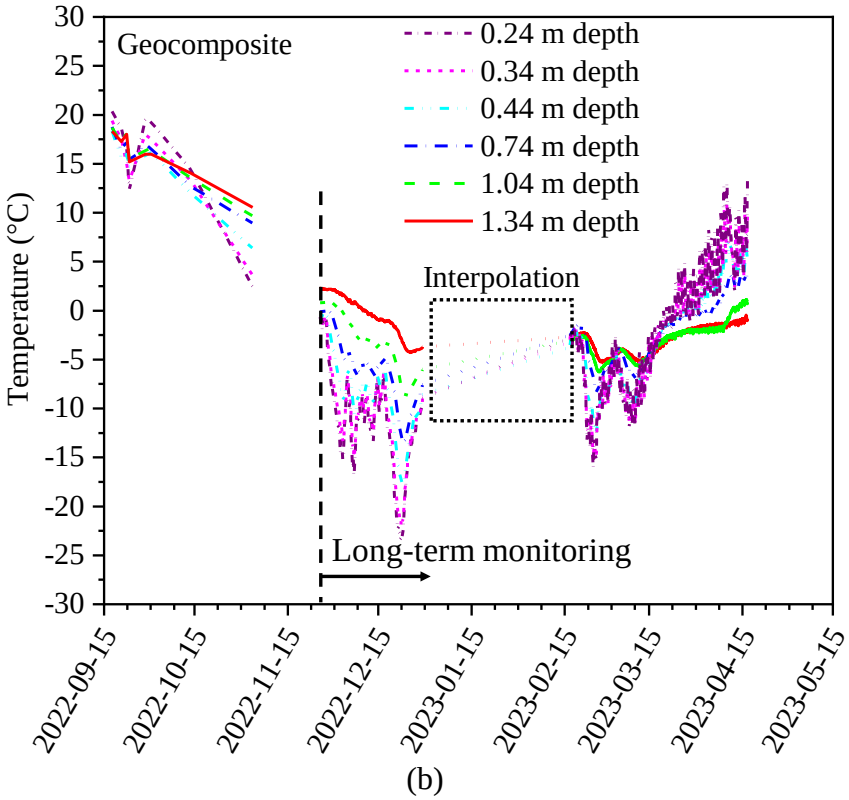

(b)

Fig. 5.45. Soil temperature evolution in: (a) Type-C geocell section and (b) geocomposite section

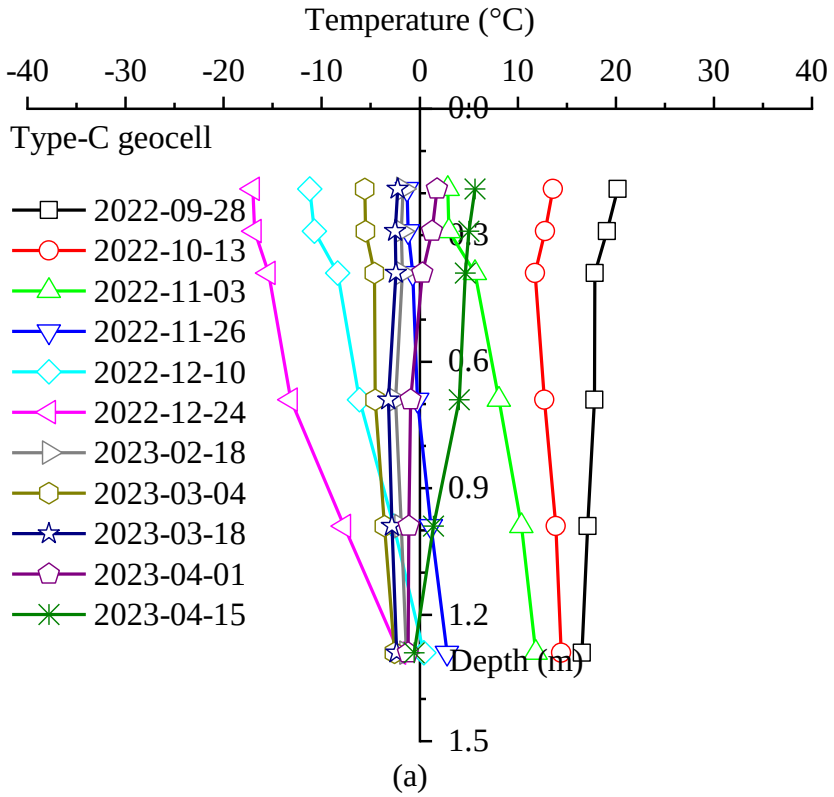

(a)

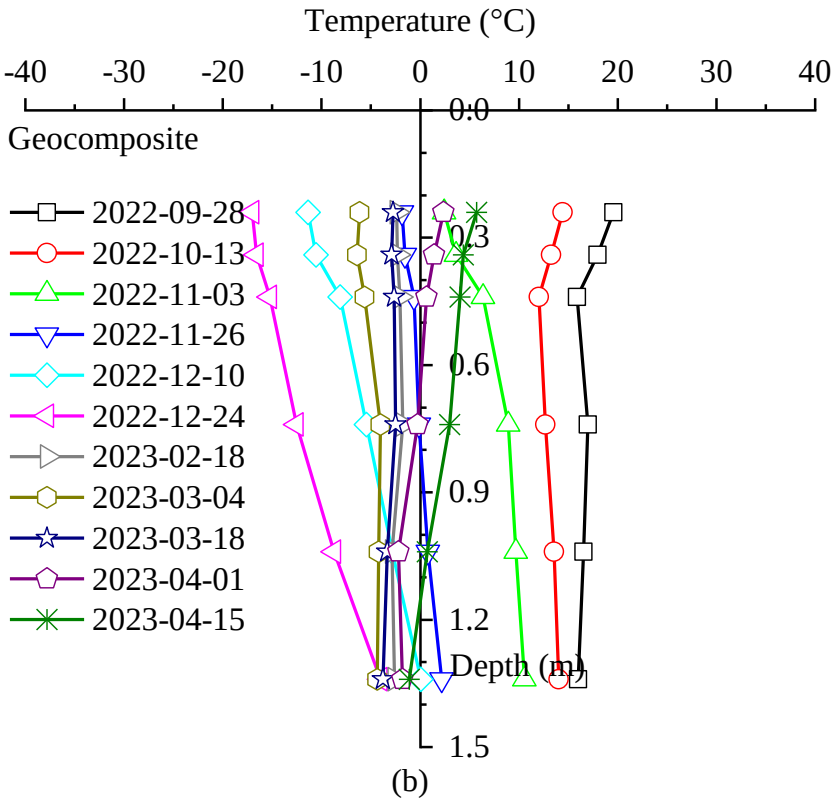

(b)

Fig. 5.46. Soil temperature profile in: (a) Type-C geocell section and (b) geocomposite section

5.6.4.2 Migration of water in soils

Calibration tests

Volumetric water content near the interface of base courses and subbases was monitored for a long term in both 6-inch Type-C geocell and geocomposite sections. As described in Section 5.4.5.1, the sensor wires were extended with 25 ft and 100 ft cables in 6-inch Type-C geocell and geocomposite sections, respectively. As a result, the currently measured voltage outputs of EC-5 moisture sensors would become larger due to the addition of electrical resistance of extension cables. Therefore, it is necessary to calibrate the extended EC-5 moisture sensors to obtain the correct relationship of voltage outputs and volumetric moisture content. The calibration tests were followed by a method recommended by Meter Group®.

Datalogger Campbell Scientific® CR1000X and Group Meter® ZL-6 were used to calibrate EC-5 moisture sensors, as illustrated in Figs. 5.47(a) and 5.47(b), respectively. The base courses or subbases passing No.4 sieve were tested under 100% and 95% compaction degree. The compaction was made in a modified compaction mold in two lifts, with 58 mm for each lift. Water with 5% or 10% volume of the mold was added incrementally into the soils so that the volumetric water content of soils could be calculated for each test. The added mass of soils for each lift was calculated by the predetermined density times the lift volume. After the completion of the first lift, the surface was scratched, and one EC-5 moisture sensor without extension was horizontally placed on the surface. The 2nd lift of compaction followed to cover the sensor and compact the soil to the desired thickness. Datalogger measured the voltage outputs of the EC-5 sensor plugged into 25-ft and 100-ft extension cables. The relation of voltage outputs and volumetric water content was obtained by performing the polynomial regression.

(a) (b)

Fig. 5.47. Photographs of calibration tests by using: (a) CR1000X and (b) ZL-6

The curves were fit with the polynomial equation as shown in Equation (5-5).

$$y = A * x^3 + B * x^2 + C * x + D \quad (5\text{-}5)$$

Where, A, B , C and D are the parameters determined from fitting curves.

y is the volumetric moisture content, %.

x is the voltage output, mV.

Fig. 5.48 compares the results of repeatability tests by using CR1000X and ZL-6. The fitting curves in two dataloggers were almost overlapped, confirming the repeatability of the measurement with the two dataloggers.

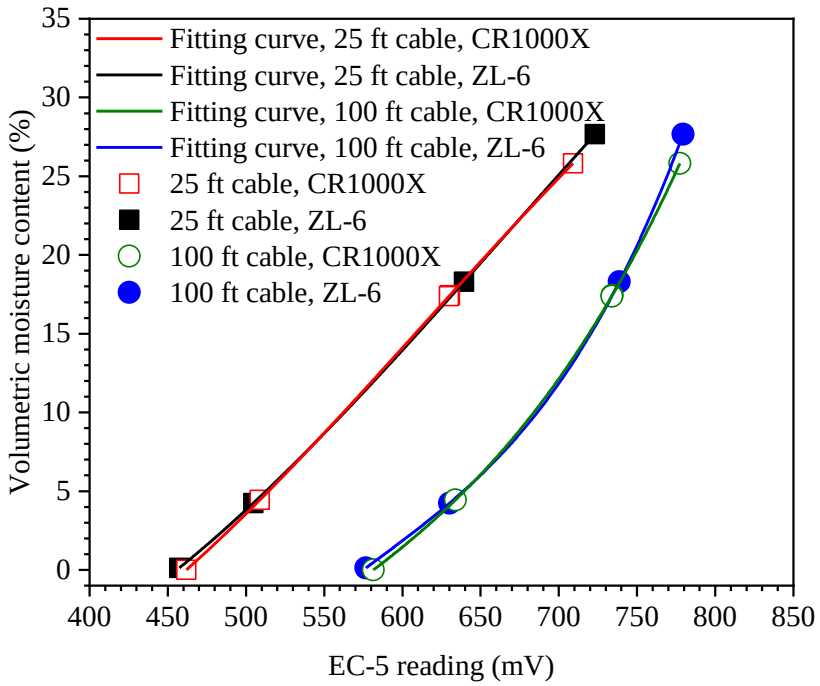

Fig. 5.48. Repeatable tests by using dataloggers of CR1000X and ZL-6

Fig. 5.49 shows the calibration results for base courses and subbases in 6-inch Type-C geocell and geocomposite sections. The parameters in the equation were determined and listed in Table 5.7.

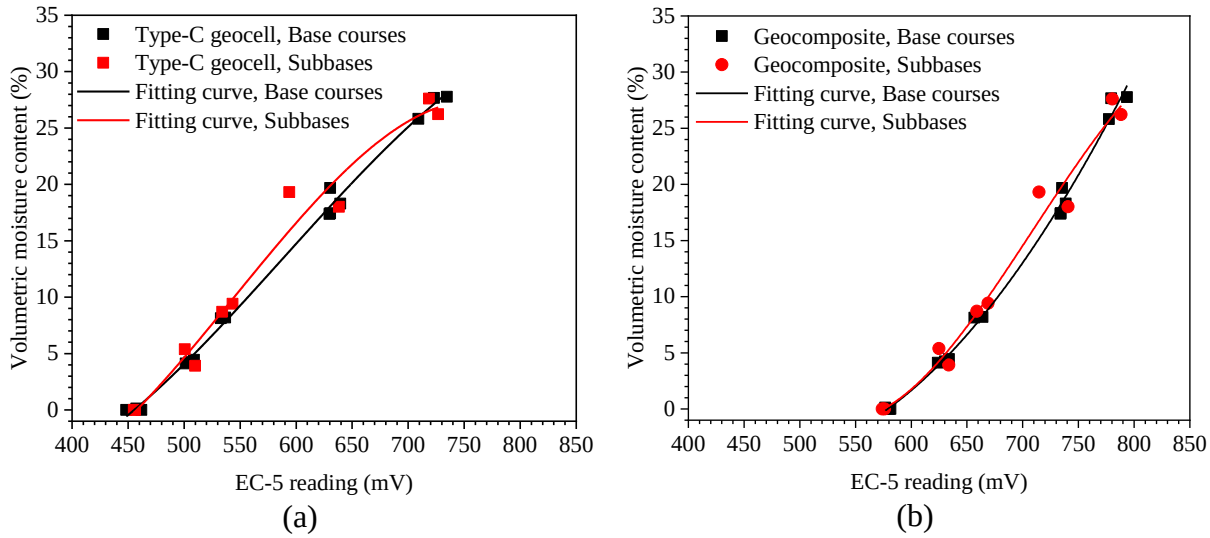

Fig. 5.49. Calibration test results for base course and subbases in: (a) 25 ft extension cable in 6-inch Type-C geocell section and (b) 100-ft extension cable in geocomposite section

Table 5.7. Parameters determined in the calibration tests

Geosynthetics section	Soil types	Parameter value			
		A	B	C	D
6-inch geocell section	Base courses	-4.95417E-07	8.76532E-04	-4.06680E-01	5.020036E+01
	Subbases	-8.78764E-07	1.44000E-03	-6.59660E-01	8.552131E+01
Geocomposite section	Base courses	-6.42266E-08	4.16904E-04	-3.46740E-01	7.348506E+01
	Subbases	-1.81758E-06	3.87000E-03	-2.58908E+00	5.561890E+02

Volumetric water content

The volumetric water content was calculated by using the calibrated functions in Table 5.7. Fig. 5.50 presents the evolution of volumetric water content in 6-inch Type-C geocell and geocomposite sections. It shows that volumetric water content decreased gradually in fall and winter as the air temperature continuously decreased to subfreezing temperature during this time. The value started to rise in the beginning of April as the soil layers started to thaw. It is obvious that the water content of the base courses at the pavement edge (340 mm depth edge in 6-inch geocell section and 390 mm depth edge in geocomposite section) experienced severe fluctuations with time. This position was close to the pavement shoulder, so it was susceptible to the penetration of freezing temperature. As a result, the water content change was more sensitive to the fluctuation of air temperature. The water contents before and after freezing season were shown in Fig. 5.51. It shows that after one seasonal F-T cycle, there was only a slight decrease in water contents at different depths inside the pavement, but an increase at the shoulder of the pavement. In the 6-inch Type-C geocell section, the average water content of subbases and base courses decreased by 2.5% and 0.7%, respectively, while in the geocomposite section, the corresponding decrease was 1.6% and 1.7%, respectively. The water content at the shoulder was increased by 8.0% and 3.8% in 6-inch Type-C geocell and geocomposite section, respectively.

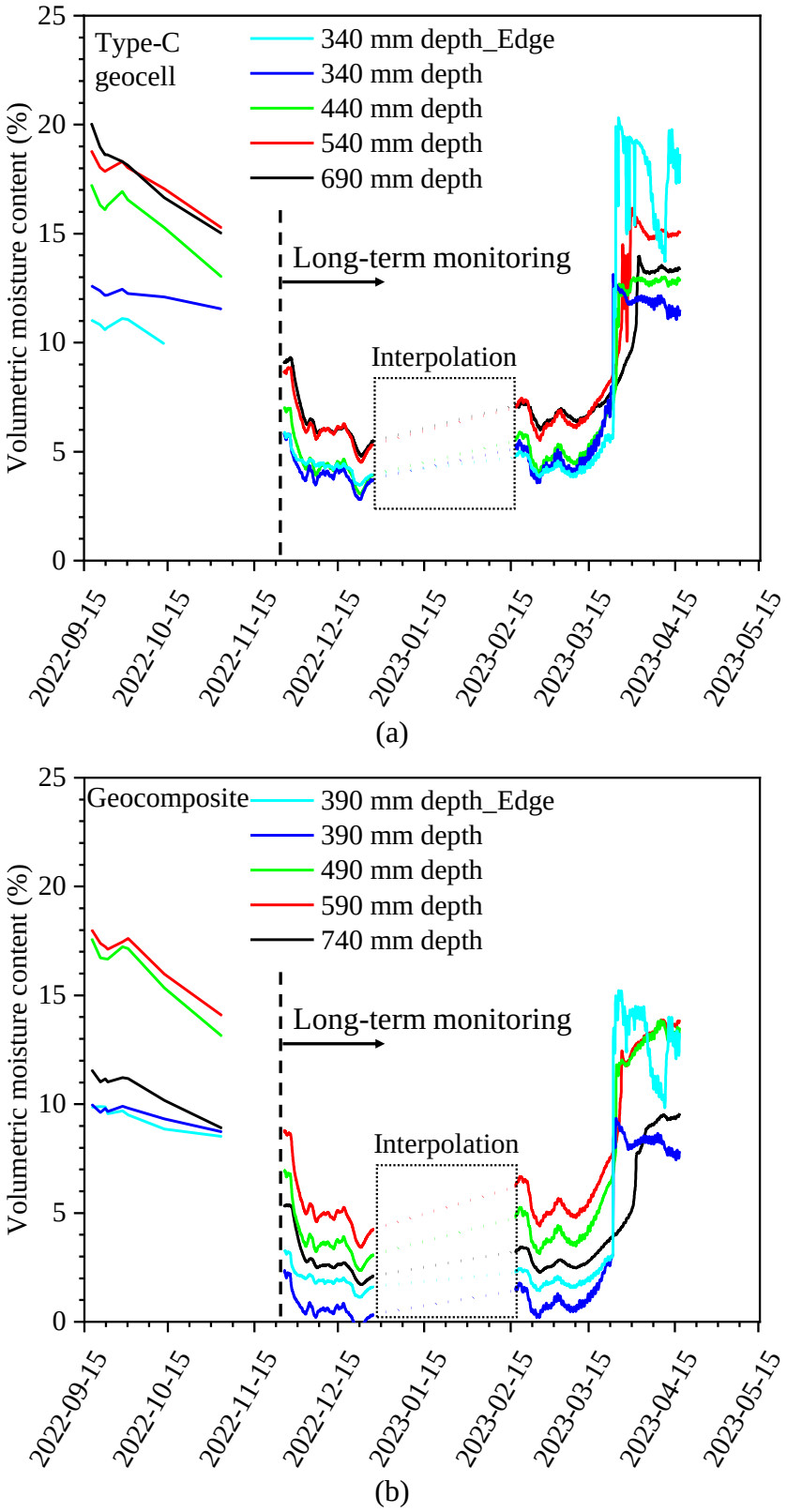

Fig. 5.50. Volumetric water content in: (a) 6-inch Type-C geocell section and (b) geocomposite section

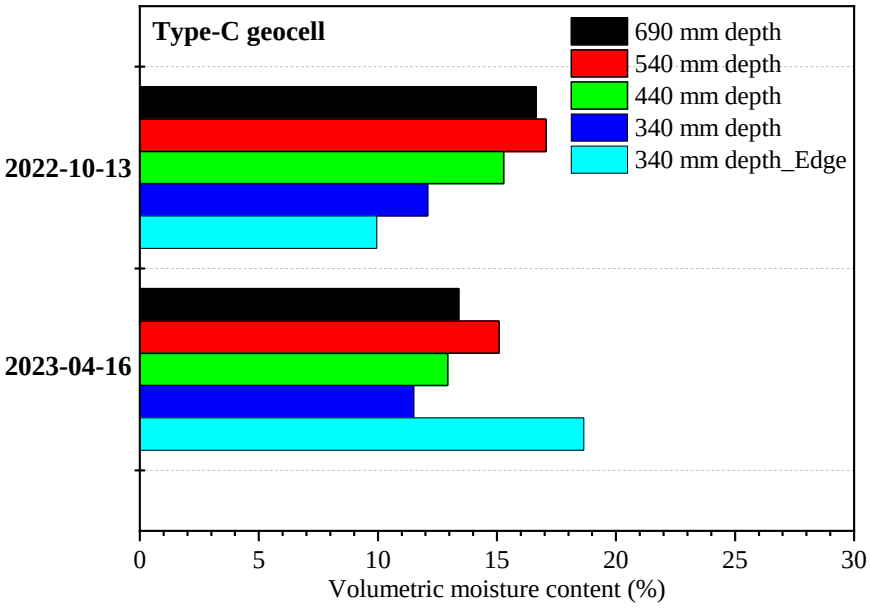

(a)

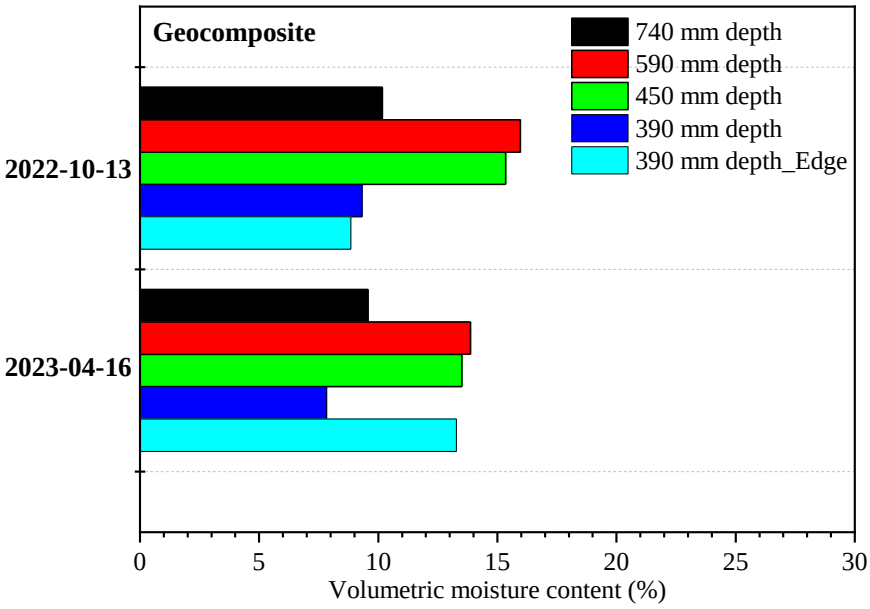

(b)

Fig. 5.51. Volumetric water content before and after the freezing season in: (a) 6-inch Type-C geocell section and (b) geocomposite section

5.7 Conclusions

This technical report presents the field tests on assessment of the freeze-thaw performance of geosynthetics-reinforced flexible pavement in Sturgeon County, Alberta. The sensors were

installed and operated successfully, proving that instrumentation design and installation were effective. Some preliminary observations are drawn from this ongoing project.

(1) In spite of some variations, results from three types of plate loading tests were generally consistent. The deformation of the asphalt surface was greater in the 4-inch Type-D geocell section than that in the other two sections. The deformation was similar between the Type-C geocell section and the geocomposite section. However, the Type-D geocell section transferred a smaller fraction of load to the subbases than the other two sections, represented by a smaller load transfer ration and a higher stress distribution angle.

(2) The trafficking tests produced a comparable amount of vertical stress at the base-subbase interface to the plate loading tests with the maximum applied pressure of 500 kPa. The deformation and load transfer results were also agreeable with those from the plate loading tests.

(3) The soil temperature in the surface layer was more sensitive to the variation of the air temperature, and the temperature in deeper layers was more stable. The soil temperature at depth of 0.2 m was decreased to -17℃, while the temperature at the depth of about 1.3 m was stable at -5℃ during the winter. The frozen depth was greater than 1.3 m below the asphalt surface.

(4) Volumetric water content of subbases and base courses inside the pavement in both 6-inch Type-C geocell and geocomposite sections decreased slightly (0.7-2.5% and 1.6-1.7%, respectively) after one seasonal freeze-thaw cycle. However, that at the shoulder increased by 8.0% and 3.8% for 6-inch Type-C geocell and geocomposite sections, respectively.

Chapter 6 Full-Scale Testing and Monitoring of Geosynthetics-Stabilized Flexible Pavement in Alberta, Canada

6.1 Abstract

Freeze-thaw (F-T) cycles are a primary contributor of pavement damages in seasonal frost regions. Geosynthetics stabilization has been a promising solution for enhancing the roadways performance in cold regions. However, in comparison with the practical applications, research on the geosynthetics stabilization in cold-region roads is scarce and its efficacy is yet to be quantified. This study presents the full-scale test on geosynthetics-stabilized sections in a flexible pavement in Sturgeon County, Alberta. It focused on the investigation of three separate test sections with bases stabilized by two types of geocells and one geogrid composite, each fully instrumented with earth pressure cells, thermocouples, and moisture sensors. This experimental program consisted of plate loading tests and trafficking tests on each test section before and after the first F-T season, and a long-term monitoring of soil temperatures, moisture contents, and loads transferred to subbases while sections were open to general traffic. The results showed seasonal F-T cycles resulted in increased pavement settlement, decreased load transfer ratio, and increased stress distribution angle under both plate loading. The traffic-induced stress on the subbases increased during the spring thaw but decreased afterwards.

6.2 Introduction

In seasonal frost regions, roadways are particularly susceptible to effects of freeze-thaw (F-T) cycles. The repetitive F-T action leads to frost heave and thaw weakening, which will degrade road structures. Qi et al. (2006) summarized that the F-T cycles could detrimentally alter physical properties of soils and reduce the mechanical strength. The freezing process results in the water migration, ice lens formation, and differential heave (Andersland and Ladanyi, 2003; Bing et al.,

2015; Konrad, 2008; Li et al., 2019). The thawing process leads to the non-uniform distribution of meltwater, thaw settlement, and mechanical weakening of bases and subbases (Bilodeau et al., 2020; Simonsen et al., 2002; Simonsen and Isacsson, 1999). These processes collectively contribute to changes in void ratio and alignment of soil fabrics, the movement of soil particles, and the weakening of bonds between soil particles (Fan et al., 2021; Othman and Benson, 1993; Pawluk, 1988; Viklander, 1998) that are responsible for destabilization of roadways, manifesting as roughness, fatigue cracking, etc. (Ishikawa et al., 2019; Johnson et al., 1975).

Various countermeasures have been investigated and implemented to mitigate F-T induced damages and enhance the serviceability and durability of roadways in cold regions, including the chemical treatment of bases with binders, the substitution of frost-susceptible soils with gravels, the installation of effective drainage systems or capillary barriers, and the stabilization of base courses with geosynthetics (Christopher et al., 2000; Edil et al., 2002; Henry and Holtz, 2001; Li et al., 2017; Pokharel et al., 2016; Rosa et al., 2017; White and Vennapusa, 2013). Geosynthetics have been successfully used to enhance the performance of earth structures for over last five decades. They have also been widely used to enhance the longevity and durability of roadways in seasonal frost regions. However, the conventional design methods for geosynthetics-stabilized bases have been predominantly developed under room temperature conditions. This oversight in accounting for the F-T effect could lead to premature degradation of these roadways. Despite the extensive applications of geosynthetics in cold-region roads, the relevant research on evaluating their efficacy in improving F-T performance and understanding the underlying mechanisms is significantly lacking.

A scarcity of research has focused on qualitative or quantitative evaluation on the efficacy of geosynthetics in enhancing the F-T performance of bases using lab-scale model tests. Dave et al.

(2022) conducted centrifuge model tests to assess the effect of geocell stabilization on thaw settlement of soils. Unfortunately, due to the limitation of their test setup, the thawing deformation was not observed even in the unstabilized section. Huang et al. (2023) utilized a customized model apparatus (Huang et al., 2021) to investigate the F-T behaviour of geocell-stabilized bases with varying fines contents. The findings revealed that after five F-T cycles, novel polymeric alloy (NPA) geocell stabilization notably reduced frost heave and thaw settlement by about 18% and 35%, respectively, and increased stiffness and ultimate bearing pressure by approximately 90% and 73%, respectively.

There has been also limited research on conducting full-scale evaluation on geosynthetics stabilized roads under F-T cycles. Pokharel et al. (2016) documented that geocell-stabilized access roads over the muskeg in Alberta, Canada performed beyond design expectations without maintenance under heavy-duty traffic loads after one to three seasonal F-T cycles. Pokharel et al. (2017) conducted a comparative full-scale field test on two parallel sections with NPA geocell-stabilized bases and cement-treated bases in a heavy-volume road in Nisku, Alberta, Canada. After three years of services, the geocell-stabilized section maintained a smooth surface without visible distresses, while the cement-treated section exhibited alligator cracks and damages on the surface after the first F-T season, even though the latter initially had the modulus approximately four times greater than the former. Henry et al. (2005) investigated the performance of a test unpaved road with sections stabilized with various geosynthetics experiencing one seasonal F-T cycle. They found that the geocell-stabilized section showed a 50% reduction in the area of distresses and a considerable increase in California Bearing Ratio (CBR) values (approximately 200%) as compared with the non-stabilized control section. Edil et al. (2002) evaluated different stabilization alternatives for a highway segment over soft subgrades in Wisconsin, discovering that

the geocell-stabilized section exhibited smaller maximum deflections in falling weight deflectometer (FWD) tests before and after the one seasonal F-T cycle as compared with sections stabilized by geotextile, geogrid and geocomposite.

The past studies indicated that most of the field studies were qualitative without or with limited instrumentation, relying heavily on surface distress observations and some simple tests [e.g., dynamic cone penetration (DCP) and FWD tests] to evaluate the effect of F-T cycles on the pavement performance. The full spectrum of geosynthetics stabilization outcomes, particularly the influence on critical design parameters such as vertical stress distribution over the subbases or subgrades and the dynamic response under traffic loads, remain unaccounted for roadways subjected to seasonal F-T cycles. The continuous monitoring of the responses (vertical stress, temperatures, and water content) of the roads in cold climatic region is rarely reported.

The objective of this study was to evaluate the F-T performance of geosynthetics-stabilized bases through a series of short-term tests and a long-term monitoring program in Alberta, Canada. This full-scale field study included three fully instrumented test sections stabilized with two types of NPA geocells and a geocomposite. The short-term tests were composed of static plate loading tests and trafficking tests before and after each seasonal F-T cycle-i.e., before the ground freezing and right after the thawing. The long-term monitoring program included the continuous monitoring of temperatures, moisture content, and earth pressure in the pavements as well as air temperatures and rainfall throughout the entire duration of the seasonal F-T cycles. This paper reports the outcomes from the first stage of study-i.e., test sections experiencing the first seasonal F-T cycle, while the overall research project would continue for additional several years. The outcomes of this field study would ultimately contribute to the quantification of the efficacy of

geosynthetics stabilization in mitigating F-T induced damages and provide insights into the underlying stabilization mechanisms.

6.3 Construction and instrumentation of test sections

6.3.1 Project information

A 4.1-km stretch of the two-lane Township Road 544, serving as the main access to ProNorth Industrial Park in Sturgeon County, Alberta, Canada, was reconstructed to be a highway. This rehabilitated highway was divided into three test sections as shown in Fig. 6.1, in which the base courses were stabilized with different types of geosynthetics: Novel Polymeric Alloy (NPA) Type-D geocell, NPA Type-C geocell, and geocomposite (i.e., a layer of nonwoven geotextile welded within the biaxial geogrid). The construction spanned from June to November 2022, following a sequence of the Type-D geocell section (200 m long), the Type-C geocell section (1,150 m long), and the geocomposite section (2,710 m long). A control section without geosynthetics stabilization was also planned for this research. However, citing the experience with the failures the existing conventionally design road has faced and as the reconstructed road had to remain open for heavy industrial and general public traffic, the County decided to rule out such a control section. Therefore, this full-scale field study only focuses on the relative performance between the three geosynthetics-stabilized sections.

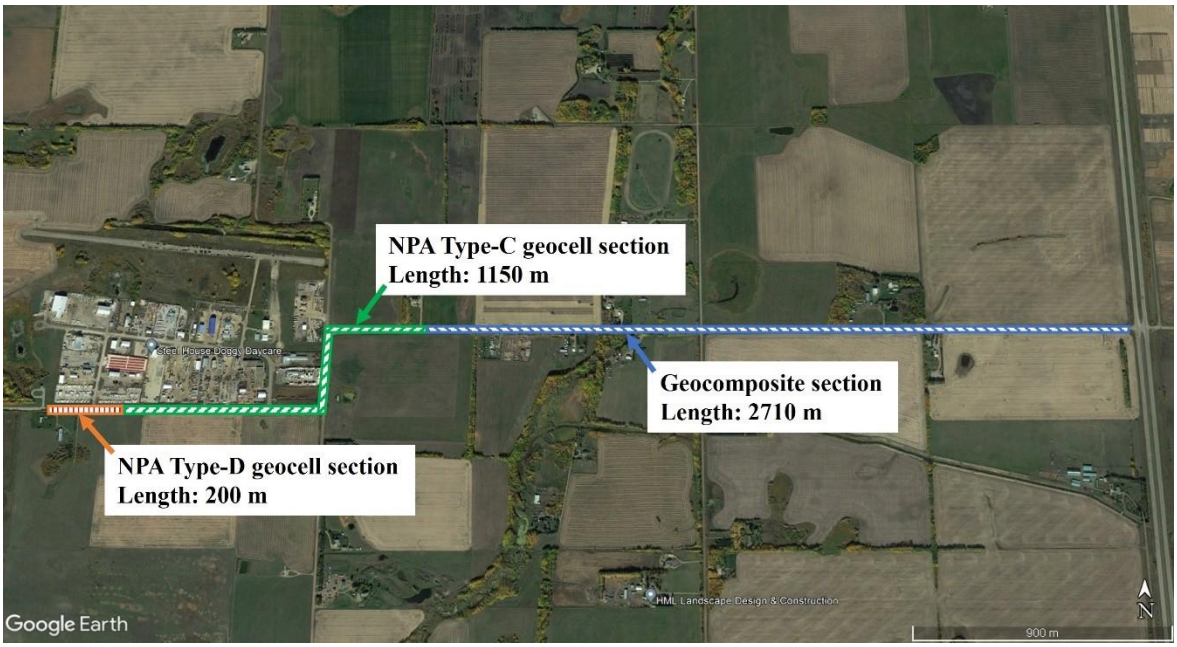

Fig. 6.1. Location of the test sections in Sturgeon County, Alberta, Canada

Geotechnical investigation was conducted in 2018 and 2019 with ten boreholes drilled to a depth of 3.8 m below the ground surface. The subsurface soils encountered were generally silty, sandy clay fills of medium plasticity underlain by native silty clay of medium plasticity with variable conditions from soft to stiff and moist to wet. No groundwater was not encountered within the borehole depth in all the boreholes except one that saw free water at a depth of 3.5 m. The weather conditions of the test sections were established by a weather station located approximately 4 km away. The monthly data recorded during 2017-2021 revealed a distinct seasonal pattern. In the coldest months (December to February), air temperatures dropped to as low as -43°C, while in the warmest months (June to August), air temperatures could be as high as 36°C. Furthermore, the period from May to July was marked by the heaviest rainfall, with the precipitation reaching up to 150 mm. The weather recordings suggest the distinct seasonal F-T cycles at the test site, which could be the major contributor to pavement deterioration, especially under heavy-duty traffic loads in this industrial park.

6.3.2 Test sections

6.3.2.1 Construction program

The rehabilitation program began with the full removal of the existing pavement structures, reaching down to native subgrades. Subsequently, a layer of woven geotextile was laid on native subgrades to serve as a separator, followed by backfilling with minus gravels, also as known as pit run materials, and the sequential compaction of subbases. The construction process continued with the compaction of base courses over the subbases, and finally, the paving of asphalt concrete pavement (ACP) layers. The structural layout of these layers is shown in Fig. 6.2(a). In the three test sections, the base courses were stabilized with 100-mm height NPA Type-D geocells, 150-mm height Type-C geocells, and geocomposites that were placed in the base or at the base-subbase interface, as shown in Fig. 6.2(b). Notably, in contrast to the conventional design incorporating the geocomposites with 300 mm thick base courses, the use of NPA geocells with base courses 50 mm thinner was authorized for the two geocell sections, upon the assurance of superior performance compared to the geocomposite section.

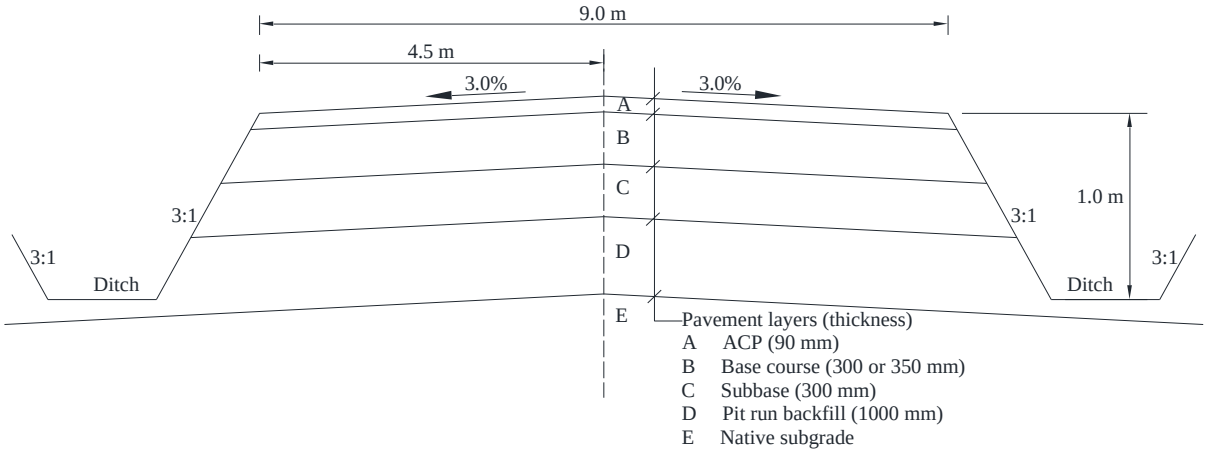

(a)

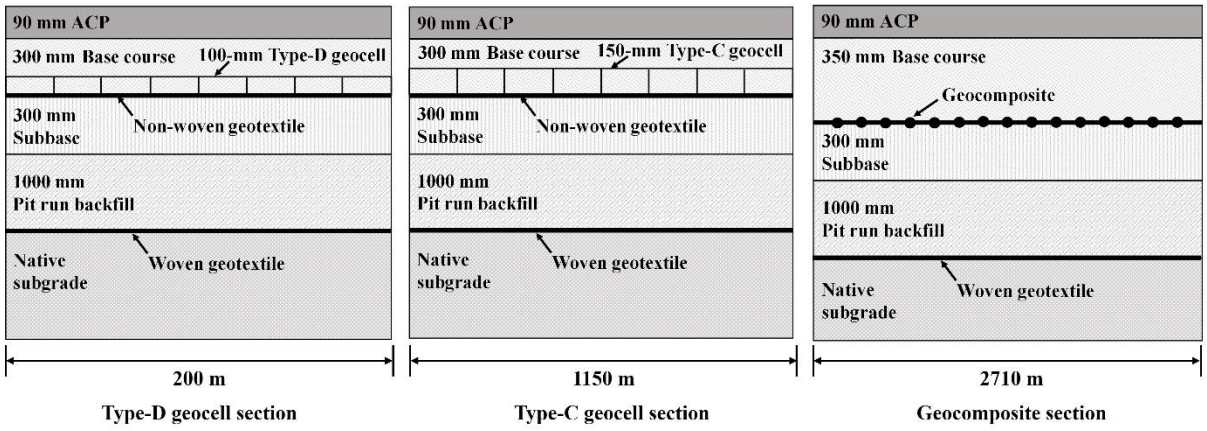

(b)

Fig. 6.2. Design of test sections: (a) general cross-section and (b) details of individual test sections

Fig. 6.3 presents the photographs of the construction of the test sections. In the two geocell sections, a layer of non-woven geotextiles was laid down first on top of the compacted subbases prior to installing the geocells. The geotextiles helped separate the subbase and the base courses against upward fines migration. The geocells were stretched and kept open by fixing the geocell edges with steel nails. The base materials were then filled into and above the geocells and compacted in a single lift by road rollers to the thickness of 300 mm with a compaction degree of no less than 95%. In the geocomposite section, the geocomposite layer was laid down directly on the subbase surface, followed by the addition of base courses. The base courses were compacted in one lift to 350 mm in thickness in the same manner as the geocell sections. After the completion

of base compaction, two layers of ACP with 50 and 40 mm thick were paved atop the bases. Fig. 6.3(d) shows the finished pavement with a 9.0 m wide two-lane surface and a 0.5 m wide ACP shoulder at each side.

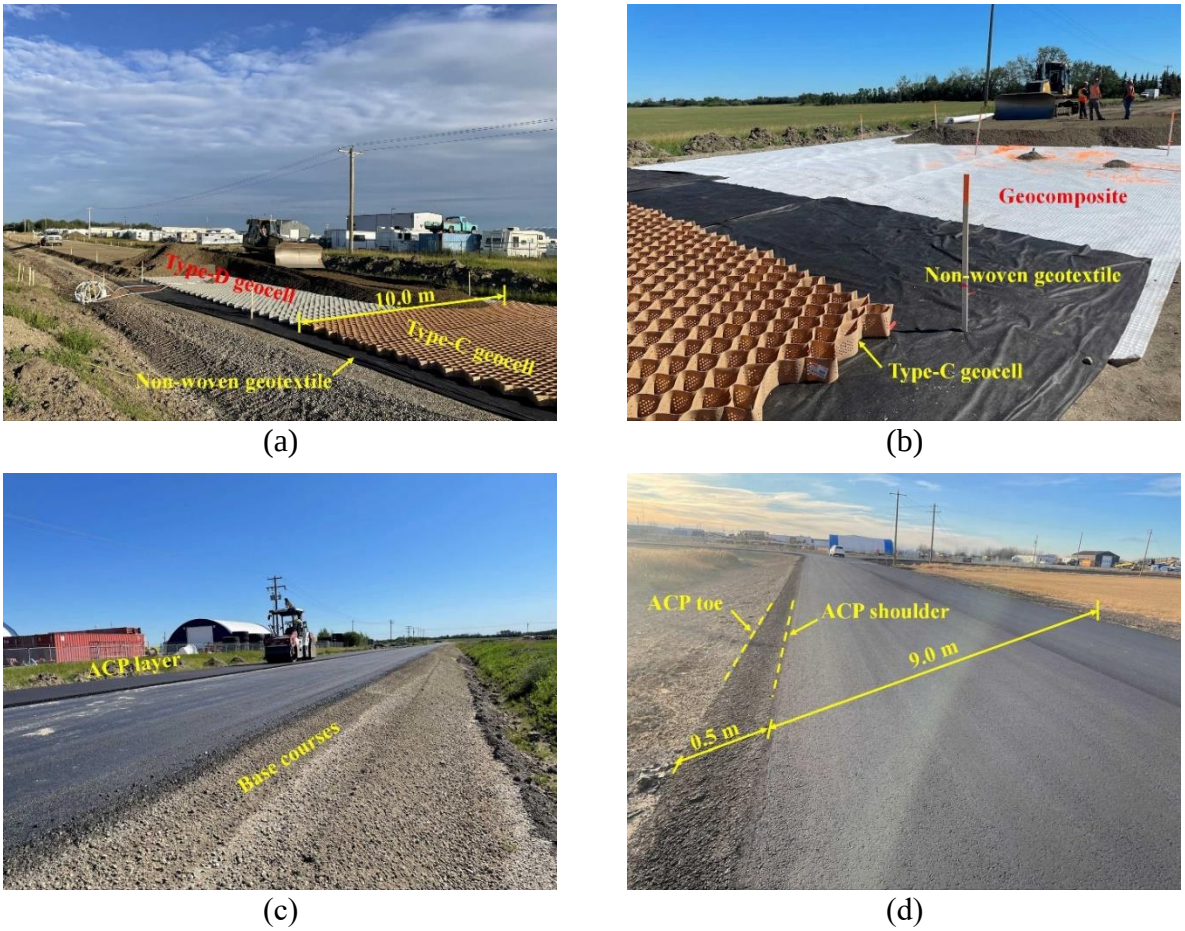

Fig. 6.3. Photographs of pavement construction: (a) and (b) the compaction of base courses in geocell and geocomposite sections, respectively, (c) the asphalt concrete layer, and (d) the finished pavement surface

The process of this rehabilitation project was separated into three major stages after backfilling the pit run materials. The first stage involved the construction of the entire Type-D geocell section plus 430 m of the Type C geocell section. It began with the compaction of subbase in June 2022 and concluded with the completion of two ACP layers by mid-August 2022. Subsequently, this part of the road was open to the public traffic. The second stage encompassed the remaining

portion of Type-C geocell section, alongside a 10-m length of the geocomposite section designed to accommodate sensor installation within this geocomposite segment. It commenced with the subbase compaction in July 2022 and ended with the paving of the first ACP layer by mid-August 2022 while leaving the second ACP layer to be constructed in the final stage. The final stage included constructing the remaining part of geocomposite section: starting with the compaction of subbases and base courses starting in August 2022, followed by paving the first layer of ACP by the end of September. At last, the construction of the second ACP layer was completed by the end of October 2022, covering the length of road in the last two stages.

6.3.2.2 Materials

Tables 6.1 and 6.2 present the basic properties of three types of geosynthetics utilized in this project. Despite being smaller in wall height, Type-D geocells have greater strength (22 kN/m) than Type-C geocells (19 kN/m). Both geocells have low thermal expansion coefficients and creep reduction factors and adapt to a wide range of operation temperatures, which ensures their applicability in extremely cold conditions. The geocomposites are manufactured by welding a layer of non-woven geotextile within a biaxial geogrid structure.

Table 6.1. Properties of NPA geocells

Properties	Values		Test standard
	Type-C	Type-D	
Seam weld splitting strength, kN/m	19	22	ISO-13426-1
Tensile strength, kN/m	19	22	ISO-10319
Long-term permanent deformation at 65℃, %	3	3	ASTM D6992
Dynamic modulus, MPa			ASTM E2254
+30℃	775	800	
+45℃	675	700	
+60℃	525	650	
Coefficient of soil-cell friction efficiency	0.95	0.95	ASTM D5321
Brittle temperature, ℃	-70	-70	ASTM E2254
Coefficient of thermal expansion, ppm/℃	135	135	ASTM E831
Distance between weld seams, mm	330	330	
Cell wall height, mm (inch)	150 (6″)	100 (4″)	
Opening cell dimension, mm × mm	245 × 210	245 × 210	

Table 6.2. Properties of geocomposites

Properties	Value			Test standard
	Geogrid	Geotextile	Composite	
Nonimal tensile strength (md/cmd)*, kN/m	30/30	7.5/11.0	-	ASTM D4595
Elongation at nominal tensile strength (md/cmd), %	8/8	70	-	ASTM D4632
Tensile strength at, kN/m				ASTM D4632
1% elongation (md/cmd)	6/6	-	-	
2% elongation (md/cmd)	12/12	-	-	
5% elongation (md/cmd)	24/24	-	-	
Grab tensile strength (md), kN	-	-	0.55	ASTM D4632
Trapezoidal tear strength, kN	-	-	0.26	ASTM D4533
Puncture force, kN	-	1.67		ISO 12236
Index puncture, kN	-	-	0.26	ASTM D4833
Aperture size (md × cmd), mm × mm	32 × 32	-	-	
Displacement at static puncture, mm	-	30	-	ISO 12236
Characteristic opening size, µm	-	90	-	ASTM D4751

*md is machine direction; cmd is cross machine direction.

Asphalt concrete pavement (ACP) was constructed with a mix of 70% of coarse aggregate, 10% of blend sand, and 20% of recycled asphalt pavement (RAP). The Marshall mix design complied with the specifications of Government of Alberta Transportation (Alberta Transportation, 2020). Fig. 6.4 displays the particle size distributions of base and subbase materials in each test section. In the figure, Type-C geocell section and geocomposite section are referred together as the materials were taken near the joint between these two sections. The result reveals the consistent grading of base courses across all the three sections but the varying gradation of subbases between Type-D geocell section and the other two sections. Therefore, the properties of subbases are presented separately in Table 6.3. Base courses and pit run materials in all sections were classified as poorly graded gravels according to Unified Soil Classification System (USCS), both containing similar amounts of sands and fines, but the pit run materials included oversized gravels (larger than 19 mm).

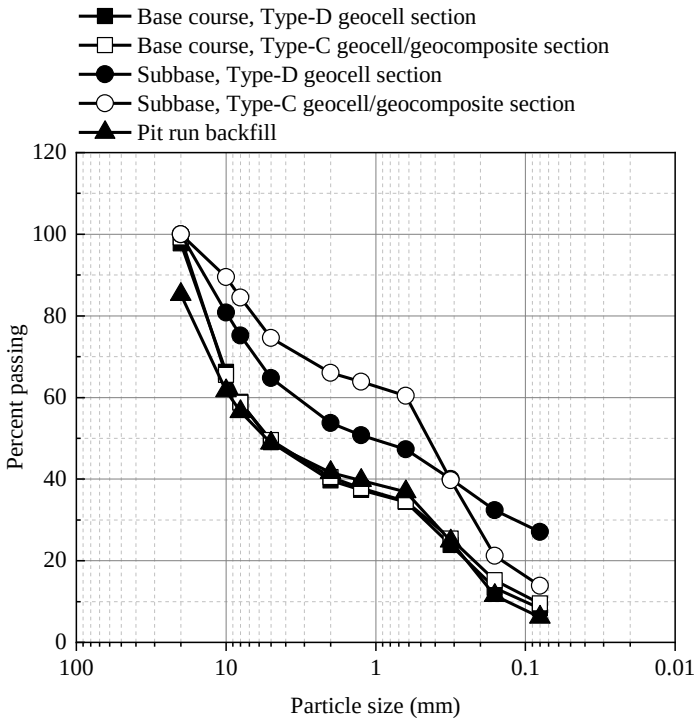

Fig. 6.4. Particle size distribution of materials in test sections

Table 6.3. Soil properties of each pavement layer

Properties	Base course	Subbase		Pit run backfill	Test standard
		Type-D geocell	Type-C geocell & geocomposite		
Mean particle size (mm)	5.142	1.115	0.471	5.465	
Uniformity coefficient	96.63	46.26	7.79	68.12	ASTM D6913
Curvature coefficient	0.31	0.05	1.09	0.16	
Fines content (%)	9.5	27.1	13.9	6.1	ASTM C117
Optimum moisture content (%)	4.4	11.2	7.7	6.7*	ASTM D698
Maximum dry density (g/cm^3)	2.14	1.95	2.11	2.18*	AASHTO T224*

*A= subbase in Type-D geocell section; B= subbase near the joint of Type-C geocell section and geocomposite section.
**Values are corrected for oversized particle (>19 mm) according to AASHTO T224.

After the compaction of base courses, DCP tests were performed in 50 mm increments in each section in accordance with ASTM D6951/D6951M. The in-situ CBR values and resilient modulus (M_r) were estimated based on the DCP test results, as given by Equation (6-1) (ASTM D6951/D6951M) and Equation (6-2) (Ali, 2005; Powell et al., 1984), respectively.

$$CBR = 292/DCP^{1.12} \text{ for DCP in mm/blow} \quad (6\text{-}1)$$

$$M_r = 17.62 CBR^{0.64} \quad (6\text{-}2)$$

Table 6.4 presents the estimated resilient modulus. It is evident that the modulus profiles remained similar between Type-C geocell and geocomposite sections, while appreciable discrepancies were found in Type-D geocell section, which had approximately 60% higher resilient modulus in base courses but 60% smaller resilient modulus in subbases and pit run materials than the other two sections.

Table 6.4. Resilient modulus of road test sections based on DCP results

Layer materials	Layer No.	Layer thickness (mm)	Resilient modulus (MPa)		
			Type-D geocell	Type-C geocell	Geocomposite
Base course	1	50	184.4	146.9	156.9
	2	50	261.1	164.0	173.2
	3	50	287.1	183.4	178.7
	4	50	277.6	152.6	169.4
	5	50	256.0 [a]	138.2	167.2
	6	50	216.4	141.3	159.5
	7	50	- [b]	-	175.1 [c]
Subbase	8	50	101.2	79.0	103.1
	9	50	135.3	129.8	186.2
	10	50	115.5	235.6	246.8
	11	50	93.3	297.7	270.7
	12	50	89.8	284.1	264.2
	13	50	99.2	229.9	288.7
Pit run material	14	50	115.0	269.2	260.2
	15	50	115.4	184.1	249.2
	16	50	107.1	155.4	210.7
	17	50	87.7	151.8	210.3
	18	50	84.9	181.1	211.6

[a] Shadow represents the soil layers stabilized by geocells.
[b] 300-mm thick base courses at geocell sections
[c] Dash line represents the location of geosynthetics.

6.3.3 Instrumentation

Fig. 6.5 illustrates the locations of the sensors in each section along with the location of a weather station and a data acquisition system near the Type-C geocell section and the geocomposite section. The sensors in each section were located 10 m from the intersection of the two adjacent sections. This distance effectively mitigated the boundary effect from the

neighboring sections while also minimizing the length of sensor cable required for connecting to a data acquisition system. A remote monitoring station that integrates the data acquisition system with a weather station was installed near the junction of the Type-C geocell and geocomposite sections (Fig. 6.5), so the real-time data from both these sections could be taken. Three types of sensors were installed in each test section: RST Instruments® LPTPC12-S earth pressure cells, Omega® and Thermo-Kinetics® Type-T thermocouples, and Meter Group® EC-5 moisture sensors. The accuracies of earth pressure cells, moisture sensors and thermocouples are 0.15% full scale, ±0.03 m^3/m^3 in mineral soils, and ±1°C or ±0.75% whichever is greater, respectively.

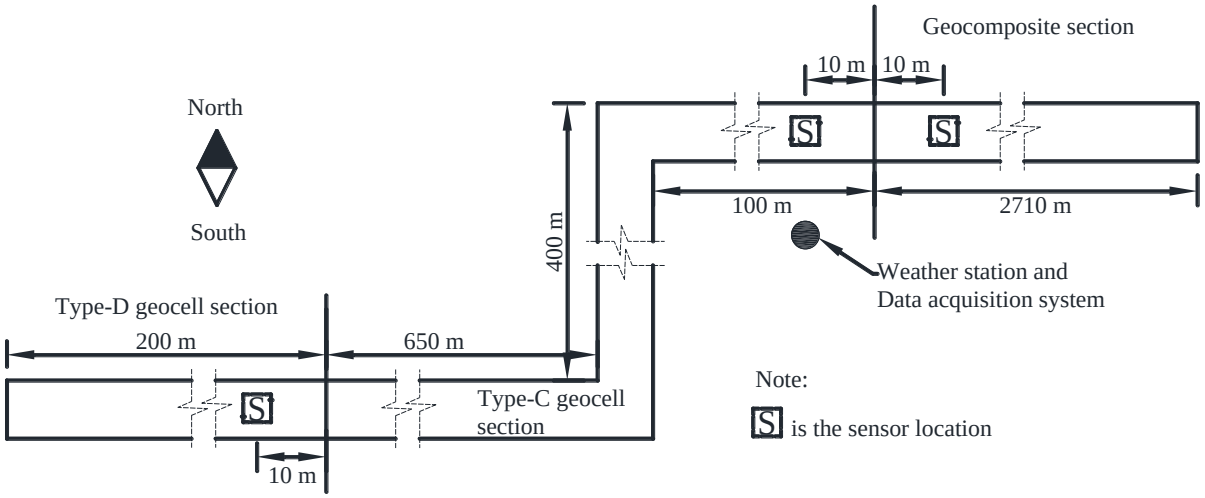

Fig. 6.5. Illustration of locations of sensors and data acquisition system

Figs. 6.6(a) and 6.6(b) show the detailed positions of the sensors in the Type-C geocell and geocomposite sections. All the sensors were installed in the east-bound lane during the construction of subbases and base courses. In each test section, earth pressure cells, thermocouples, and moisture sensors were placed separately in the longitudinal direction to minimize the interference between them. Two earth pressure cells, each with distinct measurement capacities of 2 MPa and 500 kPa, were placed at the base-subbase interface to measure the distributed stress over the subbase. The 500 kPa capacity was traditionally selected to monitor traffic loads, while

the larger capacity of 2 MPa was chosen to accommodate scenarios involving exceptionally high pressure that exceeded the conventional measurement range. These cells were positioned 2.22 m apart to capture the load from the wheels. This distance was informed by both the axle width specifications prevalent in Alberta and the dimensions of the trailers used for the trafficking load tests. The higher capacity pressure cell was located below the inner wheel path (i.e., E1) while the lower capacity pressure cell below the outer wheel path (i.e., E2). The actual positions of E1 and E2 in all test sections were shifted approximately 30 cm towards the pavement edge than the intended and those in the Type-C geocell section was shifted 14 cm greater than in the geocomposite section. This is because the edge lines for the lanes were not considered while positioning the earth pressure cells in the original design. As such, the earth pressure cells might not be located directly below the main paths of public traffic; however, during the short-term tests, the plate loads and trafficking wheel loads were applied directly above the earth pressure cells. In each test section, five moisture sensors and six thermocouples were installed at varying depths. Two moisture sensors were positioned at the same height above the base-subbase interface with one at the lane centerline (i.e., M1) and the other at the pavement edge (i.e., M5) and the remaining three sensors (M2 to M4) were embedded in subbases at the lane centerline. This arrangement was intended to detect the changes in moisture contents near the geosynthetics during the F-T process in the horizontal and vertical directions. Two thermocouples were embedded in the base courses at different heights from the base-subbase interface and the remaining four located in the subbases and pit run backfill. As with the Type-C geocell and geocomposite sections, the Type-D geocell section maintained the same sensor layout, with the only difference being the absence of moisture sensors at the pavement edge (M5) and within the subbase, the sensor M3 was positioned at the depth of 465 mm.

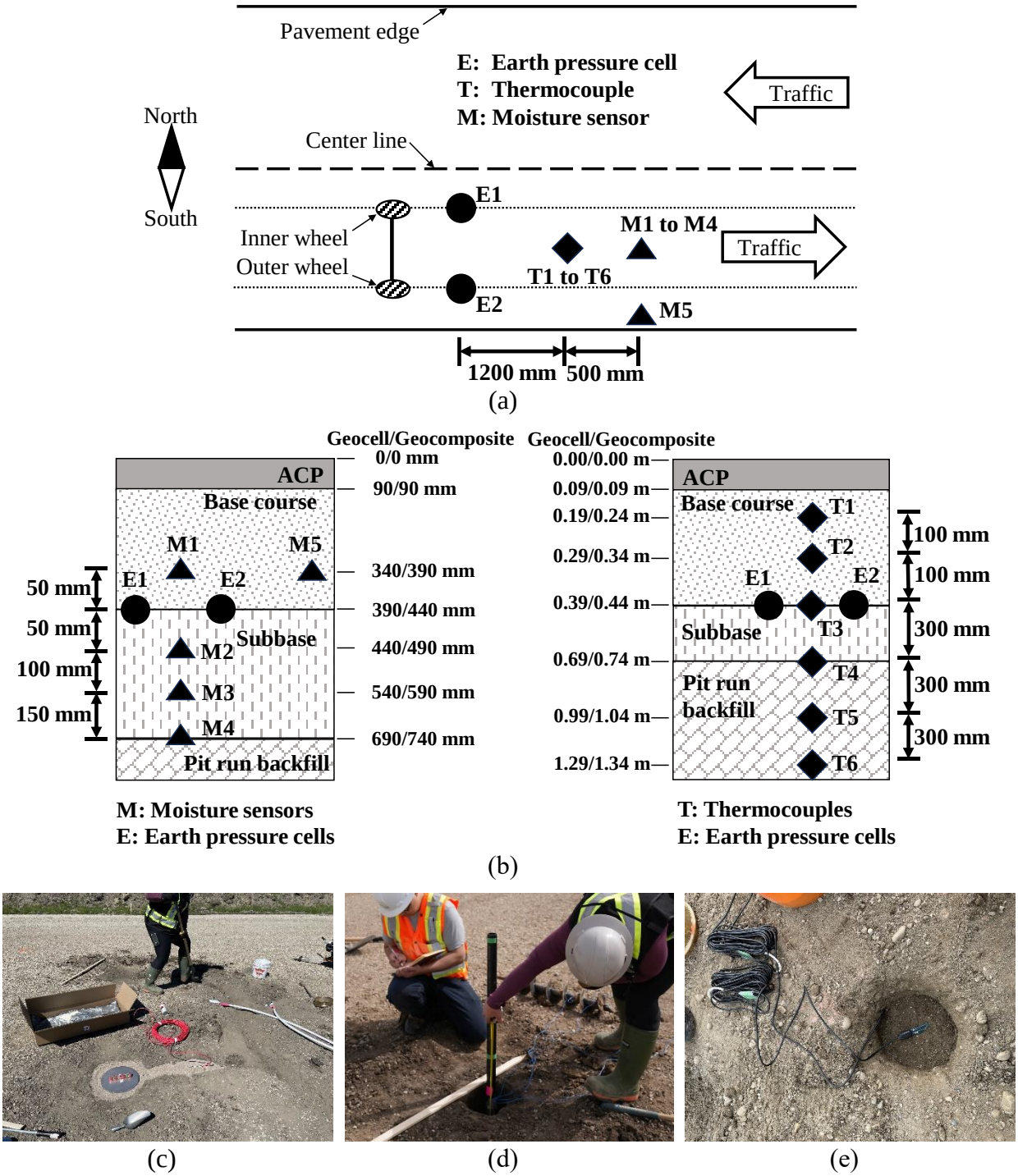

Fig. 6.6. Instrumentation of sensors in Type-C geocell and geocomposite sections: (a) top view, (b) cross-section view, (c), (d) and (e) installation of earth pressure cells, thermocouples, and moisture sensors, respectively

Figs. 6.6(c) to 6.6(d) present photographs of earth pressure cells, thermocouples, and moisture sensors in the subbase being installed, respectively. The installation procedures were generally

established based on the installation approaches reported from the previous field studies (Genc, 2019; Saevarsdottir et al., 2016; Swett et al., 2008; Timm et al., 2004). The earth pressure cells were installed following the following steps: 1) creating two shallow cavities at the subbase surface, 2) backfilling the cavities with a thin layer of air-dry sands and leveling the sand surface, 3) positioning the cells atop the sand surface, and 4) covering the cells with sand pads. The placement of sands around the cells could avoid the direct contact of the sensors with sharp-edged gravels. Thermocouples and moisture sensors were installed differently below and above the base-subbase interface. Below the interface, a borehole was required to embed the thermocouples and moisture sensors as the subbase and pit run backfill had been in place, while above the interface, they were placed during the construction of the base courses. To facilitate the installation of thermocouples below the interface, a rigid PVC tube, outfitted with four thermocouples spaced 300 mm apart, was inserted into the borehole. The in-situ soils were then backfilled and compacted around the tube. Additionally, the hollow of the PVC tube was filled with the soils to minimize the thermal influence of air on the measurements of soil temperature. Below the base-subbase interface, the moisture sensors were laid horizontally at predetermined depths in the borehole and covered with compacted backfills made of subbase materials sieved through a No.4 sieve (4.75 mm). A trench was dug near the cavities and boreholes to accommodate all sensor wires protected by PVC tubes.

Above the base-subbase interface, thermocouples and moisture sensors were installed following the placement of geosynthetics. To accurately position the thermocouples, small PVC tubes and long nails, both attached with the sensors, were used in the two geocell sections and the geocomposite section, respectively. The moisture sensors were placed at the predetermined heights and covered with the same base course materials with particles of >4.75 mm being removed. All the sensor wires enclosed in PVC tubes were extended horizontally beyond the

pavement edge. The horizontal positions of all the sensors were surveyed during the installation so that their locations could be accurately identified post-ACP paving.

All the wires from sensors below and above the base-subbase interface were connected to terminals located at the corresponding pavement shoulders. In the Type-D geocell section, the terminal was a plastic four-way hub, where readings were taken manually by plugging the wires into the datalogger during the plate load tests or trafficking load tests. In contrast, in the Type-C geocell and geocomposite sections, the terminal was a remote monitoring station set up near their border. Powered by the solar, it can continuously take the readings from the sensors in both test sections. This station customized by Campbell Scientific® housed a data acquisition system (a CR1000X datalogger component with its extension module AM16/32B multiplexer), a remote communication component (CELL205 cellular module and C2446 antenna), a power supply component (BP26 12-V rechargeable battery and SP50-L 50-W solar panel), and a weather station. The weather station comprised a Type 109 thermistor housed in a solar radiation shield and a TE525M tipping rain gauge to monitor the air temperatures and precipitation on site, respectively. The accuracies of the thermistor and rain gauge are ±0.6°C and ±1%, respectively. Key components, such as the data acquisition system and cellular module, were securely placed. This plastic container was then housed within a robust wooden enclosure and buried in the ground. This triple-layer protection was implemented to ensure the uninterrupted operation of the system, particularly in remote areas where environmental hazards and potential wildlife interference were common occurrences. Data from sensors embedded in both test sections and those installed at the weather station were collected by a datalogger and transmitted wirelessly to a central data server. This data can be conveniently accessed and downloaded to a computer using a specialized program designed for remote monitoring and retrieval.

It is also worth noting that the terminals for the Type-C geocell section and the geocomposite section were situated beyond the drainage ditches which were excavated after the completion of pavement construction. This necessitated additional lengths of wires for thermocouples and moisture sensors in these two sections. The wires were extended by 7.6 m (25 ft) and 30.5 m (100 ft) for the Type-C geocell section and the geocomposite section, respectively.

6.4 Field tests and long-term monitoring

After the completion of the pavement construction and sensor installation, a comprehensive test program was implemented, comprising both short-term tests and long-term monitoring. The short-term tests, conducted on the finished ACP surface in all test sections, included plate loading tests and trafficking tests. These were performed both before and after the first seasonal F-T cycle-i.e., before ground freezing in winter and right after ground thawing in the following spring. The long-term monitoring was performed exclusively for the Type-C geocell and geocomposite sections, which were open to public traffic throughout the entirety of the seasonal F-T cycle.

6.4.1 Field tests

The field tests were performed on November 3rd and 4th 2022 (before ground freezing) and then on May 15th to 17th 2023 (right after ground thawing). Three types of plate loading tests were carried out, featuring varying loading cycles and amplitudes: i.e., standard test, monotonic test, and cyclic test. The details of the test program are given in Table 6.5. Standard test was implemented in accordance with ASTM D1195/D1195M to determine the strain modulus of the test sections. Monotonic test, aiming to evaluate the performance under high loading conditions, imposed only one loading cycle with the greatest amplitude among the three types of plate loading tests (Huang et al., 2023; Pokharel et al., 2010). Cyclic test, which intended to investigate the

pavement responses under low-frequency cyclic loading, applied the most loading cycles among the three types of tests (McCartney et al., 2010).

Table 6.5. Program of plate loading tests

Test No.	Test type	Loading cycle	Maximum applied pressure (kPa)	Loading details (kPa)
1	Standard test	2	500	1st loading cycle:10, 80, 160, 250, 330, 420, 500 1st unloading: 250, 125, 10 2nd loading cycle: 80, 160, 250, 330, 420
2	Monotonic test	1	900	Loading: 10, 200, 400, 800, 900 Unloading: 450, 225, 10
3	Cyclic test	10	552	Loading per cycle: 10, 250, 552 Unloading per cycle: 125, 10

Fig. 6.7(a) illustrates the plate loading test setup at the project site. It was composed of a hydraulic jack connected to a hand pump with a high-pressure hose, a 300-mm diameter steel loading plate, and reference beams for mounting three dial gauges. The loading plate, located exactly above the earth pressure cell E1 [Fig 6.6(a)] was placed on the ACP surface. To ensure the full contact and uniform stress distribution between the plate and ACP surface, a thin layer of fine sands was added in between. The load was applied by the hydraulic cylinder, controlled by the pump. The load was monitored by a Dwyer® DPG-111 digital pressure gauge, mounted on the pump while the plate movement was measured by three dial gauges, placed evenly along the perimeter of the loading plate. The digital pressure gauge and the dial gauges had capacities of 34.5 MPa and 25 mm, respectively. Their corresponding accuracies were 0.25% of the full scale for the pressure gauge and 0.01 mm for the dial gauges. After completing the test setup, a preload of 10 kPa was applied for 30 seconds, and the resulting displacements were recorded. Subsequently, the loads were applied incrementally based on the schedule listed in Table 6.5. At

each increment, the load was maintained until the plate movement became stable before the next loading stage was applied. Besides the applied pressure and plate movement, the vertical stress at the base-subbase interface was measured by the earth pressure cell at a minimum sampling rate of 10 Hz.

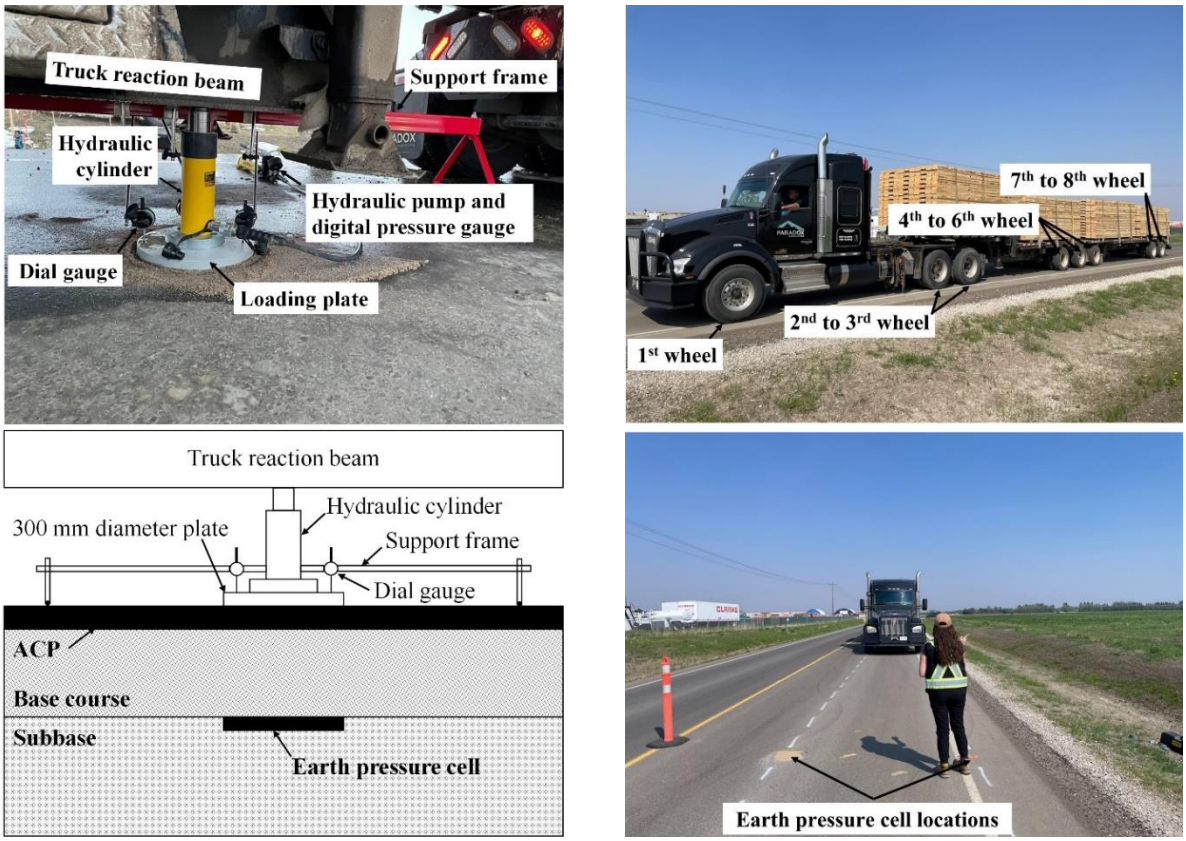

(a) (b)

Fig. 6.7. Photographs of: (a) plate loading tests and (b) trafficking tests

Following the plate loading tests, trafficking tests [Fig. 6.7(b)] were conducted to simulate realistic traffic loads. The trafficking tests involved a 40-ton trailer with eight axles traversing over the locations of two earth pressure cells [E1 and E2 in Fig. 6.6(a)] at each test section. The earth pressure readings were taken at the sampling rate of 100 Hz as the wheels of the trailer passed over the sensor locations. The first set of tests implemented in November 2022 only imposed two passes of wheel loads to each test section with a forward speed of 5 km/h and a backward speed

of 2-3 km/h in each pass. During the testing, it was noted that challenges remained in ensuring the passage of all the wheels through the designated points on the ACP surface below which the two earth pressure cells were located, particularly when the trailer was moving in reverse. Moreover, due to the lack of checking tire pressures during the tests, the tire pressures might not be kept at the same level among the wheels. The pressures of tires under the same wheels could vary between test sections too. The lessons learnt from the tests in 2022 informed the refined procedure in the second set of trafficking tests in May 2023. The trailer was run only in the forward direction per pass for a total of four passes, and the speed was maintained at 5 km/h. To guide the trailer to pass through the designated points, two temporary straight lines were marked on the ACP surface and an engineer was on site to direct the driving path. Additionally, all tire pressures were maintained at 758 kPa (110 psi) after the trailer was loaded for all the tests.

6.4.2 Long-term monitoring

Long-term monitoring was carried out in the Type-C geocell and geocomposite sections by continuously collecting the data of temperature, moisture content, and vertical stress in the test sections as well as the air temperature and rainfall starting November, 2022. During the period of September to November 2022, the test sections were still under construction, or the sensor installation was still undertaken; therefore, the temperatures and moisture contents were measured manually. Since November 25th, 2022, the data have been collected automatically by the data acquisition system, which was programmed to record soil temperatures, moisture contents, air temperatures and precipitation at one-second intervals, with hourly averages being logged. The recording of earth pressure cells was initially set at the sampling rate of 20 Hz. However, such a high sampling rate led to a dysfunction of the data acquisition system, resulting in a loss of data points from December 14th, 2022, to February 16th, 2023. Thereafter, the sampling rate for the

earth pressure cell recording was reduced to 10 Hz to ensure the functioning of future data collection.

As described previously, wire extensions were added to accommodate the construction of the pavement ditches. For the moisture sensors, the additional wire length could result in extra electrical resistance, thereby significantly increasing the voltage outputs and affecting the measurement accuracy. To establish the correct relation of voltage outputs to gravimetric moisture contents, calibration tests on EC-5 moisture sensors were imperative. The test materials were the base courses and subbases passing a No. 4 sieve, and they were prepared with the compaction degrees of 95% and 100%, which replicated the in-situ conditions of materials around the moisture sensors. The calibration tests were performed in reference to Method A as recommended by Meter Group®. Fig. 6.8 presents the calibration test results for base course and subbase collected from the three test sections. It should be noted that although the subbases between the Type-C geocell section and the geocomposite section were similar (Table 6.3), their calibration for moisture contents was different (Fig. 6.8) due to the different lengths of the wire extensions for the moisture sensors in these two sections. The relation of voltage outputs and gravimetric moisture contents was fit with the polynomial regression, as given in Equation (6-3).

$$y = A \times x^3 + B \times x^2 + C \times x + D \quad (6\text{-}3)$$

where x is the voltage output of moisture sensors (mV); y is the gravimetric moisture content (%); A, B, C and D are the parameters derived from the fitting curves, which are summarized in Table 6.6.

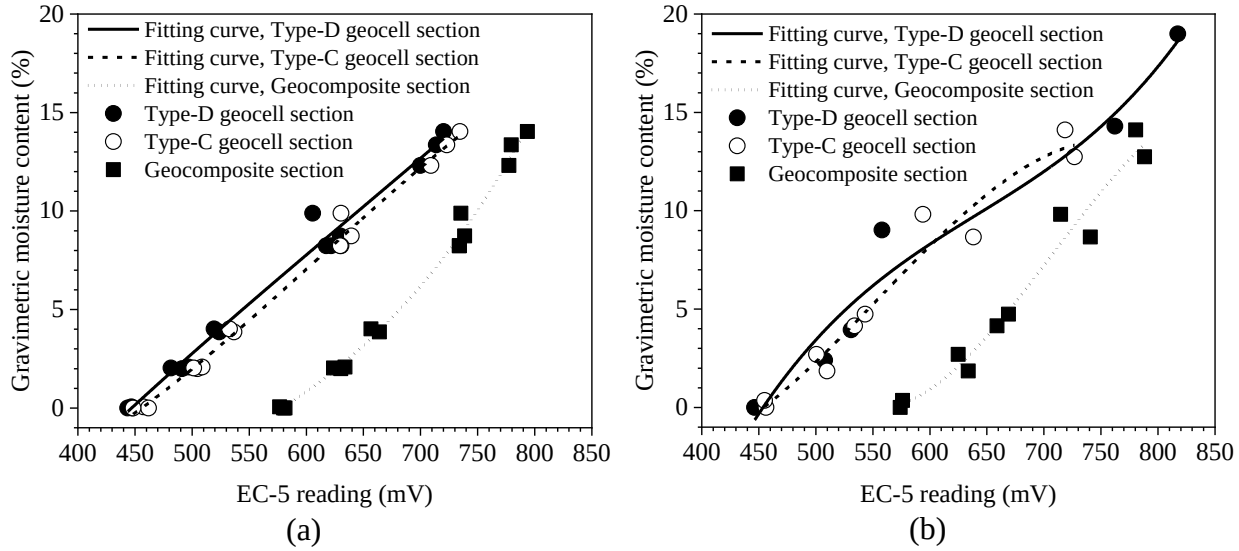

Fig. 6.8. Calibration of moisture sensors in three test sections at: (a) base courses and (b) subbases

Table 6.6. Parameters for water content determined in the calibration tests

Soil type	Geosynthetics section	Parameter value				
		A	B	C	D	R^2
Base courses	Type-D geocell section	3.5997E-08	-6.9650E-05	9.3930E-02	-3.1286E+01	0.9860
	Type-C geocell section	-1.4264E-07	2.6113E-04	-1.0680E-01	7.9325E+00	0.9925
	Geocomposite section	2.3265E-07	-3.2075E-04	1.7512E-01	-3.9028E+01	0.9927
Subbases	Type-D geocell section	4.6805E-07	-9.0100E-04	6.1385E-01	-1.3675E+02	0.9600
	Type-C geocell section	-5.0496E-07	8.4125E-04	-4.0698E-01	5.8616E+01	0.9619
	Geocomposite section	-1.0703E-06	2.2700E-03	-1.5308E+00	3.3280E+02	0.9676

6.5 Results and discussion

The outcomes of this field project encompassed short-term field test results of plate loading tests and trafficking tests immediately before the first seasonal F-T cycle (November 2022) and right after it (May 2023), and the long-term continuous monitoring of soil temperature, moisture content and traffic induced stress over the subbase in the period from November 2022 to August 2023.

6.5.1 Short-term field tests

6.5.1.1 Plate loading tests

The results of plate loading tests were represented by applied pressure-displacement curves and load transfer. The replacement-related parameters (i.e., strain modulus and stiffness) could be determined from the pressure-displacement curves. Meanwhile, the vertical stress distributed over deeper pavement layers is a critical factor in the pavement design (Huang, 2004). The load transfer ratio, defined as a ratio of the measured stress at the base-subbase interface to the applied stress on the pavement surface, was therefore utilized to understand the load transfer in the pavements. Moreover, to normalize the influence of base thickness on the stress distribution, stress distribution angle was introduced (Giroud and Han, 2004a) in Equation (6-4).

$$tan\theta = \frac{b}{2h}\left(\sqrt{\frac{p_0}{p_1}} - 1\right) \quad (6\text{-}4)$$

where, θ = the stress distribution angle (°); b = the diameter of the loading plate (mm); h is the depth between the pavement surface and the subbase surface (mm). p_0 = the applied stress by the loading plate (kPa); p_1 = the stress measured by the earth pressure cell (kPa). In this study, the load was transferred through two layers (ACP and bases) before reaching the subbase; therefore, the stress distribution angle given by Equation (6-4) was an equivalent angle for the composite two layers. In general, a less load transfer ratio or a higher stress distribution angle indicates more effective geosynthetics stabilization in the base courses.

Repeatability of the test results

The repeatability of the plate loading tests was examined at the Type-C geocell section where repeated tests were conducted during the monotonic and cyclic tests in 2023. The results of repeated tests are depicted in Fig. 6.9, alongside comparative outcomes from the Type-D geocell and geocomposite sections.

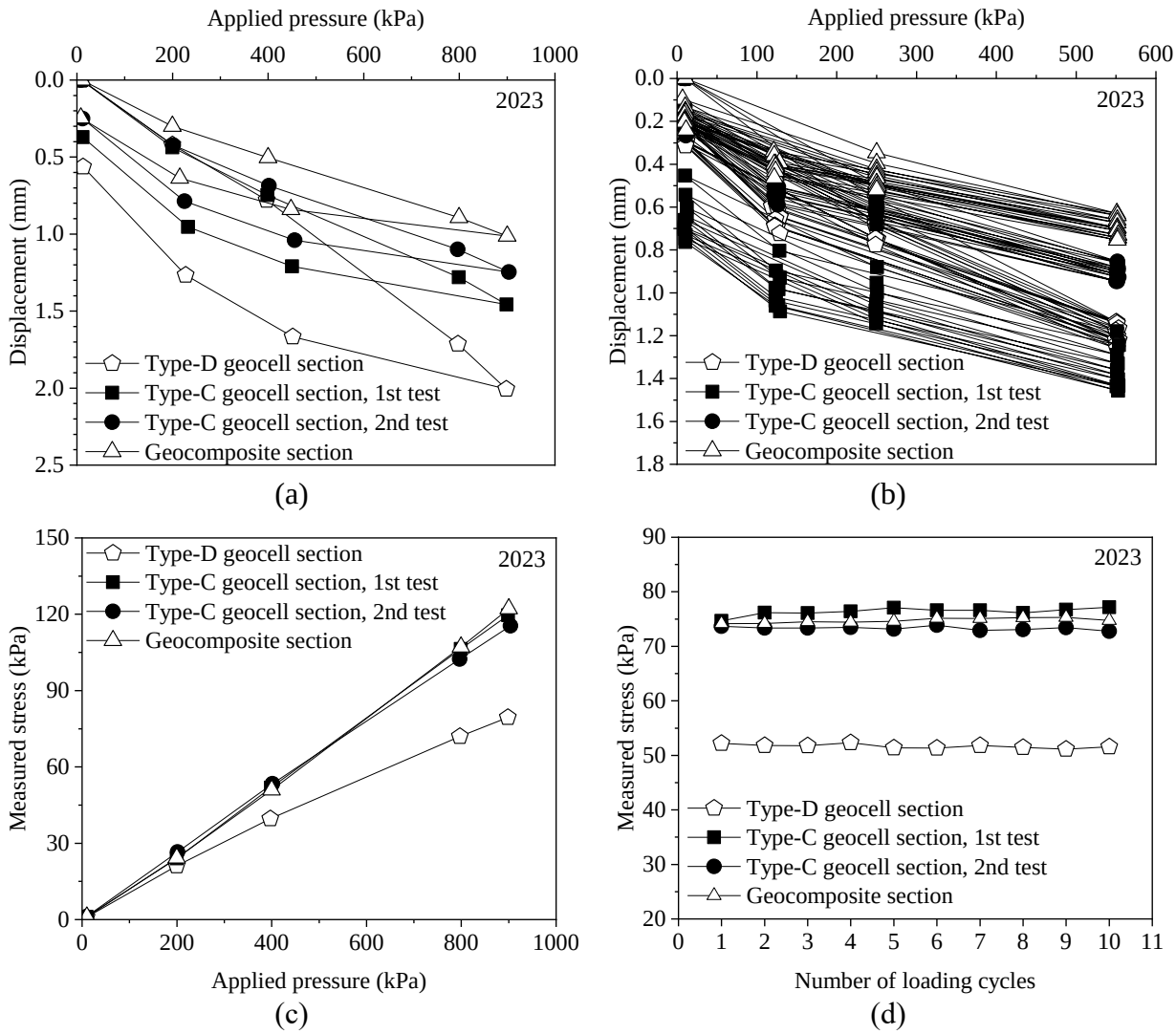

Fig. 6.9. Plate loading test results after seasonal freeze-thaw cycle: (a) and (b) pressure-displacement curves from monotonic tests (one cycle) and cyclic tests (10 cycles), respectively; (c) and (d) measured stress at base-subbase interface from one-cycle and ten-cycle loading tests, respectively

Figs. 6.9(a) and 6.9(b) reveal that based on the monotonic tests and cyclic tests, the maximum displacement of ACP surface in all test sections was below 2 mm. Such a marginal range of displacement raised concerns that the results might be sensitive to measurement errors or uncertainties: these included the seating effect, small disturbances to the sand layer between the loading plate and ACP surface, and variations in properties within the pavement sections. For instance, in the cyclic tests on the Type-C geocell section [Fig. 6.9(b)], a marked discrepancy in

the maximum displacement was observed between the two repeated tests, with the first test exhibiting up to 54% larger displacement than the second test. In contrast to displacement, the vertical stress measured at the base-subbase preserved a higher degree of consistency and reliability as demonstrated in Figs. 6.9(c) and 6.9(d). As can be seen, there were only 3%-6% differences in the measured values between the repeated tests on the Type-C geocell section.

Considering the potential uncertainties in displacement measurements and the higher consistency in vertical stress outcomes, the load transfer ratio and stress distribution angle are chosen as the primary indicators for quantifying the effectiveness of geosynthetics stabilization in improving the pavement performance under seasonal F-T cycles among the three test sections. The pressure-displacement results are used only as supplementary data for qualitative assessment.

Monotonic tests

Fig. 6.10 displays the result of the applied pressure-displacement curves measured at the three test sections. Despite being less reliable, this result is still presented for completeness and qualitative assessment. The figure clearly shows that after one seasonal F-T cycle, the displacement at the three test sections increased. This indicated the degradation of pavement stiffness. Nonetheless, the maximum displacement (measured at 900 kPa) ranging from 0.8 to 2.1 mm, was still small. It is noted that among the three test sections, the Type-D geocell section exhibited the most significant increase in the maximum displacement due to the F-T impact. This was attributed to the high fines content in the subbases in this section, which, as shown in Table 6.3, was twice that in the other two sections. According to Huang et al. (2023), the increased proportion of fines weakened the stiffness after F-T cycles, thus inducing larger displacement under plate loads.

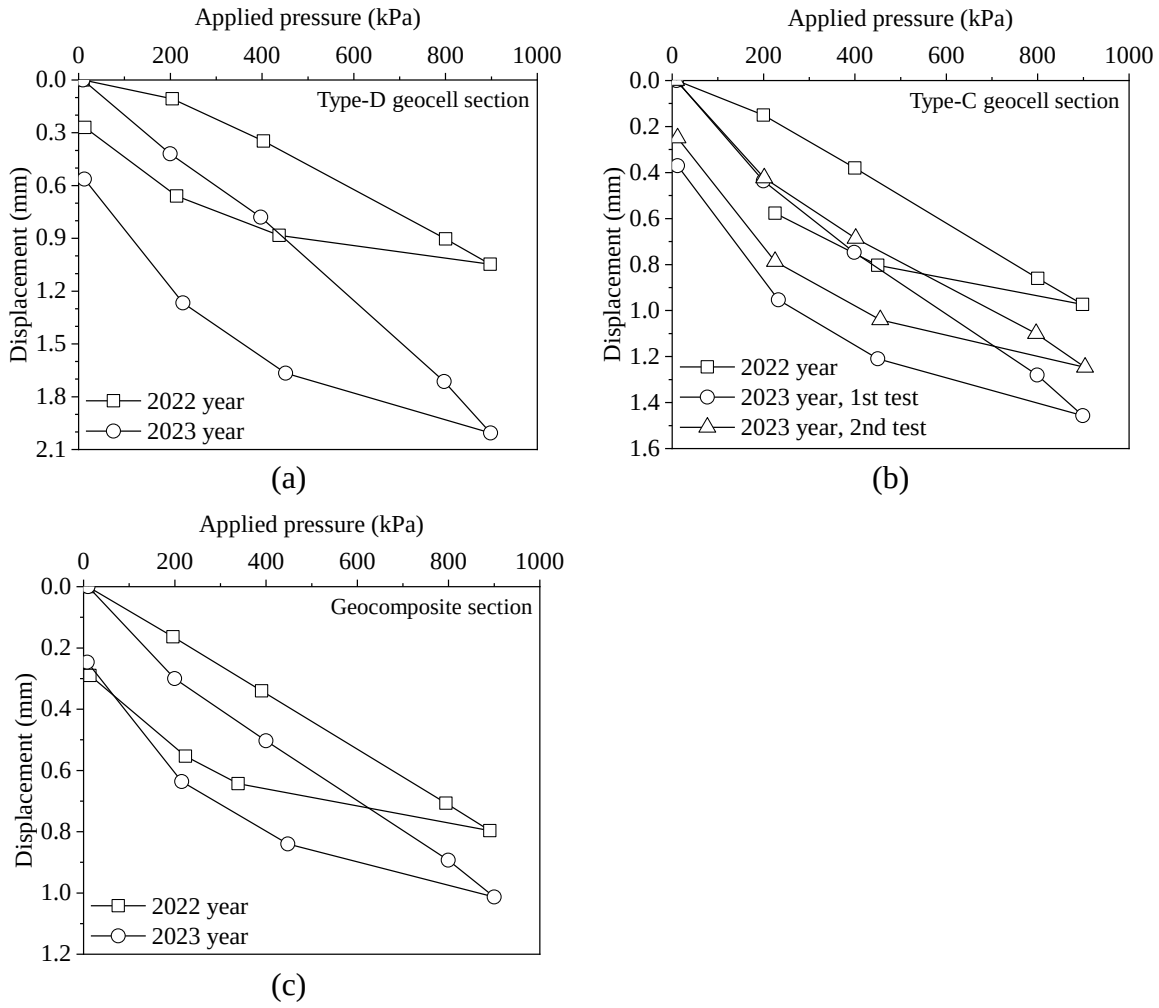

Fig. 6.10. Pressure-displacement curves of monotonic tests before (2022) and after (2023) seasonal freeze-thaw: (a) Type-D geocell section, (b) Type-C geocell section, and (c) geocomposite section

Fig. 6.11(a) presents the load transfer ratio at various loading stages for the three test sections. Before the first F-T cycle (i.e., in November 2022), as the applied load increased, the load transfer ratio for the Type-D geocell section increased slightly and then stabilized, whereas that for the Type-C geocell and geocomposite sections exhibited a substantial increase. The increase in the ratio suggests that a greater extent of subbase was engaged to respond the higher applied load, with the stiffer deep subbase in the Type-C geocell and geocomposite sections could have attributed to attracting greater load transfer. This result was aligned with the modulus profile presented in Table 6.4. After the seasonal F-T cycle (i.e., in May 2023), the load transfer ratio varied slightly with

the increase in the applied load. For the Type-D geocell section, this ratio even decreased with the applied load. In comparison, the seasonal F-T cycle generally caused the decrease in the transfer ratio, especially when the test sections were subjected to the high applied loads (e.g., 800 or 900 kPa). The less load transfer to the subbase might be due to 1) the stiffening effect of geosynthetics that slowed down the F-T induced degradation in the base courses and 2) the greater F-T induced decrease of stiffness in subbases than in bases as subbases contained greater fines content (Table 6.3). The observed decrease in the load transfer ratio with increasing applied load in the Type-D geocell section might be associated with the greater degradation in the deeper subbases (Layers 10-13 in Table 6.4) than in the other two test sections. Fig. 6.11(b) presented the distribution angle for each test section before and after the season F-T cycle. While the Type-C geocell and geocomposite sections exhibited similar load transfer ratios under high applied loads (i.e., 800 and 900 kPa), they displayed distinct differences in stress distribution angles, with the former having an angle 4° to 5° greater than the latter. This was due to that the stress distribution angle has normalized the effect of the base thickness on the stress distribution. As described previously, the geocomposite test section had 50 mm thicker base courses than the other two test sections. As expected, the Type-D geocell section exhibited the largest distribution angles, having an angle 12° to 13° greater than the geocomposite section. This enhanced performance of geocell stabilization in facilitating stress distribution aligned with findings from prior studies (e.g., Divakar et al., 2024; Pokharel et al., 2010), but the above comparisons with load transfer ratio or stress distribution angle could not be directly linked to the relative efficacy of geosynthetics stabilization as a consequence of the drastic smaller modulus in subbases in the Type-D geocell section than in the other two sections. However, the comparison in geosynthetic performance between the Type-C geocell section and the geocomposite section is possible as they had the similar modulus in the

subbase and pit run backfill. The above result demonstrated that the 300-mm Type-C geocell stabilized bases had an equivalent or better F-T performance as the 350-mm geocomposite stabilized bases.

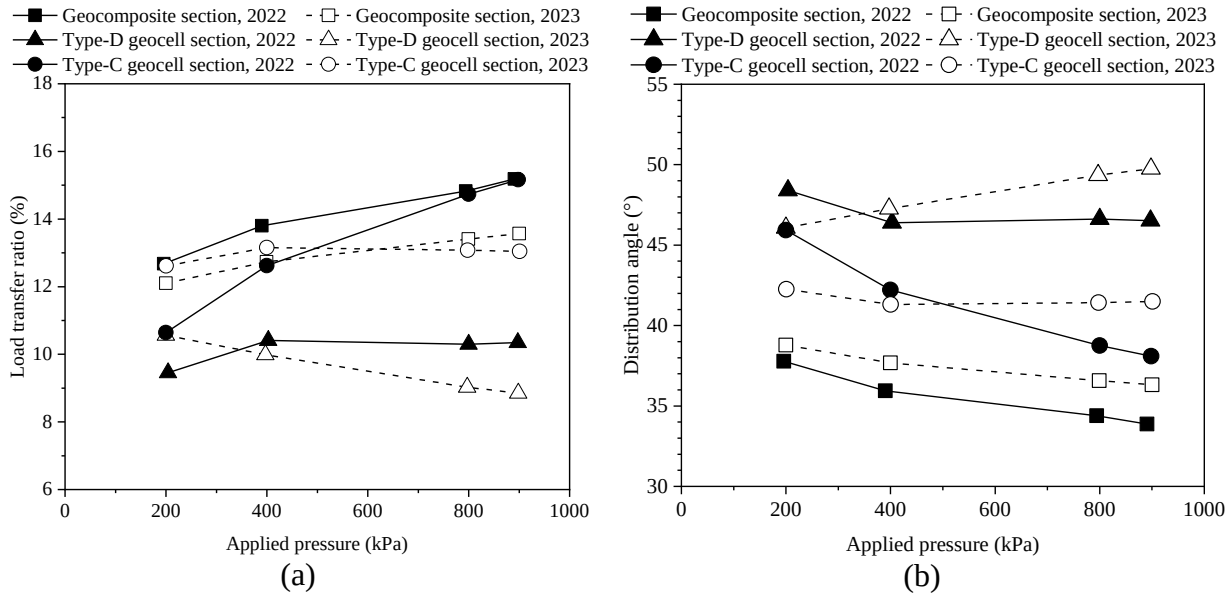

Fig. 6.11. Results of one-cycle loading tests: (a) load transfer ratio and (b) distribution angle before (2022) and after (2023) seasonal freeze-thaw cycle

Cyclic tests

Fig. 6.12 presents the applied pressure-displacement curves of cyclic tests with ten cycles for all test sections. As with the result from monotonic loading tests, the displacement became larger after one seasonal F-T cycle, confirming the negative impact of F-T on the pavement structures; however, the displacement in a range of 0.5 to 1.4 mm was also negligible and inadequate for quantitative analysis. It is also notable that the repeated plate loading induced the cumulative displacement, and the accumulation was relatively small before the F-T cycle but more pronounced after the F-T cycle.

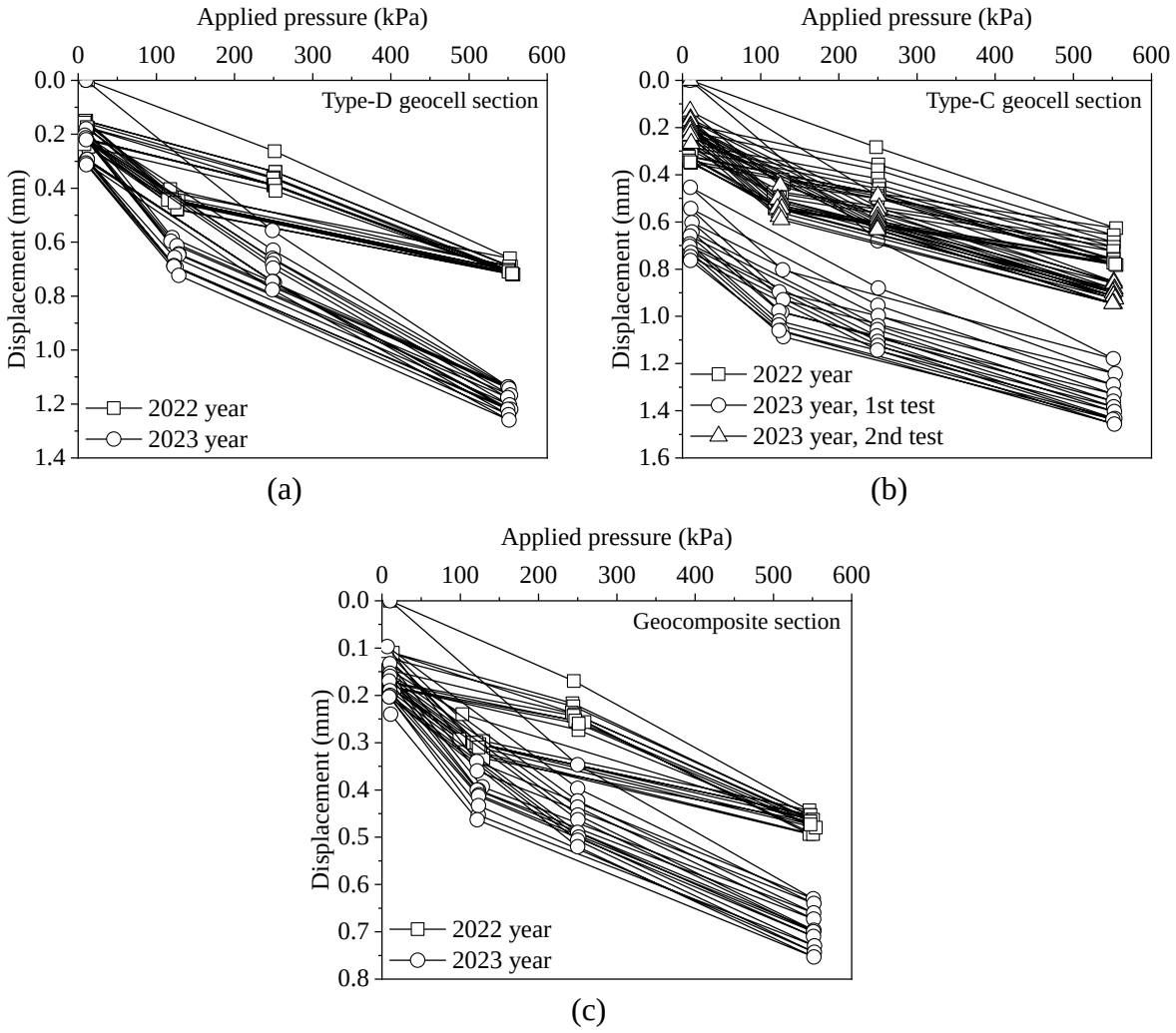

Fig. 6.12. Pressure-displacement curves of cyclic tests before (2022) and after (2023) seasonal freeze-thaw: (a) Type-D geocell section, (b) Type-C geocell section, and (c) geocomposite section

Fig. 6.13(a) illustrates the variations of load transfer ratio with loading cycles before and after the first seasonal F-T cycles based on the cyclic tests. Prior to the seasonal F-T cycle, the load transfer ratios for the Type-D geocell and geocomposite sections remained relatively stable at approximately 10.9% and 14.6%, respectively across the loading cycles, while the values for the Type-C geocell section exhibited a slight rise from about 14.9% to 16.0% with increasing loading cycles. This was due to the discrepancy of the compaction process among these three sections. As introduced in Section 6.2, the Type-D geocell section, completed and opened to the public traffic

since August 2022, had a more stabilized compaction degree due to the prolonged exposure to traffic loads. The sensors embedded in the geocomposite section were situated at the juncture of the second and third construction stages. The pavement layers surrounding these sensors experienced over compaction during the third-stage construction of subbases and base courses (for the Type-C geocell section) by rollers crossing the joint boundary and entering the geocomposite section. In contrast, the Type-C geocell section, which did not experience the additional compaction as did the other two sections. It is noted that the load transfer ratio stabilized when the number of the loading cycles was greater than 7, indicating the pavement structures in Type-C geocell section also reached a steady state as with the other two test sections before the F-T cycle. After the seasonal F-T cycle, lower load transfer ratios were observed across all test sections, which are consistent with the findings from the monotonic tests. The values remained constant with increasing the plate loading cycles. Notably, for the Type-C geocell section and the geocomposite section, the load transfer ratios were overlapped, which is also consistent with what was observed from the monotonic tests [Fig. 6.11(a)]. This was expected as the stiffness of the layers within the two sections was similar. Fig. 6.13(b) presents the stress distribution angles based on the cyclic tests. The increase in the stress distribution angles was noted after the test sections underwent a seasonal F-T cycle. As discussed previously, this is attributed to the greater degradation in subbases than in the geosynthetics stabilized bases, resulting in smaller load transmitted to the subbases. As discussed previously in the Monotonic tests section, comparison of the Type-D geocell section to the other two sections was not possible as the drastic lower stiffness in its subbases; however, the comparison between the Type-C geocell section and the geocomposite section is doable due to comparable stiffness between these two sections. The almost equal load transfer ratio reinforces the previous finding from the monotonic tests that the

300-mm Type-C geocell stabilized bases and the 350-mm geogrid composite stabilized bases performed similar under one seasonal F-T cycle. It should be emphasized that this result was derived in the pavement where geocomposite was embedded between the gravel bases and gravel subbases. This differs from the study of Henry et al. (2005). In their study, geogrids were placed between gravel bases and weak clay subgrade. It was observed that the geogrids provided almost no benefit in resisting F-T damage while geocells played a beneficial role in this regard.

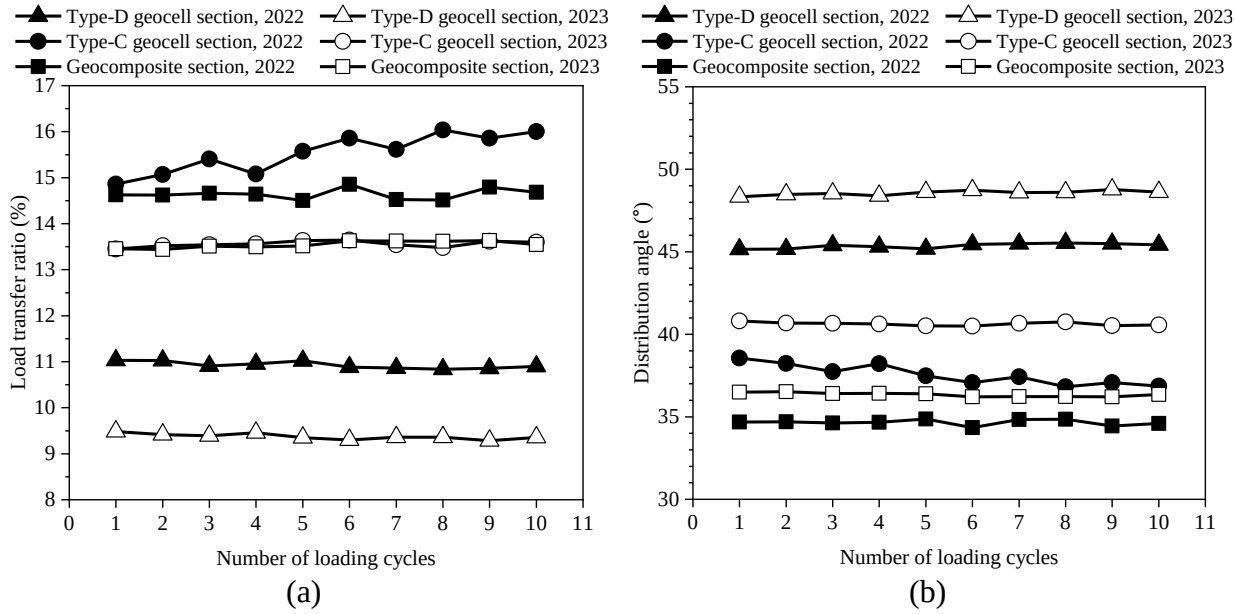

Fig. 6.13. Results of ten-cycle loading tests before (2022) and after (2023) seasonal freeze-thaw: (a) load transfer ratio and (b) distribution angle

6.5.1.2 Trafficking tests

Fig. 6.14(a) presents the typical time history of the vertical stress measured over the subbases during the passage of the trailer in the forward direction when the wheels traversed the ACP surface directly above the locations of the earth pressure cells. The eight distinct peaks occurred when the wheels were exactly above the positions of the earth pressure cells. It is noted that the pressure cells were zeroed before the trafficking tests. After that, the measured stress would represent the stress purely induced by the traffic loads.

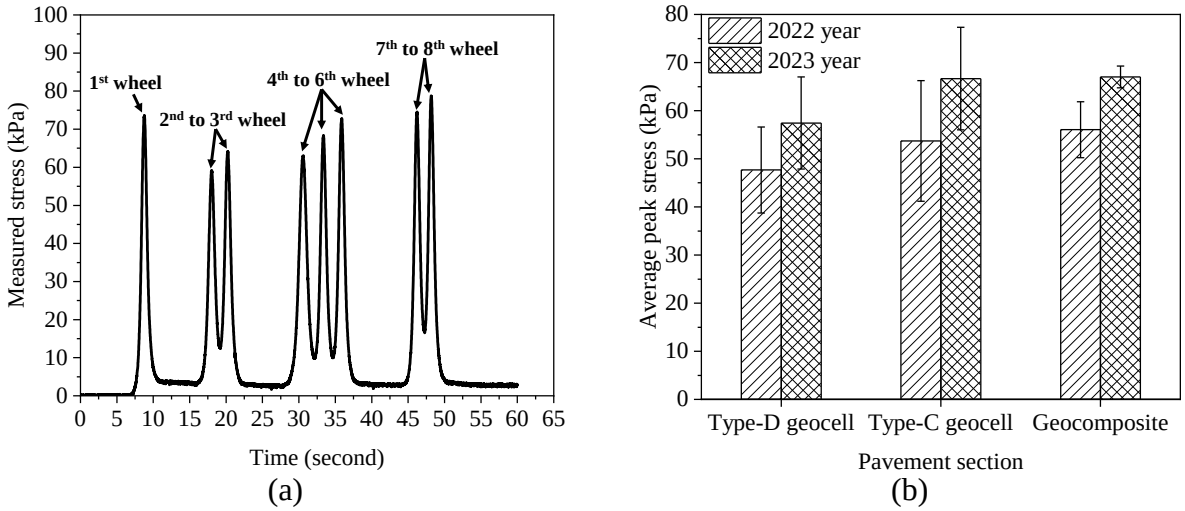

Fig. 6.14. Results of short-term trafficking tests before (2022) and after (2023) seasonal freeze-thaw: (a) time-history response of a forward pass and (b) average peak stress measured by earth pressure cells

In the trafficking tests, benefits of the geosynthetics stabilization in enhancing pavement performance was evidenced through the effective distribution of the vehicle-induced stress over the subbases. The peak pressure measured by two earth pressure cells at each test section was the primary indicator to evaluate the efficacy. It was observed that the discrepancy of the measured stresses between the three driven wheels (the first three wheels) was much greater than that between the five non-driven wheels. Therefore, the peak pressures exerted by the last five wheels (i.e., 4th to 8th wheels) were utilized for the further analysis. Fig. 6.14(b) shows the calculated average peak pressure for those induced by the five non-driven wheels before and after the first seasonal F-T cycles. The peak stresses transferred to the subbases in the Type-C geocell and geocomposite sections were close, despite the latter section having 50 mm thicker base courses than the former. In contrast, the Type-D geocell section exhibited the lowest stress at the base-subbase interface. This was expected as the Type-D section contained stiffer base courses but weaker subbases than the other two sections. After the F-T cycle, the average peak stress was increased in the three sections. The reason for this remains to be investigated with the future tests.

At this stage, it is challenging to attribute this change solely to the F-T effect, considering the difference in tire pressures between the tests conducted in 2022 and 2023. In 2022, the tire pressures were unregulated, whereas in 2023, tire pressures were maintained at 758 kPa (110 psi). The trafficking tests would continue for subsequent seasonal F-T cycles, which would enable gathering more consistent data to sort out the primary cause.

6.5.2 Long-term monitoring

6.5.2.1 Soil temperature and moisture content

Soil temperatures

Figs. 6.15(a) and 6.15(b) depict the daily variations in temperature at different depths for the Type-C geocell section and the geocomposite section, respectively. Each data point in the figure represents the 24-hour average temperature. The figure also includes the daily air temperature. Starting in October 2022, the ground temperatures in these two test sections dropped gradually from the surface. The freezing process commenced in the base courses in late November 2022 and the frost line reached a depth of 1.3 m by mid-December. According to a local geotechnical investigation in southwest Edmonton, it has been determined that the frozen depth can extend up to 2.4 m (City of Edmonton, 2015).

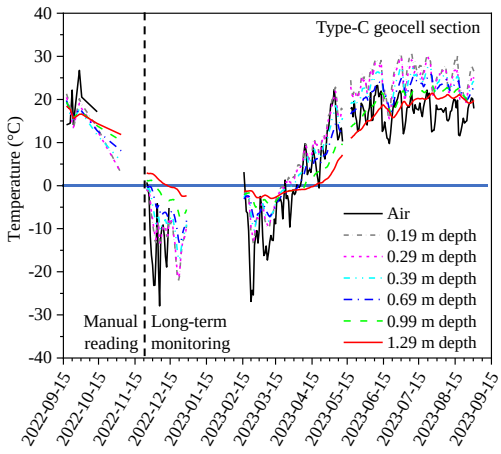

(a)

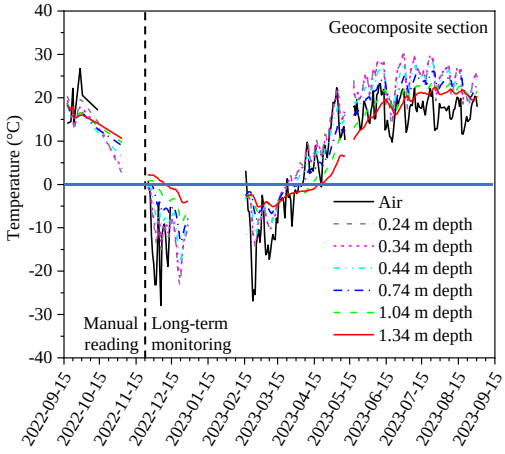

(b)

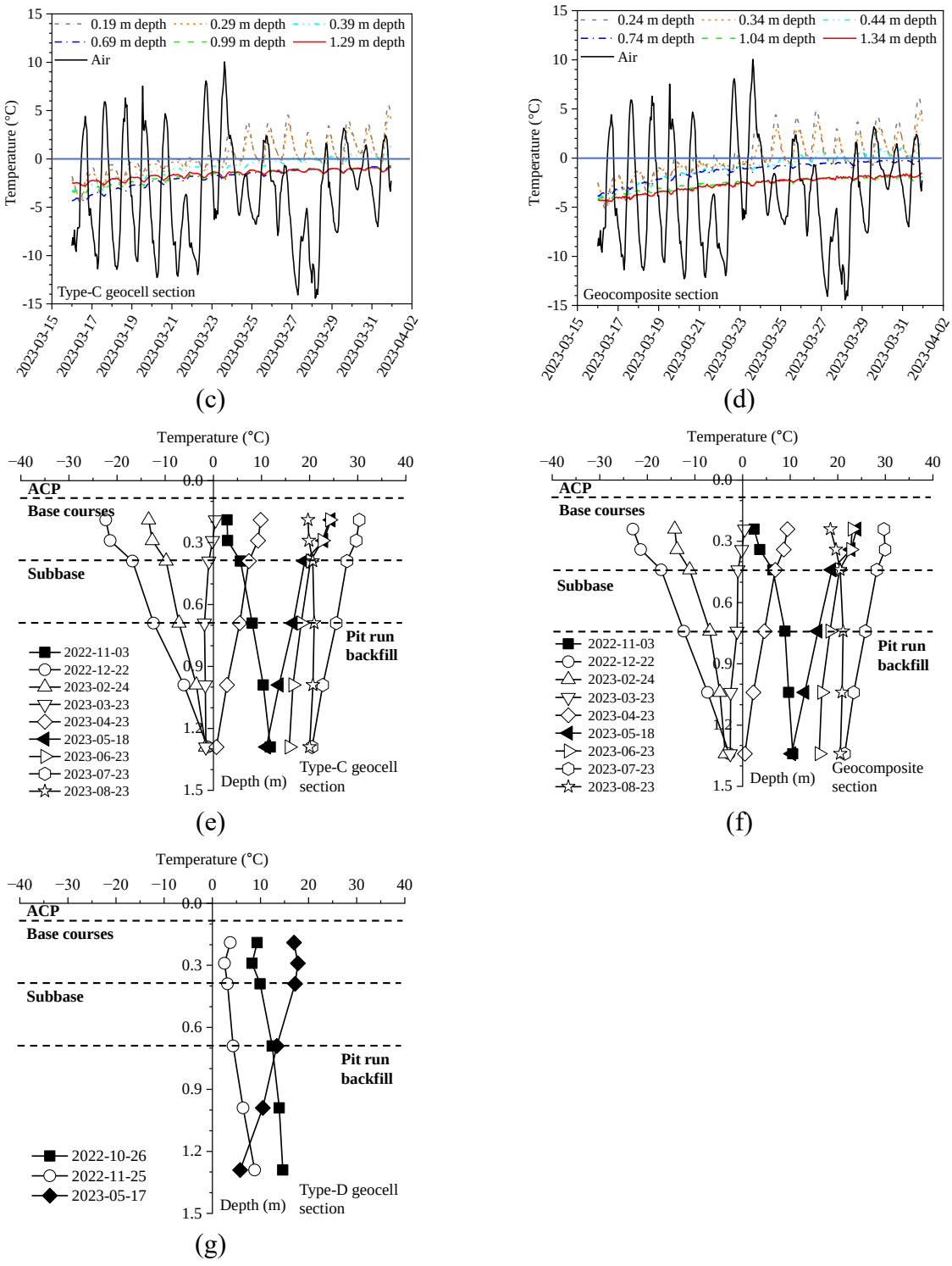

Fig. 6.15. Soil temperature: evolutions and profiles at Type-C geocell section [(a), (c) &(e)], geocomposite section [(b), (d) & (f)], and (g) profile at Type-D geocell section

During the spring season, ground temperatures at all depths began to rise from mid-March 2023, leading to full thawing at the depth of 1.3 m by late April. Much like the freezing process, the

thawing also occurred progressively from the surface downwards. Figs. 6.15(c) and 6.15(d) show the hourly temperature fluctuation during the early thawing season from mid-March to early April. The base course layer was more sensitive to the variations of air temperatures than the sublayers (i.e., subbases and pit run layers). It is evident that the base courses underwent intermittent F-T cycles on a daily basis while the sublayers remained frozen. During this period, water would be trapped in the base courses and experienced intermittent cyclic freezing and thawing, which is much like a closed system simulated in the lab test setting. This process could result in significant deterioration of base courses and pavement distresses under traffic loads. Therefore, the forgoing results suggest that additional inspection and maintenance would be necessary during the early thawing season.

Figs. 6.15(e) to 6.15(g) present the temperate profiles along the depth at selected times for all the test sections. On November 3rd 2022 and May 15th 2023 when the field tests were performed, the ground was fully unfrozen and thawed, respectively. The figures also show that the upper layers were more susceptible to the variations of air temperatures during the freezing season- e.g., the winter temperature of base courses decreased low to -23°C, while it maintained at around -4°C at depth of 1.3 m. This resulted in a larger temperature gradient in the base courses compared to the subbases. For instance, from December 2022 to February 2023, the temperature gradient in the base courses varied from -32°C/m to -19°C/m while that in the subbases was comparatively less severe, ranging from -17°C/m to -9°C/m. In the summer, the temperatures in the pavement layers were relatively uniform, ranging between 20°C and 30°C.

Gravimetric moisture content

Figs. 6.16(a) and 6.16(b) illustrate the evolution of gravimetric moisture content at varying depths for the Type-C geocell and geocomposite sections, respectively. The precipitation was also

added to the figures to assess the effect of rainfall on variations in moisture contents in the pavements. It is noted that the precipitation data between 2nd July 2023 and 22nd September 2023 were taken from a nearby weather station due to an obstruction in the orifice of the rain gauge. Additionally, the moisture content data at a depth of 740 mm in the geocomposite test section have been unavailable since 15th June 2023 due to a malfunctioning moisture sensor at this depth. The comparison of Fig. 6.16 to Fig. 6.15 indicates that during the freezing season, the moisture content decreased as the corresponding temperature dropped. The readings reached a plateau when the temperature fell below the freezing point. Conversely, during the thawing season, the moisture content gradually increased due to the melting of ice. It reached the peak in early April when the base courses and subbases were fully thawed. As shown in Figs. 6.16(c) and 6.16(d), the moisture content in the base courses at the pavement shoulder increased remarkably after early spring thawing (on April 5, 2023), rising from 7.2% to 8.6% and from 4.1% to 6.0% in the Type-C geocell section and the geocomposite sections, respectively. However, moisture content in the base courses below the center of the lane [i.e., M1 in Fig. 6.6(b)] decreased only slightly. Since late April 2023, moisture content in the subbases tended to increase over time. It is hypothetical that the increase in moisture in the subbases was primarily due to the uptake of water in the pit-run gravels which were exposed to the water flow at the ditch bottom [Fig. 6.2(a)] during the precipitation since May 2023. Consequently, this led to the filtration of water into the pit-run layers. Whether the presence of non-woven geotextile layer in the Type-C geocell and geocomposite sections facilitate the horizontal infiltration is unknown. The moisture content in the subbases immediately below the geosynthetics was increased in the geocomposite section but remained relatively unchanged in the Type-C geocell section. Moisture content in the Type-D geocell section was manually measured at the times when the field tests were conducted, with the

vertical profile presented in Fig. 6.16(e). While the moisture content in the base course layer exhibited almost no changes, that in the subbase layer increased considerably.

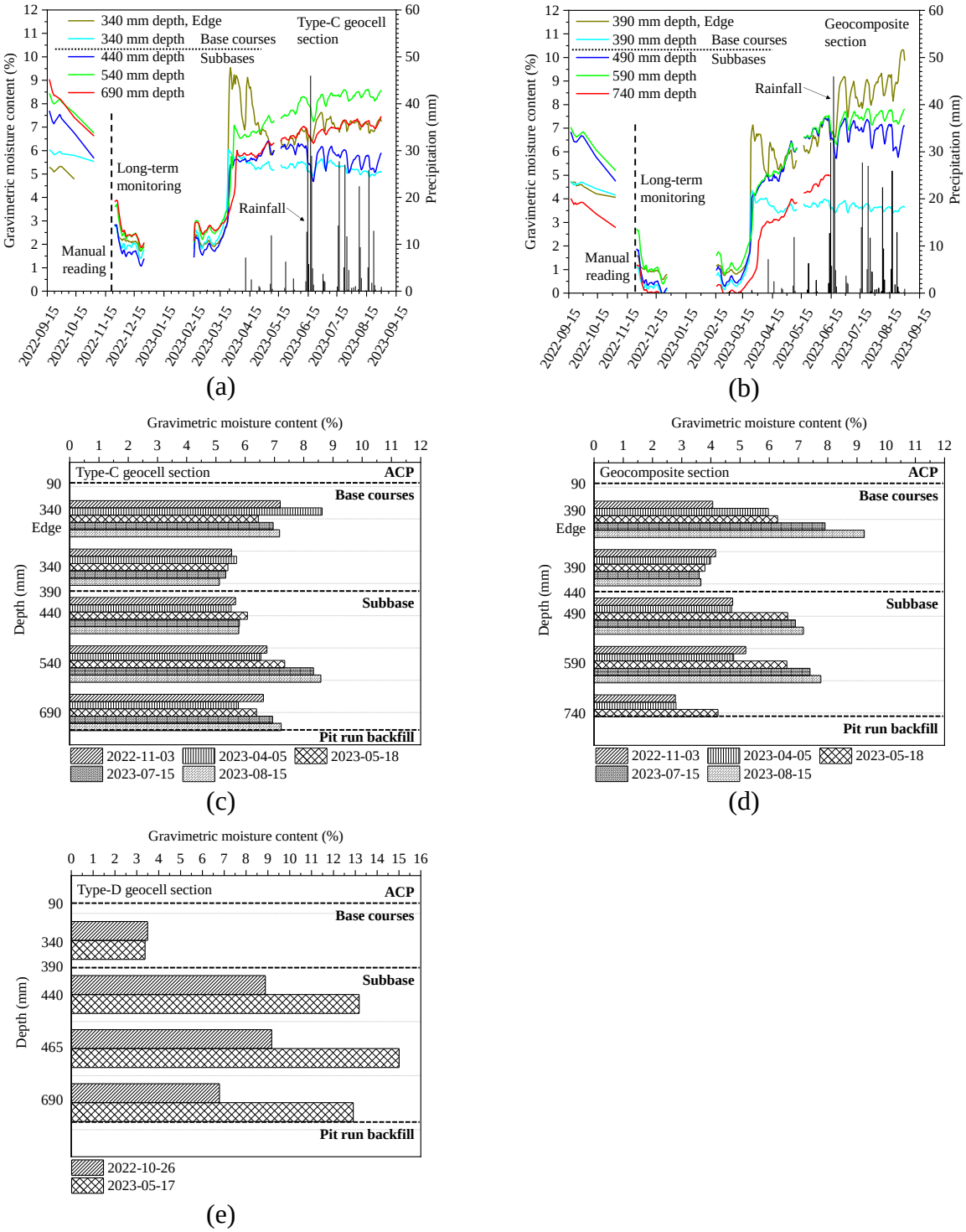

Fig. 6.16. Moisture content: evolution and profile at Type-C geocell section [(a) & (c)], geocomposite section [(b) & (d)], and (e) profile at Type-D geocell section

6.5.2.2 Earth pressure monitoring

Long-term monitoring of general traffic-induced stress over the subbase could provide insights into the long-term performance of geosynthetics stabilized bases. The readings of earth pressure cells in the Type-C geocell and geocomposite sections were continuously taken since November 2023. Fig. 6.17 presents the recorded stress without zeroing the initial readings over one-hour period. The traffic induced stress was determined by subtracting the initial reading from the peak values. It is important to note that interpreting these peak stresses was complex as a result of variations in vehicle weights, tire pressures, passing speeds, and the potential offset of wheels from the designated points for the earth pressure cells upon their passage. This was compounded by a lack of the real-time traffic volumes. To address this issue, the monthly average peak stress was computed to compare the load transfer to the subbase layer in the two test sections (Bayat et al., 2012; Duong et al., 2019) and to derive the general trend over the F-T cycle.

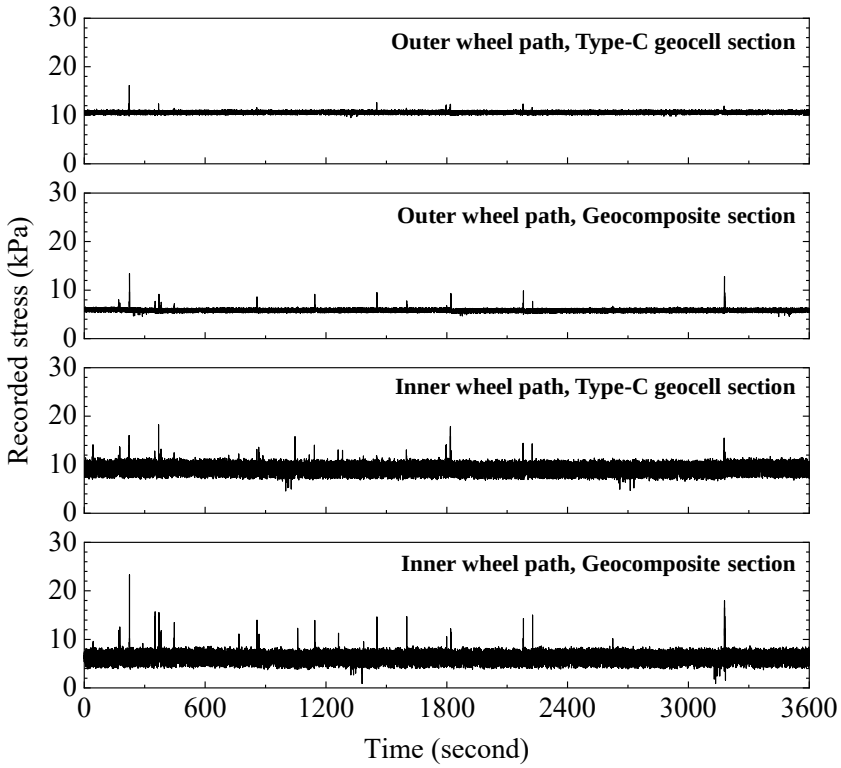

Fig. 6.17. Typical stress recordings in an hour period under real traffic loads

Before proceeding with the data analysis, a data reduction and filtration program coded by Python was implemented to reduce hundreds of millions of data points that had been continuously collected at a sampling of 10 Hz for several months. At no traffic loads, the earth pressure cells registered readings between -5 and 2 kPa. This is treated as inherent measurement errors of these sensors. To rule out this impact, wheel passes generating the induced stress at the base-subbase interface in excess of 3 kPa were counted as the effective wheel passes. Fig. 6.18(a) summarizes the weekly cumulative effective wheel passes distributed on the hourly basis. Specifically, each data point in the figure represents the sum of traffic within the same hour each day over seven days. The use of the hourly counts accumulated over a week was to facilitate the presentation of traffic counts, particularly for the outer wheel path due to small traffic detected by E2 [Fig. 6.6(a)] in any given hour. A significant frequency of wheel passes was observed between 6 am and 6 pm. The low counts of wheel passes over E2 were attributed to its position. As discussed previously, E1 and E2 were positioned to monitor the trailer's wheel loads, which, however, might not match the axle tracks of other types of vehicles. For example, E2, being near the edge of the pavement, could easily miss the outer wheels if the vehicles had small axle tracks. Consequently, the 12-hour data recorded from E1 are used as the daily wheel pass counts, with the monthly cumulative counts presented in Fig. 6.18(b). Notably, the figure indicates no wheel passes during the freezing season, with traffic increasing in March 2023. This result aligns with the onset of the seasonal thawing in the base courses. April 2023 saw the marked rise in wheel passes as the base courses and subbases fully thawed, and the wheel passes varied less significantly afterwards.

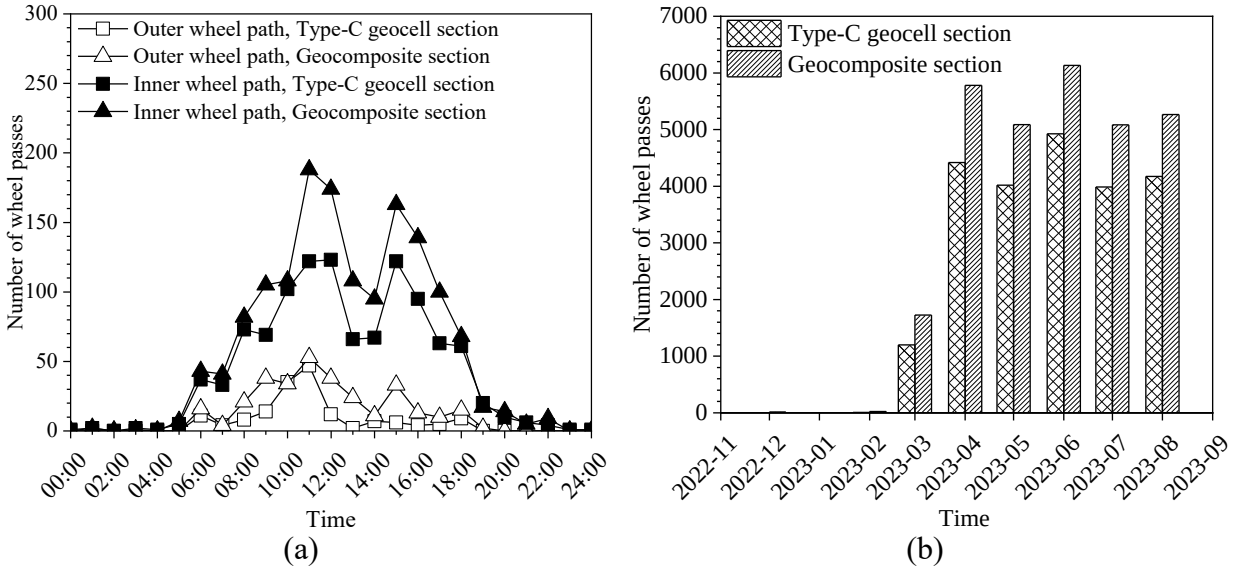

Fig. 6.18. Traffic performance monitoring: (a) 24-hr distribution of cumulative wheel passes over a week and (b) recorded monthly number of wheel passes at inner wheel path

Fig. 6.19(a) illustrates the monthly average of stress measured by E1 at the threshold of 3 kPa for the two test sections along with the maximum values. The range of the maximum stress measured (lines in Fig. 6.19) was comparable to that from the cyclic plate loading tests (Fig. 6.13) and trafficking tests (Fig. 6.14) with a range of 50 to 90 kPa. Considering the offset of E1 from the main track path as discussed previously, the actual maximum stress directly below the track could be greater. In comparison, the average stress measured at the base-subbase interface (bars Fig. 6.19) was much lower than that from the plate loading and trafficking tests. Fig. 6.19 also reveals that during the thawing seasons, the monthly average stress recorded in both Type-C geocell and geocomposite sections exhibited an increase, and afterwards, the stress tended to decrease and then stabilize. This trend applied for both the average stress and the maximum stress. This process was associated with the pavement thaw weakening in the spring, followed by its recovery in the summer. It can be observed that the Type-C geocell section reached the peak stress and the steady state both earlier than the geocomposite section.

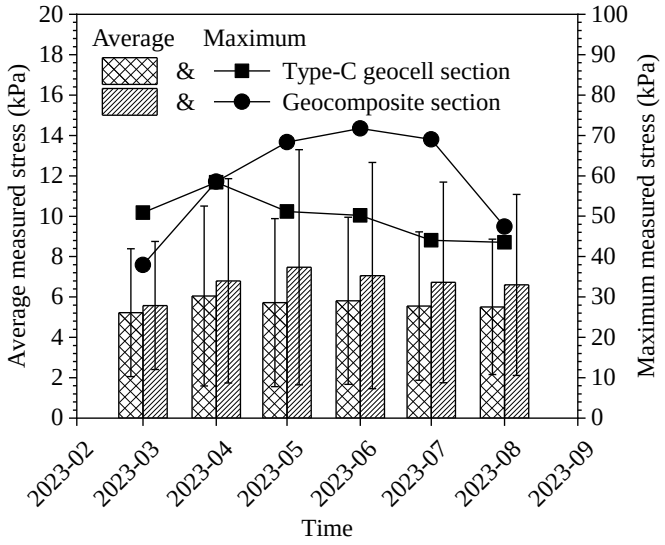

Fig. 6.19. Average stress measured by earth pressure on a monthly basis

6.6 Conclusions

This paper presents a comprehensive full-scale investigation into the performance of geocell and geogrid-geotextile composite (or geocomposite) stabilized bases in the flexible pavements in Alberta, Canada. The test sections were fully instrumented and evaluated with short-term field tests before and after the seasonal F-T cycle and the 12-month performance monitoring. The following conclusions are drawn from this full-scale study:

(1) One seasonal F-T cycle resulted in the increase in pavement settlement under either monotonic or cyclic plate loading, while the settlement after the F-T cycle was negligible with its maximum values ranging between 0.5 and 2 mm. The seasonal F-T cycle also led to more cumulative settlement induced by cyclic plate loading. In comparison to the small settlement that was sensitive to measurement errors and uncertainties, the stress results were much more consistent in the repeated tests.

(2) After one seasonal F-T cycle, the load stress ratio measured from the cyclic plate loading tests decreased by 1% to 2.5% while the distribution angle increased by 2° to 4°, respectively. This

was attributed to that the subbases with higher fines content experienced greater F-T degradation in stiffness than the base courses that were stabilized by geosynthetics.

(3) Of the three test sections, the Type-D geocell section exhibited higher stiffness in base courses and lower stiffness in subbases than the Type-C geocell section and the geocomposite section. This explains why it had a less load transfer ratio or a greater stress distribution angle than the other two sections. Both plate loading tests and trafficking tests indicated that the 300-mm Type-C geocell stabilized bases had an equivalent or better performance as the 350-mm geocomposite stabilized bases in both pre-freezing and post-thawing conditions. This result was different from Henry et al. (2005) that indicated no benefit from geogrid stabilization in reducing the F-T impact after one seasonal F-T cycle because the present study placed the geogrid composite between two gravel layers (i.e, base and subbase) while Henry et al. (2005) placed the geogrid between gravel and clay layers (i.e., base and subgrade).

(4) The 12-month monitoring indicates that in the spring thaw, the base course layer could experience repeated daily intermittent F-T cycles while the sublayers remained frozen. During and after the spring thawing, moisture content in the base courses below the pavement center slightly decreased while that in the subbases increased. The changes in moisture content in the subbases below the pavement center were similar to those in bases at the pavement edge, indicating both were affected by precipitation.

(5) The earth pressure monitoring during the spring thawing and post-thawing seemed to indicate that the Type-C geocell section gained the post-thaw recovery earlier than the geocomposite.

References

AASHTO., 2004. Standard specification for materials for aggregate and soil-aggregate subbase, base, and surface courses. AASHTO M147-65, Washington, DC.

AASHTO, T224. Standard method of test for correction for coarse particles in the soil compaction test. American Association of State Highway and Transportation Officials, Washington, D.C, USA.

Abu-Farsakh, M., Hanandeh, S., Mohammad, L. and Chen, Q., 2016. Performance of geosynthetic reinforced/stabilized paved roads built over soft soil under cyclic plate loads. Geotextiles and Geomembranes, 44(6), 845-853.

Adams, M.T. and Collin, J.G., 1997. Large model spread footing load tests on geosynthetic reinforced soil foundations. Journal of Geotechnical and Geoenvironmental Engineering, 123(1), 66-72.

Aghda, S.T.T., Ghanbari, A. and Mehrjardi, G.T., 2019. Evaluating the applicability of geocell-reinforced dredged sand using plate and wheel load testing. Transportation Infrastructure Geotechnology, 6(1), 21-38.

Alberta Transportation, 2020. Standard specifications for highway construction. Edmonton, Alberta, Canada.

Ali, O., 2005. Evaluation of the Mechanistic Empirical Pavement Design Guide. Research Report, NCHRP 1-37A, National Research Council of Canada, Institute for Research in Construction, Canada.

Allen T.M., 1983. Properties of geotextiles in cold regions applications. M.Sc. Thesis, Civil Engineering Department, the Oregon State University.

Al-Qadi, I.L., Brandon, T.L., Valentine, R.J., Lacina, B.A. and Smith, T.E., 1994. Laboratory

evaluation of geosynthetic-reinforced pavement sections. Transportation Research Record, (1439), 25-31.

Andersland, O.B., Ladanyi, B., 2004. Frozen ground engineering, second ed. John Wiley & Sons, Inc., Hoboken, USA.

Arenson, L.U., Azmatch, T.F., Sego, D.C. and Biggar, K.W., 2008. A new hypothesis on ice lens formation in frost-susceptible soils. Proceedings of the Ninth International Conference on Permafrost, 1, Fairbanks, Alaska, USA, June 2008, pp. 59-64.

ASTM C117-17. Standard test method for materials finer than 75-μm (No. 200) sieve in mineral aggregates by washing. ASTM International, West Conshohocken, PA, USA.

ASTM D1195/D1195M-21. Standard Test Method for Repetitive Static Plate Tests of Soils and Flexible Pavement Components for Use in Evaluation and Design of Airport and Highway Pavements. ASTM International, West Conshohocken, PA, USA.

ASTM D1883. Standard Test Method for California Bearing Ratio (CBR) of Laboratory-compacted Soils. ASTM International, West Conshohocken, PA, USA.

ASTM D2940/D2940M. Standard Specification for Graded Aggregate Material for Bases or Subbases for Highways or Airports. ASTM International, West Conshohocken, PA, USA.

ASTM D4533/D4533M-15. Standard test method for trapezoid tearing strength of geotextiles. ASTM International, West Conshohocken, PA, USA.

ASTM D4595/D4595M-23. Standard test method for tensile properties of geotextiles by the wide-width method. ASTM International, West Conshohocken, PA, USA.

ASTM D4632/D4632M-15a. Standard test method for grab breaking load and elongation of geotextiles. ASTM International, West Conshohocken, PA, USA.

ASTM D4751-21a. Standard test methods for determining apparent opening size of a geotextile.

ASTM International, West Conshohocken, PA, USA.

ASTM D4833/D4833M-07. Standard test method for index puncture resistance of geomembranes and related products. ASTM International, West Conshohocken, PA, USA.

ASTM D5321/D5321M. Standard test method for determining the shear strength of soil-geosynthetic and geosynthetic-geosynthetic interfaces by direct shear. ASTM International, West Conshohocken, PA, USA.

ASTM D5918. Standard test methods for frost heave and thaw weakening susceptibility of soils. ASTM International, West Conshohocken, PA, USA.

ASTM D6913/D6913M. Standard test methods for particle-size distribution (gradation) of soils using sieve analysis. ASTM International, West Conshohocken, PA, USA.

ASTM D 6951/D6951M-18. Standard Test Method for Use of the Dynamic Cone Penetrometer in Shallow Pavement Applications. ASTM International, West Conshohocken, PA, USA.

ASTM D698. Standard test methods for laboratory compaction characteristics of soil using standard effort (12,400 ft-lbf/ft^3 (600 kN-m/m^3)). ASTM International, West Conshohocken, PA, USA.

ASTM D6992. Standard test method for accelerated tensile creep and creep-rupture of geosynthetic materials based on time-temperature superposition using the stepped isothermal method. ASTM International, West Conshohocken, PA, USA.

ASTM E2254. Standard test method for storage modulus calibration of dynamic mechanical analyzers. ASTM International, West Conshohocken, PA, USA.

ASTM E831. Standard test methods for linear thermal expansion of solid materials by thermomechanical analysis. ASTM International, West Conshohocken, PA, USA.

Babić, B., Prager, A. and Rukavina, T. (2000). Effect of fine particles on some characteristics of

granular base courses. Materials and Structures, 33(7), 419-424.

Barker W.R., Alexander D.R., 2012. Determining the effective modulus of subgrade reaction for design of rigid airfield pavements having base layers. Technical Report No. ERDC/GSL-TR-12-20, Engineering Research and Development Center, Geotechnical and Structures Laboratory.

Bathurst, R.J. and Karpurapu, R. (1993). Large-scale triaxial compression testing of geocell-reinforced granular soils. Geotechnical Testing Journal, 16(3), 296-303.

Bayat, A., Knight, M.A. and Soleymani, H.R., 2012. Field monitoring and comparison of thermal- and load-induced strains in asphalt pavement. International Journal of Pavement Engineering, 13(6), pp.508-514.

Bilodeau, J.P., Yi, J. and Doré, G., 2020. Assessment of Flexible Pavement Response during Partial Thawing Conditions Using Accelerated Pavement Testing. Journal of Cold Regions Engineering, 34(2), p.04020007.

Bing, H., He, P., Zhang, Y., 2015. Cyclic freeze–thaw as a mechanism for water and salt migration in soil. Environmental earth sciences, 74(1), 675-681.

Bolch, T. and Christiansen, H.H., 2015. Mountains, lowlands, and coasts: the physiography of cold landscapes. In Snow and Ice-Related Hazards, Risks and Disasters, Elsevier, Inc., Boston, pp. 201-217.

British Columbia Ministry of Transportation and Infrastructure (2020). Standard specifications for highway construction. Victoria, British Columbia, Canada.

Calhoun, C.C., 1972. Development of Design Criteria and Acceptance of Specifications for the Plastic Filter Cloth. Technical report 5-72-7. U.S. Army Corps of Engineers, Waterways Experiment Station, Vicksburg, Mississippi.

Campbell, G.S., Huffaker, E.M., Wacker, B.T. and Wacker, K.C., 2005. Use of the line heat source

method to measure thermal conductivity of insulation and other porous materials. In Proceedings of the 27th international thermal conductivity conference and 15th international thermal expansion symposium (Thermal conductivity 27/Thermal expansion 15), October 26-29, Knoxville, Tennessee, USA, pp. 187-195.

Cetin, A., Kaya, Z., Cetin, B. and Aydilek, A.H. (2014). Influence of laboratory compaction method on mechanical and hydraulic characteristics of unbound granular base materials. Road Materials and Pavement Design, 15(1), 220-235.

Chamberlain, E.J. (1987). A freeze-thaw test to determine the frost susceptibility of soils. Special Report 89-1, US Army Corps of Engineers, Cold Regions Research and Engineering Laboratory, Hanover, New Hampshire, USA.

Chang, T.-T., Chang, C.-H., Pei, S.-W., 2007. Investigation of the bearing capacity and dynamic-elastic behavior of mechanical stabilization of sandy subgrade using geocells. In: Proceedings of the Transportation Research Board 86th Annual Meeting, January 21-25, Washington DC, USA.

Chatterjee, A.K., Pokharel, S.K. and Breault, M., 2022. Staged road construction in very weak subgrade using polymeric geocell. Proceedings of Transportation Association of Canada 2022 Conference and Exhibition-Changing Ways for our Changing Climate, Edmonton, Alberta, Canada, October 2022, pp. 1-18.

Christopher, B., Hayden, S., Zhao, A., 2000. Roadway base and subgrade geocomposite drainage layers. Testing and Performance of Geosynthetics in Subsurface Drainage, L. David Suits, James B. Goddard, and John S. Baldwin, Editors, ASTM stock number STP 1390, Proceedings of a symposium held in Seattle, Washington, USA, June 1999, pp.35-51.

Christopher, B.R., Schwartz, C.W., Boudreaux, R. and Berg, R.R., 2006. Geotechnical aspects of

pavements (No. FHWA-NHI-05-037). United States. Federal Highway Administration.

Clarke, R.E., Pianella, A., Shabani, B., Rosengarten, G., 2017. Steady-state thermal measurement of moist granular earthen materials. Journal of Building Physics, 41(2), 101-119.

Clarke, R.E., Rosengarten, G. and Shabani, B., 2015. Flexible buffer materials to reduce contact resistance in thermal insulation measurements. In Proceedings of the 32nd international thermal conductivity conference and 20th international thermal expansion symposium (Thermal conductivity 32/Thermal expansion 20), West Lafayette, Indiana, USA, pp.64-73.

Corte, A.E., 1962. The frost behavior of soils. I. Vertical sorting. Highway Research Board Bulletin, 317, 9-34.

Dash, S.K., 2010. Influence of relative density of soil on performance of geocell-reinforced sand foundations. Journal of Materials in Civil Engineering, 22(5), 533-538.

Dash, S.K., Krishnaswamy, N.R. and Rajagopal, K., 2001. Bearing capacity of strip footings supported on geocell-reinforced sand. Geotextiles and Geomembranes, 19(4), 235-256.

Dash, S.K., Rajagopal, K. and Krishnaswamy, N.R., 2004. Performance of different geosynthetic reinforcement materials in sand foundations. Geosynthetics International, 11(1), pp.35-42.

Dave, B.S., Solanki, C.H. and Desai, A.K., 2022. Modelling the deformation behaviour of an unsaturated soil reinforced with geocell for different freezing-thawing cycles. Innovative Infrastructure Solutions, 7(2), p.138.

DeMerchant, M.R., Valsangkar, A.J., Schriver, A.B., 2002. Plate load tests on geogrid-reinforced expanded shale lightweight aggregate. Geotextiles and Geomembranes, 20(3), 173-190.

Duong, N.S., Blanc, J., Hornych, P., Bouveret, B., Carroget, J. and Le Feuvre, Y., 2019. Continuous strain monitoring of an instrumented pavement section. International Journal of Pavement Engineering, 20(12), pp.1435-1450.

Dutta, S. and Mandal, J.N., 2016. Model studies on geocell-reinforced fly ash bed overlying soft clay. Journal of Materials in Civil Engineering, 28(2), 04015091.

Edil, T.B., Benson, C.H., Bin-Shafique, M., Tanyu, B.F., Kim, W.-H., Senol, A., 2002. Field evaluation of construction alternatives for roadways over soft subgrade. Transportation Research Record, 1786(1), 36-48.

Emersleben, A., Meyer, N., 2008. Bearing capacity improvement of gravel base layers in road constructions using geocells. In: Proceedings of the 12th International Conference of International Association for Computer Methods and Advances in Geomechanics, October 1-6, Goa, India, pp.3538-3545.

EN ISO 10319:2015., 2015. Geosynthetics - Wide-width tensile test.

EN ISO 12236:2006., 2006. Geosynthetics - Static puncture test.

EN ISO 13426-1:2019., 2019. Geotextiles and geotextile-related products - Strength of internal structural junctions - Part 1: Geocells.

Fakher, A. and Jones, C.J., 1996. Discussion: bearing capacity of rectangular footings on geogrid-reinforced sand. Journal of Geotechnical Engineering, 122(4), pp.326-327.

Fan, W., Yang, P. and Yang, Z.J., 2021. Freeze-thaw impact on macropore structure of clay by 3D X-ray computed tomography. Engineering Geology, 280, p.105921.

Fredlund D.G., Rahardjo H., Fredlund M.D., 2012. Unsaturated soil mechanics in engineering practice, John Wiley & Sons, Hoboken, New Jersey.

Genc, D., 2019. Development, installation and preliminary data collection of an environmental sensor system for freeze-thaw monitoring under granular-surfaced roadways. Master dissertation, CCEE Department, Iowa State University.

George, A.M., Banerjee, A., Puppala, A.J. and Saladhi, M., 2019. Performance evaluation of

geocell-reinforced reclaimed asphalt pavement (RAP) bases in flexible pavements. International Journal of Pavement Engineering, 1-11.

Ghazavi, M. and Roustaei, M., 2013. Freeze–thaw performance of clayey soil reinforced with geotextile layer. Cold Regions Science and Technology, 89, 22-29.

Giroud, J.P., Han, J., 2004a. Design method for geogrid-reinforced unpaved roads. I. development of design method. Journal of Geotechnical and Geoenvioronmental Engineering, ASCE 130 (8), 775-786.

Giroud, J.P., Han, J., 2004b. Design method for geogrid-reinforced unpaved roads. II. Calibration and Applications. Journal of Geotechnical and Geoenvioronmental Engineering, ASCE 130 (8), 787-797.

Green, J.L. and Hall, J.W., 1975. Nondestructive vibratory testing of airport pavements. Volume 1. Experimental test results and development of evaluation methodology and procedure. ARMY ENGINEER WATERWAYS EXPERIMENT STATION VICKSBURG MS.

Guido, V.A., Chang, D.K. and Sweeney, M.A., 1986. Comparison of geogrid and geotextile reinforced earth slabs. Canadian Geotechnical Journal, 23(4), 435-440.

Guo, J., Han, J., Schrock, S.D., Parsons, R.L. and Sun, X., 2018. Experimental study on geocell-stabilized unpaved shoulders. GeoShanghai 2018 International Conference: Ground Improvement and Geosynthetics, Lin Li, Bora Cetin and Xiaoming Yang, Editors, Springer, Proceedings of a conference held in Shanghai, China, May 2018, pp. 390-398.

Guo, J., Han, J., Zhang, X. and Li, Z., 2019. Evaluation of moisture reduction in aggregate base by wicking geotextile using soil column tests. Geotextiles and Geomembranes, 47(3), 306-314.

Han, J. and Jiang, Y., 2013. Use of geosynthetics for performance enhancement of earth structures in cold regions. Sciences in Cold and Arid Regions, 5(5), 517-529.

Han, J., Pokharel, S.K., Parsons, R.L., Leshchinsky, D. and Halahmi, I., 2010. Effect of infill material on the performance of geocell-reinforced bases. Proceedings of 9th International Conferences on Geosynthetics, São Paulo, Brazil, May 2010, pp. 1503-1506.

Han, J., Pokharel, S.K., Yang, X., Manandhar, C., Leshchinsky, D., Halahmi, I. and Parsons, R.L., 2011. Performance of geocell-reinforced RAP bases over weak subgrade under full-scale moving wheel loads. Journal of Materials in Civil Engineering, 23(11), pp.1525-1534.

Hatipoglu, B., Edil, T.B. and Benson, C.H., 2008. Evaluation of base prepared from road surface gravel stabilized with fly ash. GeoCongress 2008: Geotechnics of Waste Management and Remediation, Milind V. Khire, Akram N. Alshawabkeh and Krishna R. Reddy, Editors, ASCE Geotechnical Special Publication No. 177, Proceedings of sessions held in New Orleans, Louisiana, USA, March 2008, pp. 288-295.

Hegde, A., Kadabinakatti, S. and Sitharam, T.G., 2014. Protection of buried pipelines using a combination of geocell and geogrid reinforcement: experimental studies. Ground Improvement and Geosynthetics, 289-298.

Helstrom, C.L., Humphrey, D.N., Hayden, S.A., 2006. Geogrid reinforced pavement structure in a cold region. In: Proceedings of the 13th International Conference on Cold Regions Engineering, July 23-26, Orono, Maine, USA, pp. 1-12.

Henry, K.S. and Holtz, R.D., 2001. Geocomposite capillary barriers to reduce frost heave in soils. Canadian Geotechnical Journal, 38(4), 678-694.

Henry, K.S., Olson, J.P., Farrington, S.P. and Lens, J., 2005. Improved performance of unpaved roads during spring thaw, Technical Report, ERDC/CRREL TR-05-1. Engineer Research and Development Center, Cold Regions Research and Engineering Laboratory, Hanover, New Hampshire, USA.

Henry, K.S., Stormont, J.C., Holtz, R.D., 2000. Geosynthetic capillary barriers in pavements. In: Proceedings of the Specialty Conference on Performance Confirmation of Constructed Geotechnical Facilities, April 9-12, Amherst, Massachusetts, USA, pp. 350-364.

Heukelom, W. and Klomp, A., 1962. Dynamic testing as a means of controlling pavements during and after construction. In International Conference on the Structural Design of Asphalt Pavements, University of Michigan, Ann Arbor (Vol. 203, No. 1).

Hohmann-Porebska, M., 2002. Microfabric effects in frozen clays in relation to geotechnical parameters. Applied clay science, 21(1-2), 77-87.

Hotineanu, A., Bouasker, M., Aldaood, A. and Al-Mukhtar, M., 2015. Effect of freeze–thaw cycling on the mechanical properties of lime-stabilized expansive clays. Cold Regions Science and Technology, 119, 151-157.

Huang, M., Lin, C. and Pokharel, S.K., 2021. Freeze–thaw effects on mechanical behavior of geocell-reinforced sands from element and model tests. International Journal of Geosynthetics and Ground Engineering, 7(2), 1-13.

Huang, M., Lin, C. and Pokharel, S.K., 2023. Freeze-thaw behavior of geocell-reinforced bases considering different fines contents. Geosynthetics International, 1-18.

Huang, M., Lin, C., Pokharel, S.K., Tura, A. and Mukhopadhyaya, P., 2021. Model tests of freeze-thaw behavior of geocell-reinforced soils. Geotextiles and Geomembranes, 49(3), 669-687.

Huang, Y.H. 2004. Pavement analysis and design, second ed. Pearson Prentice Hall, Inc., Upper Saddle River, New Jersey, USA.

Huang, Y., Chen, Y., Wang, S., Wu, M. and Wang, W., 2022. Effects of freeze–thaw cycles on volume change behavior and mechanical properties of expansive clay with different degrees of compaction. International Journal of Geomechanics, 22(5), 04022050.

Ishikawa, T., Lin, T., Kawabata, S., Kameyama, S. and Tokoro, T., 2019. Effect evaluation of freeze-thaw on resilient modulus of unsaturated granular base course material in pavement. Transportation Geotechnics, 21, 100284.

Johnson, A.E., 2012. Freeze-thaw performance of pavement foundation materials. Master dissertation, Iowa State University, Ames, Iowa, USA.

Johnson, T.C., Berg, R.L., Carey, K.L. and Kaplar, C.W., 1975. Roadway design in seasonal frost areas. Research Report, NCHRP 26, Cold Regions Research and Engineering Lab, Hanover, New Hampshire, USA.

Jong, D.-T., Bosscher, P.J., Benson, C.H., 1998. Field assessment of changes in pavement moduli caused by freezing and thawing. Transportation Research Record, 1615(1), 41-48.

Kargar, M. and Mir Mohammad Hosseini, S.M., 2018. Influence of reinforcement stiffness and strength on load-settlement response of geocell-reinforced sand bases. European Journal of Environmental and Civil Engineering, 22(5), 596-613.

Kawabata, S., Ishikawa, T., Kameyama, S., 2016. Effects of freeze-thaw history on bearing capacity of granular base course materials. Procedia engineering, 143, 828-835.

Konrad, J.M., 2008. Freezing-induced water migration in compacted base-course materials. Canadian Geotechnical Journal, 45(7), pp.895-909.

Konrad, J.M. and Lemieux, N., 2005. Influence of fines on frost heave characteristics of a well-graded base-course material. Canadian Geotechnical Journal, 42(2), 515-527.

Lai, Y., Zhang, S., Yu, W., 2012. A new structure to control frost boiling and frost heave of embankments in cold regions. Cold Regions Science and Technology, 79, 53-66.

Lee, I.K., White, W., Ingles, O.G., 1983. Geotechnical Engineering. Copp Clark Pitman, Inc., pp. 57-89.

Lee, W., Bohra, N., Altschaeffl, A., White, T., 1995. Resilient modulus of cohesive soils and the effect of freeze–thaw. Canadian Geotechnical Journal, 32(4), 559-568.

Leroueil, S., Tardif, J., Roy, M., Rochelle, P.L., 1991. Effects of frost on the mechanical behaviour of Champlain Sea clays. Canadian Geotechnical Journal, 28(5), 690-697.

Li, A., Niu, F., Xia, C., Bao, C. and Zheng, H., 2019. Water migration and deformation during freeze-thaw of crushed rock layer in Chinese high-speed railway subgrade: Large scale experiments. Cold Regions Science and Technology, 166, p.102841.

Li, C. and Ashlock, J., 2017. Collection of freeze-thaw performance data on Vail Avenue. Project HR-3013, Iowa Department of Transportation, Ames, Iowa, USA.

Li, C., Ashlock, J., White, D., Vennapusa, P., 2017a. Permeability and stiffness assessment of paved and unpaved roads with geocomposite drainage layers. Applied Sciences, 7(7), 718.

Li, C., Ashlock, J.C., White, D.J., Vennapusa, P.K.R., 2019. Mechanistic-based comparisons of stabilized base and granular surface layers of low-volume roads. International Journal of Pavement Engineering, 20(1), 112-124.

Lin, C., Presler, W., Zhang, X., Jones, D. and Odgers, B., 2017. Long-term performance of wicking fabric in Alaskan pavements. Journal of Performance of Constructed Facilities, 31(2), D4016005.

Li, C., Vennapusa, P.K.R., Ashlock, J., White, D.J., 2017b. Mechanistic-based comparisons for freeze-thaw performance of stabilized unpaved roads. Cold Regions Science and Technology, 141, 97-108.

Li, L., Liu, J., Zhang, X., Li, P. and Saboundjian, S., 2019. Characterizing permanent deformation of Alaskan granular base-course materials. Journal of Materials in Civil Engineering, 31(11), 04019267.

Liu, J., Zhang, X., Li, L. and Saboundjian, S., 2018. Resilient behavior of unbound granular materials subjected to a closed-system freeze-thaw cycle. Journal of Cold Regions Engineering, 32(1), 04017015.

Liu, Z., Liu, J., Wang, Q. and Liu, J., 2018. Compressive strength and frost heave resistance of different types of semi-rigid base materials after freeze-thaw cycles. Sciences in Cold and Arid Regions, 7(4), 365-369.

Lu, J., Zhang, M., Zhang, X., Pei, W. and Bi, J., 2018. Experimental study on the freezing–thawing deformation of a silty clay. Cold Regions Science and Technology, 151, 19-27.

Lu, Y., Liu, S., Zhang, Y., Wang, L. and Li, Z., 2021. Hydraulic conductivity of gravelly soils with various coarse particle contents subjected to freeze–thaw cycles. Journal of Hydrology, 598, 126302.

Lu, Z., She, J., Wu, X. and Yao, H., 2019a. Cumulative strain characteristics of compacted soil under effect of freeze-thaw cycles with water supply. Transportation Geotechnics, 21, 100291.

Lu, Z., Xian, S., Yao, H., Fang, R. and She, J., 2019b. Influence of freeze-thaw cycles in the presence of a supplementary water supply on mechanical properties of compacted soil. Cold Regions Science and Technology, 157, 42-52.

Mamatha, K.H., Dinesh, S.V., 2019. Performance evaluation of geocell-reinforced pavements. International Journal of Geotechnical Engineering, 13(3), 277-286.

Matthews, T. and Sandercock, J., 2016. Alternative Energy Program. Solar Photovoltaic Reference Array Report.

McCartney, J.S., Cox, B.R., Wood, C.M. and Curry, B., 2010. Evaluation of geosynthetic-reinforced flexible pavements using static plate load tests. Technical Report, FHWA/MT-02-008/20040, University of Colorado Boulder, Colorado, USA.

Mehrjardi, G.T., Behrad, R. and Tafreshi, S.M., 2019. Scale effect on the behavior of geocell-reinforced soil. Geotextiles and Geomembranes, 47(2), 154-163.

Mengelt, M., Edil, T.B. and Benson, C.H., 2006. Resilient modulus and plastic deformation of soil confined in a geocell. Geosynthetics International, 13(5), 195-205.

Mitchell, J.K. and Soga, K., 2005. Fundamentals of soil behavior, John Wiley & Sons., Hoboken, USA.

Nair, A.M. and Latha, G.M., 2016. Repeated load tests on geosynthetic reinforced unpaved road sections. Geomechanics and Geoengineering, 11(2), 95-103.

NCHRP, 1974. Roadway design in seasonal frost areas. National cooperative highway research program, synthesis of highway practice, NCHRP Report No. 26. Transportation Research Board, Washington, DC.

Officials, T., 2008. Mechanistic-empirical pavement design guide: A manual of practice. AASHTO: Washington, DC, USA.

Othman M.A., Benson C.H., 1992. Effect of freeze-thaw on the hydraulic conductivity of three compacted clays from Wisconsin. Proceedings of 71st Annual Meeting, National Research Council, Washington, DC, Transportation Research Record, No. 1369, pp. 118-125.

Othman, M.A. and Benson, C.H., 1993. Effect of freeze–thaw on the hydraulic conductivity and morphology of compacted clay. Canadian Geotechnical Journal, 30(2), 236-246.

Pawluk, S., 1988. Freeze-thaw effects on granular structure reorganization for soil materials of varying texture and moisture content. Canadian Journal of Soil Science, 68(3), pp.485-494.

Pokharel, S., 2010. Experimental study on geocell-reinforced bases under static and dynamic loading. Ph.D. dissertation, CEAE Department, the University of Kansas.

Pokharel, S., Han, J., Leshchinsky, D., Parsons, R.L., Halahmi, I., 2010. Investigation of factors

influencing behavior of single geocell-reinforced bases under static loading. Geotextiles and Geomembranes, 28(6), 570-578.

Pokharel, S., Martin, I., Norouzi, M., Breault, M., 2015. Validation of geocell design for unpaved roads. Proceedings of Geosynthetics 2015, Oregon, Portland, USA, February 2015, pp. 15-18.

Pokharel, S., Norouzi, M., Eng, P., Breault, M., 2017. New advances in novel polymeric alloy geocell-reinforced base course for paved roads. Proceedings of 2017 Conference of the Transportation Association of Canada, St. John's, Newfoundland, Canada, September 2017, pp. 1-16.

Pokharel, S., Norouzi, M., Martin, I. and Breault, M., 2016. Sustainable road construction for heavy traffic using high strength polymeric geocells. Proceedings of Resilient Infrastructure 2016, CSCE, London, Ontario, Canada, June 2016.

Powell, W.D., Potter, J.F., Mayhew, H.C. and Nunn, M.E., 1984. The structural design of bituminous roads, Laboratory Report, TRRL LR 1132. Transport and Road Research Laboratory, Department of Transport, Crowthorne, Berkshire, England.

Qi, J., Ma, W. and Song, C., 2008. Influence of freeze-thaw on engineering properties of a silty soil. Cold regions science and technology, 53(3), 397-404.

Qi, J., Vermeer, P.A., Cheng, G., 2006. A review of the influence of freeze-thaw cycles on soil geotechnical properties. Permafrost and periglacial processes, 17(3), 245-252.

Rajagopal, K., Chandramouli, S., Parayil, A., Iniyan, K., 2014. Studies on geosynthetic-reinforced road pavement structures. International Journal of Geotechnical Engineering, 8(3), 287-298.

Rajagopal, K., Krishnaswamy, N.R. and Latha, G.M., 1999. Behaviour of sand confined with single and multiple geocells. Geotextiles and Geomembranes, 17(3), 171-184.

Rea, M., Mitchell, J. K., 1978. Sand reinforcement using paper grid cells. In: Proceedings of the

Regular Meeting. Rocky Mountain Coal Mining Institute, April 24-28, Pittsburgh, Pennsylvania, USA, pp 644-663.

Rosa, M.G., Cetin, B., Edil, T.B. and Benson, C.H., 2017. Freeze–thaw performance of fly ash–stabilized materials and recycled pavement materials. Journal of Materials in Civil Engineering, 29(6), 04017015.

Roustaei, M., Eslami, A. and Ghazavi, M., 2015. Effects of freeze–thaw cycles on a fiber reinforced fine grained soil in relation to geotechnical parameters. Cold Regions Science and Technology, 120, 127-137.

Saevarsdottir, T., Erlingsson, S. and Carlsson, H., 2016. Instrumentation and performance modelling of heavy vehicle simulator tests. International Journal of Pavement Engineering, 17(2), pp.148-165.

Saride, S., Rayabharapu, V.K., Vedpathak, S., 2015. Evaluation of rutting behaviour of geocell reinforced sand subgrades under repeated loading. Indian Geotechnical Journal, 45(4), 378-388.

Shadmand, A., Ghazavi, M. and Ganjian, N., 2018. Load-settlement characteristics of large-scale square footing on sand reinforced with opening geocell reinforcement. Geotextiles and Geomembranes, 46(3), 319-326.

Shen, J., Wang, Q., Chen, Y., Han, Y., Zhang, X. and Liu, Y., 2022. Evolution process of the microstructure of saline soil with different compaction degrees during freeze-thaw cycles. Engineering geology, 304, 106699.

Simonsen, E., Isacsson, U., 1999. Thaw weakening of pavement structures in cold regions. Cold regions science and technology, 29(2), 135-151.

Simonsen, E., Janoo, V.C., Isacsson, U., 2002. Resilient properties of unbound road materials during seasonal frost conditions. Journal of Cold Regions Engineering, 16(1), 28-50.

Svec, O.J., Goodrich, L.E., Palmer, J.H.L., 1983. Heat transfer characteristics of in-ground heat exchangers. International Journal of Energy Research, 7(3), 265-278.

Swett, L., Mallick, R.B. and Humphrey, D.N., 2008. A study of temperature and traffic load related response in different layers in an instrumented flexible pavement. International Journal of Pavement Engineering, 9(5), pp.303-316.

Syed, I., Scullion, T. and Randolph, R.B., 2000. Tube suction test for evaluating aggregate base materials in frost- and moisture- susceptible environments. Transportation Research Record, 1709(1), 78-90.

Tafreshi, S.M., Sharifi, P. and Dawson, A.R., 2016. Performance of circular footings on sand by use of multiple-geocell or-planar geotextile reinforcing layers. Soils and Foundations, 56(6), 984-997.

Tanyu, B.F., Aydilek, A.H., Lau, A.W., Edil, T.B., Benson, C.H., 2013. Laboratory evaluation of geocell-reinforced gravel subbase over poor subgrades. Geosynthetics International, 20(2), 47-61.

Tester, R.E. and Gaskin, P.N., 1996. Effect of fines content on frost heave. Canadian Geotechnical Journal, 33(4), 678-680.

Thakur, J.K., Han, J., Pokharel, S.K., Parsons, R.L., 2012. Performance of geocell-reinforced recycled asphalt pavement (RAP) bases over weak subgrade under cyclic plate loading. Geotextiles and Geomembranes, 35, 14-24.

Timm, D.H. and Priest, A.L., 2004. Dynamic pavement response data collection and processing at the NCAT test track. NCAT Report, 4(03).

Timm, D.H., Priest, A.L. and McEwen, T.V., 2004. Design and instrumentation of the structural pavement experiment at the NCAT test track. Research Report, NCAT Report 04-01, National

Center for Asphalt Technology, Auburn University, Auburn, Alabama, USA.

Tingle, J.S. and Jersey, S.R., 2005. Cyclic plate load testing of geosynthetic-reinforced unbound aggregate roads. Transportation research record, 1936(1), 60-69.

Transportation Officials, 1993. AASHTO Guide for Design of Pavement Structures, 1993 (Vol. 1). Aashto.

Viklander, P., 1998. Permeability and volume changes in till due to cyclic freeze/thaw. Canadian Geotechnical Journal, 35(3), 471-477.

Viswanadham, B.V.S. and König, D., 2004. Studies on scaling and instrumentation of a geogrid. Geotextiles and Geomembranes, 22(5), 307-328.

Wang, D., Ma, W., Niu, Y., Chang, X., Wen, Z., 2007. Effects of cyclic freezing and thawing on mechanical properties of Qinghai-Tibet clay. Cold regions science and technology, 48(1), 34-43.

Wang E.L., Xu X.Y., 2008. Experimental study on tensile characteristics of plastic geogrid under low temperature. Rock and Soil Mechanics, 29(6), pp.1507-1511.

Wang, J.Q., Zhang, L.L., Xue, J.F. and Tang, Y., 2018. Load-settlement response of shallow square footings on geogrid-reinforced sand under cyclic loading. Geotextiles and Geomembranes, 46(5), 586-596.

Wang, T.L., Yue, Z.R., Ma, C. and Wu, Z., 2014. An experimental study on the frost heave properties of coarse grained soils. Transportation Geotechnics, 1(3), 137-144.

Wei, H., Jiao, Y. and Liu, H., 2015. Effect of freeze–thaw cycles on mechanical property of silty clay modified by fly ash and crumb rubber. Cold Regions Science and Technology, 116, 70-77.

White, D.J., Gieselman, H.H., Douglas, C., Zhang, J. and Vennapusa, P., 2010. In-Situ Compaction Measurements for Geosynthetic Stabilized Subbase: Weirton, West Virginia. EERC Publication

ER10-05.

White, D.J. and Vennapusa, P., 2013. Low-cost rural surface alternatives: literature review and recommendations. Project No. TR-632, Iowa Department of Transportation, Ames, Iowa, USA.

Wong, L.C. and Haug, M.D., 1991. Cyclical closed-system freeze–thaw permeability testing of soil liner and cover materials. Canadian Geotechnical Journal, 28(6), 784-793.

Xie, S.B., Jian-jun, Q., Yuan-ming, L., Zhi-wei, Z. and Xiang-tian, X., 2015. Effects of freeze-thaw cycles on soil mechanical and physical properties in the Qinghai-Tibet Plateau. Journal of Mountain Science, 12(4), 999-1009.

Yang, K.H., Chiang, J., Lai, C.W., Han, J. and Lin, M.L., 2020. Performance of geosynthetic-reinforced soil foundations across a normal fault. Geotextiles and Geomembranes.

Yang, Z., Liu, X., Zhang, L., Niu, F., Ling, X., Li, G. and Shi, W., 2021. Dynamic behavior of geosynthetic-reinforced expansive soil under freeze-thaw cycles. Advances in Civil Engineering, 2021, pp.1-11.

Yoo, C. and Abbas, Q., 2020. Laboratory investigation of the behavior of a geosynthetic encased stone column in sand under cyclic loading. Geotextiles and Geomembranes.

Zeinali, A., Dagli, D., Edeskär, T., 2016. Freezing-thawing laboratory testing of frost susceptible soils. In: Proceedings of Nordic Geotechnical Meeting: Challenges in Nordic Geotechnics. May 25-28. Reykjavik, Iceland, pp. 267-276.

Zhang, L., Ma, W., Yang, C., 2018. Investigation on the effects of freeze-thaw action on the pore water pressure variations of soils. Journal of Offshore Mechanics and Arctic Engineering, 140(6), 062001.

Zhang, M., Zhang, X., Lai, Y., Lu, J. and Wang, C., 2020. Variations of the temperatures and volumetric unfrozen water contents of fine-grained soils during a freezing–thawing process.

Acta Geotechnica, 15(3), 595-601.

Zhang, L., Zhao, M., Shi, C., Zhao, H., 2010. Bearing capacity of geocell reinforcement in embankment engineering. Geotextiles and Geomembranes, 28(5), 475-482.

Zhang, W., Guo, A. and Lin, C., 2019. Effects of cyclic freeze and thaw on engineering properties of compacted loess and lime-stabilized loess. Journal of Materials in Civil Engineering, 31(9), 04019205.

Zheng, H., Sasaki, Y. and Kanie, S., 2020. Image processing method for observing ice lenses produced by the frost heave process. Cold Regions Science and Technology, 171, 102977.

Appendices

Appendix A presents the photographs of water on the surface of unreinforced and reinforced soils before and after F-T cycles to Chapter 2 Figs. S.2.1 to S.2.6.

Appendix B presents the Supplementary Materials to Chapter 3 Figs. S.3.1 to S.3.6.

Appendix A: Supplementary Figures of Chapter 2

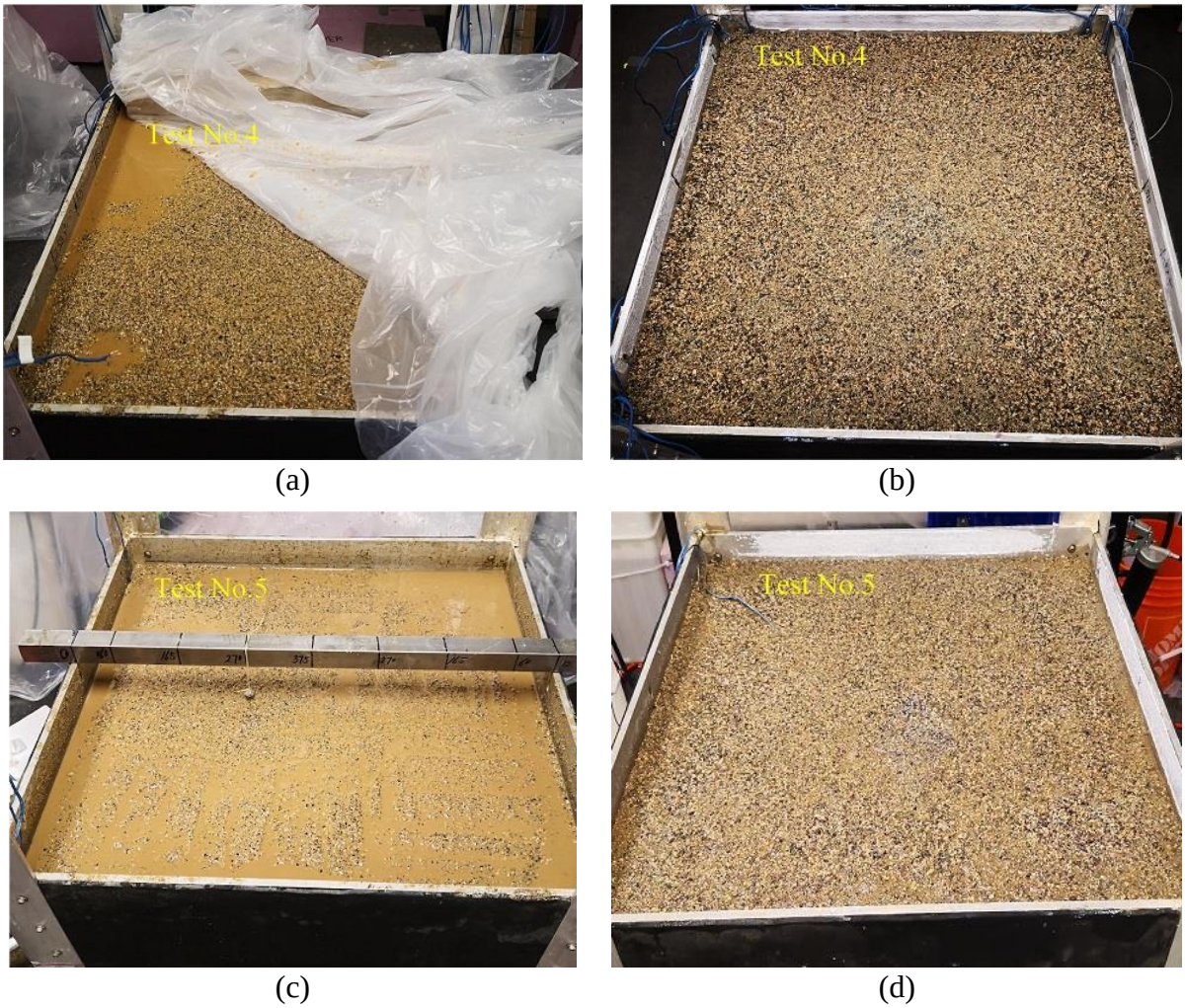

(a) (b)

(c) (d)

Fig. S.2.1. Photographs of moisture on the surface of unreinforced soil with 0% fines: (a) before 1 F-T cycle, (b) after 1 F-T cycle, (c) before 5 F-T cycles and (d) after 5 F-T cycles

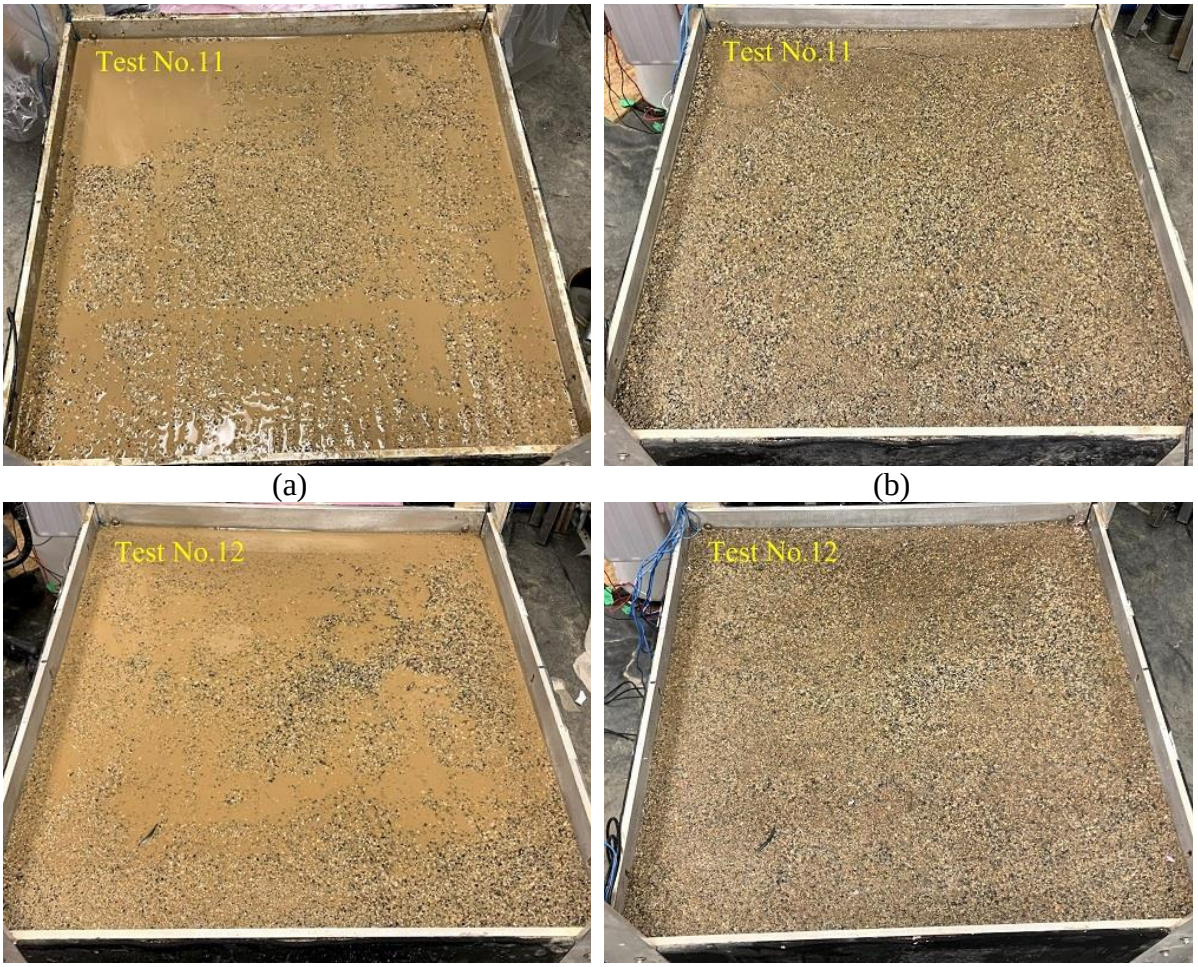

(a) (b)

(c) (d)

Fig. S.2.2. Photographs of moisture on the surface of reinforced soil with 0% fines: (a) before 1 F-T cycle, (b) after 1 F-T cycle, (c) before 5 F-T cycles and (d) after 5 F-T cycles

1

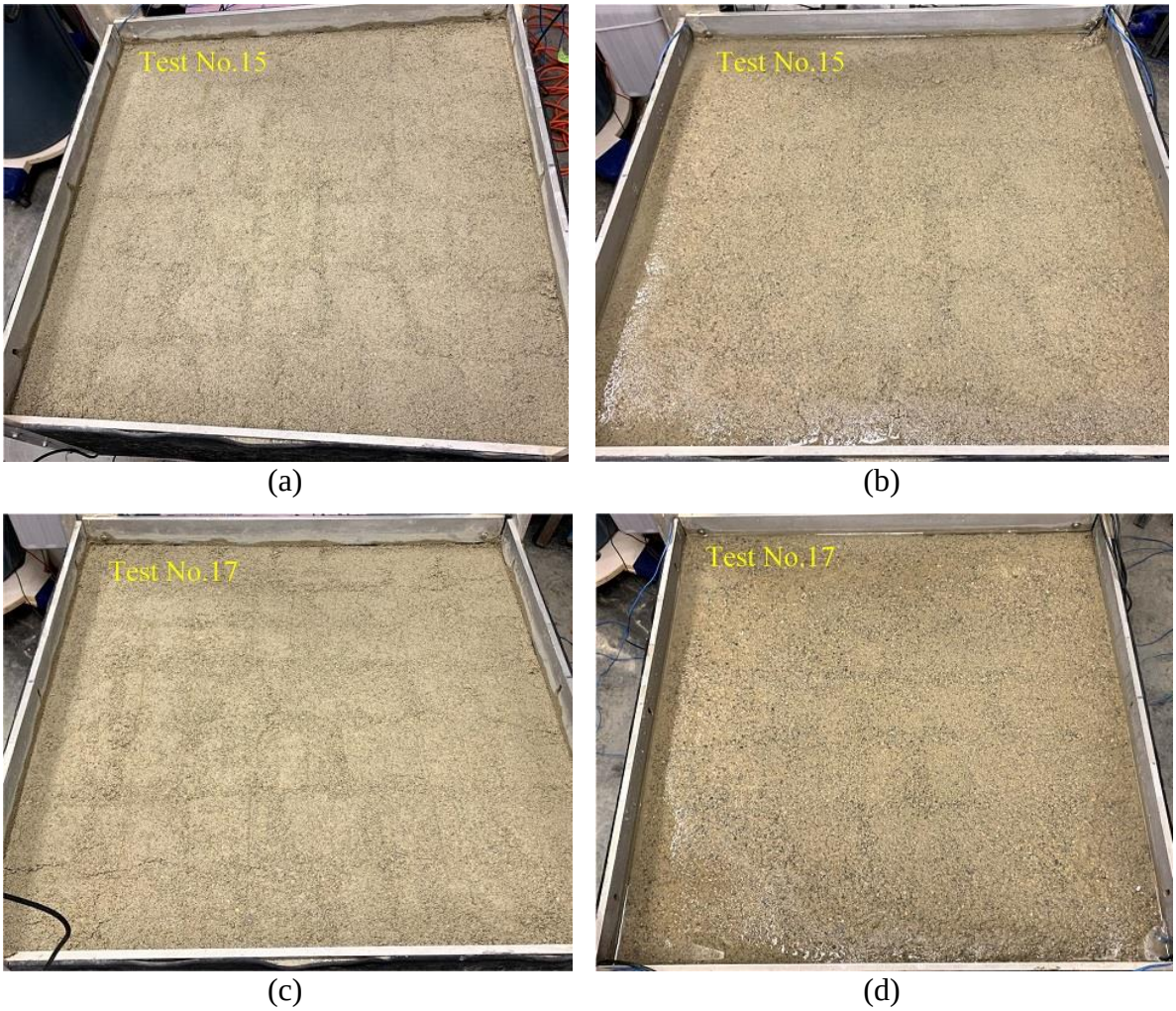

Fig. S.2.3. Photographs of water on the surface of unreinforced soil with 5% fines: (a) before 1 F-T cycle, (b) after 1 F-T cycle, (c) before 5 F-T cycles and (d) after 5 F-T cycles

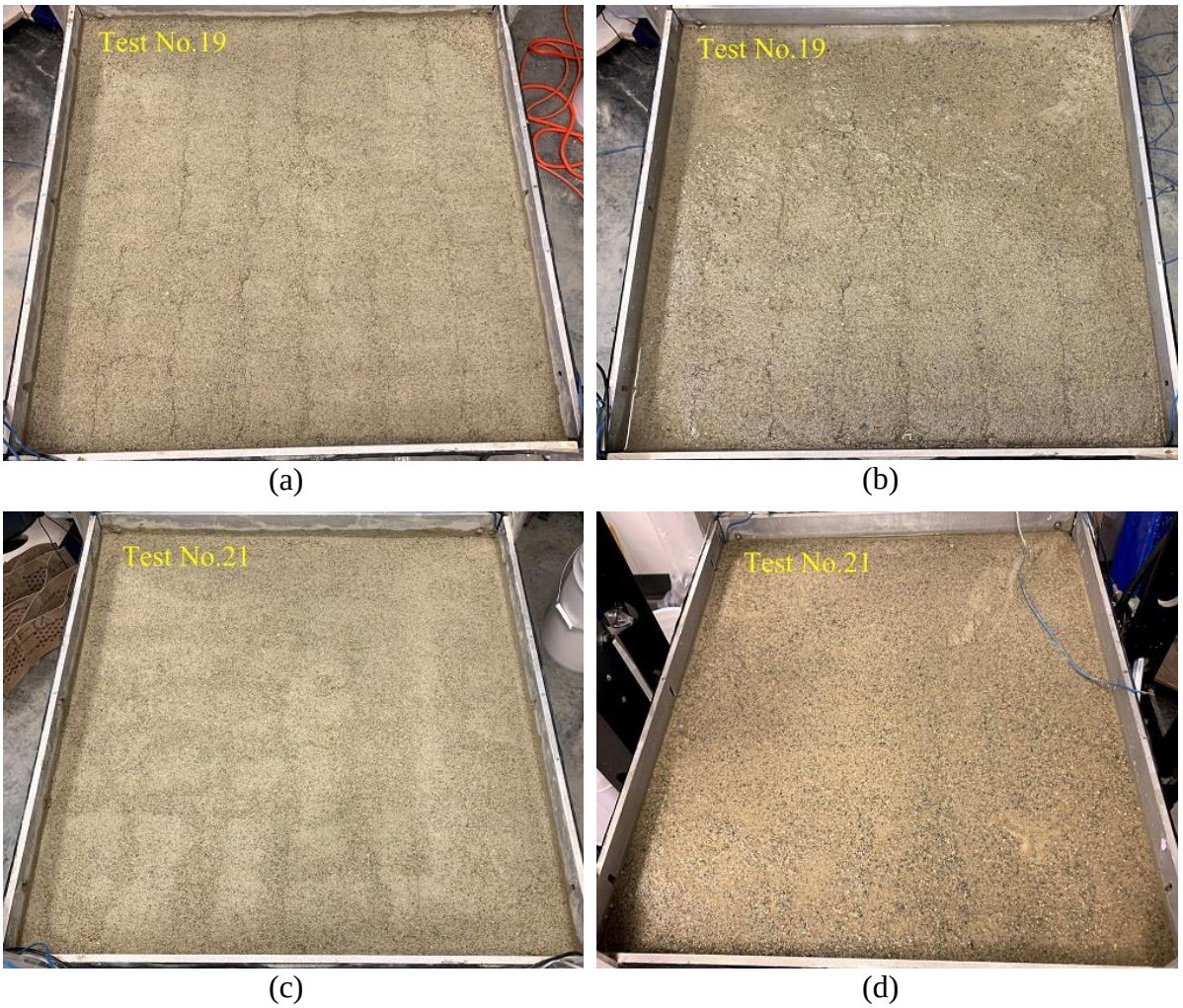

Fig. S.2.4. Photographs of water on the surface of reinforced soil with 5% fines: (a) before 1 F-T cycle, (b) after 1 F-T cycle, (c) before 5 F-T cycles and (d) after 5 F-T cycles

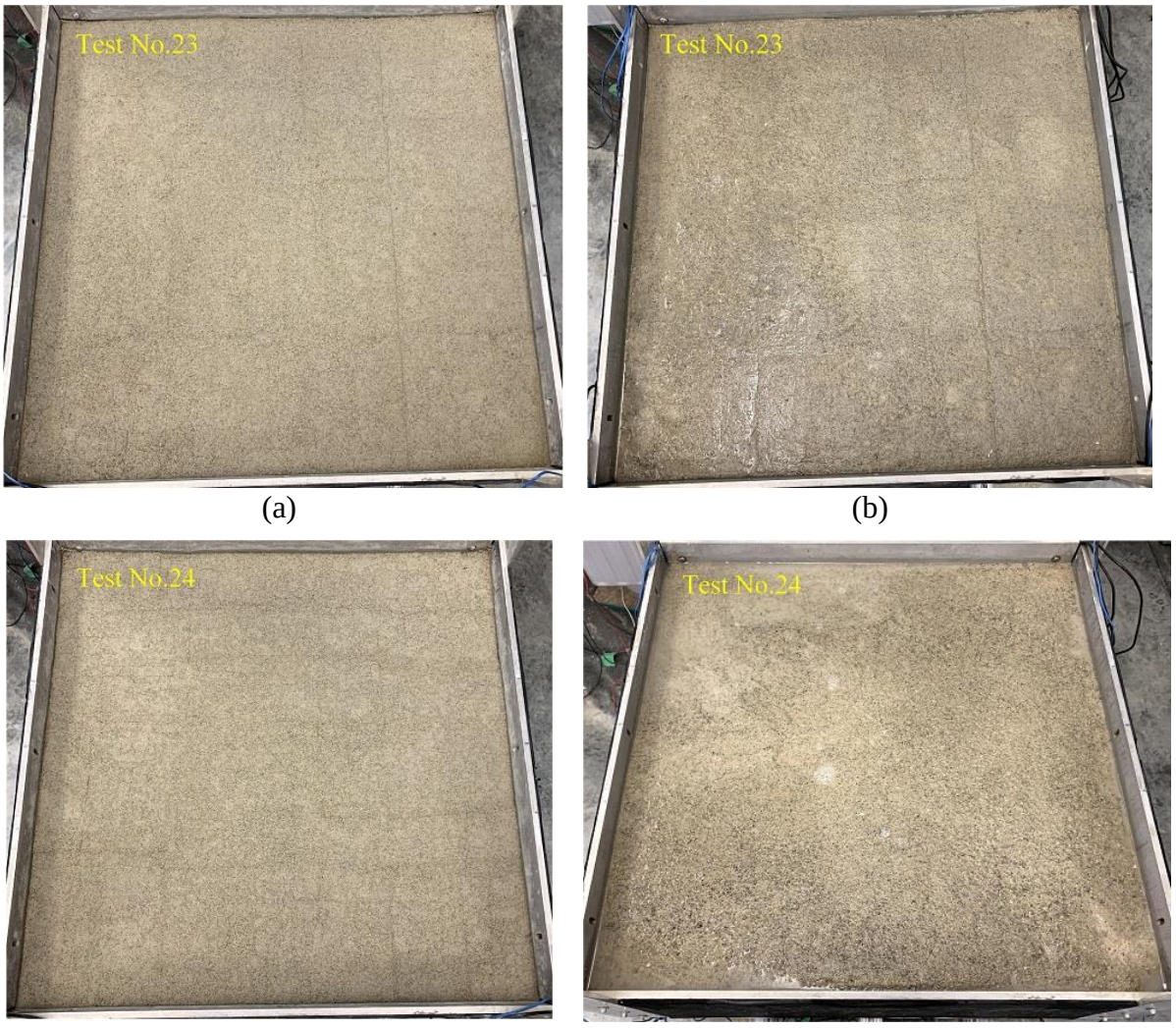

Fig. S.2.5. Photographs of water on the surface of unreinforced soil with 12% fines: (a) before 1 F-T cycle, (b) after 1 F-T cycle, (c) before 5 F-T cycles and (d) after 5 F-T cycles

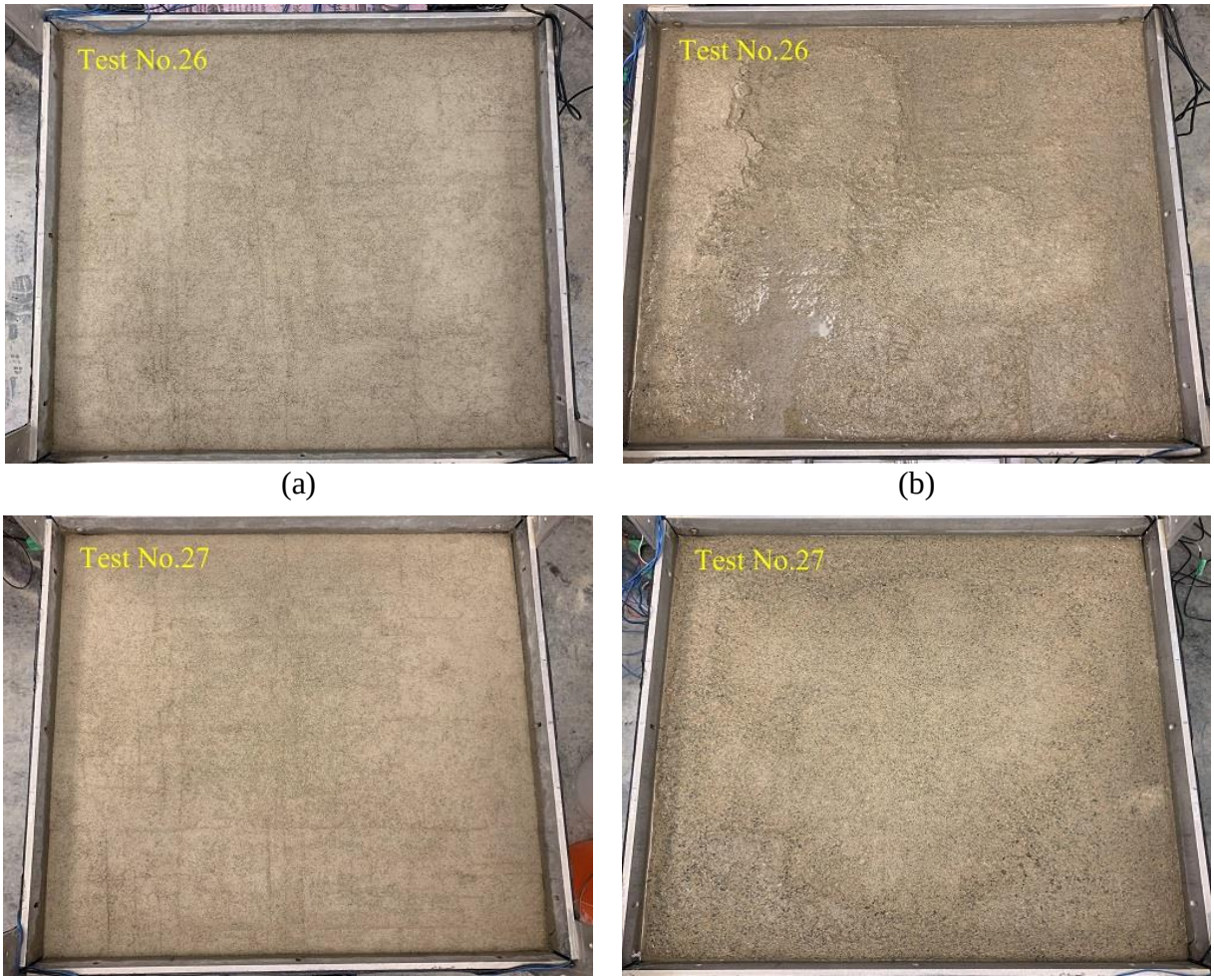

Fig. S.2.6. Photographs of water on the surface of reinforced soil with 12% fines: (a) before 1 F-T cycle, (b) after 1 F-T cycle, (c) before 5 F-T cycles and (d) after 5 F-T cycles

Appendix B: Supplementary Figures of Chapter 3

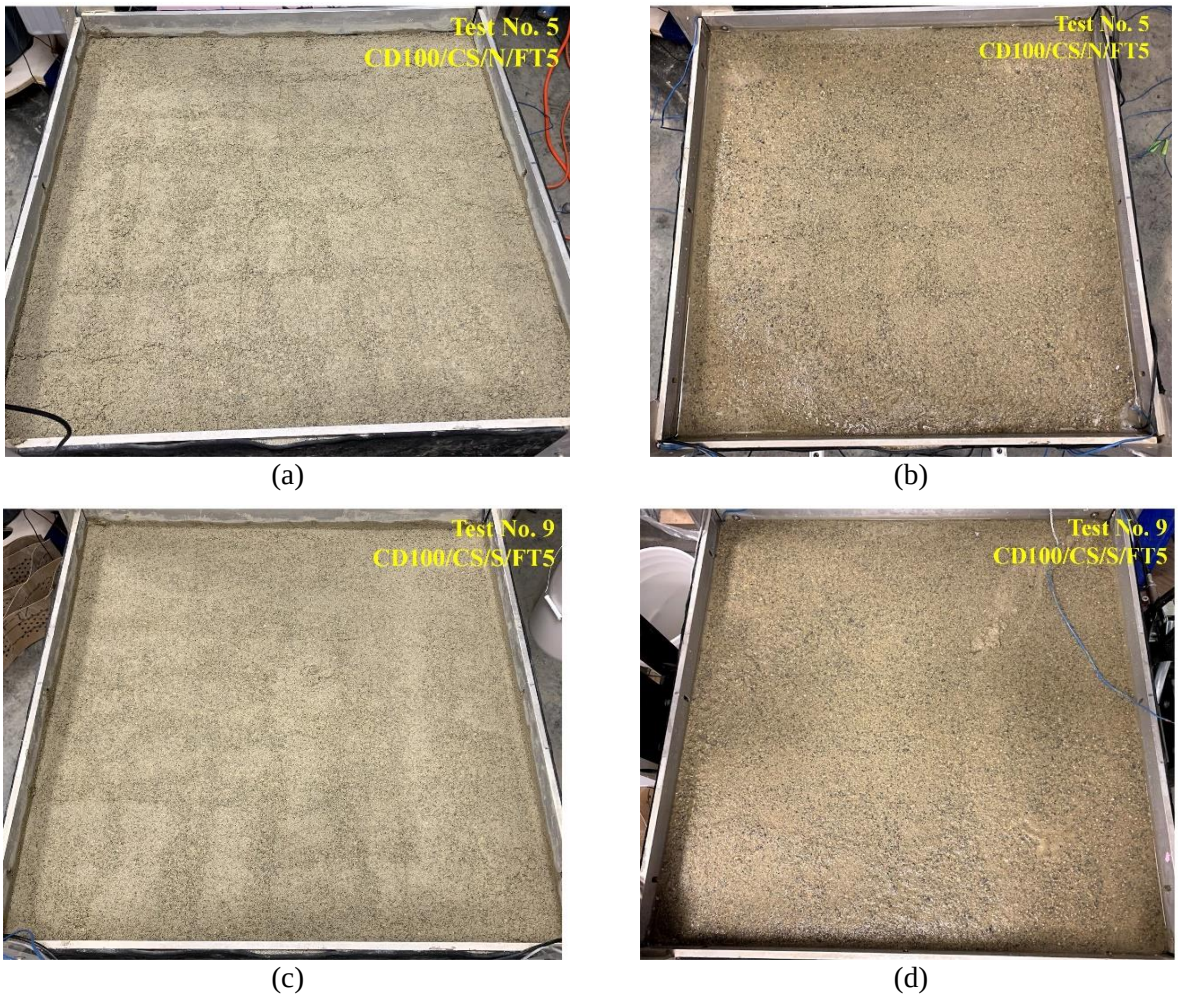

Fig. S.3.1. Observations of water on base surface (100% compaction) in a closed system: (a) and (b) non-stabilized bases before and after five F-T cycles, respectively, (c) and (d) stabilized bases before and after five F-T cycles, respectively

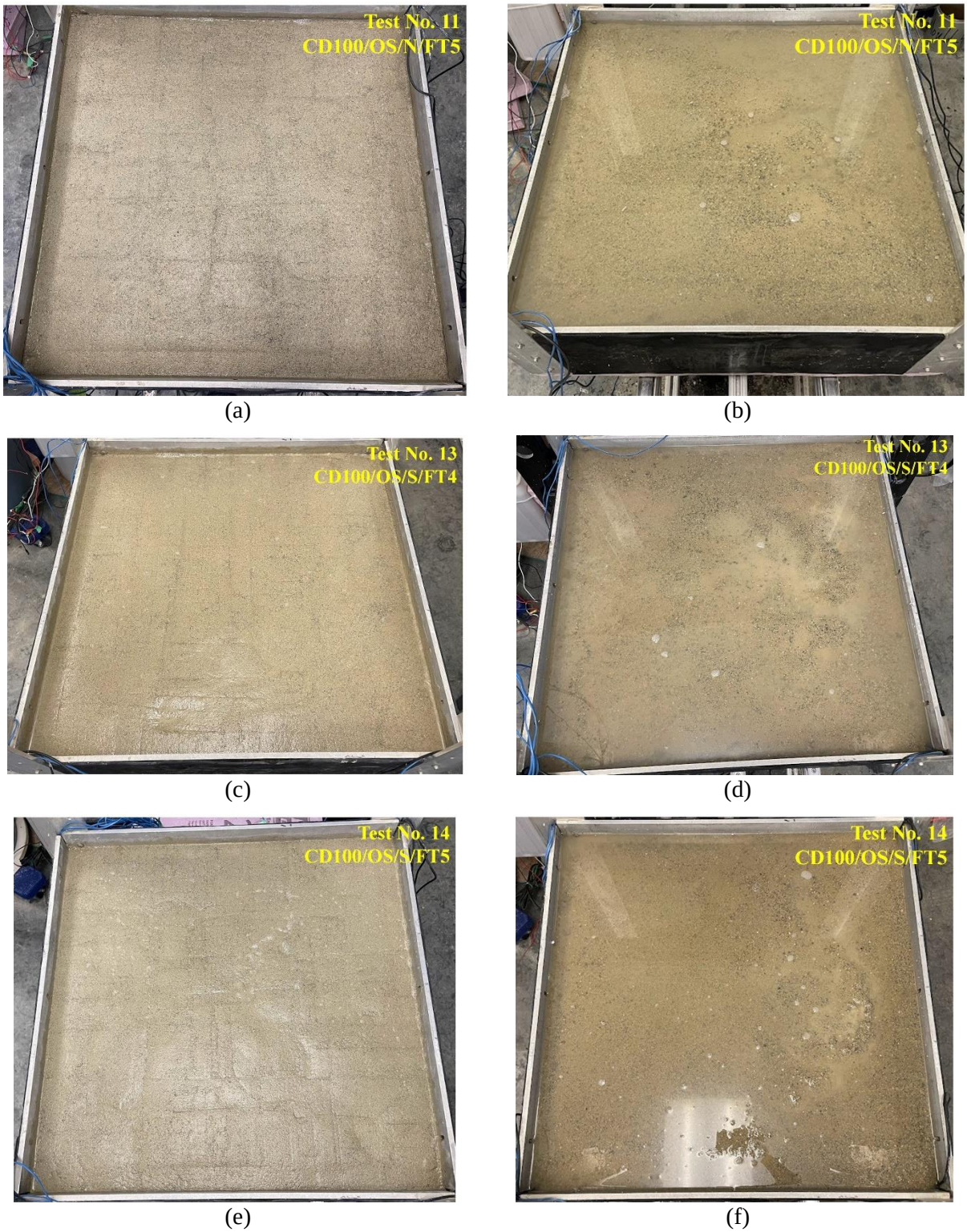

Fig. S.3.2. Observations of water on base surface (100% compaction) in an open system: (a) and (b) non-stabilized bases before and after five F-T cycles, respectively, (c) and (d) stabilized bases before and after four F-T cycles, respectively, (e) and (f) stabilized bases before and after five F-T cycle

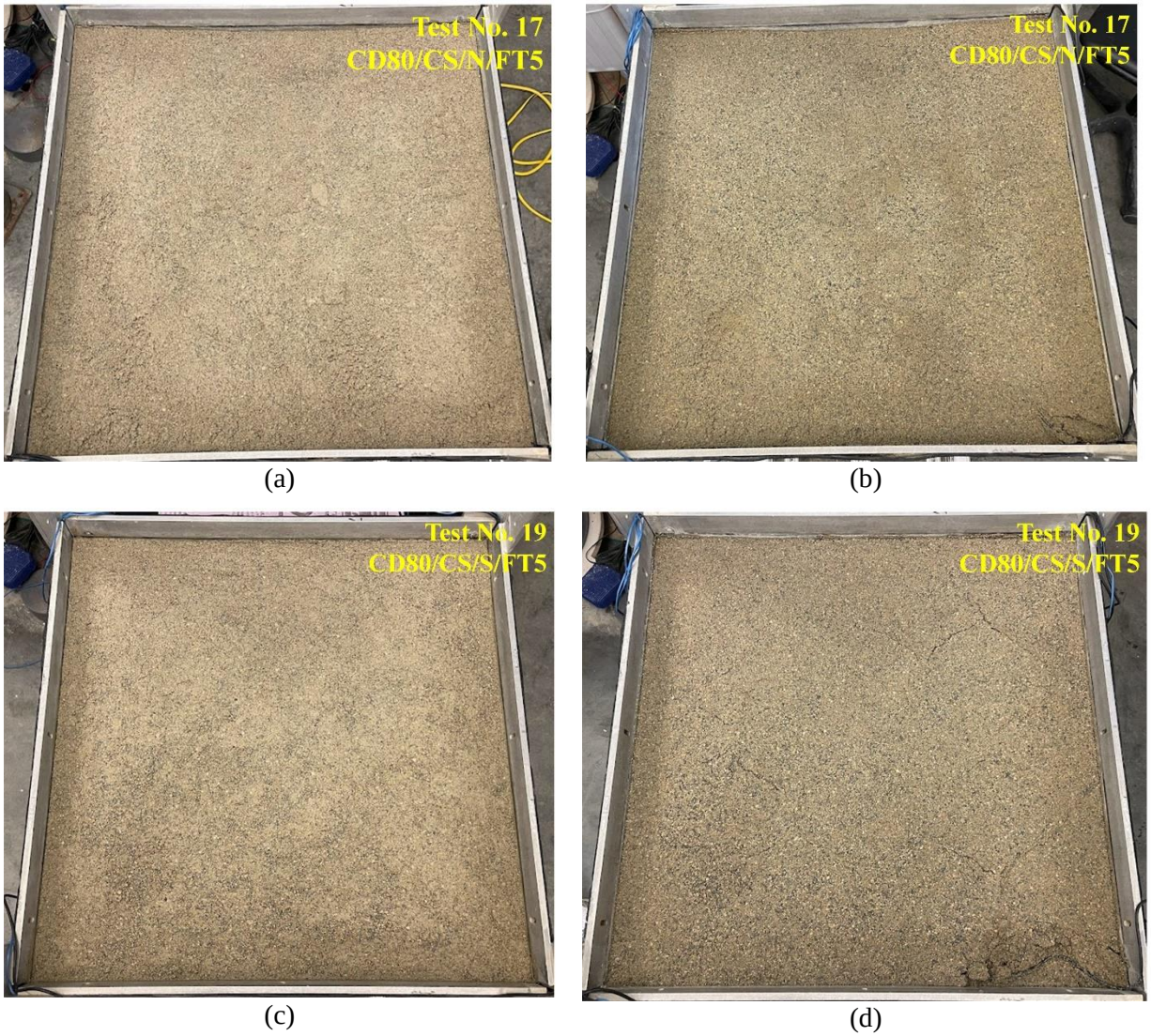

Fig. S.3.3. Observations of water on base surface (80% compaction) in a closed system: (a) and (b) non-stabilized bases before and after five F-T cycles, respectively, (c) and (d) stabilized bases before and after five F-T cycles, respectively

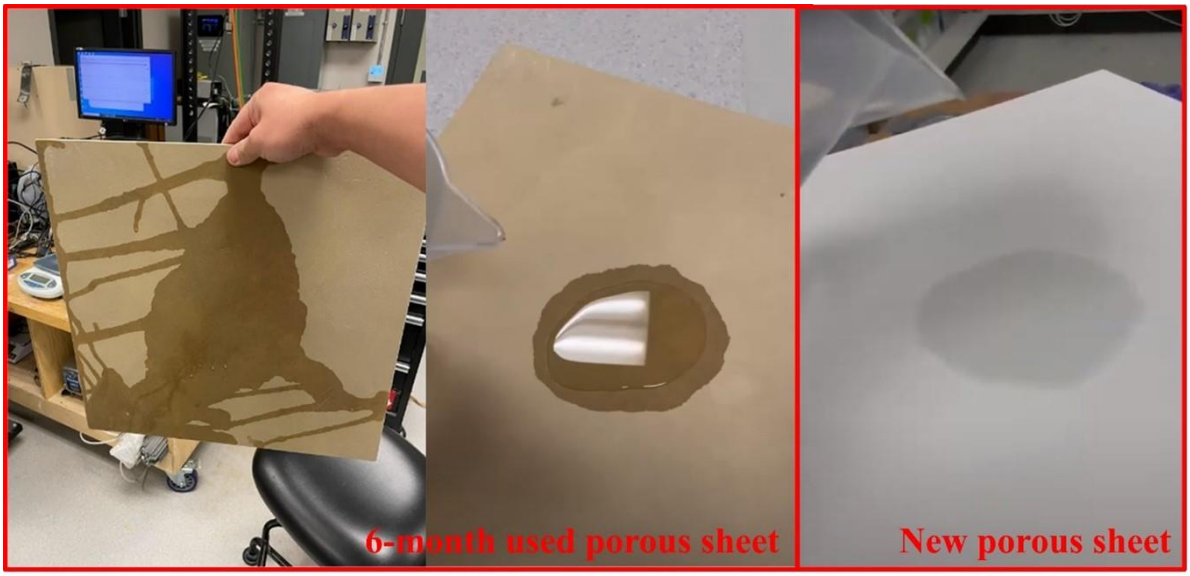

Fig. S.3.4. Visible comparison of the permeability of the porous sheet after six months

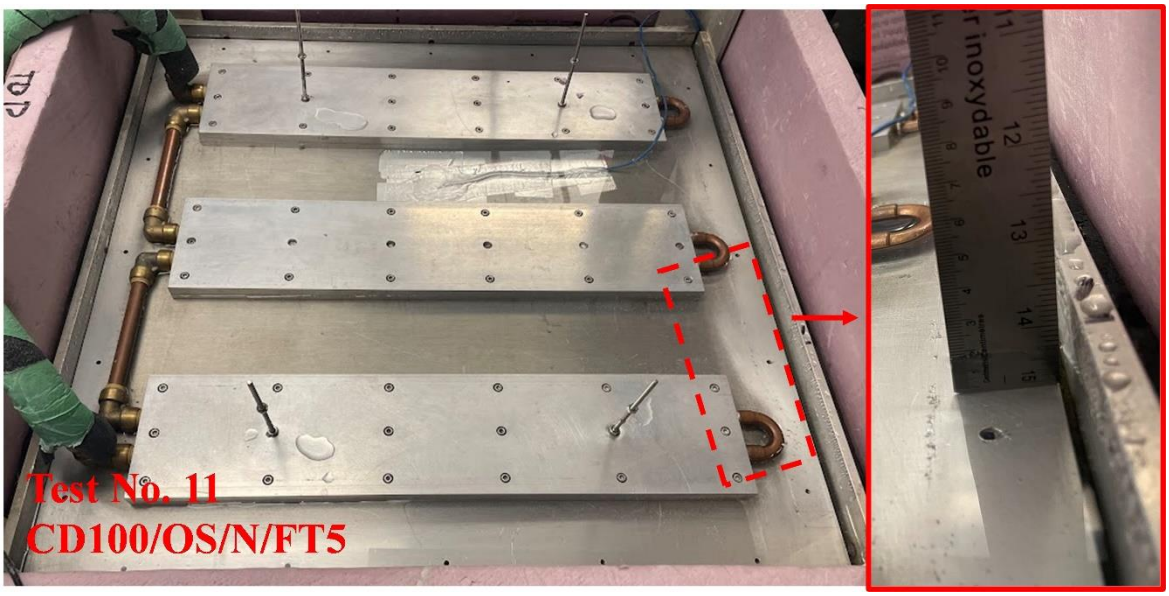

(a)

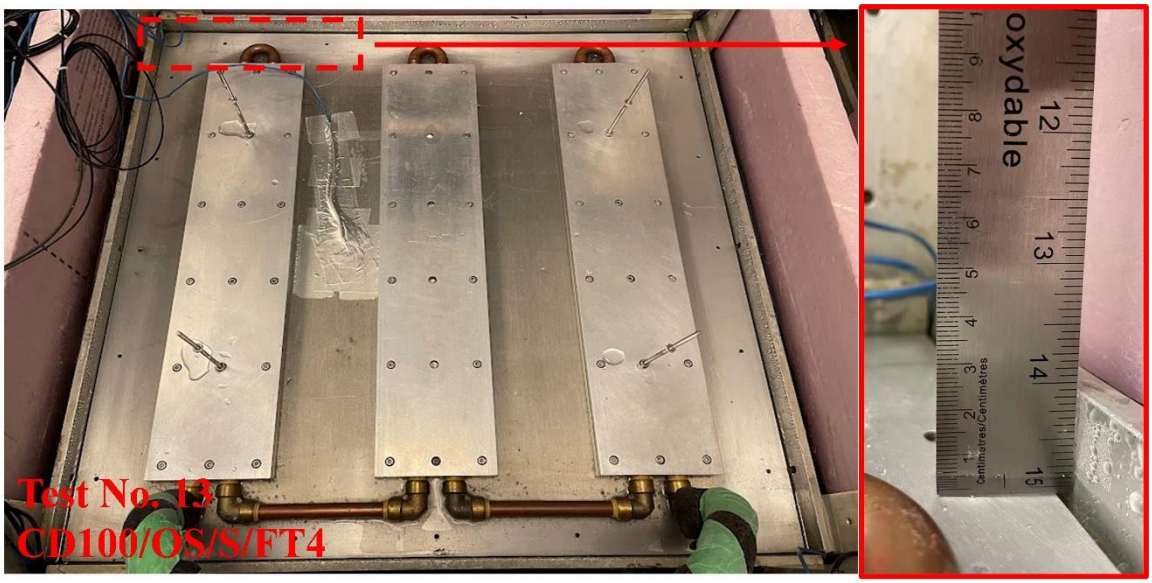

(b)

Fig. S.3.5. Water accumulated on top of the cooling plate after the second F-T cycle in an open system of: (a) non-stabilized bases and (b) stabilized bases

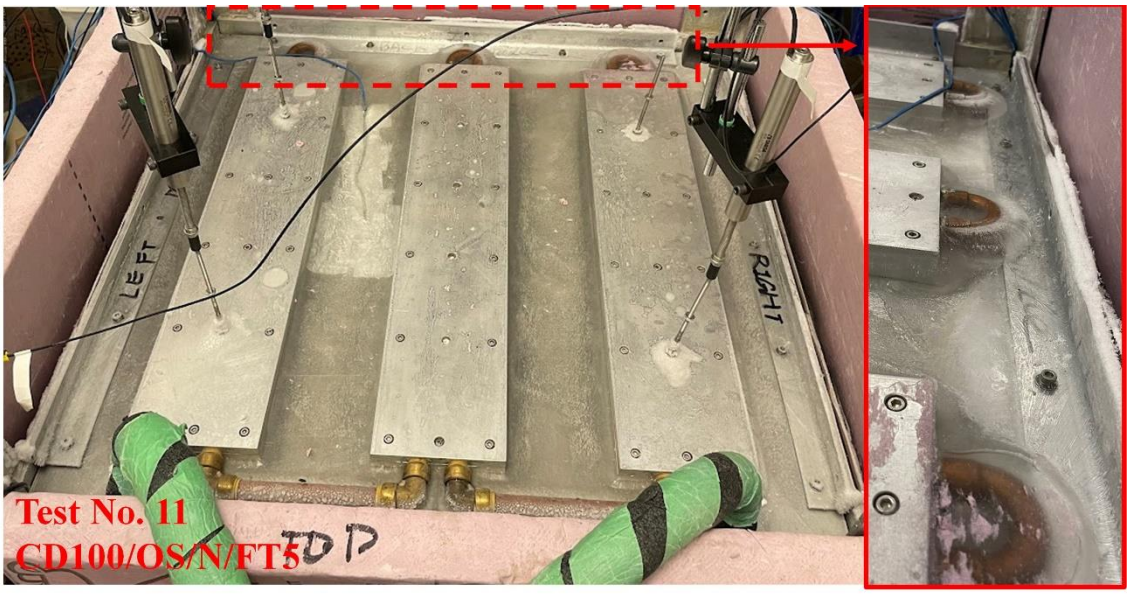

(a)

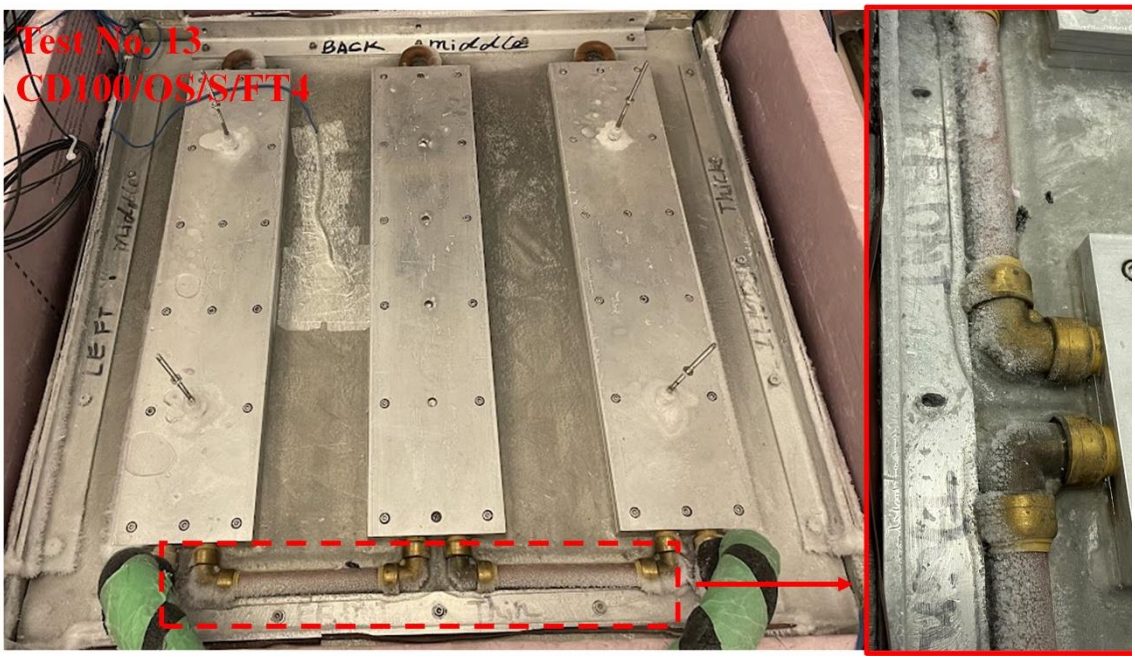

(b)

Fig. S.3.6. Ice accumulated on top of the cooling plate after the third freezing stage in an open system of: (a) non-stabilized bases and (b) stabilized bases